Temporal and spatial features of the turbulent kinetic energy cascade

Ryo Araki

To cite this version:

Ryo Araki. Temporal and spatial features of the turbulent kinetic energy cascade. Other. Ecole Centrale de Lyon, 2023. English. NNT : 2023ECDL0035 . tel-04473864

HAL Id: tel-04473864
https://theses.hal.science/tel-04473864v1

Submitted on 22 Feb 2024

N° d'ordre NNT: 2023ECDL0035

THÈSE de DOCTORAT DE L'UNIVERSITÉ DE LYON
opérée au sein de l'École Centrale de Lyon

École Doctorale N° 162
Mécanique Énergétique Génie Civil Acoustique

Spécialité de doctorat : Mécanique des Fluides

Soutenue publiquement le 20/09/2023 par
ARAKI Ryo

Temporal and Spatial Features of the Turbulent Kinetic Energy Cascade

---

Devant le jury composé de

BOS, Wouter	Chargé de Recherche HDR CNRS	Directeur de Thèse
CHEVILLARD, Laurent	Chargé de Recherche HDR CNRS	Rapporteur
CHIBBARO, Sergio	Professeur Université Paris Saclay	Rapporteur
DUBRULLE, Bérengère	Directeur de Recherche CNRS	
DUGUET, Yohann	Chargé de Recherche HDR CNRS	
GOTO, Susumu	Professeur Osaka University	Directeur de Thèse
PUMIR, Alain	Directeur de Recherche CNRS	

Temporal and Spatial Features
of the Turbulent Kinetic Energy Cascade

ARAKI Ryo

September 2023

Temporal and Spatial Features of the Turbulent Kinetic Energy Cascade

A dissertation submitted to
THE GRADUATE SCHOOL OF ENGINEERING SCIENCE
OSAKA UNIVERSITY
in partial fulfillment of the requirements for the degree of
DOCTOR OF PHILOSOPHY IN SCIENCE

By

ARAKI Ryo

September 2023

Abstract

Three-dimensional turbulence is characterised by a multi-scale mechanism in which the energy injected by external forcing and/or boundary conditions is transferred to smaller scales, where it is dissipated into heat by molecular viscosity. Although this *energy cascade* is a commonly accepted conceptual picture of turbulence, providing the basis for statistical theory, its precise understanding is yet missing. This thesis consists of three parts and investigates the turbulent kinetic energy cascade from time, space, and scale-point of view.

The first part discusses quasi-cyclic temporal behaviour observed in turbulence driven by a steady forcing. To construct a minimal three-equation model reproducing quasi-cyclic behaviour, lower-Reynolds-number periodic flow is decomposed into scales representing the external forcing, energetic modes, and energy dissipation. Furthermore, the similarity between this low-dimensional model and turbulence is assessed using phase-space orbits and bifurcation analysis.

The second part discusses the physical-space locality of nonlinear interactions in turbulence. More specifically, the relation between the spatial locality and the multi-scale nature of nonlinear interactions is discussed using a system in which the nonlinear term of the Navier–Stokes equations is restricted in a space-local sense. The results show that the nonlinear interactions restricted to a space-local domain of radius R can sustain the energy cascade for wavenumbers $\gtrsim 1/R$.

The third part discusses nonequilibrium scaling of turbulence induced by large-scale fluctuations. First, large-scale inhomogeneity is considered as a perturbation around the $k^{-5/3}$ wavenumber scaling of the energy spectrum, allowing us to derive a nonequilibrium scaling correction proportional to $k^{-7/3}$. This nonequilibrium scaling, decaying faster than the equilibrium scaling as a function of the wavenumber, is confirmed numerically. Furthermore, by applying the same methodology for large-scale inhomogeneity and unsteadiness, a unified description of the scaling law between the fluctuations of the normalised energy dissipation rate and the Reynolds number is proposed.

Keywords: Energy cascade, unsteady turbulence, inhomogeneous turbulence, direct numerical simulation

Résumé

La turbulence tridimensionnelle est caractérisée par un mécanisme multi-échelle dans lequel l'énergie injectée par un forçage externe et/ou des conditions aux limites est transférée à des échelles plus petites jusqu'à ce qu'elle soit dissipée en chaleur par la viscosité moléculaire. Bien que cette *cascade d'énergie* soit une image conceptuelle communément acceptée, fournissant la base de la théorie statistique de la turbulence, sa compréhension précise fait encore défaut. Cette thèse se compose de trois parties et étudie la cascade d'énergie cinétique turbulente du point de vue du temps, de l'espace et de l'échelle.

La première partie traite du comportement temporel quasi-cyclique observé dans un écoulement turbulent maintenu par un forçage constant. Pour construire un modèle minimal à trois équations reproduisant un comportement quasi-cyclique, l'écoulement à faible nombre de Reynolds est décomposé en échelles représentant le forçage externe, les modes énergétiques et la dissipation d'énergie. De plus, la similitude entre ce modèle à basse dimension et la turbulence est évaluée à l'aide d'orbites dans l'espace des phases et d'une analyse de bifurcation.

La deuxième partie discute la localité dans l'espace physique des interactions non linéaires dans la turbulence. Plus précisément, la relation entre la localité spatiale et la nature multi-échelle des interactions non linéaires est examinée à l'aide d'un système dans lequel le terme non linéaire des équations de Navier–Stokes est restreint dans l'espace. Les résultats montrent que les interactions non linéaires restreintes à un domaine spatial local de rayon R peuvent entretenir la cascade d'énergie à des nombres d'onde $\gtrsim 1/R$.

La troisième partie discute le comportement hors équilibre de la turbulence induite par des fluctuations à grande échelle. Tout d'abord, l'inhomogénéité à grande échelle est considérée comme une perturbation autour de du spectre d'énergie d'équilibre (proportionnel à $k^{-5/3}$), ce qui nous permet de dériver une correction proportionnelle à $k^{-7/3}$. Cette correction, qui décroît plus rapidement que le spectre d'équilibre (en fonction du nombre d'ondes), est confirmée numériquement. De plus, en appliquant la même méthodologie pour l'inhomogénéité et l'instabilité, une description unifiée de la relation entre les fluctuations du taux de dissipation d'énergie normalisé et le nombre de Reynolds sont proposés.

Mots clés: Cascade d'énergie, turbulence instationnaire, turbulence inhomogène, simulation numérique directe

要旨

3次元の乱流は「外力や境界条件によって大スケールへ注入されたエネルギがより小さなスケールへ輸送され，最後は分子粘性によって熱として散逸する」というマルチスケール機構によって特徴づけられる．この「エネルギカスケード」は乱流の統計理論に基礎づけを与える広く受けいれられた概念的描像であるものの，その精緻な理解はいまだ得られていない．本学位論文は三部からなり，乱流の運動エネルギカスケードを時間・空間・そしてスケールの観点から議論する．

第一部では，定常な外力で駆動される乱流にみられる時間準周期的なふるまいを議論する．Reynolds数の低い周期流を外力・エネルギ・エネルギ散逸率を代表するスケールに分割することで，準周期変動を再現するミニマルな3方程式モデルを構築する．また，相空間での軌道や分岐解析を通じて，この低自由度のモデルと乱流の類似性を評価する．

第二部では，乱流の非線形相互作用の物理空間における局所性を議論する．具体的には，Navier–Stokes方程式の非線形項を空間局所に制限した系を通じて，非線形相互作用の空間局所性とマルチスケール性の関係を調べる．その結果，半径Rの空間局所領域で定義される非線形相互作用が波数$\gtrsim 1/R$でのエネルギカスケードを維持しうることを明らかにした．

第三部では，大スケール変動が励起する乱流の非平衡スケーリングを議論する．まず，大スケールの非一様性をエネルギスペクトルの$k^{-5/3}$波数スケーリング周りの摂動として考慮することで，$k^{-7/3}$に比例する非平衡スケーリング修正を導出する．この平衡スケーリングより波数の関数としてはやく減衰する非平衡スケーリングは数値的に確認された．さらに，同様の手法を大スケールの非一様性と非定常性に対して適用することで，無次元化されたエネルギ散逸率とReynolds数の変動の間に統一的に成立するスケーリング則を提案する．

キーワード：エネルギカスケード，非定常乱流，非一様乱流，直接数値計算

Acknowledgements

On the evening of October 4, 2020, I was waiting for the flight to France at the Kansai International Airport. Being in the middle of the COVID-19 pandemic, I was alone in the pretty much empty international departures concourse. The flight to the Paris Charles de Gaulle Airport was almost vacant, too; I could lie down to rest using three seats next to me. I still remember that half-exciting and half-anxious mixed feeling on that day about spending three years in a country I had never been to. This is how my PhD has started.

After three years, I am now completing my PhD thesis. First and foremost, I express my sincerest gratitude to my two supervisors. Wouter J. T. Bos guided me all the way through my PhD. The works compiled in this thesis have been conducted in a double degree program (cotutelle) between École Centrale de Lyon and Osaka University. Even though the COVID-19 pandemic and the corresponding very strict immigration restriction policy of Japan prohibited me from going to Japan, I have been a member of the Fluid Mechanics Group (Goto lab) in Osaka during my PhD, too. Susumu Goto has been my supervisor for six years since I joined the lab in my final year of undergraduate and he taught me how to be a researcher through his enthusiasm for research.

I spend my daily life with cheeful lab members at Laboratoire de Mécanique des Fluides et d'Acoustique (LMFA). I thank Tong Wu, Wesley Agoua, Henri Lam, Bruce (Xi Yuan) Yin, and Smiron Varghese for daily discussion, conversation, and occasional hang out. I also thank the past and present members of the Goto lab. In particular, I acknowledge Kiwamu Yoshii. Although we shared the same office at Osaka University for less than half a year, we share enthusiasm on many topics.

During the three years, I have been interacting with many inspiring researchers. First, I appreciate my collaborators. I owe Tomohiro Tanogami a lot of things. He introduced me to the field of information thermodynamics and how turbulence and its energy cascade can be described in such a way. With Yohann Duguet, we planned to extend our study of the minimal model of quasi-cyclic behaviour from a dynamical system's point of view. I began a new project with Adrián Lozano-Durán and Alberto Vela-Martín, which is still in its very preliminary stage and is not included in this thesis. I look forward to finding new turbulence properties from an information-theoretic point of view. Next, I thank the researchers in the lab: Benjamin Miquel, Michio Otsuki, and Yutaro Motoori. In particular, I thank Masanobu Inubushi for his critical comments on my research and advice on my career. Finally, I thank my thesis committee members: Fujihiro Hamba, Genta Kawahara, and Kazuyasu Sugiyama, for Osaka-side and Laurent Chevillard, Sergio Chibbaro, Bérengère Dubrulle, Yohann Duguet, and Alain Pumir for Lyon-side. Their comment greatly helped me to revise and improve my thesis.

I have been fortunate to have financial support from several scholarship foundations during my study. I sincerely thank the Fujii International Scholarship Foundation for their support during the final year of the bachelor, Yoshida Scholarship Foundation for the master, and Takenaka Scholarship Foundation for the overseas PhD. Without their support, my career would have been completely different. I also appreciate opportunities to interact with other scholarship students, in which I can make invaluable friends.

Here, I acknowledge the city of Lyon and Écully, where I spend three years. Although it is true that the PhD is often highly stressful, the occasional free afternoon in this beautiful city offers great refreshment. In particular, I love walking around *Vieux Lyon* (Old Lyon) and the promenade along the two rivers: *le Rhone* and *la Saône*. I have many more great memories in Lyon; the view of the city from *Fourviére*, a variety of activities offered in *Parc de la Tête-d'Or* (Park of the Golden Head), cuisine in *bouchon*, splendid *Fête des Lumiéres* (Festival of Lights) in December, and so on. I will miss Lyon a lot and definitely come back in the near future.

Finally, I thank my family for their continuous support, which leads me to who I am today.

List of Publications

Parts of this thesis are or will be included in the following publications:

1. Araki, Ryo and Susumu Goto (2021). Quasiperiodic fluctuations of von Kármán turbulence driven by viscous stirring. *Physical Review Fluids* **6** (8), p. 084603
2. Araki, Ryo, Wouter J. T. Bos, and Susumu Goto (2023a). Minimal model of quasi-cyclic behaviour in turbulence driven by Taylor–Green forcing. *Fluid Dynamics Research* **55** (3), p. 035507. arXiv: `2112.03417 [flu-dyn]`
3. Araki, Ryo, Wouter J. T. Bos, and Susumu Goto (2023b). Space-local Navier–Stokes turbulence. *arXiv preprint*. arXiv: `2308.07255 [flu-dyn]`
4. Araki, Ryo and Wouter J. T. Bos (2022). Inertial range scaling of inhomogeneous turbulence. *arXiv preprint*. arXiv: `2210.14516 [flu-dyn]`
5. Bos, Wouter J. T. and Ryo Araki (in preparation). Analysis of the normalized dissipation rate in inhomogeneous and unsteady turbulence

This thesis does not include the content of the following publications:

6. Tanogami, Tomohiro and Ryo Araki (2022). Information-thermodynamic bound on information flow in turbulent cascade. *arXiv preprint*. arXiv: `2206.11163 [stat-mech]`

List of Figures

List of Tables

List of Frequently Used Symbols

Acronyms

DNS	Direct Numerical Simulation (defined on page 7)
DoF	Degrees of Freedom (defined on page 32)
HIT	Homogeneous and Isotropic Turbulence (defined on page 13)
K41	Kolmogorov 1941 (theory) (defined on page 19)
LBM	Lattice Boltzmann Method (defined on page 58)
LEH	Local Equilibrium Hypothesis (defined on page 12)
PDF	Probability Distribution Function (defined on page 65)
POD	Proper Orthogonal Decomposition (defined on page 34)
QCB	Quasi-Cyclic Behaviour (defined on page 28)
RHS	Right Hand Side (defined on page 7)
SPO	Stable Periodic Orbit (defined on page 28)
SSA	Strain Self-Amplification (defined on page 124)
UPO	Unstable Periodic Orbit (defined on page 22)
VS	Vortex Stretching (defined on page 124)

Greek characters

δ_{ij}	Kronecker's delta function (defined on page 10)
$\epsilon(k)$	Cumulative energy dissipation spectrum at wavenumber k (defined on page 13)
ϵ	Energy dissipation rate (defined on page 7)
ϵ_{ijk}	Levi-Civita symbol (permutation symbol) (defined on page 20)
η	Kolmogorov length scale (defined on page 14)
λ	Taylor micro length scale (defined on page 65)
ν	Kinematic viscosity (defined on page 6)
Ω	Domain of the flow (defined on page 6)
Ω_k	Spherical shell of radius k (defined on page 10)
$\mathit{\Pi}(k)$	Energy flux spectrum at wavenumber k (defined on page 12)
$\boldsymbol{\omega}$	Vorticity field $= (\omega_x, \omega_y, \omega_z)$ (defined on page 7)
$\boldsymbol{\mathit{\Omega}}$	Rate-of-rotation tensor (defined on page 8)

Latin characters

i	imaginary unit (defined on page 9)
Re	Reynolds number (defined on page 7)
$\boldsymbol{A}$	Velocity gradient tensor (defined on page 8)
$\boldsymbol{f}$	Forcing field $= (f_x, f_y, f_z)$ (defined on page 6)
$\boldsymbol{k}$	Fourier mode $= (k_x, k_y, k_z)$; also $\boldsymbol{p}$, $\boldsymbol{q}$ (defined on page 9)
$\boldsymbol{N}$	Nonlinear term $= (N_x, N_y, N_z)$ (defined on page 67)
$\boldsymbol{S}$	Rate-of-strain tensor (defined on page 8)
$\boldsymbol{u}$	Velocity field $= (u_x, u_y, u_z)$ (defined on page 6)
$\boldsymbol{x}$	Physical space coordinate $= (x, y, z)$ (defined on page 6)
C_ϵ	Normalised energy dissipation rate (defined on page 16)
C_K	Kolmogorov constant (defined on page 14)
$E(k)$	Energy spectrum at wavenumber k (defined on page 10)
$F(k)$	Energy injection spectrum at wavenumber k (defined on page 10)
f_0	Forcing amplitude (defined on page 37)
H	Helicity (defined on page 7)
K	Energy (defined on page 7)
k	Wavenumber (defined on page 10)
L	Macroscopic length scale (defined on page 7)
P	Energy input rate (defined on page 7)
p	Pressure field (defined on page 6)
$P_{ij}(\boldsymbol{k})$	Orthogonal projection tensor for vector $\boldsymbol{k}$ (defined on page 10)
R	Radius of the space-local domain (defined on page 62)
$T(k)$	Energy transfer spectrum at wavenumber k (defined on page 10)
T	Macroscopic time scale (defined on page 31)
t	Time (defined on page 6)
U	Macroscopic velocity scale (defined on page 7)
X	Characteristic velocity of the forced modes (defined on page 43)
Y	Characteristic velocity of the energetic modes (defined on page 43)
Z	Characteristic velocity of the residual modes (defined on page 47)

Mathematical operators

$\cdot^{\lessgtr}$	Band-pass filter (defined on page 65)
$\cdot^{<}$	Low-pass filter (defined on page 12)
$\cdot^{>}$	High-pass filter (defined on page 12)
$\langle\cdot\rangle_{\mathrm{ens}}$	Ensemble average (defined on page 85)

$\langle\cdot\rangle_\Omega$	Spatial average (defined on page 7)
$\langle\cdot\rangle_{\mathrm{phase}}$	Temporal phase average (defined on page 38)
$\langle\cdot\rangle_t$	Temporal average (defined on page 9)

Superscripts

$\cdot^*$	Complex conjugate (defined on page 10)
$\cdot^{\mathcal{L}}$	Defined by the integral length (defined on page 107)
$\cdot^{\mathrm{L}}$	Spatially local component (defined on page 62)
$\cdot^{\mathrm{NL}}$	Spatially nonlocal component (defined on page 70)
$\cdot^{k_f}$	Defined by the forcing length (defined on page 103)

Subscripts

$\cdot_\eta$	Kolmogorov length related quantity (defined on page 13)
$\cdot_\omega$	Enstrophy related quantity (defined on page 19)
$\cdot_f$	Forcing length related quantity (defined on page 13)
$\cdot_X$	X related quantity (defined on page 43)
$\cdot_Y$	Y related quantity (defined on page 43)
$\cdot_Z$	Z related quantity (defined on page 47)

Table of Contents

Overview of the Thesis

This thesis investigates turbulence by focusing on one of the most important concepts in turbulence research: *the energy cascade*. In three-dimensional turbulence, it represents an overall tendency for the energy to transfer from large to small scales. Despite its wide acceptance as a key ingredient of the statistical description of turbulence, the precise mechanism of the energy cascade has been at the centre of debate in the community for over a century. This thesis consists of three parts, investigating quasi-cyclic temporal behaviour, spatial locality, and nonequilibrium scaling of turbulence, respectively. In other words, we investigate turbulence and energy cascade from three different perspectives: time, space, and scale.

Chapter 1 is a general introduction. We first introduce the concept of energy cascade with the role of inviscid invariants and focus on its scale-local nature (§ 1.1). Next, we review how this idea led to the equilibrium and nonequilibrium theory of turbulence (§ 1.2). We discuss the Kolmogorov–Onsager theory of small-scale universality of turbulence, emphasising the assumption of equilibrium in the small scales. We also discuss the invalidity of such an assumption and the nonequilibrium nature of turbulence. Then, we further investigate a few candidates for the physical mechanism of the energy cascade (§ 1.3), which has been an open question in the turbulence community to this day.

Part I: Quasi-cyclic temporal fluctuations of turbulence and its minimal model

The main topic of Part I is the origin of quasi-cyclic temporal fluctuations observed in turbulence. Turbulence is often referred to as a typical example of chaos, which indeed captures the unpredictable nature of turbulence. An interesting feature in certain types of turbulence is the observation of quasi-cyclic fluctuations in random time signals.
In Chap. 2, we review these robust quasi-cyclic temporal fluctuations, discussing the concept of periodic orbits and highlighting an example of a closed system called von Kármán flow (§ 2.1). We also briefly review reduced-order modelling of developed and transitional turbulence (§ 2.2).
In Chap. 3, we first observe and quantify the quasi-cyclic fluctuations of a flow in a box with periodic boundary conditions maintained by a steady forcing (§ 3.1). We then *extract* a minimal three-equation model from a low-Reynolds number periodic flow by regrouping energetic modes at different scales (§ 3.2). The minimal model qualitatively reproduces quasi-cyclic behaviour, and we further conduct a bifurcation analysis to discuss the similarity between the steady-chaotic or periodic-chaotic transition in the minimal model and laminar-turbulent transition in real turbulence (§ 3.3).

Part II: Space-local Navier–Stokes turbulence

Turbulence generally contains structures of different sizes. The energy cascade picture can be understood as the energy exchange between structures of similar scales, known as the scale locality of turbulence. However, the scale-space representation of turbulence does not provide its physical-space description. The main topic of Part II is the other locality of turbulence, in physical space.
In Chap. 4, we first review studies on the physical-space locality of turbulence (§ 4.1). We then introduce the space-local velocity field, defined by the neighbouring vorticity field via a truncated Biot–Savart law (§ 4.2). We then conduct a post-process analysis on a turbulence dataset to compute the turbulence spectra with the space-local velocity and evaluate how spatially local turbulence is (§ 4.3).
In Chap. 5, we examine the physical-space locality of turbulence by employing the space-local velocity field *in situ* in numerical simulation. We define a new system called the space-local Navier–Stokes equations by

restricting the nonlinear term in space-local sense (§ 5.1). The direct numerical simulation of the space-local system exhibits qualitatively different behaviour compared to the post-process analysis reported in § 4.3 (§ 5.2). In particular, we focus on two scaling regimes in Fourier space. We observe that the $E(k) \propto k^{-5/3}$ scaling of the energy spectrum, corresponding to energy cascade, survives under the space-local constraint in scales smaller than the filter size (§ 5.3). This result illustrates the physical space-locality of the turbulent energy cascade, which should not be confused with the well-known scale locality. It is shown that enstrophy production is suppressed in scales larger than the filter size, and an alternative scaling, representing a conservative enstrophy cascade, emerges (§ 5.4).

Part III: Nonequilibrium scaling in inhomogeneous or unsteady turbulence

The well-known $E(k) \propto k^{-5/3}$ scaling of the energy spectrum is based on the equilibrium description of turbulence. However, turbulence is a nonequilibrium phenomenon, particularly in its large scales, as reviewed in § 1.2. In Part III, we focus on nonequilibrium scaling of turbulence due to large-scale modulation.

In Chap. 6, we discuss a correction to the $E(k) \propto k^{-5/3}$ scaling due to the large-scale inhomogeneity. We first review past theories on scaling corrections due to large-scale unsteadiness and anisotropy (§ 6.1). Then, we theoretically examine the effect of weak statistical inhomogeneity as a perturbation to the equilibrium scaling (§ 6.2). To do so, we decompose $E(k) = E_0(k) + E_1(k)$, where the subscript “0” and “1” indicates the equilibrium and nonequiilbrium contributions, respectively. Our examination yields $E_1(k) \propto k^{-7/3}$, which is assessed by direct numerical simulation of turbulence with a single inhomogeneous direction, known as Kolmogorov flow (§ 6.3).

In Chap. 7, we discuss nonequilbrium scaling of the normalised energy dissipation rate C_ϵ against the Reynolds number Re_λ. We first review the scaling of the parametric plot of $C_\epsilon(\boldsymbol{x}, t)$ as a function of $\mathrm{Re}_\lambda(\boldsymbol{x}, t)$, for the case of both spatial inhomogeneity and temporal unsteadiness (§ 7.1). Then, we conduct a similar perturbation analysis, as done for the energy spectrum in Chap. 6, for C_ϵ in terms of both inhomogeneous and unsteady fluctuations (§ 7.2). These theoretical findings yield the same scaling exponents and are numerically examined (§ 7.3). We further investigate the choice of the macroscopic length scale and how it changes the scaling (§ 7.4). We then linearise the newly obtained scaling expressions to obtain relations which can be compared to observations (§ 7.5). We also discuss the influence of the large-scale energy distribution on the C_ϵ scaling (§ 7.6).

The final Chap. 8 provides a summary as well as some perspectives for the three parts of the thesis. The construction of the thesis is summarised in Fig 1.

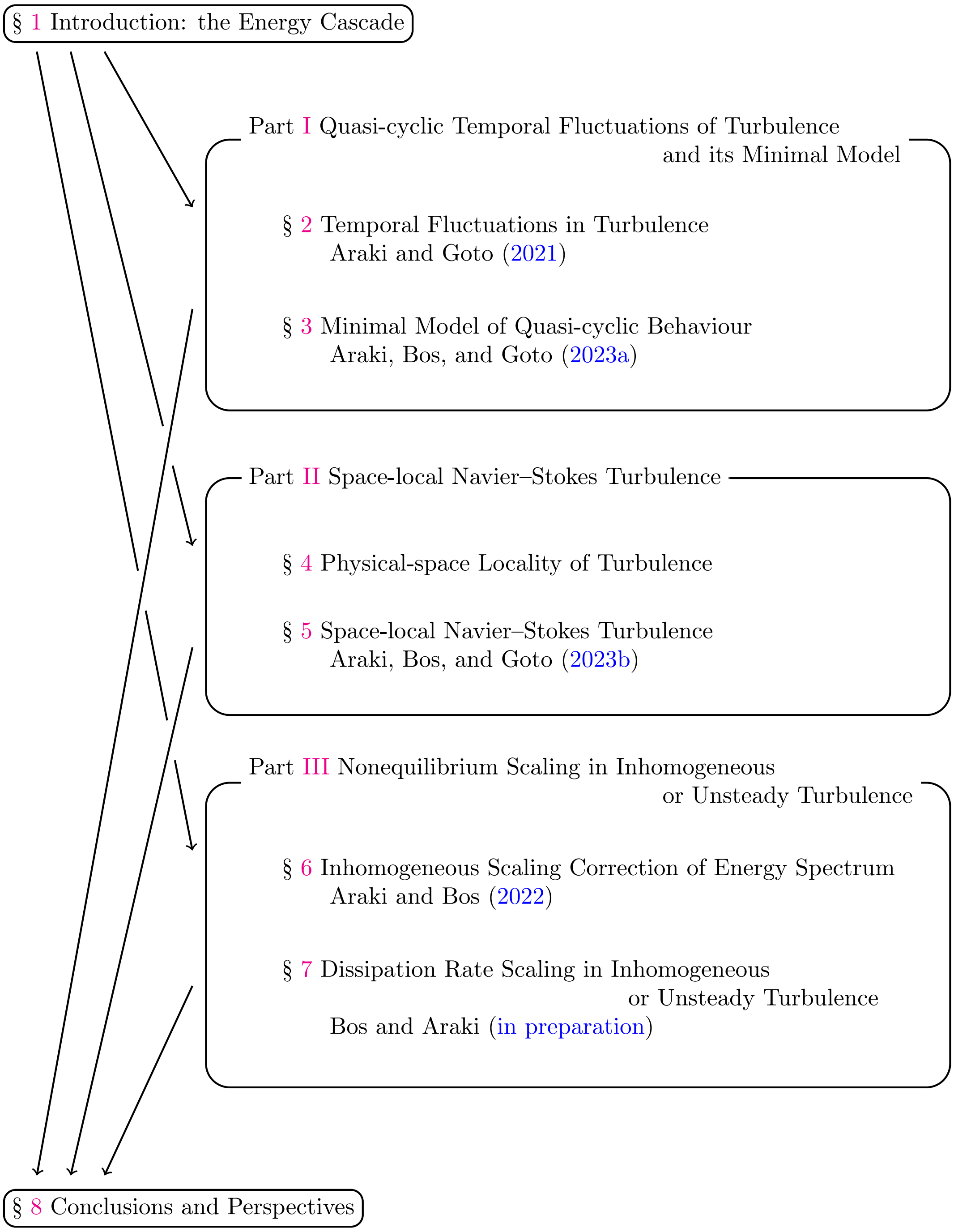

Figure 1: Overview of the construction of the thesis. For the annotated references, see “List of Publications” on p. v.

1 Introduction: the Energy Cascade

This chapter is devoted to reviewing important concepts and past research on the energy cascade, representing the transfer of energy from large to small scales in three-dimensional turbulence. In § 1.1, we discuss energy transfer in turbulent flow. In § 1.2, we review Kolmogorov's famous 1941 theory on the small-scale universality of turbulence by emphasising the local equilibrium hypothesis. In this sense, Kolmogorov's 1941 theory describes the *equilibrium* state of turbulence. Note that it is not equivalent to the concept in statistical mechanics. We also discuss the *nonequilibrium* aspect of turbulence by focusing on the violation of the local equilibrium hypothesis. In § 1.3, we examine the physical mechanism of the energy cascade. Although it provides the phenomenological picture of turbulence, its precise mechanism has been a long-standing open question to this day. An important subject that we will not discuss in this thesis is the interaction of the energy cascade with solid walls. For discussions of that topic, we refer to Jiménez (2012) and Motoori and Goto (2019).

1.1 Energy cascade in three-dimensional turbulence

A one hundred years ago, Lewis F. Richardson, who dreamed about weather prediction[1], described the motion of *whirls* in cumulus clouds in a parody of Jonathan Swift's poem[2] as (Richardson 1922, CH. 4/8/0, p. 66):

> We realize thus that: *big whirls have little whirls that feed on their velocity, and little whirls have lesser whirls and so on to viscosity* — in the molecular sense.

This poem has, thanks to its brevity and rich insight on the physical phenomena, been cited numerous times in textbooks, monographs, and research articles over a century[3].

---

[1] He wrote in the preface of his book (Richardson 1922, p. vii):

> Perhaps some day in the dim future it will be possible to advance the computations faster than the weather advances and at a cost less than the saving to mankind due to the information gained. But that is a dream.

See Lynch (2022) for his projects, perception of his book, and the dawn of weather forecasting.

[2] However, Richardson did not explicitly mention this in his book. The poem reads (De Morgan 1872, p. 377):

> Great fleas have little fleas upon their backs to bite 'em,
> And little fleas have lesser fleas, and so *ad infinitum*.
> And the great fleas themselves, in turn, have greater fleas to go on;
> While these again have greater still, and greater still, and so on.

[3] During its propagation, the poem is often converted into the four-line format. In Hunt, Eames, et al. (2010), the poem is introduced as:

> Great whirls have little whirls
> That feed on their velocity
> And little whirls have lesser whirls
> and so on to viscosity

Note that the terms "that" and "their" may refer to different things here. The authors also proposed that the original poem "might be modified as follows:"

> Great whirls gobble smaller whirls
> And feed on their velocity; but
> Where great whirls grind, they also slow,
> And little whirls begin to grow
> - stretching out with high vorticity

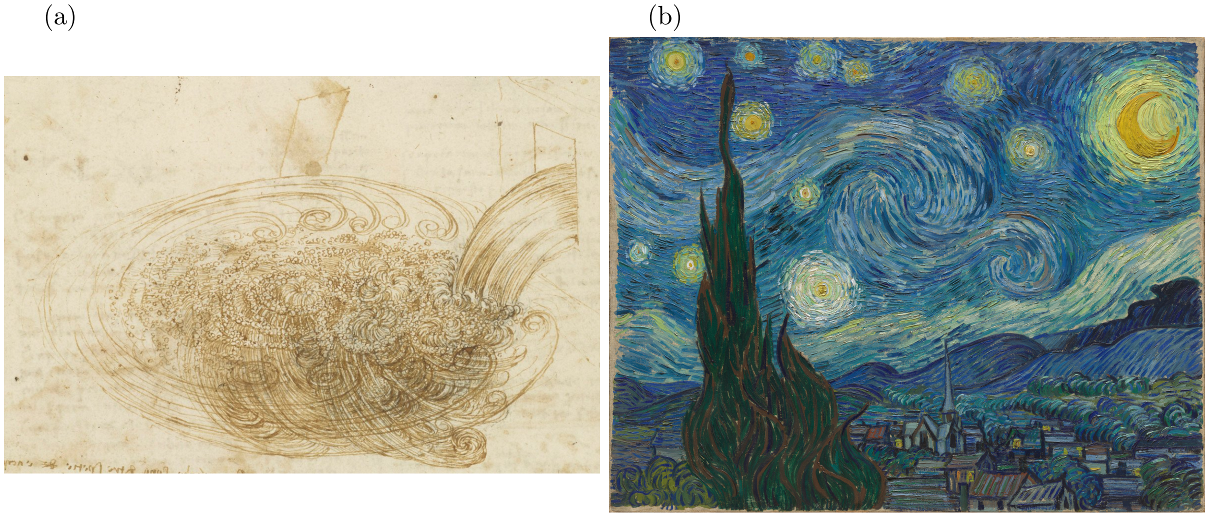

Figure 1.1: (a) A sketch of pouring water into a pool with resulting turbulent eddies by Leonardo da Vinci. Adapted from Royal Collection at Windsor, RCIN 912660v. (b) The Starry Night by Vincent van Gogh. Adapted from The Museum of Modern Art, 472.1941.

We remark here that the concept of whirls of various scales was captured before Richardson. Figure 1.1(a) is one of the most famous paintings of turbulence drawn by Leonardo da Vinci, who introduced the term "turbolenza". He depicted multi-scale eddies in water pouring into a pool, and their size even exhibits a power-law scaling (Marusic and Broomhall 2021, Figure 13). See Marusic and Broomhall (2021) for a review of da Vinci's works in fluid mechanics. Figure 1.1(b) is another example of turbulence in a popular painting: Vincent van Gogh's "The Starry Night". His iconic brushwork fills the sky with swirling patterns, which were later found to agree with the turbulence theory (Aragón et al. 2008; Beattie and Kriel 2019).

In this section, we review the notion of an energy cascade in three-dimensional turbulence. First, in § 1.1.1, we define the inviscid invariants of the Navier–Stokes equations and the cascade of energy. In § 1.1.2, we discuss the scale-space description of the energy cascade, emphasising its locality.

1.1.1 Inviscid invariants and their cascades

We begin our discussion with the Navier–Stokes equations

$$\frac{\partial \boldsymbol{u}}{\partial t} + (\boldsymbol{u}\cdot\boldsymbol{\nabla})\boldsymbol{u} = -\boldsymbol{\nabla} p + \nu\nabla^2\boldsymbol{u} + \boldsymbol{f}, \tag{1.1}$$

defined in the three-dimensional domain $\boldsymbol{x} = (x, y, z) \in \Omega$ with time t. For simplicity, we restrict ourselves to a triply periodic domain of size 2π: $0 \leq x_i \leq 2\pi$ with $x_i \in \{x, y, z\}$. Throughout this thesis, we consider turbulence far away from walls. Here, $\boldsymbol{u}(\boldsymbol{x}, t) = (u_x, u_y, u_z)$ denotes the three-dimensional velocity field satisfying the incompressibility condition,

$$\boldsymbol{\nabla}\cdot\boldsymbol{u} = 0. \tag{1.2}$$

A scalar field $p(\boldsymbol{x}, t)$ denotes the pressure (divided by density ρ) and $\boldsymbol{f}(\boldsymbol{x}, t) = (f_x, f_y, f_z)$ is the forcing vector field driving the flow. The kinematic viscosity is denoted by ν. The curl of the velocity $\boldsymbol{\omega} = \boldsymbol{\nabla}\times\boldsymbol{u}$

> Up to the limit of viscosity.
>
> -

In Tamai (2016), Richardson's poem is cited in the one-line form but with slightly different wording:

> *Big whorls have little whorls Which feed on their velocity, And little whorls have lesser whorls And so on to viscosity.*

and Swift's poem is introduced in the one-line form, again with a slightly different choice of words:

> *Great fleas have little fleas Upon their backs to bite'em, And little fleas have lesser fleas And so ad infinitum.*

is called the vorticity field, and its governing equation reads

$$\frac{\partial \boldsymbol{\omega}}{\partial t} + (\boldsymbol{u} \cdot \boldsymbol{\nabla})\boldsymbol{\omega} = (\boldsymbol{\omega} \cdot \boldsymbol{\nabla})\boldsymbol{u} + \nu \nabla^2 \boldsymbol{\omega} + \boldsymbol{\nabla} \times \boldsymbol{f}. \tag{1.3}$$

We observe several differences between the vorticity and Navier–Stokes equations. First, the pressure gradient term disappears since

$$\boldsymbol{\nabla} \times \boldsymbol{\nabla} p = 0. \tag{1.4}$$

Second, we have two nonlinear terms emerging from the advection term $(\boldsymbol{u} \cdot \boldsymbol{\nabla})\boldsymbol{u}$; The vortex advection $(\boldsymbol{u} \cdot \boldsymbol{\nabla})\boldsymbol{\omega}$ and the vortex stretching $(\boldsymbol{\omega} \cdot \boldsymbol{\nabla})\boldsymbol{u}$ terms, respectively.

By non-dimensionalising the variables in (1.1), one obtains a single nondimensional quantity characterising the flow, called the Reynolds number

$$\mathrm{Re} \equiv \frac{UL}{\nu}. \tag{1.5}$$

Here, U and L denote appropriately defined characteristic velocity and length scales, respectively[4]. For large values of Re (small values of ν), the nonlinear term $(\boldsymbol{u} \cdot \boldsymbol{\nabla})\boldsymbol{u}$ dominates the flow compared to the viscous term $\nu \nabla^2 \boldsymbol{u}$ and the flow becomes *turbulent*.

Turbulent flow can be found in every aspect of our daily life. When we fully open the tap, turbulent water flows into the sink to make larger noise and splash than the half-opened tap. When boarding an aeroplane, the captain sometimes makes a warning announcement to fasten your seatbelt to be safe under vibration caused by turbulent air motion. On a schematic level, turbulence is described as the complex motion of a fluid. However, despite its common appearance, providing a precise definition of turbulence is difficult. Rather, we can describe turbulence with its characteristics: multi-scale nonlinear interactions and their self-similarity, statistical universality, and anomalous scaling, to name a few. Given its importance in such a wide range of applications, turbulence has been studied extensively using theory, experiments, and simulations.

Numerical simulations of turbulence, such as Direct Numerical Simulation (DNS) numerically solving the discretised Navier–Stokes equations (1.1), require extremely large computational resources. The history of the largest DNS in the last two decades can be found in Aoyama et al. (2005), Ishihara, Gotoh, et al. (2009), Yeung, Donzis, et al. (2012), Ishihara, Kaneda, et al. (2013), Yeung, Zhai, et al. (2015), Yeung, Sreenivasan, et al. (2018), and Buaria, Pumir, Bodenschatz, and Yeung (2019). Figure 1.2 visualises the fine-scale structures in one of the largest DNS of turbulence to this day (Buaria, Pumir, Bodenschatz, and Yeung 2019).

In the following, we focus on the invariants of the Navier–Stokes equations (1.1) to introduce the concept of a cascade. Here, an invariant means a global quantity which does not evolve in time. When we consider the inviscid ($\nu = 0$) and force-free ($\boldsymbol{f} = \boldsymbol{0}$) system, we find two global invariants: the total kinetic energy and helicity:

$$K \equiv \frac{1}{2} \langle \boldsymbol{u} \cdot \boldsymbol{u} \rangle_\Omega \quad \text{and} \quad H \equiv \frac{1}{2} \langle \boldsymbol{\omega} \cdot \boldsymbol{u} \rangle_\Omega \,, \tag{1.6}$$

respectively. Here, the bracket with subscript Ω denotes the spatial average

$$\langle \cdot \rangle_\Omega \equiv \frac{1}{(2\pi)^3} \int_\Omega (\cdot) \, \mathrm{d}\boldsymbol{x} \,. \tag{1.7}$$

Once we go back to the viscous ($\nu \neq 0$) and forced ($\boldsymbol{f} \neq \boldsymbol{0}$) case, we have a governing equation for the kinetic energy

$$\frac{\mathrm{d}K}{\mathrm{d}t} = P - \epsilon, \tag{1.8}$$

where the Right Hand Side (RHS) consists of the energy injection rate and the energy dissipation rate:

$$P \equiv \langle \boldsymbol{f} \cdot \boldsymbol{u} \rangle_\Omega \quad \text{and} \quad \epsilon \equiv 2\nu \left\langle \boldsymbol{S}^2 \right\rangle_\Omega \,, \tag{1.9}$$

---

[4] Many definitions of the Reynolds numbers employ different definitions for U and L to focus on different flow characteristics. Examples include *global* Reynolds number, *local* Reynolds number, *integral-scale* based, *Taylor-scale* based, *intet*, and so on.

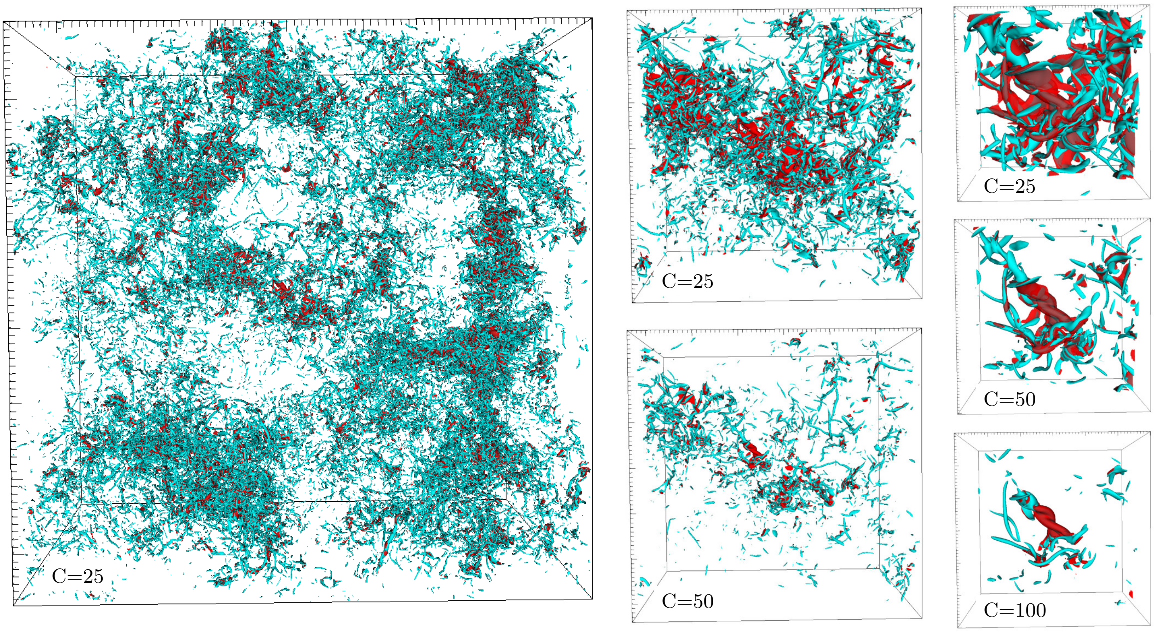

(a) $(2000\eta)^3$ (b) $(600\eta)^3$ (c) $(150\eta)^3$

Figure 1.2: Visualisation of enstrophy (cyan) and energy dissipation (red) in turbulence obtained by the DNS of 8192^3 resolutions with the Taylor-scale Reynolds number of $R_\lambda = 650$. The centre of the domain visualised in panel (a) is successively zoomed in for panels (b) and (c). The sub-labels denote the approximate domain sizes in the Kolmogorov length scale η. In each panel, the contour threshold is denoted by C at the left-bottom corner. Adapted from Buaria, Pumir, Bodenschatz, and Yeung (2019, Figure 1).

respectively. Here, we define the symmetric/antisymmetric decomposition of the velocity gradient tensor:

$$\boldsymbol{A} = \boldsymbol{S} + \boldsymbol{\Omega}, \quad \leftrightarrow \quad \underbrace{\frac{\partial u_i}{\partial x_j}}_{A_{ij}} = \underbrace{\frac{1}{2}\left(\frac{\partial u_i}{\partial x_j} + \frac{\partial u_j}{\partial x_i}\right)}_{S_{ij}} + \underbrace{\frac{1}{2}\left(\frac{\partial u_i}{\partial x_j} - \frac{\partial u_j}{\partial x_i}\right)}_{\Omega_{ij}}. \tag{1.10}$$

The symmetric part $\boldsymbol{S}$ is often called rate-of-strain tensor and the antisymmetric part $\boldsymbol{\Omega}$ rate-of-rotation tensor. Note that the energy dissipation rate in (1.9) is often expressed in alternative forms. For example, by using the velocity gradient tensor,

$$\epsilon^{\text{pseudo}} = \nu \left\langle \boldsymbol{A}^2 \right\rangle_\Omega . \tag{1.11}$$

This quantity is called *pseudo*-energy dissipation rate and is not strictly equivalent to the original definition (1.9). See Appendix A for details. Another common definition is by the square of the vorticity vector:

$$\epsilon^{\text{homogeneous}} = \nu \left\langle \boldsymbol{\omega}^2 \right\rangle_\Omega . \tag{1.12}$$

This is an estimation of the energy dissipation rate and equivalent to (1.9) when the flow is statistically homogeneous. See Appendix B for details. The helicity equation can be obtained by taking the inner product of (1.1) with $\boldsymbol{\omega}$.

One important remark on (1.9) is that the energy dissipation rate is a positive definite quantity, whereas the energy injection rate can be positive or negative. Now, we consider the so-called statistically steady flow, in which the time-average of (1.8) is zero:

$$\left\langle \frac{\mathrm{d}K}{\mathrm{d}t} \right\rangle_t = \langle P \rangle_t - \langle \epsilon \rangle_t = 0. \tag{1.13}$$

Here, the bracket with subscript t denotes the time average

$$\langle \cdot \rangle_t \equiv \lim_{T\to\infty} \frac{1}{T} \int_0^T (\cdot)\, \mathrm{d}t\,. \tag{1.14}$$

Under this assumption, there is a balance between the energy injection and dissipation rates in a time-average sense. Since $\epsilon > 0$, this balance implies that $\langle P \rangle_t$ is positive, which does not necessarily hold instantaneously.

Based on the injection-dissipation balance (1.13), we consider the scales corresponding to P and ϵ. The energy injection rate P is defined by an inner product of the forcing $\boldsymbol{f}$ and the velocity field $\boldsymbol{u}$; more energy is injected when the two vector fields are aligned. The energy dissipation rate ϵ is defined by the square of the strain-rate tensor S_{ij}, and thus it takes larger values when there is a strong velocity gradient. In this thesis, we consider a case where the energy injection takes place at the largest scales of the flow (forcing scale; energy injection scale), and the energy dissipation occurs at the smallest scales (viscous scale; dissipation scale). However, it is important to note that this large-scale injection and small-scale dissipation picture, often implicitly assumed, is not trivial. For example, Vela-Martín and Jiménez (2021, p. 13) wrote that “the energy dissipation is a consequence, rather than a cause, of the energy cascade.”

Since two terms on the RHS of (1.13) represent different scales in turbulence and must be balanced under the assumption of statistical stationarity, there needs to be a transfer of energy from large to small scales. This energy transfer is caused by the nonlinear term of the Navier–Stokes equations. Since its spatial average is zero, the nonlinear term represents energy redistribution. In other words, it does not produce or eliminate energy. The question is how it redistributes energy among different scales. Is there a direct energy transfer from the forcing scale to the dissipation scale? Or are there more complicated interactions, including the intermediate scales between them? Turbulence research has found that the latter is the case; there is a multi-step mechanism to transfer energy from large to small scales. This leads to the concept of *energy cascade*[5]. In the next subsection, we will review this concept from scale space.

1.1.2 Scale-local nature of the energy cascade

In this subsection, we review the concept and nature of energy cascade in scale space. First, we define the Fourier transform of the velocity field

$$\boldsymbol{u}(\boldsymbol{k}) = \frac{1}{(2\pi)^3} \int \boldsymbol{u}(\boldsymbol{x}) \exp(-\mathrm{i}\boldsymbol{k}\cdot\boldsymbol{x})\, \mathrm{d}\boldsymbol{x}\,, \tag{1.15}$$

and associated inverse transform

$$\boldsymbol{u}(\boldsymbol{x}) = \int \boldsymbol{u}(\boldsymbol{k}) \exp(\mathrm{i}\boldsymbol{k}\cdot\boldsymbol{x})\, \mathrm{d}\boldsymbol{k}\,, \tag{1.16}$$

respectively. Note that we do not employ annotations to express the Fourier-space quantities. Instead, we explicitly denote the Fourier mode $\boldsymbol{k}$ as an argument in the following.

The Fourier transform of the Navier–Stokes equations (1.1) yields

$$\frac{\partial u_i(\boldsymbol{k})}{\partial t} = -\mathrm{i}k_m P_{ij}(\boldsymbol{k}) \int \delta(\boldsymbol{k}-\boldsymbol{p}-\boldsymbol{q}) u_j(\boldsymbol{p}) u_m(\boldsymbol{q})\, \mathrm{d}\boldsymbol{p}\, \mathrm{d}\boldsymbol{q} - \nu k^2 u_i(\boldsymbol{k}) + f_i(\boldsymbol{k}), \tag{1.17}$$

with the incompressibility condition

$$\mathrm{i}\boldsymbol{k}\cdot\boldsymbol{u}(\boldsymbol{k}) = \mathrm{i}k_j u_j(\boldsymbol{k}) = 0. \tag{1.18}$$

For the full derivation process, see, for example, Pope (2000, § 6.4.2) and Lesieur (2008, § 5.3). We also assume solenoidality for the forcing term $k_j f_j = 0$. To express the nonlinear term (including the pressure

---

[5] The term “cascade” was first used by Onsager in 1945 (Onsager 1945; Eyink and Sreenivasan 2006). See § 1.3.1 for more details.

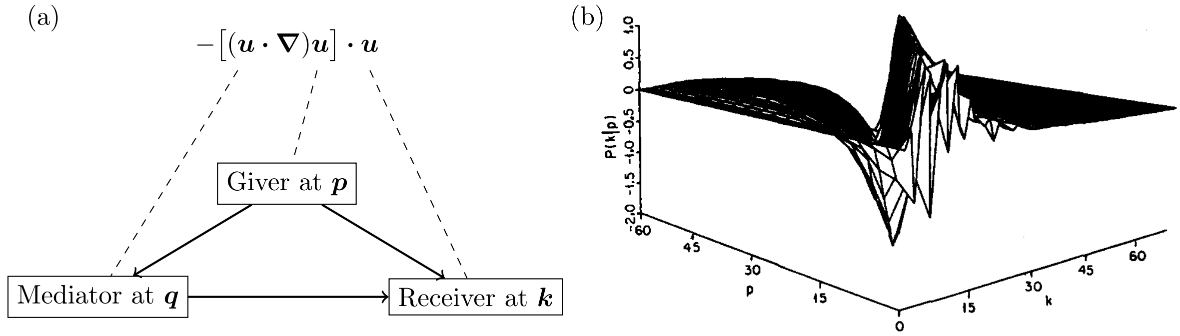

Figure 1.3: (a) Schematic of the mode-to-mode energy transfer from *giver* $\boldsymbol{p}$ to *receiver* $\boldsymbol{k}$ with the aid of *mediator* $\boldsymbol{q}$. The figure is drawn after Verma (2019, Figure 4.3). (b) The surface of function $P(k|p)$ interpreted as the energy transfer between wavenumber bands k and p. Adapted from Domaradzki and Rogallo (1990, Figure 6).

gradient), we use the projection

$$P_{ij}(\boldsymbol{k}) = \delta_{ij} - \frac{k_i k_j}{k^2} \tag{1.19}$$

and Kronecker's delta function δ_{ij}.

The nonlinear term of (1.17) in the integral form has a constraint $\boldsymbol{k} = \boldsymbol{p} + \boldsymbol{q}$, known as *triad interaction.* It denotes that the energy transfer in Fourier space is possible only between the three modes $(\boldsymbol{k}, \boldsymbol{p}, \boldsymbol{q})$ when they satisfy this condition.

By computing a dot product of (1.17) with $u_i^*(\boldsymbol{k})$, where $\cdot^*$ denotes the complex conjugate, one obtains an equation for energy at mode $\boldsymbol{k}$,

$$\frac{\partial E(\boldsymbol{k})}{\partial t} = \underbrace{-\mathrm{i}k_m P_{ij}(\boldsymbol{k}) \int \delta(\boldsymbol{k}-\boldsymbol{p}-\boldsymbol{q}) u_i^*(\boldsymbol{k}) u_j(\boldsymbol{p}) u_m(\boldsymbol{q})\, \mathrm{d}\boldsymbol{p}\, \mathrm{d}\boldsymbol{q}}_{T(\boldsymbol{k})} \underbrace{- 2\nu k^2 E(\boldsymbol{k})}_{\epsilon(\boldsymbol{k})} + \underbrace{f_i(\boldsymbol{k}) u_i^*(\boldsymbol{k})}_{F(\boldsymbol{k})}, \tag{1.20}$$

where $E(\boldsymbol{k}) = \left|\boldsymbol{u}(\boldsymbol{k})\right|^2/2 = u_i(\boldsymbol{k}) u_i^*(\boldsymbol{k})/2$. The RHS of (1.20) consists of: (i) nonlinear energy transfer T at $\boldsymbol{k}$ with all the combination of Fourier modes $(\boldsymbol{k}, \boldsymbol{p}, \boldsymbol{q})$ satisfying the triad interaction condition $\boldsymbol{k} = \boldsymbol{p} + \boldsymbol{q}$, (ii) energy dissipation rate ϵ at $\boldsymbol{k}$, and (iii) energy injection rate F at $\boldsymbol{k}$. Figure 1.3(a) shows the schematic of energy transfer in Fourier space with triad interactions. The integrand of $T(\boldsymbol{k})$ in (1.20) denotes the energy transfer from the *giver* mode $\boldsymbol{p}$ to the *receiver* mode $\boldsymbol{k}$ with the aid of the *mediator* mode $\boldsymbol{q}$, which corresponds to the advection velocity.

Next, we average (1.20) over a shell of radius $k = |\boldsymbol{k}|$ in Fourier space to obtain

$$\frac{\partial E(k)}{\partial t} = F(k) + T(k) - 2\nu k^2 E(k). \tag{1.21}$$

Here, the energy spectrum

$$E(k) = \int E(\boldsymbol{k})\, \mathrm{d}\Omega_k \tag{1.22}$$

represents energy density at wavenumber k. The notation $\int \mathrm{d}\Omega_k$ denotes the integral over spherical shells of radius k. The RHS terms

$$F(k) \equiv \int F(\boldsymbol{k})\, \mathrm{d}\Omega_k \quad \text{and} \quad T(k) \equiv \int T(\boldsymbol{k})\, \mathrm{d}\Omega_k \tag{1.23}$$

are called energy injection and energy transfer spectra, respectively. The last term $2\nu k^2 E(k)$ is the energy dissipation spectrum.

A question here is the scale locality of the energy transfer $T(k)$ in three-dimensional turbulence. In other words, how does an individual triangle consisting of three Fourier modes $(\boldsymbol{k}, \boldsymbol{p}, \boldsymbol{q})$ contribute to $T(k)$?

A pioneering theoretical investigation was done by Kraichnan (1971b). Figure 1.3(b) shows the first numerical evidence that the energy transfer between wavenumbers k and p[6] shows

> A valley and a ridge seen along the diagonal $k = p$ in this plot reflects the local nature of the energy transfer.

Ohkitani and Kida (1992) investigated the triad interactions in more detail by categorising them into six groups according to the energy gain/loss of the largest, intermediate, and smallest wavenumbers. They found strong interactions in nonlocal nonlinear interactions with large differences in scale. However, the largest scale does not contribute to the energy cascade in the triad, as two comparable scales dominate it. Waleffe (1992) investigated triad interactions with the helical decomposition of the velocity field to discuss the stability and the energy transfer. Eyink (2005) decomposed the velocity in scale and space to investigate various cascades, including energy and helicity in three-dimensional turbulence and inverse enstrophy and direct energy cascade in two-dimensional configurations. He established a sufficient condition of the locality of the energy cascade. Domaradzki and Carati (2007) found significant cancellation of the local transfer through nonlocal interactions in the global energy transfer with smooth and sharp filters. Biferale et al. (2012) uncovered an inverse energy cascade in three-dimensional turbulence by considering only a subset of the nonlinear triad interactions. Cardesa, Vela-Martín, and Jiménez (2017) traced the space-time position of a given structure, defined by isocounters of intense bandpass-filtered energy, at four different scales. The intersection ratio of vortices of different scales reveals a signature of energy cascade; the eddies of a given scale emerge inside larger eddies with twice the size, while they give rise to eddies with half the size before dying out. This observation with a characteristic scale ratio of two supports the scale-local nature of the energy cascade.

1.2 Equilibrium and nonequilibrium aspects of turbulence

Although turbulence is a typical example of strongly out-of-equilibrium phenomena, earlier theoretical works were directed to the "equilibrium" aspect of turbulence. In this section, we review both "equilibrium" and "nonequilibrium" aspects of turbulence. Here, we remark that the definition of these terms does not coincide with statistical mechanics. In the following, we omit the quotation for readability. In § 1.2.1, we first introduce an assumption on the equilibrium in the small scales of turbulence, which is called the local equilibrium hypothesis. Then, in § 1.2.2, we review the famous Kolmogorov's 1941 theory on universal small-scale turbulence statistics. This theory sets the paradigm of current turbulence research. In § 1.2.3, we investigate the nonequilibrium aspect of turbulence associated with the breakdown of Taylor's dissipation law, which can be understood as an extension of the local equilibrium hypothesis. In § 1.2.4, we apply a similar discussion for two-dimensional turbulence to highlight the qualitative difference between two- and three-dimensional turbulence.

1.2.1 Local equilibrium hypothesis

We begin our discussion by recasting (1.21):

$$\frac{\partial E(k,t)}{\partial t} = F(k,t) + T(k,t) - 2\nu k^2 E(k,t), \tag{1.26}$$

which is the governing equation of the energy spectrum. Here, we explicitly denote the time dependency. Note that the RHS consists of the energy injection $F(k,t)$, energy transfer $T(k,t)$, and the energy dissipation $2\nu k^2 E(k,t)$ at scale k and at time t, respectively.

---

[6] Note that it is not possible to describe $P(k|p)$ in Fig. 1.3(b) as the energy transfer from wavenumber p to k, as depicted in Fig. 1.3(a). It is because the nonlinear term in Domaradzki and Rogallo (1990) is defined in a symmetric form:

$$-\frac{\mathrm{i}}{2} P_{nlm}(\boldsymbol{k}) \int \mathrm{d}^3 p \, u_l(\boldsymbol{p},t) u_m(\boldsymbol{k}-\boldsymbol{p},t) \tag{1.24}$$

where

$$P_{nlm}(\boldsymbol{k}) = k_m \left(\delta_{nl} - \frac{k_n k_l}{k^2} \right) + k_l \left(\delta_{nm} - \frac{k_n k_m}{k^2} \right). \tag{1.25}$$

By integrating (1.26) in the wavenumber domain, one obtains the energy equation

$$\frac{\mathrm{d}K}{\mathrm{d}t}(t) = P(t) - \epsilon(t), \tag{1.27}$$

where the kinetic energy

$$K(t) \equiv \int_0^\infty E(k,t)\,\mathrm{d}k\,, \tag{1.28}$$

the power input

$$P(t) \equiv \int_0^\infty F(k,t)\,\mathrm{d}k\,, \tag{1.29}$$

and the energy dissipation rate

$$\epsilon(t) \equiv 2\nu \int_0^\infty k^2 E(k,t)\,\mathrm{d}k\,. \tag{1.30}$$

Note that the integral of the nonlinear transfer term is zero:

$$\int_0^\infty T(k,t)\,\mathrm{d}k = 0. \tag{1.31}$$

Refer to § 1.1.1 for the inviscid invariants of the Navier–Stokes equations.

We now consider decomposing the integral in (1.27) into low- and high-wavenumber contributions. This leads us to the set of equations for large- and small-scale energy,

$$\frac{\partial K^<}{\partial t}(k,t) = P^<(k,t) - \mathit{\Pi}(k,t) - \epsilon^<(k,t) \quad \text{and} \tag{1.32}$$

$$\frac{\partial K^>}{\partial t}(k,t) = \mathit{\Pi}(k,t) - \epsilon^>(k,t). \tag{1.33}$$

Here, the superscripts $\cdot^<$ and $\cdot^>$ denote large-scale (low-wavenumber) and small-scale (high-wavenumber) quantities, respectively. Each term is defined by decomposing the integral of (1.28)– (1.30), for example,

$$K^<(k,t) \equiv \int_0^k E(p,t)\,\mathrm{d}p \qquad \text{and} \quad K^>(k,t) \equiv \int_k^\infty E(p,t)\,\mathrm{d}p\,, \tag{1.34}$$

$$\epsilon^<(k,t) \equiv 2\nu \int_0^k p^2 E(p,t)\,\mathrm{d}p \quad \text{and} \quad \epsilon^>(k,t) \equiv 2\nu \int_k^\infty p^2 E(p,t)\,\mathrm{d}p\,. \tag{1.35}$$

For the power input term, we restrict $F(k,t)$ to appear only at the low-wavenumber region. It is an assumption which we employ for the rest of this thesis. For the integral of the energy transfer function, we take advantage of (1.31) to define the energy flux

$$\mathit{\Pi}(k,t) \equiv -\int_0^k T(k,t)\,\mathrm{d}k = \int_k^\infty T(k,t)\,\mathrm{d}k\,, \tag{1.36}$$

so that the sum of (1.32) and (1.33) reduces to (1.27).

We now focus on the small-scale equation (1.33). Under the assumption that the temporal evolution of the small-scale energy $K^>(k,t)$ is slow, namely,

$$\frac{\partial K^>}{\partial t}(k,t) \ll \epsilon^>(k,t), \tag{1.37}$$

it follows that

$$\mathit{\Pi}(k,t) \approx \epsilon^>(k,t). \tag{1.38}$$

This is the formal expression of the Local Equilibrium Hypothesis (LEH) (Goto and Vassilicos 2016a), and is depicted in Fig. 1.4. The LEH expresses the instantaneous balance at scale k between the energy

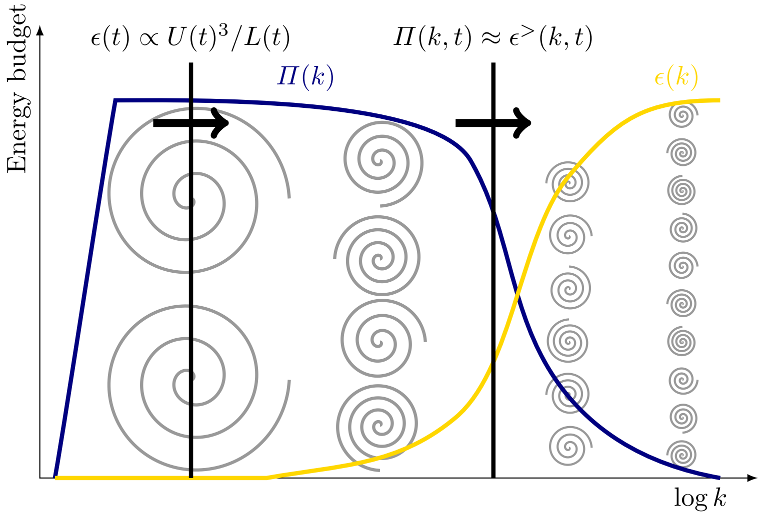

Figure 1.4: Schematic of the local equilibrium hypothesis. The horizontal and vertical axis denotes the wavenumber k in log form and the energy budget, respectively. Energy flux spectrum $\Pi(k)$ and cumulative energy dissipation spectrum $\epsilon(k)$ are shown along with a schematic picture of vortices of different scales. The vertical lines with a horizontal arrow represent Taylor's dissipation law and the local equilibrium hypothesis, respectively.

flux across that scale and the energy dissipation rate in the smaller scales. In turbulence research, it represents the equilibrium aspect of turbulence. Again, we remark that the usage of this term is different from statistical mechanics.

1.2.2 Kolmogorov–Onsager theory of the small-scale universality

The current paradigm of turbulence research relies on the work of Kolmogorov (1941a). In this subsection, we review Kolmogorov's two similarity hypotheses to derive Kolmogorov's universal energy spectrum

$$E(k) = C_K \epsilon^{2/3} k^{-5/3} \quad \text{for} \quad k_f \ll k \ll k_\eta, \tag{1.39}$$

by emphasising the importance of the LEH (1.38) discussed in the last subsection (§ 1.2.1).
First, we introduce the local homogeneous and isotropy hypotheses according to Kolmogorov (1941a). The local homogeneous hypothesis states that the statistics of velocity difference between two points in the four-dimensional space (x_1, x_2, x_3, t) depend on the difference between two points and not their position. The local isotropy hypothesis states that under the local homogeneous hypothesis, the statistics are invariant regarding rotations and reflections of the original coordinate. Turbulent flow satisfying these hypotheses is called Homogeneous and Isotropic Turbulence (HIT).
For the local isotropy hypothesis, Kolmogorov (1941a) stated:

> [...] it seems very likely that in the case of an arbitrary turbulent flow with sufficiently large Reynolds number[7]
>
> $$\mathrm{Re} = LU/\nu \tag{1.40}$$
>
> in sufficiently small regions G of the four-dimensional space (x_1, x_2, x_3, t) not lying close to the boundaries of the flow or other singularities of it, the hypothesis of local isotropy holds with high accuracy.
>
> Here, by "small regions" are meant those whose linear dimensions and time scales are small relative to L and
>
> $$T = U/L, \tag{1.41}$$
>
> respectively.

---

[7] Here L and U dare the typical length and velocity scales for the flow as a whole.

Furthermore, Kolmogorov claimed that the local isotropy hypothesis cannot be proved rigorously. In the footnote spanning two-thirds of a page, there is the following statement:

> By virtue of the chaotic mechanism of transfer of motion from lower-order fluctuations to higher-order ones, it is natural to assume that, within the limits of space regions which are small as compared to $l^{(1)}$ ($= l$, where l is the Prandtl mixing length), small-scale higher-order fluctuations are subject to an approximately spatially isotropic statistical regime. Within short time intervals this regime can naturally be regarded as being stationary, even when the flow as a whole is non-stationary.

Thus, Kolmogorov (1941a) claimed the idea of local equilibrium in the local isotropy hypothesis. If we translate the above discussion to Fourier space, we obtain the LEH (1.38). Now, we introduce two similarity hypotheses:

The first similarity hypothesis states that for very large (but finite) Reynolds number, the small-scale ($k \gg k_f$) statistics of turbulence can be uniquely determined by the parameters ν and ϵ. By defining the dissipation length scale

$$\eta \equiv \left(\frac{\nu^3}{\epsilon}\right)^{1/4}, \tag{1.42}$$

we can express the statistics with ϵ and η. This allows us to express the energy spectrum as

$$E(k) = \epsilon^{2/3} k^{-5/3} F(k\eta) \quad \text{for} \quad k_f \ll k, \tag{1.43}$$

where F denotes a universal nondimensional function of a nondimensional argument.

The second similarity hypothesis further states that the small-scale statistics, this time larger than the viscous length scale $k \ll k_\eta = \eta^{-1}$, can be uniquely determined by the single parameter ϵ. The energy spectrum can be expressed as

$$E(k) = C_K \epsilon^{2/3} k^{-5/3} \quad \text{for} \quad k_f \ll k \ll k_\eta, \tag{1.44}$$

where C_K is a universal constant of order unity called the Kolmogorov constant.

Figure 1.5 shows the energy spectrum of turbulence in various flow configurations, including theory, numerical simulation, and experiment to support the robustness of the similarity hypotheses. Remarkably, after the normalisation, all spectra collapse for $k_f \ll k$ (the first similarity hypothesis). In the intermediate range of $k_f \ll k \ll k_\eta$, there is a universal $k^{-5/3}$ scaling described by (1.44) (the second similarity hypothesis).

Kolmogorov's theory on small-scale universality has set the paradigm of turbulence research. Many textbooks (Tennekes and Lumley 1972; Frisch 1995, § 5–7; Pope 2000, § 6.1; Tsinober 2009, § 5; Lesieur 2008, § 6; Davidson 2015, § 5), lecture notes (George 2013, § 14, Eyink 2007-2008), and review articles (Hunt and Vassilicos 1991; Lumley 1992; Nelkin 1994; Sreenivasan and Antonia 1997; Hunt, Sandham, et al. 2001; Dubrulle 2019) discuss this theory in more detail.

We note some historical remarks to conclude this subsection. In the 1941 works of Kolmogorov (Kolmogorov 1941a; Kolmogorov 1941b; Kolmogorov 1941c), the analysis was conducted in real space. The Fourier-space expression (1.44) was first derived by Obukhov (Obukhov 1941a; Obukhov 1941b). Around the same time, several other researchers, including Onsager (Onsager 1945; Onsager 1949), Heisenberg (Heisenberg 1948), and Weizsäcker (Weizsäcker 1948), reached the same result independently. To highlight the contribution by Onsager, we name this subsection as "Kolmogorov–Onsager theory of the small-scale universality". For more detail on the historical aspects, see Frisch (1995, § 6.5) and Eyink and Sreenivasan (2006, § 4–5) as well as § 1.3.1.

1.2.3 Taylor's dissipation law and its violation

In this subsection, we discuss the extension of the LEH and its validity. The LEH serves as a keystone for a more applicational aspect of turbulence, along with the theory of small-scale universality. To see this, we first assume that the LEH is valid at the largest wavenumber of the flow, $k \to L(t)^{-1}$, where $L(t)$ is the time-dependent macroscopic length scale. Then, (1.38) becomes

$$\Pi(L^{-1}, t) \approx \epsilon(t), \tag{1.45}$$

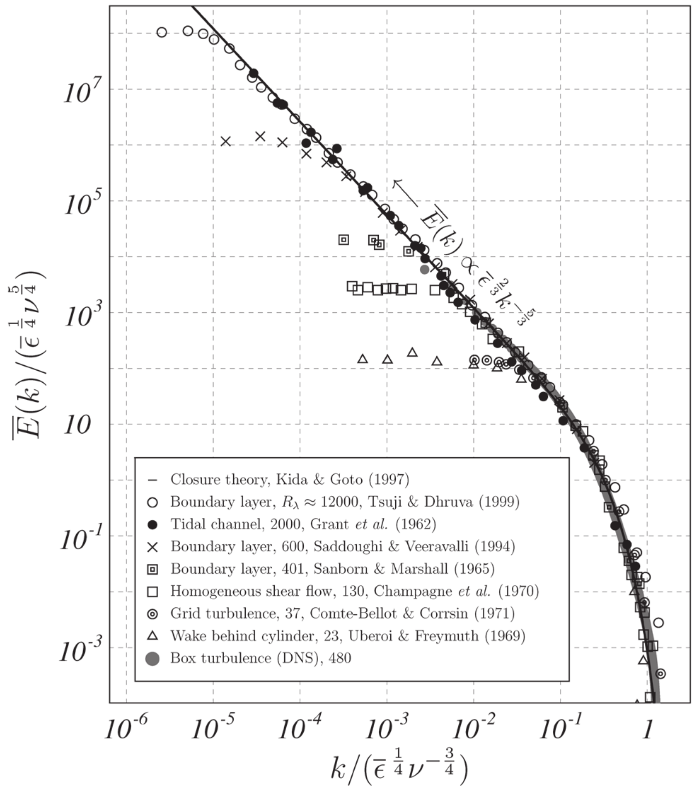

Figure 1.5: Energy spectrum in various types of turbulence normalised by the small-scale representatives: averaged energy dissipation rate $\bar{\epsilon}$ and kinematic viscosity of the fluid ν. Values in the legend denote the Taylor-scale based Reynolds number $R_\lambda = u'\lambda/\nu$, where u' is the standard deviation of a single velocity component and λ is the Taylor length scale. Adapted from Goto (2018, Figure 1).

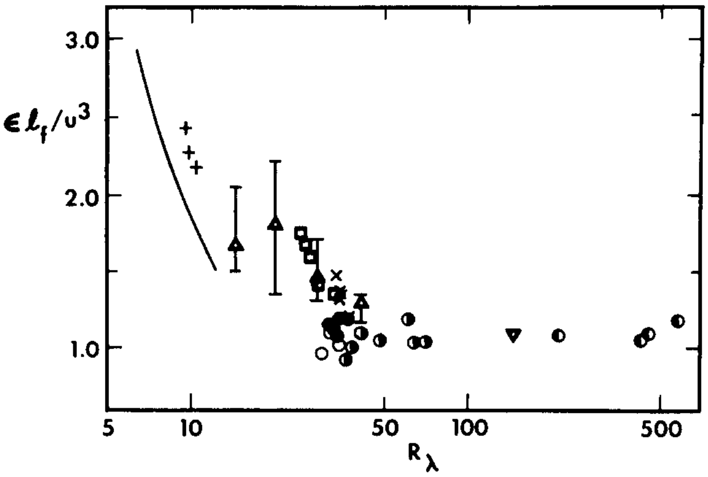

Figure 1.6: Normalised energy dissipation rate C_ϵ as a function of the Taylor-scale Reynolds number Re_λ. Adapted from Sreenivasan (1984, Figure 1).

since $\epsilon^{>}(k,t) \to \epsilon(t)$ holds in this limit. By modelling the largest-scale energy flux as

$$\Pi(L^{-1},t) \propto \frac{U(t)^3}{L(t)}, \tag{1.46}$$

where $U(t)$ denotes the macroscopic velocity, we obtain

$$\epsilon(t) \propto \frac{U(t)^3}{L(t)}. \tag{1.47}$$

This relation is called Taylor's dissipation law (Taylor 1935)[8]. By introducing the scaling coefficient C_ϵ to rewrite (1.47) as

$$\epsilon(t) = C_\epsilon \frac{U(t)^3}{L(t)}, \tag{1.48}$$

Taylor's dissipation law allows us to measure the microscopic energy dissipation rate by the macroscopic quantities. Here, we call C_ϵ the normalised energy dissipation rate. Figure 1.6 shows the Reynolds number dependency of C_ϵ evaluated from (1.48) in a statistical sense (Sreenivasan 1984). It suggests that C_ϵ tends to be independent of Re_λ:

$$C_\epsilon = \frac{\langle\epsilon\rangle\langle L\rangle}{\langle U\rangle^3} = \text{const.} \quad \text{as} \quad \mathrm{Re}_\lambda \nearrow . \tag{1.49}$$

This constancy of C_ϵ at higher Reynolds numbers has been reported in both DNS (Sreenivasan 1998; Kaneda, Ishihara, et al. 2003) and experiment (Cadot et al. 1997). Thus, this scaling has been employed in numerous research papers and industrial applications through turbulence models (Frisch 1995, § 7.2). Refer to Lumley (1992) and Vassilicos (2015) for the review on C_ϵ.

However, a naive implementation of Taylor's dissipation law (1.47) is problematic, as does the assumption and modelling procedures based on it. Indeed, the statistical relation (1.49) is valid and gives a good estimation of the average energy dissipation rate. However, it is not necessarily the case for an instantaneous balance (1.48), as there can be an imbalance between large- and small-scale dynamics associated with the nonequilibrium nature of turbulence. For a review of equilibrium and nonequilibrium dissipation scaling, see Vassilicos (2015) and references therein. In Chap. 7 of this thesis, we will investigate the nonequilibrium scaling of C_ϵ for inhomogeneous or unsteady flows.

The invalidity of LEH has been investigated in various flow configurations, including wall-bounded flows (Jiménez 2012), decaying turbulence under rotation (Valente and Dallas 2017), wake of side-by-side square cylinder (Zhou et al. 2020). George (2014) claimed that the LEH is "not satisfied in general for non-stationary and inhomogeneous flows", despite the fact that the hypothesis has been a basis for the Kolmogorov's 1941 theory of turbulence. Silva and Pereira (2005) investigated the LEH in the context of subgrid-scale modelling. Recently, in Kaneda and Yamamoto (2021), the LEH is extended to shear flow with several hypotheses to discuss the influence of mean shear on the dissipation-scale statistics. In Fig. 1.7, the temporal imbalance between the loss rate of energy at scale k and dissipated energy in scales smaller than k (Goto and Vassilicos 2016a). It is clear that by decreasing k (or focusing on larger scales), there is a larger imbalance between these two quantities. The same authors extended the analysis in decaying turbulence (Goto and Vassilicos 2016b). Bos, Shao, et al. (2007) and Fang and Bos (2023) investigated the influence of spectral imbalance on the normalised energy dissipation rate. McComb et al. (2010) claimed that Taylor's dissipation law (1.47) should be interpreted as estimating the peak inertial range energy flux rather than the energy dissipation rate. In Valente, Onishi, et al. (2014), the systematic imbalance between the energy flux to the fine scale and its dissipation was investigated. In Rubinstein and Clark (2017), the concept of "equilibrium" was investigated, and the conclusion was similar to McComb et al. (2010); the energy dissipation rate cannot be equivalent to the large-scale energy flux. In Vela-Martín and Jiménez (2021), the "out-of-equilibrium" energy flux was investigated. Recently, Steiros has been working on a generalization of the turbulence theory for out-of-equilibrium effects and cascades far from initial conditions (Steiros 2022a; Steiros 2022b).

One of the pioneering works on the nonequilibrium balance of energy budget in turbulence was Yoshizawa (1994). This study investigated the nonequilibrium property of the inertial-range statistics of energy with

---

[8] It is sometimes called the Taylor–Kolmogorov relation (or dissipation law) (Rubinstein and Clark 2017), as Kolmogorov (1941b) first derived this dissipation law. See also Goto and Vassilicos (2016a) for historical remark.

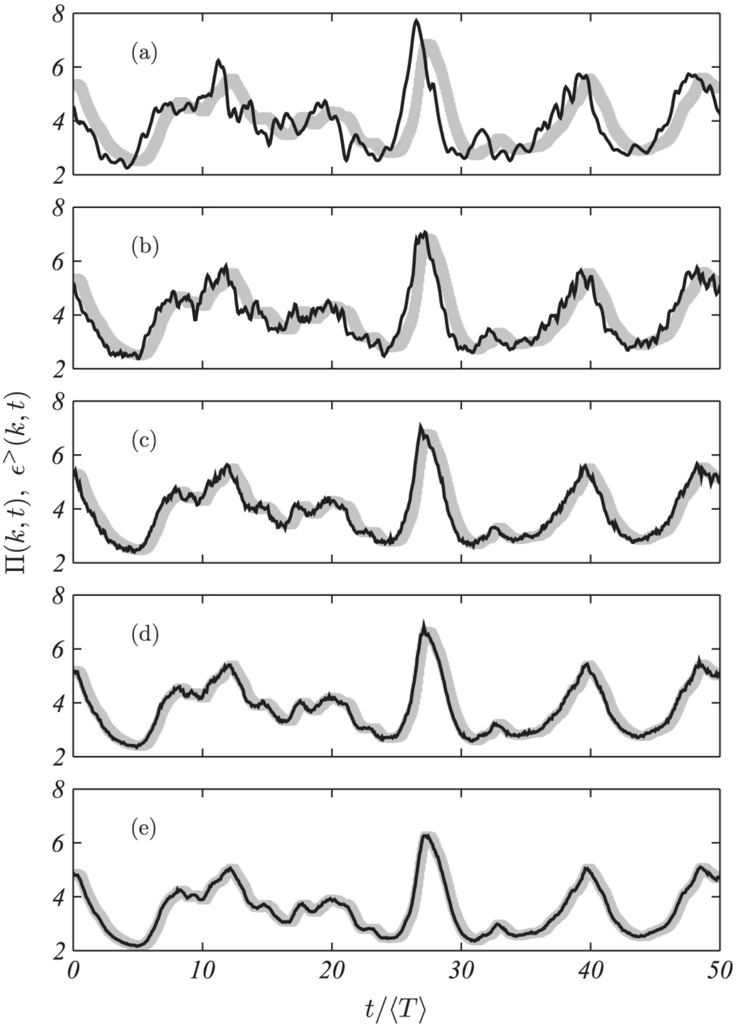

Figure 1.7: Time series of the energy dissipation rate $\epsilon^{>}(k,t)$ (thick grey line) high-pass filtered at given k and the energy loss rate $\Pi(k,t)$ (thin black line) at scale k for five different values of k, obtained in turbulence with averaged Taylor-scale Reynolds number of $\langle R_\lambda \rangle = 490$. The value of k increases from panel (a) to (e). Adapted from Goto and Vassilicos (2016a, Figure 5).

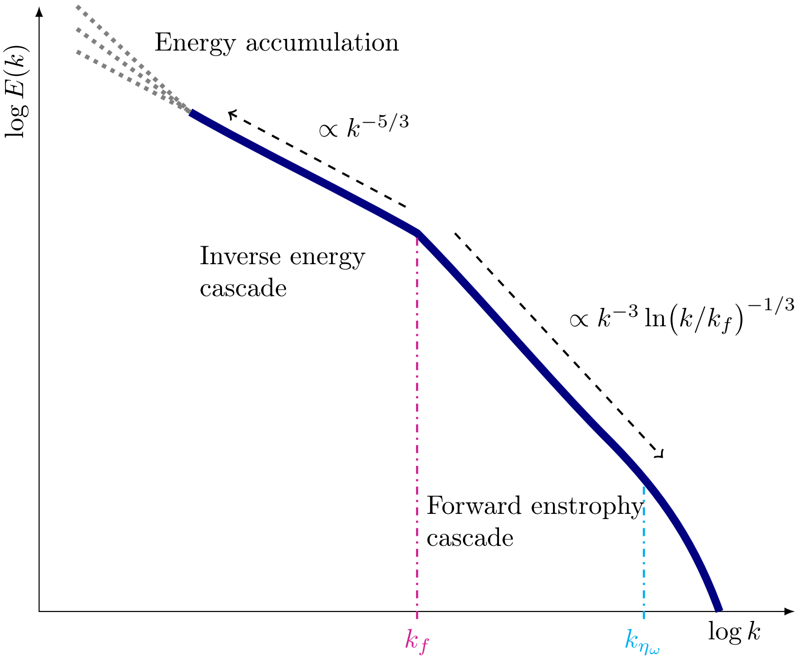

Figure 1.8: A schematic of the energy spectrum of two-dimensional Navier–Stokes turbulence. Dotted lines in the largest scales represent energy accumulation. Dashed arrows denote $k^{-5/3}$ scaling of the inverse energy cascade and k^{-3} (plus logarithmic correction) scaling of the forward enstrophy cascade, respectively. Vertical dash-dotted lines denote the forcing wavenumber k_f and the Kolmogorov wavenumber associated with enstrophy dissipation k_{η_ω}, respectively.

the Lagrangian derivative of the energy transfer. A $k^{-7/3}$ scaling correction gives the deviation from the equilibrium scaling. This correction due to unsteadiness was further investigated in (Rubinstein, Clark, et al. 2004; Woodruff and Rubinstein 2006; Horiuti and Tamaki 2013). In Chap. 6 of the thesis, we will investigate the inhomogeneity-induced $k^{-7/3}$ scaling correction.

In terms of turbulence modelling, Edeling et al. (2018) proposed a return-to-eddy-viscosity model, which explicitly considers the contributions from the departure of the small scales from the local equilibrium (Duraisamy, Iaccarino, et al. 2019). Bos (2020) proposed a simple model in near-field grid turbulence. Vela-Martín (2022) discussed the nonequilibrium effect in subgrid-scale modelling.

1.2.4 Cascades in two-dimensional turbulence

When we consider turbulent flow confined in the two-dimensional plane $\boldsymbol{x}_{2\mathrm{D}} = (x, y) \in \Omega_{2\mathrm{D}}$, it exhibits qualitatively different properties from three-dimensional turbulence. We begin with the governing equations of two-dimensional velocity field $\boldsymbol{u} = (u_x, u_y)$ and corresponding one-dimensional vorticity field ω perpendicular to $\boldsymbol{x}_{2\mathrm{D}}$. The Navier–Stokes equations are identical to the three-dimensional ones (1.1), and the kinetic energy

$$K \equiv \frac{1}{2}\left\langle \boldsymbol{u}\cdot\boldsymbol{u}\right\rangle_{\Omega_{2\mathrm{D}}} \tag{1.50}$$

remains invariant in the inviscid and force-free limit. On the other hand, the vorticity equation reads

$$\frac{\partial\omega}{\partial t} + (\boldsymbol{u}\cdot\boldsymbol{\nabla})\omega = \nu\nabla^2\omega + (\boldsymbol{\nabla}\times\boldsymbol{f})_z, \tag{1.51}$$

and there is no vortex stretching term as ω is perpendicular to $\boldsymbol{u}$. Since the nonlinear term is conservative, the enstrophy

$$\varOmega \equiv \frac{1}{2}\left\langle \omega^2\right\rangle_{\Omega_{2\mathrm{D}}} \tag{1.52}$$

is also an inviscid invariant. This is the critical difference compared to the three-dimensional case (1.3), where there is vortex stretching (enstrophy production). In the following, we consider cascades of two invariants of two-dimensional turbulence: inverse energy cascade and forward enstrophy cascade as depicted in Fig. 1.8. For reference, see textbooks Lesieur (2008, § 8) and Davidson (2015, § 10) as well as review articles (Kraichnan and Montgomery 1980; Tabeling 2002; Kellay and Goldburg 2002; Boffetta and Ecke 2012; Alexakis and Biferale 2018).

First, we consider the enstrophy cascade. In Fourier space, the enstrophy spectrum can be expressed as $k^2E(k)$ and its equation reads

$$\frac{\partial k^2 E(k)}{\partial t} = k^2 F(k) + k^2 T(k) - 2\nu k^4 E(k), \tag{1.53}$$

which is obtained by multiplying the energy equation (1.21) by k^2. Note that due to the inviscid conservation of enstrophy, the enstrophy transfer satisfies

$$\int_0^\infty k^2 T(k)\,\mathrm{d}k = 0. \tag{1.54}$$

By conducting a similar analysis for enstrophy as already done for energy in § 1.2.1, we can define the enstrophy dissipation rate

$$\epsilon_\omega = 2\nu \int_0^\infty k^4 E(k)\,\mathrm{d}k\,, \tag{1.55}$$

and corresponding length scale

$$k_{\eta_\omega} \equiv \left(\frac{\epsilon_\omega}{\nu^3}\right)^{1/6}. \tag{1.56}$$

By assuming that the statistics in the inertial range ($k_f \ll k \ll k_{\eta_\omega}$) can be determined by the single parameter ϵ_ω, a dimensional analysis yields

$$E(k) = C_K' \epsilon_\omega^{2/3} k^{-3} \quad \text{for} \quad k_f \ll k \ll k_{\eta_\omega}. \tag{1.57}$$

This is the k^{-3} scaling of the energy spectrum associated with the enstrophy cascade. Furthermore, due to the nonlocal nature of the enstrophy cascade, the k^{-3} scaling (1.57) is subject to a logarithmic correction (Kraichnan 1971b):

$$E(k) = C_K' \epsilon_\omega^{2/3} k^{-3} \Big[\ln\big(k/k_f\big)\Big]^{-1/3} \quad \text{for} \quad k_f \ll k \ll k_{\eta_\omega}. \tag{1.58}$$

The $\ln\big(k/k_f\big)$ correction acts to suppress the diverging integral of enstrophy: $\int k^2 E(k)$.

Next, we consider the inverse energy cascade. Thanks to Fjortoft's theorem (Fjørtoft 1953) [Also see Lesieur (2008, § 8.3)], there is no energy transfer towards smaller scales ($k > k_f$) associated with the enstrophy cascade. Thus, the injected energy can only be transferred to larger scales ($k < k_f$). An analogy of the discussion for the three-dimensional turbulence in § 1.2.2 yields the same scaling for different wavenumber regime (Kraichnan 1967; Leith 1968):

$$E(k) = C_K'' \epsilon^{2/3} k^{-5/3} \quad \text{for} \quad k \ll k_f. \tag{1.59}$$

There are multiple candidates for the physical mechanism of the inverse energy cascade (Davidson 2015, § 10.1.4). Since the dissipation term does not act strongly on the largest wavenumbers, temporal evolution of $E(k,t)$ is associated with energy accumulation at scales of the size of the flow domain.

1.3 Physical-space mechanism behind the energy cascade

The essence of Kolmogorov's 1941 theory (hereafter, K41 theory) is that one cannot distinguish the statistics of the small-scale structures of a given turbulence from different flow realisations. The small-scale universality of the K41 theory has set the paradigm of turbulence research for the last eighty years.

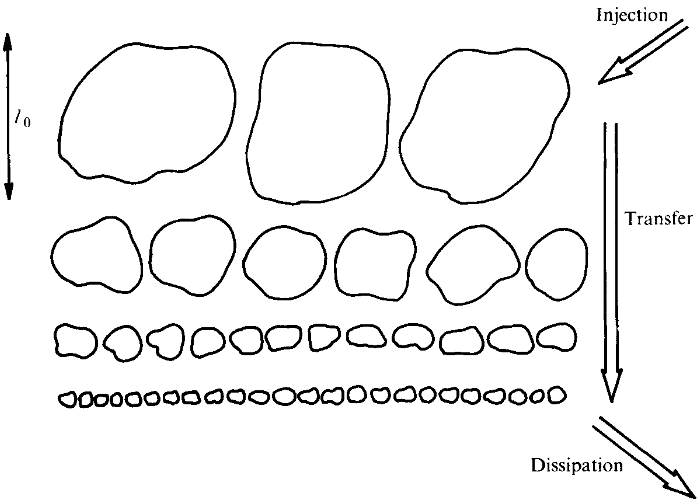

Figure 1.9: Classical schematic of energy cascade with space-filling eddies for various scales, accounting for the K41 theory. Adapted from Frisch, Sulem, et al. (1978, Figure 1). A similar schematic with scale annotations can be found in Frisch (1995, Figure 7.2).

However, the scale-space description does not provide how the structures of various scales are generated and sustained in physical space. Thus, the following question:

> How are the multi-scale structures in turbulent flow sustained? In particular, how does the energy *cascade* from large to small scales in physical space?

has been one of the central questions in the turbulence research community, on which we still do not have a consensus. That means we are still far from the physical-space description of turbulence as a counterpart of the K41 theory in scale space. For example, Fig. 1.9 shows a schematic of the energy cascade by space-filling vortices of various scales. This schematic may give the impression that the largest-scale vortices are "breaking up" as energy cascades down to smaller scales. This picture is common in the turbulence community, but to what extent is it true?

This section reviews candidates for the energy cascade mechanism phenomenologically and quantitatively. In particular, we focus on the two processes: vortex stretching (§ 1.3.1) and strain self-amplification (§ 1.3.2). In Appendix C, we review several other candidates for the energy cascade mechanism, such as instability, vortex reconnection, and spiral vortex scenario. In § 1.3.3, we briefly review the intermittency of turbulence in relation to the energy cascade.

1.3.1 Vortex stretching

Vortex stretching is the most commonly accepted mechanism of energy cascade. For a detailed review including quotations from the historical works, see Eyink (2007-2008, § IV (A)). We have two nonlinear terms in the vorticity equation (1.3): the vortex advection term $(\boldsymbol{u}\cdot\boldsymbol{\nabla})\boldsymbol{\omega}$ and the vortex stretching term $(\boldsymbol{\omega}\cdot\boldsymbol{\nabla})\boldsymbol{u}$. It is the latter term we focus on in this subsection, as its name indicates the mechanism. By taking inner product of (1.3) and $\boldsymbol{\omega}$, we obtain the enstrophy equation

$$\frac{\partial \Omega}{\partial t} + u_j \frac{\partial \Omega}{\partial x_j} = \omega_i S_{ij} \omega_j + \nu \frac{\partial^2 \Omega}{\partial x_k^2} - \nu \left(\frac{\partial \omega_i}{\partial x_j}\right)^2 + \omega_i \epsilon_{ijk} \frac{\partial f_j}{\partial x_k}, \tag{1.60}$$

where ϵ_{ijk} denotes the Levi-Civita symbol. The first term on the RHS, $\omega_i S_{ij} \omega_j$, corresponds to the vortex stretching and is called the enstrophy production term.

Figure 1.10 shows the schematic of vortex stretching between vortices of different scales. A similar schematic can be found in, for example, Tennekes and Lumley (1972, Figure 8.4) and Johnson (2021a, Figure 1). In the final paragraph of Taylor (1938), he wrote:

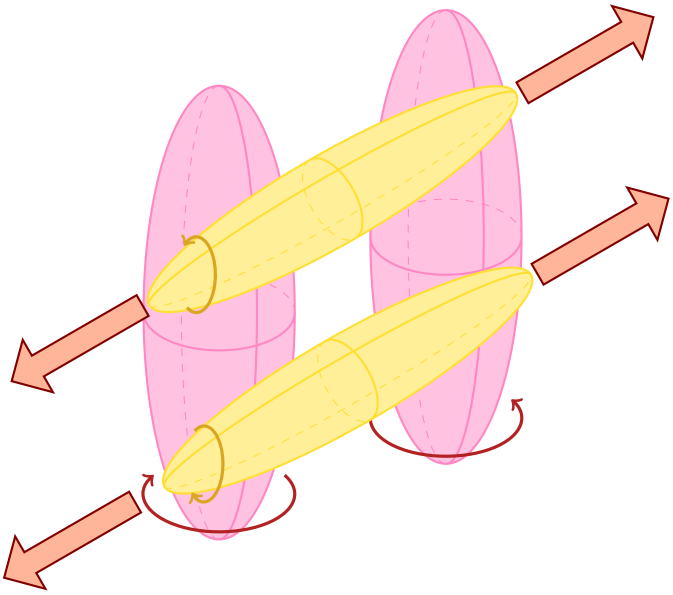

Figure 1.10: Schematic of vortex stretching between large-scale vortices (red) and small-scale vortices (yellow). Aligned large-scale vortices with counter-rotating direction induce strain field between them; small-scale vortices are stretched in anti-parallel configuration to the large-scale vortices.

> It seems that the stretching of vortex filaments must be regarded as the principal mechanical cause of the high rate of dissipation which is associated with turbulent motion.

In Onsager (1949, p. 282), a similar idea is presented as:

> Now it is very reasonable to expect that a vortex line – of any line which is deformed by the motion of the liquid – will tend to increase in length as a result of more or less haphazard motion. This process tends to make the texture of the motion ever finer, and greatly accelerates the viscous dissipation.

Note that both Taylor (1938) and Onsager (1949) argue vortex stretching to be the main cause of energy dissipation by viscosity and *not* energy cascade. However, we remark that Onsager had the idea that the vortex stretching is related to the inertial range dynamics (Eyink and Sreenivasan 2006, § IV A). Although there are no published works, Onsager had been working on extending Taylor's idea to the "cascade" of energy, which he first used in the context of turbulence theory in a letter to Chia-Chiao Lin (Eyink and Sreenivasan 2006, Appendix B) and a one-page paragraph (Onsager 1945). In the former, Onsager wrote

> The distribution law (19) [the $-5/3$ spectrum] is compatible with the hypothesis that the mean rate of stretching of vortex lines is given by the average rate of deformation in the liquid.

In another place of the same letter, he remarked that

> The selection rule for the 'modulation' factor in each term of (8) [the nonlinear term of the Navier–Stokes equations in Fourier space] suggests a 'cascade' mechanism for the process of dissipation, and also furnishes a dynamical basis for an assumption which is usually made on dimensional grounds only.

In the textbook Tennekes and Lumley (1972), the vortex stretching is related to the energy cascade:

> When vorticity finds itself in a strain-rate field, it is subject to stretching. On the basis of conservation of angular momentum, we expect that the vorticity in the direction of a positive strain rate is amplified, while the vorticity in the direction of a negative strain rate is attenuated.
> [...]
> Vortex stretching involves an exchange of energy, because the strain rate performs deformation work on the vortices that are being stretched.

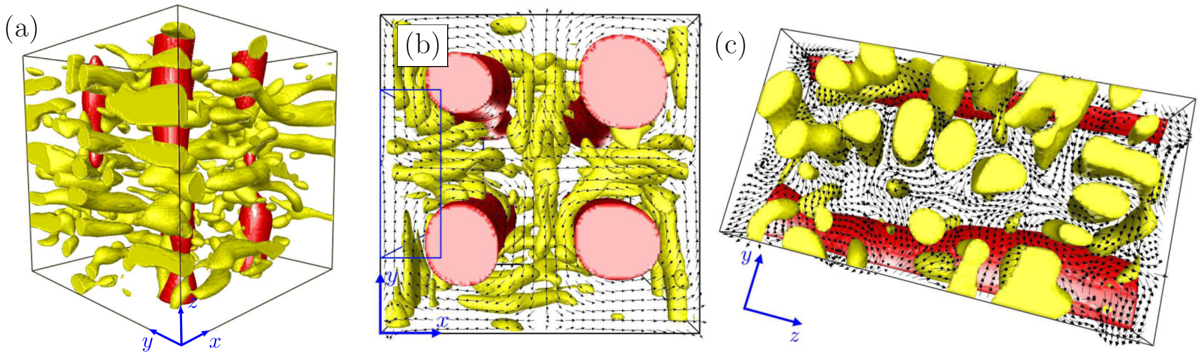

Figure 1.11: (a) Visualisation of coarse-grained vortex structures with the larger (red) and the smaller (yellow) scales. (b) Same visualisation as panel (a) with a different angle. (c) Cropped domain in panel (b) (blue frame). Arrows denote the large-scale velocity field for panels (b) and (c). Adapted from Goto, Saito, et al. (2017, Figure 3).

Indeed, Fig. 8.4 of Tennekes and Lumley (1972, p. 257) is essentially same as Fig. 1.10. Although Tennekes and Lumley's remark was rather schematic, much study has been conducted since then.

Numerical evidence of vortex stretching and generation of the fine-scale structures are reported (Melander and Hussain 1993; Jiménez, Wray, et al. 1993; Nomura and Post 1998; Pullin and Saffman 1998) and discussed in association with intermittency (Siggia 1977; Buaria, Bodenschatz, et al. 2020). Also see Fig. 1.2. Recent analysis includes the large-deviation theory (Johnson and Meneveau 2016), Unstable Periodic Orbit (UPO) (Lucas and Kerswell 2017; van Veen, Vela-Martín, et al. 2019), and artificial suppression of vortex stretching (Bos 2021).

Goto (2008) proposed that the energy cascade occurs by stretching of smaller-scale vortices by the large-scale strain induced by pairs of vortex tubes in anti-parallel configurations. This analysis was motivated by the picture previously proposed by Melander and Hussain (1993): The large-scale vortex tube generates smaller anti-parallel pairs of vortex around it and cascades the energy. Furthermore, the importance of vortices in the anti-parallel configurations was pointed out by Siggia (1985). Goto (2008) defined the internal energy in each subdomain of the flow to be Galilei invariant and employed the Lagrangian framework to define its energy transfer rate. Goto (2012) and Goto, Saito, et al. (2017) investigated scale-by-scale vortex stretching between the anti-parallel vortex tubes of different scales in higher Reynolds numbers to find that the energy transfer due to vortex stretching is the most efficient at a scale ratio of about two. Similar finding was observed by other groups (Eyink 2006; Leung et al. 2012; Doan et al. 2018) and also in wall-bounded flows (Lozano-Durán et al. 2016; Motoori and Goto 2019). From these findings, vortex stretching is a convincing candidate responsible for the physical mechanism of the scale-local energy cascade. See Fig. 1.11 for the hierarchical vortex structures. Mathematical support for this finding is given in Gibbon et al. (1999), Yoneda (2020), Yoneda et al. (2022), and Tsuruhashi et al. (2022). See also Appendix D.

1.3.2 Strain self-amplification

Indeed, the vortex stretching mechanism has been the primary candidate for the energy cascade since 1940s. However, it has not been the consensus for the turbulence community (Tsinober 2009, § 6.2.1). In this subsection, we review another important candidate for the phenomena: self-amplification of strain. It was first proposed by Tsinober (Tsinober et al. 1999; Tsinober 2000; Galanti and Tsinober 2000). The governing equation of the rate-of-strain tensor reads (Nomura and Post 1998, (2.2)):

$$\frac{\partial S_{ij}}{\partial t} + u_k \frac{\partial}{\partial x_k} S_{ij} = -S_{ik}S_{kj} - \frac{1}{4}\left(\omega_i\omega_j - \delta_{ij}\omega_k\omega_k\right) - \frac{\partial^2 p}{\partial x_i \partial x_j} + \nu \frac{\partial^2 S_{ij}}{\partial x_k \partial x_k}, \tag{1.61}$$

where the RHS terms consist of self-interaction, local interaction with vorticity, pressure Hessian, and viscous diffusion, respectively. Note that we omit the forcing term for simplicity. When multiplying (1.61)

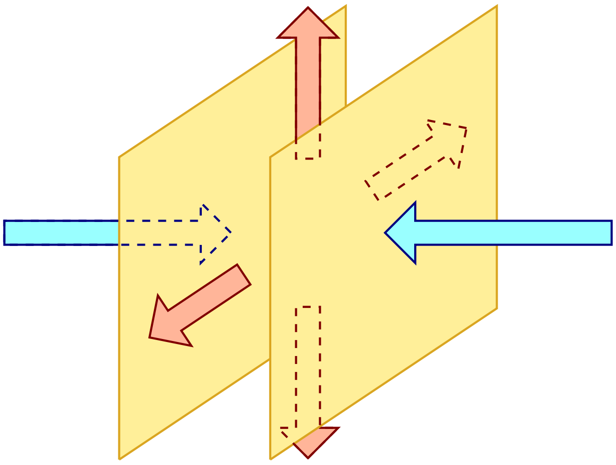

Figure 1.12: Schematic of strain self-amplification.

by S_{ij}, we obtain the equation of the squared strain $|S|^2 = 2S_{ij}S_{ij}$ (Vela-Martín 2019, (4.3)):

$$\frac{1}{4}\left(\frac{\partial|S|^2}{\partial t} + u_j\frac{\partial}{\partial x_j}|S|^2\right) = -S_{ij}S_{jk}S_{ki} - \frac{1}{4}\omega_i S_{ij}\omega_j - S_{ij}\frac{\partial^2 p}{\partial x_i \partial x_j} + \nu S_{ij}\frac{\partial^2 S_{ij}}{\partial x_k \partial x_k}. \tag{1.62}$$

The first term on the RHS, $-S_{ij}S_{jk}S_{ki}$, is called the strain self-amplification term.
Figure 1.12 shows a schematic of this energy cascade process where a strain-concentrated region (between two parallel planes) is subject to compression along with one axis (eigenvalue) and extension for the other two axes. This highlights the difference against the vortex stretching with one extension axis and two compression axes. For example, a similar schematic can be found in Johnson (2021a, Figure 2).
The strain self-amplification process may be easily understood in the one-dimensional Burgers equation

$$\frac{\partial u}{\partial t} + u\frac{\partial u}{\partial x} = 0. \tag{1.63}$$

Figure 1.13 shows its temporal evolution, where an initially smooth velocity profile given by $\sin(2\pi x)$ leads to a finite-time singularity. Here, the same level of velocity gradient is confined in a smaller domain as time evolves. In other words, the solution amplifies the velocity gradient by itself. Thus, the energy is transferred to the smaller scales (higher Fourier modes) as time evolves, thanks to the self-amplification of the velocity gradient.
In Tsinober (2009, § 6.2.2), the importance of the strain self-amplification is emphasised for four reasons:

1. Nonlocal correlation between the strain and vorticity,
2. Energy dissipation ϵ is directly associated with strain S_{ij} and not with vorticity ω_i [see (1.9)],
3. Vortex stretching is essentially a process of strain-vorticity interactions,
4. Strain-dominated regions appear to be the most active in turbulence.

In Carbone and Bragg (2020), they answered to the title of the paper “Is vortex stretching the main cause of the turbulent energy cascade?” unfavourably by claiming that the strain self-amplification plays the dominant role in the average behaviour of the energy cascade. In contrast, vortex stretching plays a more important role in the fluctuations of the cascade about its average behaviour. Similarly, Johnson (2020) and Johnson (2021a) concluded that the contributions of the strain self-amplification to energy transfer are higher than that of vorticity stretching[9]. We will review these recent articles in more detail in Appendix D. The investigations of the physical space mechanism point to a common problem in turbulence research; since the system is multi-scale, nonlinear and nonlocal, it is tremendously difficult to disentangle the effect of a particular structure or interaction from the rest of the dynamical features. For example, in

---

[9] Also, see the same author’s *Physics Today* article (Johnson 2021b).

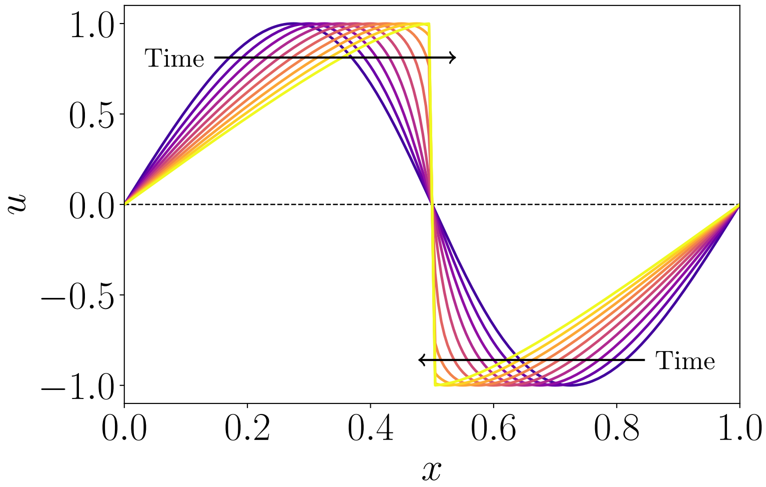

Figure 1.13: Temporal evolution of the one-dimensional inviscid Burgers equation. Simulation is conducted by an open-source project CFD Julia (Pawar and San 2019). Time evolves from dark to light colours.

Chap. 3, we illustrate that even at very low Reynolds numbers, the flow dynamics are determined by an intricate interplay between a large number of Fourier modes.

1.3.3 Intermittency and the energy cascade

In the previous section § 1.2, we discussed the scale-space description of turbulence. However, as we reviewed in this section, the physical-space description of energy cascade employs various flow structures, particularly vortices in various scales. The complex multi-scale interactions of such structures induce highly intermittent fine-scale structures. For example, see Fig. 1.2, where we observe dense clusters and voids of the fine-scale structures in the domain.

The inhomogeneous nature of turbulence fragilizes the validity of the K41 theory, where the globally averaged energy dissipation rate ϵ determines the statistics. Kolmogorov himself corrected his 1941 theory in Kolmogorov (1962), where he proposed a refined similarity hypothesis with the energy dissipation rate locally averaged in space. This introduces corrections to the inertial range scaling, particularly for higher-order moments. The quest for an appropriate description of these higher-order moments (or heavy tails of probability distribution function), which are observed both in Eulerian and Lagrangian statistics (Anselmet et al. 1984; Chevillard, Castaing, et al. 2006), has resulted in a wealth of models. The list of models for the intermittency includes the She-Leveque (She and Lévêque 1994) (or Log-Poisson (Dubrulle 1994)) model and multifractal descriptions (Parisi and Frisch 1985), to name a few. For reference, Frisch (1995, § 8) is devoted to the intermittency of turbulence.

We stress that in this thesis, where the energy cascade is its main topic, we mainly investigate second-order quantities such as kinetic energy. For these lower-order statistics, the influence of intermittency is not dramatic (Bos, Chevillard, et al. 2012). Therefore, we will not focus on the influence of intermittency in the rest of this thesis.

Part I

Quasi-cyclic Temporal Fluctuations of Turbulence and its Minimal Model

2 Temporal Fluctuations in Turbulence

Turbulence is often referred to as an example of chaos. Here, the most important aspect of chaos is not the randomness but the sensitivity to the initial conditions, which means that two realisations of the same system with slightly different initial conditions can eventually evolve into completely different states. However, behind this sensitivity which makes it almost impossible to predict a turbulent flow in all of its details, sometimes there seems to be a more deterministic underlying mechanism when one considers the temporal fluctuations of turbulence. In this chapter, we review such organised structures in the temporal domain of turbulence. In § 2.1, we discuss the temporal Quasi-Cyclic Behaviour (QCB) of turbulence associated with the energy cascade. In § 2.2, we review reduced-order modelling of turbulence. In particular, we focus on modelling developed turbulence and briefly address laminar-turbulent transition.

2.1 Temporal (quasi-)cyclic modulation associated with the energy cascade

In the Introduction (§ 1.3), we reviewed the concept and possible energy cascade mechanism in physical space. In this section, we discuss that this phenomenological picture also captures the temporal dynamics of turbulence. In particular, we review temporal Quasi-Cyclic Behaviour (QCB) observed in turbulence. In § 2.1.1, we discuss the consequence of the Local Equilibrium Hypothesis (LEH) breakdown. The imbalance between large- and small-scale energy associated with the energy cascade dynamics leads to an intrinsic unsteady nature, which can cause QCB in certain kinds of turbulent flows. In § 2.1.2, we first introduce the concept of the Unstable Periodic Orbit (UPO), which can be understood as a *skeleton* of turbulence *embedded* in complex fluctuations, followed by a concise review on its relation with the energy cascade. In § 2.1.3, we focus on a closed system where the top and bottom rid of cylindrical disks rotate in opposite directions to excite turbulence in the domain: von Kármán flow.

2.1.1 Intrinsic unsteadiness and quasi-cyclic behaviour of turbulence

The LEH (§ 1.2.1) sets the foundation of turbulence theory in equilibrium. However, as depicted in Fig. 1.7, the balance between the energy flux and dissipation does not hold. The imbalance between these large- and small-scale quantities reflects the intrinsic unsteadiness of turbulence. Figure 2.1(a) quantifies this time delay using the two-time correlation function. Similar results are reported in, for example, Pearson, Yousef, et al. (2004, Figure 3), Cardesa, Vela-Martín, Dong, et al. (2015, Figure 2 (b)), and Wan et al. (2010). In particular, the earliest result is probably presented in Meneveau and Lund (1994, Figure 4) where a two-time energy correlation in fluid "blob" within the Lagrangian framework was computed. The correlation peak is always observed with a time delay, characterised by the typical time scale of the cascade, a function of the length scale or the size of the "blob" (Lumley 1992). These observations support the forward energy cascade and the causality between large and small scales of turbulence, leading to intrinsic unsteadiness (Bos, Shao, et al. 2007). Cardesa, Vela-Martín, Dong, et al. (2015) investigated the scale-by-scale energy flux and their time delay between different scales to find the scale-local (or step-wise) dynamics. Goto and Vassilicos (2015) and Goto and Vassilicos (2016a) investigated the energy dissipation rate scaling in unsteady turbulence.

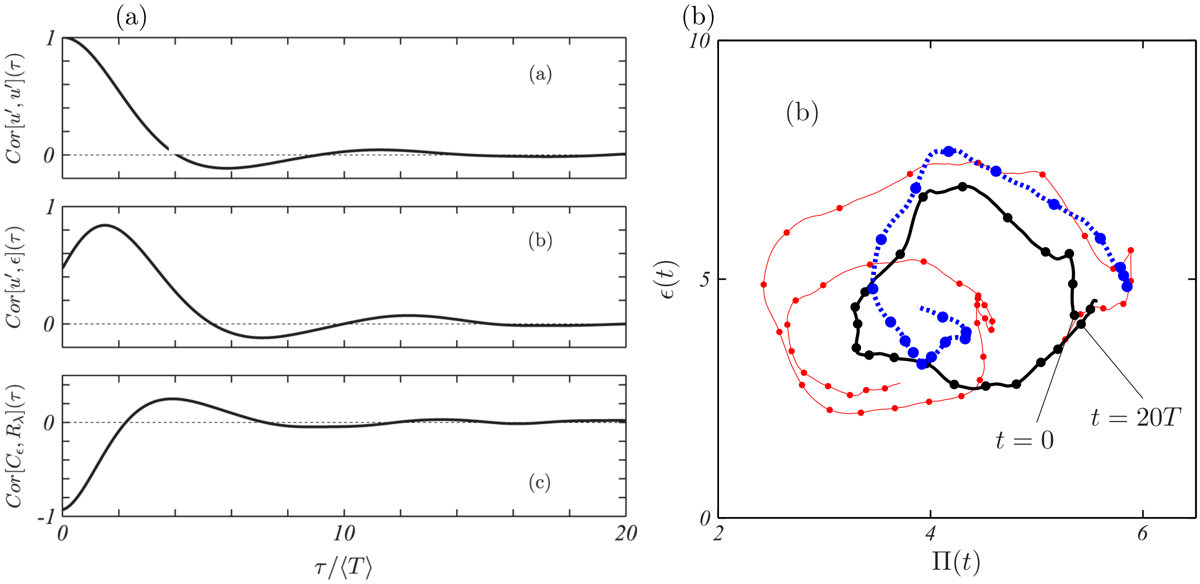

Figure 2.1: (a) Two-time correlation function of (a-a) self correlation of the turbulent velocity $u'(t) = \sqrt{2/3K(t)}$ defined by the kinetic energy. (a-b) the turbulent velocity $u'(t)$ and the energy dissipation rate $\epsilon(t)$. (a-c) The normalised energy dissipation rate $C_\epsilon(t)$ and the Taylor-scale Reynolds number $R_\lambda = u'\lambda/\nu$. Adapted from Goto and Vassilicos (2016a, Figure 3 (b)). (b) Time series of the energy input rate $\Pi(t)$ against the energy dissipation rate $\epsilon(t)$ in turbulence driven by a steady body force (3.2). Different Reynolds numbers are overlapped; the value increases from the thin red curve, then the black curve and the dotted blue line corresponds to the highest Re. Time evolves counter-clockwise. Adapted from Goto, Saito, et al. (2017, Figure 15 (b)).

We proceed to consider the recurrence of a kind of "cycle" in temporal fluctuations. A number of laminar and turbulent flows display QCB. An illustrative example is vortex shedding behind an obstacle. For low Reynolds number (Re), the so-called von Kármán vortex street behind a cylinder is perfectly periodic, which corresponds to a Stable Periodic Orbit (SPO) in phase space. Even when the flow becomes fully turbulent at higher Re, this periodicity is still present, though the stochastic nature of turbulent motion prevents the system from being perfectly periodic.

Figure 2.1(b) shows the temporal evolution of turbulence in a periodic domain under a steady forcing (3.2) for three different Reynolds numbers. The counter-clockwise cycle between the energy input rate and energy dissipation rate indicates that turbulence undergoes two states: input surpasses dissipation and vice versa. This close-to-periodic motion, embedded in turbulent fluctuations, is what we will call QCB. The three similar curves suggest the robustness of the quasi-cyclic temporal evolution of turbulence. The QCB is also found in turbulent channel flow, where a Self-Sustaining Process (SSP) governs the dynamics (Johansson and Alfredsson 1982; Luchik and Tiederman 1987; Waleffe 1995; Hamilton et al. 1995; Panton 2001; Hwang and Cossu 2010). In particular, in small channel flow domains (the so-called minimal flow unit), close to periodic behaviour is observed (Jiménez and Moin 1991, Fig. 6). These observations suggest that such temporal dynamics might be a general feature of turbulence. We note here that the characteristic time scale of such QCB cannot be universal for different flow configurations, since it is determined by the largest-scale motion of the flow. This remark is related to the original "Landau's objection" to the K41 theory (Frisch 1995, § 6.4).

2.1.2 Periodic orbit as a skeleton of the energy cascade

Deterministic Navier–Stokes equations can be considered a dynamical system with a large number of degrees of freedom. Indeed, in its early days, dynamical system theory focused on low-dimensional models. However, fast-developing computational resources allow researchers to investigate various *solutions* of turbulence, such as steady, travelling-wave, and periodic solutions (Kawahara, Uhlmann, et al. 2012). Figure 2.2 shows the first discovered Unstable Periodic Orbit (UPO) embedded in turbulent channel flow (Kawahara and Kida 2001). These invariant solutions are low dimensional in phase space compared

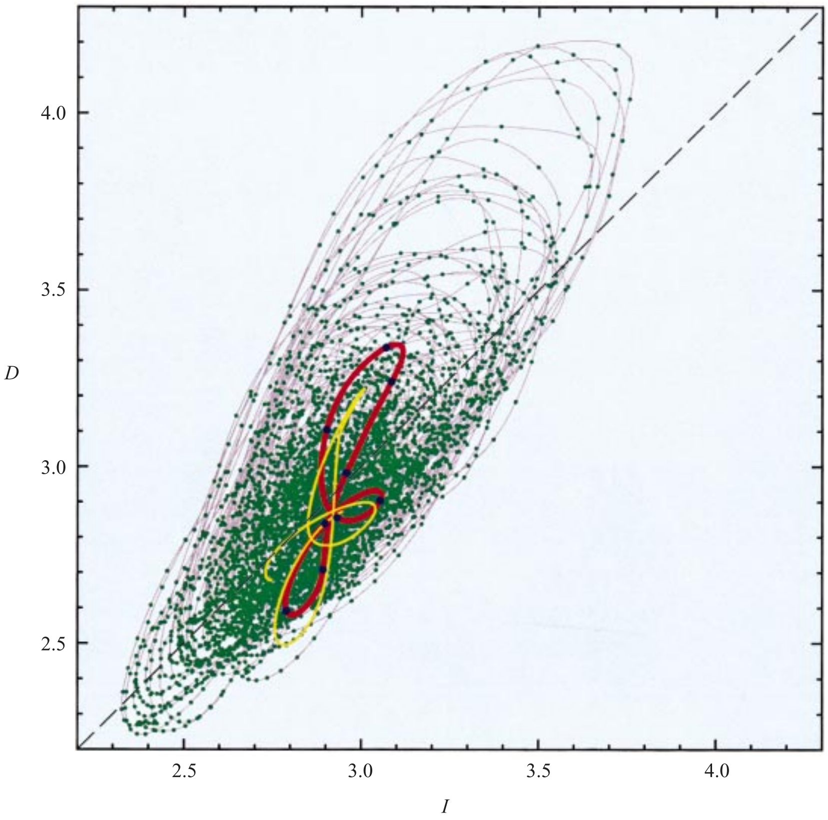

Figure 2.2: The projection of an Unstable Periodic Orbit (UPO) onto the 2D portrait of the normalised energy input rate I and the energy dissipation rate $\epsilon(t)$. A periodic orbit is denoted by the red closed line. The turbulence time series is also shown in the grey line, where the green dots denote the constant time interval. The yellow line is a cut of the turbulent trajectory and shows a typical behaviour of turbulence approaching the periodic orbit. Adapted from Kawahara and Kida (2001, Figure 1).

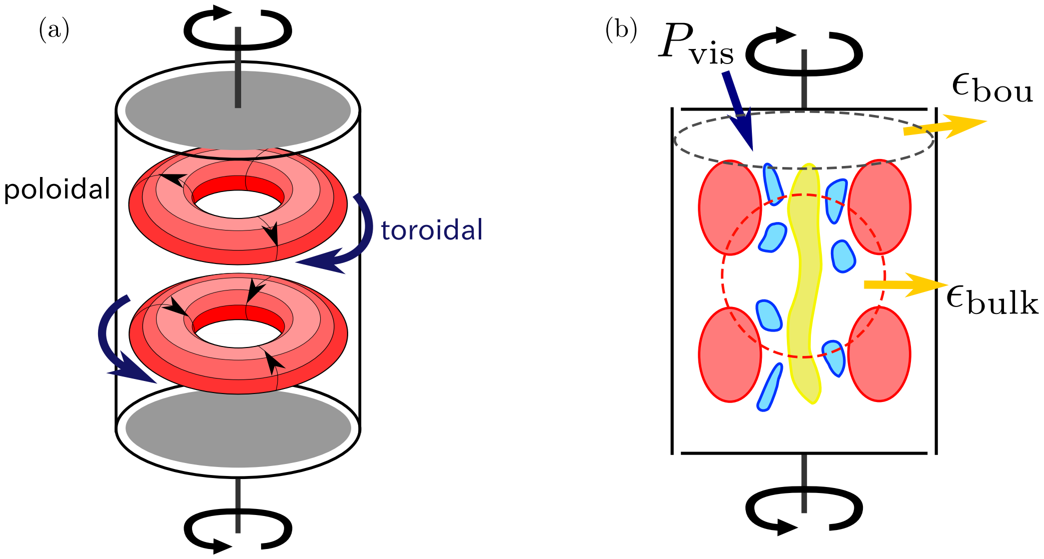

Figure 2.3: (a) A schematic of von Kármán flow with its large-scale vortex structures in a pair of doughnut-like shapes. Arrows on the vortex structures denote toroidal and poloidal rotation directions. (b) A schematic of vortex structures and energy cycle of von Kármán flow in its meridional plane. Red, yellow, and blue denote large, intermediate, and small-scale vortex structures generated by the energy cascade. P_{vis} denotes the energy injection via viscous force at the rotating disks, while ϵ_{bou} and ϵ_{bulk} denotes the energy dissipation at the boundary and bulk regions of the flow, respectively. Note that both panels visualise the system with smooth disks (without blades).

to turbulence but possess many key turbulence properties, such as universal statistics, coherent large-scale structures, and dynamical processes. However, the connection of the periodic solution with energy cascade dynamics has not been investigated until recently. In van Veen, Vela-Martín, et al. (2019), a UPO was identified in turbulence driven by a deterministic forcing[1]. This UPO shows the energy cascade dynamics between vortices of different scales, similar to Goto, Saito, et al. (2017).

2.1.3 Quasi-cyclic behaviour in von Kármán flow: a closed system under constant forcing

In this subsection, we review the mechanism of such QCB in a realistic flow setup called von Kármán flow, a counter-rotating lid and bottom cover drive fluid in a cylinder. The content is based on the following:

> Araki, Ryo and Susumu Goto (2021). Quasiperiodic fluctuations of von Kármán turbulence driven by viscous stirring. *Physical Review Fluids* **6** (8), p. 084603.

Figure 2.3 shows the apparatus of the system with the distinctive large-scale structures in panel (a) and the schematic vortex structures in its meridional plane in panel (b). One of the intriguing properties of this system is the qualitatively different behaviour of the normalised energy dissipation rate C_ϵ where the flow is driven by either smooth or rough disks, associated with viscous and inertial stirring, respectively (Cadot et al. 1997). With inertial stirring, C_ϵ is independent of the Reynolds number Re. On the other hand, the viscous stirring setup finds that C_ϵ does depend on Re even in the high Re limit. However, when we consider only the bulk domain of the system, C_ϵ remains approximately constant in this limit. The inertially-stirred von Kármán flow has been widely used in experimental investigations, as the system can realise high-Re turbulence. These studies consider fluid acceleration (Mordant et al. 2002), possible singularities of the solution of the Navier-Stokes equation (Saw et al. 2016), intermittency with weak Kolmogorov–Kármán–Howarth–Monin formulation (Dubrulle 2019), and interscale energy transfer (Knutsen et al. 2020). Furthermore, the von Kármán flow with inertial stirring sometimes shows interesting behaviours such as bistable turbulent states (Ravelet et al. 2004) and related slow reversal of the flow (Torre and Burguete 2007). For the context of QCB, Labbé et al. (1996) and Pinton et al. (1999)

---

[1] We employ the same two-dimensional Taylor–Green forcing in Chap. 3; see (3.2).

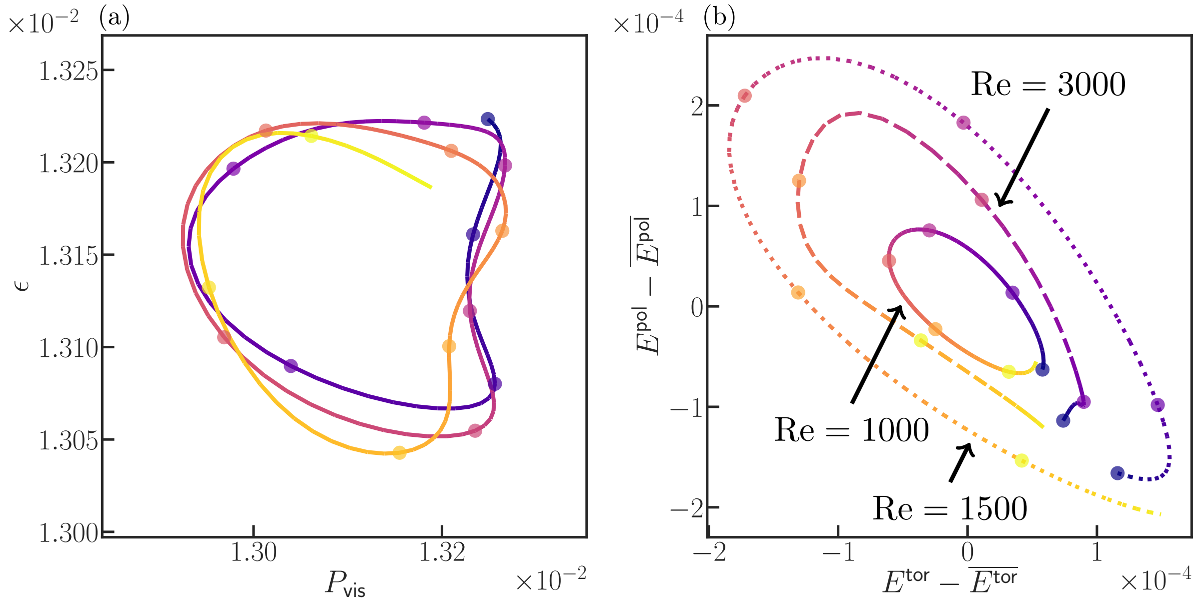

Figure 2.4: Quasi-cyclic temporal evolution in von Kármán flow driven by the viscous forcing at Re = 1500. (a) The energy input rate $P_{\text{vis}}(t)$ and energy dissipation rate $\epsilon(t)$. Adapted from Araki and Goto (2021, Figure 2 (b)). (b) The toroidal energy $E^{\text{tor}}(t)$ and the The poloidal energy $E^{\text{pol}}(t)$ for different Reynolds numbers. Adapted from Araki and Goto (2021, Figure 7). For both panels, the colour gradient from dark to light represents the temporal evolution, and two consecutive dots denote the time interval of T.

showed significant temporal fluctuations in the energy input rate, and the decay of a strong event takes a long time of about 20 times the period of the disk rotation. This result is similar to box turbulence [see Fig. 2.1(b)].

To investigate the origin of such QCB in a wall-bounded flow with time-independent forcing, we conduct a Direct Numerical Simulation (DNS) of the von Kármán flow with smooth disks. Figure 2.4(a) shows the temporal evolution in terms of the viscous energy injection $P_{\text{vis}}(t)$ and dissipation $\epsilon(t)$ at Re = 1500, where the Reynolds number is defined by the radius of the rotating disk R and the period of its rotation T as

$$\text{Re} = \frac{2\pi R^2}{\nu T}. \tag{2.1}$$

Here, we notice a counter-intuitive clockwise cycle between $P_{\text{vis}}(t)$ and $\epsilon(t)$, which infers that the energy dissipation *increases* (decreases) after the energy input *decreases* (increases). We employ two decompositions to understand this paradox: boundary-bulk decomposition for the domain and toroidal-poloidal decomposition for the flow components.

For the boundary-bulk decomposition, we find that the energy cycle of the viscous-driven von Kármán flow consists of two different scenarios, as schematically shown in Fig. 2.4(b). In the vicinity of the rotating disks, there is an almost instantaneous balance between the viscous injection and dissipation of energy, resulting in close to constant kinetic energy. In the bulk of the flow, the energy injection is residual of the viscous energy injection and the dissipation at the boundary region. Here, we need the other decomposition of toroidal and poloidal components to understand the energy cycle in the bulk of the system. When we denote the toroidal and poloidal components of the kinetic energy by E^{tor} and E^{pol}, we find the following cycle in bulk: (i) When the toroidal energy $E^{\text{tor}}(t)$ is small, the toroidal velocity and toroidal-poloidal energy transfer are also small. Then, because of the large shear rates on the rotating disks, viscous stirring (and associated energy injection) develops the toroidal flow. (ii) It triggers the centrifugal instability to generate the energy transfer from toroidal to poloidal components with a finite time delay. (iii) Then, the poloidal energy $E^{\text{pol}}(t)$ increases with the phase difference against $E^{\text{tor}}(t)$. (iv) The development of the vortical structures with the growing $E^{\text{pol}}(t)$ triggers the energy dissipation around them. (v) At the same time, $E^{\text{tor}}(t)$ decreases as $E^{\text{pol}}(t)$ develops due to the angular momentum transfer.

Following the above analysis, we conclude that the QCB of the viscous-driven von Kármán flow can be clearly observed in the exchange of energy between toroidal and poloidal components: $E^{\mathrm{tor}}(t)$ and $E^{\mathrm{pol}}(t)$. We demonstrate the QCB in a range of Re ($1000 \leq \mathrm{Re} \leq 3000$) in Fig. 2.4(b), claiming the robustness of our scenario. The mysterious relation between the viscous energy injection $P_{\mathrm{vis}}(t)$ and dissipation $\epsilon(t)$, shown in Fig. 2.4(a), can be understood by the two different energy cycles in the boundary and bulk regions of the flow. In other words, while the phase of $\epsilon(t)$ is determined by the boundary energy cycle with instantaneous balance, that of $P_{\mathrm{vis}}(t)$ is affected by the bulk energy cycle between $E^{\mathrm{tor}}(t)$ and $E^{\mathrm{pol}}(t)$ with a finite time delay. Here, we remark that this conclusion is related to the seminal experiments by Cadot et al. (1997); it is essential to distinguish the boundary and bulk regions to understand dynamics and statistics of the viscous-stirring von Kármán turbulence.

Note that the physical mechanism of this QCB is the energy exchange between the toroidal and poloidal components through centrifugal instability and the angular momentum transfer and is different from the energy exchange between the largest-scale vortices and smaller ones through the energy cascade as in box turbulence (Yasuda, Goto, et al. 2014; Goto and Vassilicos 2016a; Goto, Saito, et al. 2017). Nevertheless, since the non-negligible temporal fluctuations of the energy transfer rate lead to the temporal fluctuations of the inter-scale energy flux and dissipation rate, these cycles are equally important for describing the nonequilibrium statistics of turbulence. Thus, although turbulence in the examined range of Re is not fully developed, we speculate that the proposed picture may hold for higher Re.

Even though we have identified the key ingredients that seem to play a role in the observed QCB, we do not know how these ingredients exactly give rise to such dynamics. For this purpose, we would ideally develop a minimal model displaying the same qualitative dynamics.

2.2 Reduced-order modelling of turbulence

Turbulence is a complex problem with tens of millions of Degrees of Freedom (DoF) interacting in a complex manner. How can the essential DoFs (the nonlinearity determining the system) be extracted from this complexity? In this section, we review attempts to reproduce key turbulence characteristics with as small as possible number of DoF. In § 2.2.1, we introduce some important minimal models of physical phenomena. Historically, such a minimal model led to the discovery of chaos. In § 2.2.2, we focus on the minimal turbulence model. In particular, we discuss how to model highly complex behaviour in developed turbulence. In § 2.2.3, we focus on the minimal transition model from a laminar to a turbulent state.

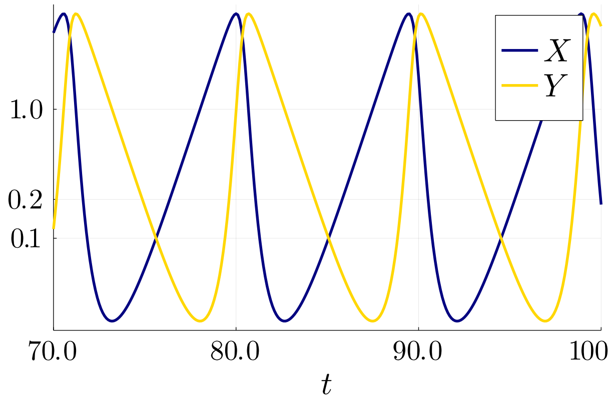

Figure 2.5: Time series of the Lotka–Volterra system.

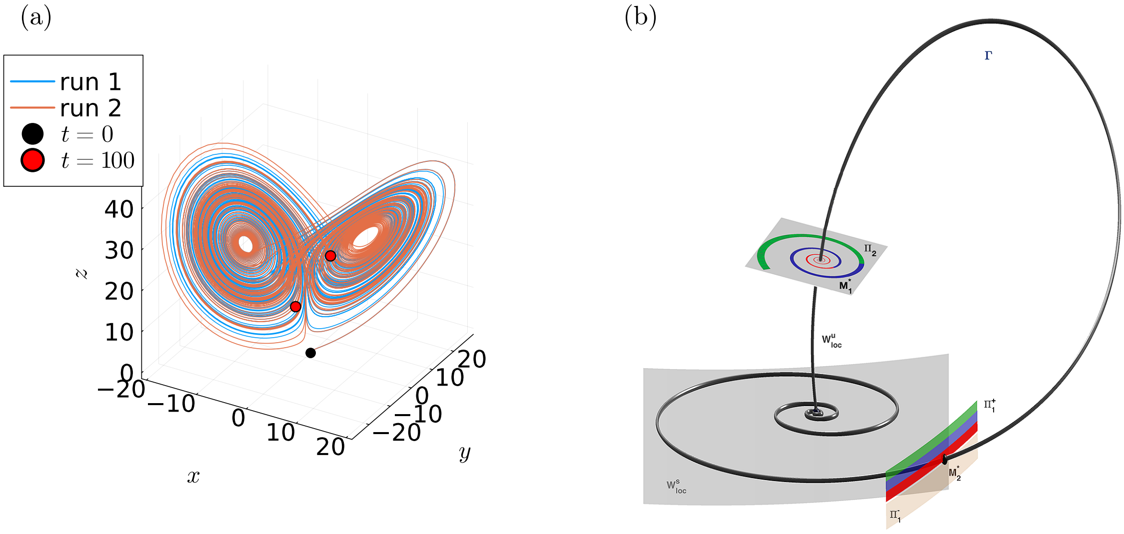

Figure 2.6: Attractors of minimal models of chaos: (a) Lorenz model and (b) Šilnikov orbit adapted from Šilnikov and Šilnikov (2007). (a) Two orbits of slightly different initial conditions are shown. (b) Γ is a Homoclinic loop. W^s and W^u denote the stable and unstable manifolds, respectively, and their cross-section is Π_1 and Π_2, respectively.

2.2.1 Minimal model of physical phenomena and chaos

Physicists love minimal descriptions of complex phenomena. One of the most famous examples is the Lotka–Volterra model (Lotka 1920), mimicking the evolution of the number of prey x and predator y:

$$
\begin{cases}
\dfrac{\mathrm{d}x}{\mathrm{d}t} = ax - bxy, & (2.2)\\[2ex]
\dfrac{\mathrm{d}y}{\mathrm{d}t} = cxy - dy. & (2.3)
\end{cases}
$$

Here, the four parameters denote the prey birth rate a, the predation rate b and c, and the predator death rate d. This minimalistic model for population dynamics represents the following physical processes: i) The number of prey indivisuals x grows exponentially with a growth rate a, proportional to the current x. ii) Number of prey x decreases (and predator y increases) when they encounter. This is proportional to xy. iii) Number of predators y decreases when there is no prey, and this death rate is proportional to y. Figure 2.5 shows the behaviour of the Lotka–Volterra system. See Hirsch et al. (2012, § 11.2) and Guckenheimer and Holmes (2013, § 2.3) for more detailed analysis.

In 1963, Lorenz proposed a system consisting of three ODEs (Lorenz 1963):

$$
\begin{cases}
\dfrac{\mathrm{d}x}{\mathrm{d}t} = \sigma(y - x), & (2.4)\\[2ex]
\dfrac{\mathrm{d}y}{\mathrm{d}t} = rx - y - xz, & (2.5)\\[2ex]
\dfrac{\mathrm{d}z}{\mathrm{d}t} = xy - bz. & (2.6)
\end{cases}
$$

Here, the three variables (x, y, z) denote convection velocity and thermal gradient in two directions. The Lorenz model can be described as an extreme case of Galerkin truncation applied to the Rayleigh–Benard system. See § 2.2.2 for more details on Galerkin truncation. Because of this truncation, the nonlinear terms of the Lorenz model does not represent scale-by-scale interactions. The three parameters are the Prandtl number σ, Rayleigh number r, and the system size b. Figure 2.6(a) shows a trajectory of this system, indicating a set in which the solution is eventually trapped, called the Lorenz attractor. This Lorenz system unveils a deterministic phenomenon but is unpredictable because a small disturbance in the initial condition results in a completely different outcome. It is the first recognised example of deterministic chaos. See also Hirsch et al. (2012, § 14), Guckenheimer and Holmes (2013, § 2.3), and Strogatz (2014, § 9). During the 1960s and 1970s, many low-dimensional models exhibiting chaos were invented, including the Rössler model, which is even simpler than the Lorenz model (Rössler 1976; Rössler 1979). Theoretical considerations by Šilnikov allowed to predict that in the specific case of a dynamical system evolving on a homoclinic orbit with a saddle focus, chaos is expected for a well-defined set of parameters. After linearization, this dynamics can be described by (Šilnikov 1965):

$$\begin{cases} \dfrac{\mathrm{d}x}{\mathrm{d}t} = -\rho x - \omega y + F_x(x,y,z), \\ \dfrac{\mathrm{d}y}{\mathrm{d}t} = \omega x - \rho y + F_y(x,y,z), \\ \dfrac{\mathrm{d}z}{\mathrm{d}t} = \gamma x + F_z(x,y,z). \end{cases} \tag{2.7}$$

Here, $\boldsymbol{x} = (x, y, z)$ are the three variables and F_i with $i \in \boldsymbol{x}$ are specific to the considered dynamical system. The interactions of the linearised system are governed by the real parameters ρ, ω, and γ. The Šilnikov attractor is shown in Fig. 2.6(b). See also Hirsch et al. (2012, § 16.1) and Guckenheimer and Holmes (2013, § 6.5). A similar saddle-focus dynamics is also observed in the model we develop in Chap. 3. We conclude this subsection by noting that a data-scientific approach in both dynamical systems and chaos has recently been developed and has gained great attention (Brunton, Proctor, et al. 2016; Brunton and Kutz 2022).

2.2.2 Reduced-order models of developed turbulence

Next, we review minimal models of turbulence. Since turbulence has a large number of degrees of freedom, its low-dimensional description has been pursued by many researchers with great enthusiasm. There are many systematic approaches, such as proper orthogonal decomposition (POD) or Galerkin truncation. POD analysis enables one to extract modes which dominate the key dynamics of complex systems (Berkooz et al. 1993; Holmes et al. 1996). This framework was pioneered by Lumley (Bakewell Jr and Lumley 1967; Payne and Lumley 1967), and has been used to extract coherent (low-dimensional) structures in turbulent flows (Arndt et al. 1997; Galletti et al. 2004; Tinney et al. 2008; Podvin 2009) and to achieve optimal control (Bergmann et al. 2005; Van Doren et al. 2006; Liberge and Hamdouni 2010). Reduced-Order Modelling (ROM) is often based on POD analysis (Hall et al. 1999; Ilak and Rowley 2008; Wang, Akhtar, et al. 2012; Xiao et al. 2015). For a broad overview of recent advancements on data analysis, see Taira, Brunton, et al. (2017) and Taira, Hemati, et al. (2020).

Compared to this data-oriented approach, Galerkin truncation aims to approximate the discretised system by a finite number of basis functions Brunton and Kutz 2022, § 12. This approach aims to reproduce the large-scale dynamics of turbulence rather than its small-scale statistics. Kraichnan (1988) pioneered such an approach to obtain a reduced description of turbulence. Rempfer (2000) investigated the inconsistency between the bifurcations of the real system and truncated low-dimensional models. Both approaches are sometimes combined (Couplet et al. 2003; Borggaard et al. 2011). Galerkin truncation-aided ROM includes transition in a parallel shear flow (Eckhardt and Mersmann 1999), flow past a step (Couplet et al. 2003), two-dimensional magnetohydrodynamics (Carbone, Telloni, et al. 2021). POD and Galerkin truncation are widely used in turbulence research (Berkooz et al. 1993; Holmes et al. 1996).

For the SSP of wall-bounded flow discussed in § 2.1.1, a low-order model was first proposed in Waleffe (1997). Later, a Restricted Nonlinear (RNL) model was examined to investigate the maintenance mechanism of plane Couette flow (Thomas, Lieu, et al. 2014; Thomas, Farrell, et al. 2015). Recently, Yalnız et al. (2021) constructed a ROM based on periodic orbits and probabilistic connection between them. For more detail of ROM, Chevillard and Meneveau (2006) and Meneveau (2011) reviews low-dimensional models of velocity gradient tensor in Lagrangian frame and Ahmed et al. (2021) reviewed key publications of Reduced-Order Model (ROM), where Table 1 is dedicated for a chronological list on the projection method in fluid dynamics and Table 2 for closure modelling.

A caricature of developed turbulence is called a shell model of turbulence, where “shell” means a spherical shell in Fourier space. The pioneering model by Gledzer (1973), Yamada and Ohkitani (1987), and

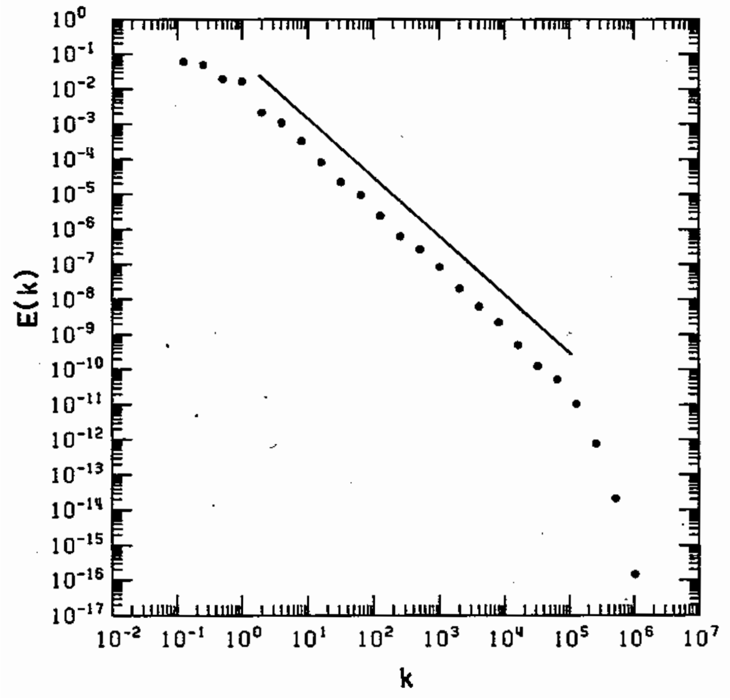

Figure 2.7: The time-averaged energy spectrum of the GOY shell model. The solid line denotes the $k^{-5/3}$ scaling. Adapted from Ohkitani and Yamada (1989, Figure 1).

Ohkitani and Yamada (1989) is called the GOY (Gledzer–Ohkitani–Yamaha) model

$$\left(\frac{\mathrm{d}}{\mathrm{d}t} + \nu k_n^2\right) u_n = \mathrm{i}\big(k_n u_{n+2}^* u_{n+1}^* - b k_{n-1} u_{n+1}^* u_{n-1}^* + c k_{n-2} u_{n-1}^* u_{n-2}^*\big) + f_n, \tag{2.8}$$

which describes the temporal evolution of a complex variable $u_n \in \mathbb{C}$ of representing the velocity in Fourier space averaged over the nth shell. Note that u_n^* means the complex conjugate of u_n. Here, k_n denotes the wavenumber and f_n is the forcing of the nth shell. Model parameters are the kinematic viscosity ν and the free parameters b and c. The nonlinear term for the shell n consists of the shells $n+2, n+1, n-1$ and $n-2$, representing the scale-local dominance of the nonlinear interactions of turbulence. This model reproduces space-averaged statistics of turbulence, such as kinetic energy spectrum (as shown in Fig. 2.7), velocity structure functions, intermittency, and so on. Note that earlier attempts include Obukhov (1971), where a step-by-step energy cascade model similar to a shell model was proposed, and Siggia (1977), where intermittency was discussed by the reduced equations.

In real turbulence, an overwhelming number of nonlinear interactions govern chaotic behaviour. In contrast, the shell model retains nonlinear interactions only between neighbouring shells. This simplification reflects the scale-local nature of nonlinear interactions of real turbulence, as discussed in § 1.1.2. Thus, the similarity between the shell model and real turbulence supports the scale-local view of turbulence. For more details on shell models of turbulence, including Sabra model (L'vov et al. 1998), refer to a review article (Biferale 2003) and a textbook (Ditlevsen 2010).

2.2.3 Reduced-order model of laminar-turbulent transition

In the previous subsection, we reviewed low-order modelling of developed turbulence. Another important objective of fluid mechanics research is to understand the transition from a laminar state to turbulence. For the laminar-turbulent transition, refer to recent review articles (Tuckerman et al. 2020; Graham and Floryan 2021; Wu 2023; Avila et al. 2023).

Moehlis et al. (2004) constructed a Fourier-mode-based model to find a subcritical and intermittent transition to turbulence with exponential lifetime distributions. Seshasayanan and Manneville (2015) derived a Galerkin truncated model of plane Couette flow, confirming the original problem's boundary condition.

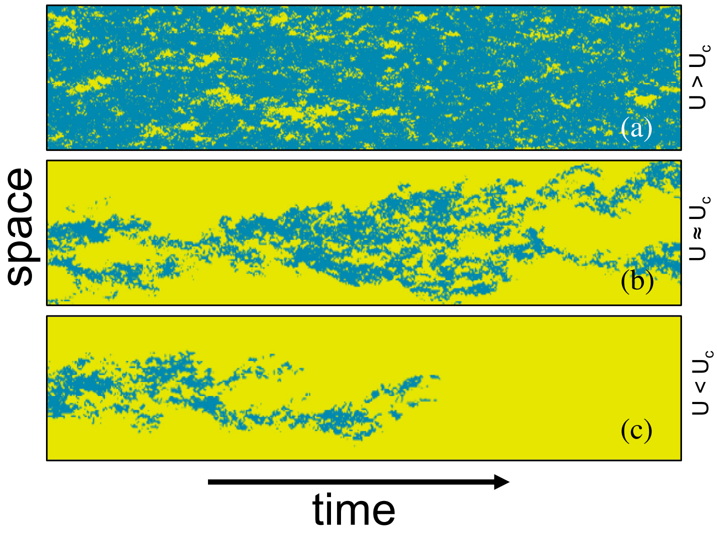

Figure 2.8: Space-time plot of the laminar-turbulent transition observed in the predator-prey model. The blue and yellow regions denote the turbulent and laminar regions, respectively. The variable U is equivalent to the Reynolds number, and U_c denotes the critical value. Adapted from Wang, Shih, et al. (2022, Figure 4).

This model reproduces a spatiotemporal pattern of the flow (Duguet et al. 2012). Chantry et al. (2016) considered a four Fourier-modes equation of shear flow to capture various turbulent-laminar patterns from a turbulent spot, band, and uniform turbulence. This model is based on flows without walls, indicating that the boundary layer of the wall is not essential to form such turbulent-laminar patterns. Seshasayanan, Dallas, et al. (2021) investigated a laminar-turbulent transition in two-dimensional Kolmogorov flow with boundary conditions mimicking a channel flow. They obtained the four-equation model to study the bifurcation process of the flow, which is different from the doubly periodic case.
Recently, a stochastic predator-prey model was proposed (Shih et al. 2016; Goldenfeld and Shih 2017; Wang, Shih, et al. 2022) to reproduce DP universal class hidden in laminar-turbulent transition (Sano and Tamai 2016; Lemoult et al. 2016; Klotz et al. 2022). Figure 2.8 shows the space-time plot of the laminar-turbulent pattern generated Wang, Shih, et al. (2022).

3 Minimal Model of Quasi-cyclic Behaviour

This chapter investigates the quasi-cyclic behaviour of turbulence observed in a turbulent flow and its minimal modelling. The contents are based on the following:

> Araki, Ryo, Wouter J. T. Bos, and Susumu Goto (2023a). Minimal model of quasi-cyclic behaviour in turbulence driven by Taylor–Green forcing. *Fluid Dynamics Research* **55** (3), p. 035507. arXiv: `2112.03417 [flu-dyn]`.

In § 3.1, we investigate a quasi-cyclic temporal fluctuations observed in box turbulence. Then, in § 3.2, we construct a minimal model reproducing these features. § 3.3 investigates the detail of the model, including its temporal dynamics and bifurcation analysis. We conclude this chapter in § 3.4.

3.1 Observation of quasi-cyclic behaviour

To illustrate the features we want to reproduce and guide the formulation of a minimal model reproducing these features, we conduct numerical simulations of both turbulent and temporally periodic flows with the same type of forcing. More precisely, we conduct DNS of three-dimensional incompressible flow governed by the Navier–Stokes equations,

$$\frac{\partial \boldsymbol{u}}{\partial t} + (\boldsymbol{u} \cdot \boldsymbol{\nabla})\boldsymbol{u} = -\boldsymbol{\nabla} p + \nu \nabla^2 \boldsymbol{u} + \boldsymbol{f}, \tag{3.1}$$

with a steady forcing of the two-dimensional Taylor–Green type (Yasuda, Goto, et al. 2014; Goto, Saito, et al. 2017; van Veen, Kawahara, et al. 2018),

$$\boldsymbol{f} = (-f_0 \sin x \cos y, f_0 \cos x \sin y, 0), \tag{3.2}$$

and the continuity equation, $\boldsymbol{\nabla} \cdot \boldsymbol{u} = 0$. Here, $\boldsymbol{u}$, p, and $\boldsymbol{f}$ are the velocity, pressure, and forcing fields, respectively. The forcing amplitude f_0 is set to unity. The only control parameter is the kinematic viscosity ν. We employ a pseudo-spectral method in a $(2\pi)^3$ periodic box.

We use an in-house parallelised code (Delache et al. 2014) to conduct DNS. It employs a pseudo-spectral method with the 2/3 dealiasing rule for spatial discretisation and the Adams–Bashforth scheme in the time domain. The initial condition is generated in Fourier space by Rogallo's method (Rogallo 1981).

We perform DNS in a $(2\pi)^3$ triply periodic box. We focus on two distinct flows: three-dimensional periodic and turbulent. The SPO is obtained by the DNS with 64^3 Fourier modes by adjusting the viscosity to $\nu = 0.102$. This corresponds to the value of the Reynolds number (3.3) of $\mathrm{Re} = 5.83$. We use 128^3 Fourier modes to simulate turbulent flow at $\nu = 0.02$ ($\mathrm{Re} = 29.7$). For the phase averaging procedure. Note that we discard the transient part from the analysis. This interval is approximately $1.08 \times 10^4 T$ with T defined in (3.3).

We define the Reynolds number and the characteristic timescale of large-scale flow as

$$\mathrm{Re} \equiv \frac{\sqrt{f_0}}{\left|\boldsymbol{k}_f\right|^{3/2} \nu} \quad \text{and} \quad T \equiv \frac{1}{\sqrt{\left|\boldsymbol{k}_f\right| f_0}} = 0.840, \tag{3.3}$$

respectively. Here, $\boldsymbol{k}_f = (\pm 1, \pm 1, 0)$ is the wavevector of the forcing (3.2).

Figure 3.1 shows the temporal evolution of the energy input rate $P(t) \equiv \langle \boldsymbol{f} \cdot \boldsymbol{u} \rangle$ against the energy dissipation rate $\epsilon(t)$ given by $\nu \left\langle |\boldsymbol{\omega}|^2 \right\rangle$ for various Reynolds numbers. Here, $\langle \cdot \rangle$ denotes the spatial average and $\boldsymbol{\omega} \equiv \boldsymbol{\nabla} \times \boldsymbol{u}$.

Figure 3.1(a) shows the turbulent time series, where the time-averaged Taylor scale-based Reynolds number $\langle \mathrm{Re}_\lambda \rangle_t$ is about 90. Note that $\langle \cdot \rangle_t$ denotes the time average. We also show the snapshot of this flow in Fig. 3.2(a). The time series exhibits QCB in a counter-clockwise direction behind the chaotic fluctuations. This time delay between the large- and small-scale representatives (i.e. $P(t)$ and $\epsilon(t)$) reflects the causal nature of the energy cascade.

We apply a phase average to the complex time series of $P(t)$ and $\epsilon(t)$ conditioned on the local maxima of $P(t)$ in order to extract smooth, time-delayed oscillations shown in Fig. 3.1(b).

In the following, we explain the detailed procedure of the phase averaging shown in Fig. 3.1(b). We first describe the flow observed at $\mathrm{Re} = 29.7$ (Re_λ is about 90) in Fig. 3.2. Figure 3.2(a) shows isosurfaces of $|\boldsymbol{\omega}|$ capturing small-scale structures, whereas the forcing-induced columnar vortices emerge by visualising the isosurfaces of $|\boldsymbol{\omega}^<|$. Here, $\boldsymbol{\omega}^< \equiv \boldsymbol{\nabla} \times \boldsymbol{u}^<$, which is obtained by applying a low-pass filter to the velocity field, defined as $\boldsymbol{u}^<(\boldsymbol{x}) \equiv \int \mathrm{d}\boldsymbol{r}\, G(r/r_0)\boldsymbol{u}(\boldsymbol{x}+\boldsymbol{r})$ with G being the Gaussian function. We set $r_0 = 2$. Figure 3.2(b) shows the temporal evolution of the energy input rate $P(t)$ and the energy dissipation rate $\epsilon(t)$. Both time signals exhibit significant fluctuations with a clear time-delayed correlation. See Fig. 3.1(a) for the two-dimensional projection of the same time series.

To conduct the phase-averaging, first, we pick up the local maxima of $P(t)$ [Fig. 3.3(a)] with the following two criteria: (i) It must be larger than $\langle P \rangle_t + \sigma(P)$ where $\langle \cdot \rangle_t$ and $\sigma(\cdot)$ denote the time average and the standard deviation, respectively. The horizontal pink line indicates this value in Fig. 3.3(a). (ii) The temporal gap between two consecutive local maxima must be larger than $\tau_\mathrm{max}/2$ where τ_max is the time for the second peak of the autocorrelation function of P (note that the first peak is at $\tau = 0$). We denote the identified local maximum of $P(t)$ and the corresponding time by P_0 and t_0, respectively. Second, the segments of the time series of $P(t)$ around the local maximum P_0 are overlapped, as shown in Fig. 3.3(b). We normalise the segments by P_0 to avoid overestimation due to huge intermittent peaks. Third, we compute the average over the overlapped and normalised time series to obtain the phase averaged time series $\langle P \rangle_\mathrm{phase}$ shown in Fig. 3.3(c).

We apply a similar procedure to $\epsilon(t)$. However, the time is shifted for t_0, and $\epsilon(t)$ is normalised by P_0 so that we can evaluate the time delay and the relative amplitude difference between the two quantities. The pink vertical dashed line shows the time delay in Fig. 3.3(c), which is $2.80T$. Figure 3.1(b) is a parametric plot of Fig. 3.3(c).

We denote the phase-averaged quantities by $\langle \cdot \rangle_\mathrm{phase}$. These results suggest that the QCB of turbulent flow driven by the steady body force (3.2) is robust. Such QCB is also shown in Fig. 12 of Goto, Saito, et al. (2017) for two different forcing types at even higher Re. The physical origin of QCB is rooted in the energy cascading process from larger to smaller scales. Since the coherent structures at these scales are composed of a large number of Fourier modes, to describe the QCB in terms of Fourier modes, we need to understand the underlying nonlinear interactions among them. However, identifying the direct cause of QCB from tens of thousands of excited Fourier modes seems illusory. Thus, we decrease Re to reduce the complexity of the flow.

In Fig. 3.1(c), we show the phase-averaged plots of the parametric time series of $P(t)$ and $\epsilon(t)$ for four different values of Re. The change in the shape of the parametric plots is gradual, suggesting that the quasi-cyclic orbit in the turbulent flow is continuously connected to an SPO at $\mathrm{Re} \approx 5.83$, which is also shown in Fig. 3.1(d) for comparison. As will be shown in Fig. 3.4 below, the SPO at $\mathrm{Re} = 5.83$ is not the laminar solution of the system which corresponds to a purely two-dimensional structure resulting from a balance between viscous stress and the forcing (3.2). We emphasise that this SPO plays a key role in constructing our model.

We find that the amplitude and the period of the periodic and quasi-cyclic flows monotonically increase when we decrease Re from 29.7 to 5.83. This does not prove that the dynamics are identical, but the turbulent QCB and periodic flow seem to share the same driving mechanism. Note that in high-Reynolds-number turbulence beyond $\mathrm{Re} = 30$, the amplitude and period seem to saturate to values of the same order as in Fig. 3.1(b) (see Fig. 12 of Goto, Saito, et al. (2017)).

In Fig. 3.4, we visualise the periodic flow (i.e. SPO) discussed in Fig. 3.1(d), similar to the three-dimensional periodic solution reported in van Veen, Kawahara, et al. (2018, Fig. 5). We distinguish four large-scale columnar vortices associated with the Taylor–Green force (3.2) and counter-rotating pairs of smaller vortices perpendicular to them. Note that we do not perform low-pass filtering [see Fig. 3.2(a)].

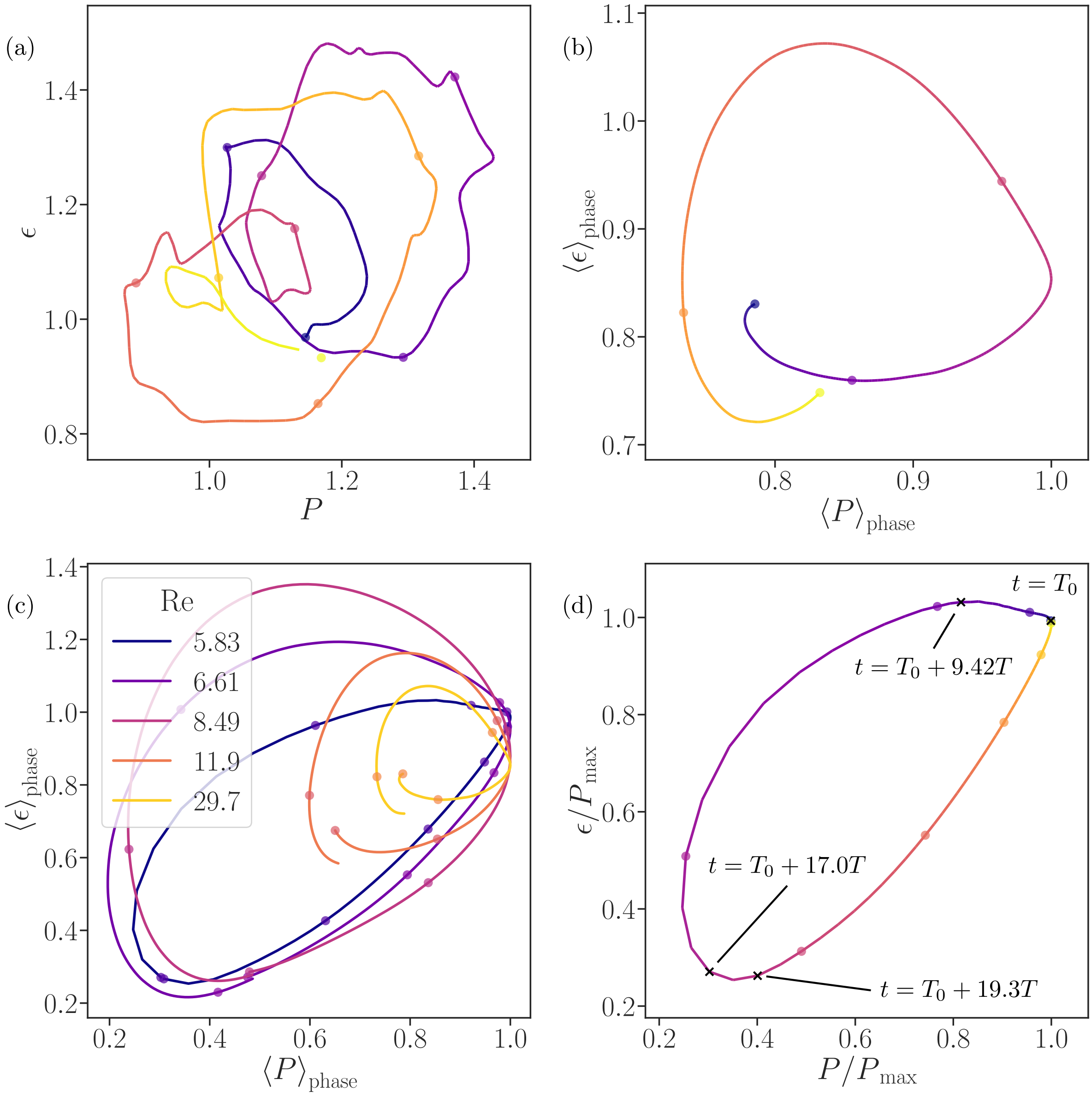

Figure 3.1: (a) Parametric plots of the instantaneous values of the energy dissipation rate $\epsilon(t)$ and the energy input rate $P(t)$ for the turbulent flow at Re $= 29.7$ for $50T$ [see Fig. 3.2(b)]. (b) Phase-averaged values $\langle P\rangle_{\mathrm{phase}}$ and $\langle\epsilon\rangle_{\mathrm{phase}}$ at Re $= 29.7$ [same as in (a)] for $20T$. (c) Parametric plots of the phase averaged values $\langle P\rangle_{\mathrm{phase}}$ and $\langle\epsilon\rangle_{\mathrm{phase}}$ at four different values of Re (29.7, 11.9, 8.49, and 6.61). Note that the orbit in panel (b) at Re $= 29.7$ is re-plotted in panel (c). (d) The SPO at Re $= 5.83$ is shown with a coloured line. Note that this orbit is also shown in panel (c). The gap between two consecutive dots corresponds to $5T$ for all panels. In panels (a), (b), and (d), the time evolves from dark to light colours. Four black cross symbols in panel (d) denote the instances shown in Fig. 3.4.

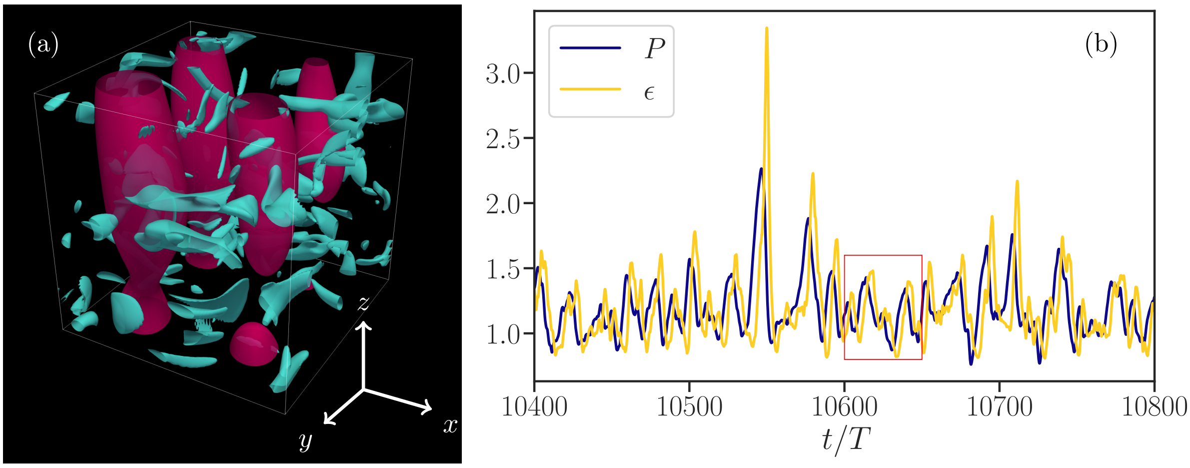

Figure 3.2: (a) A snapshot of the turbulent flow at Re = 29.7 ($\mathrm{Re}_\lambda \approx 90$). Isosurfaces of $|\boldsymbol{\omega}| = 20$ (blue) and low-pass filtered $|\boldsymbol{\omega}^<| = 4$ (red) are visualised. (b) Time series of energy input rate $P(t)$ and energy dissipation rate $\epsilon(t)$ of the same flow. The red rectangle denotes the time interval examined in Fig. 3.1(a).

Nevertheless, we can observe a one-step energy cascading process from the four large-scale columnar vortices to smaller-scale lateral vortices. More concretely, we observe only large-scale vortices at $t = T_0$ [Fig. 3.4(a)], then the energy cascade starts to create smaller-scale vortices [Fig. 3.4(b), $t = T_0 + 9.42T$], while the large-scale vortices get weaker [Fig. 3.4(c), $t = T_0 + 17.0T$]. Afterwards, the energy dissipation dominates to weaken smaller-scale vortices, and then the entire system becomes calm [Fig. 3.4(d), $t = T_0 + 19.3T$]. When small-scale vortices disappear, energy input by the external force exceeds dissipation to reestablish the large-scale vortices, and the system returns to the initial state [Fig. 3.4(a)]. We emphasise that this periodic behaviour is similar to turbulent QCB observed at higher Re (Fig. 3.2). This similarity manifests itself in the continuous change between the SPO and turbulence seen in Fig. 3.1.

In the next section, we analyse the SPO to unveil the essential physics behind QCB. Even though we have not rigorously shown the connection between the SPO and turbulence, we hope to obtain new insights into QCB in Navier–Stokes flow by dissecting the SPO.

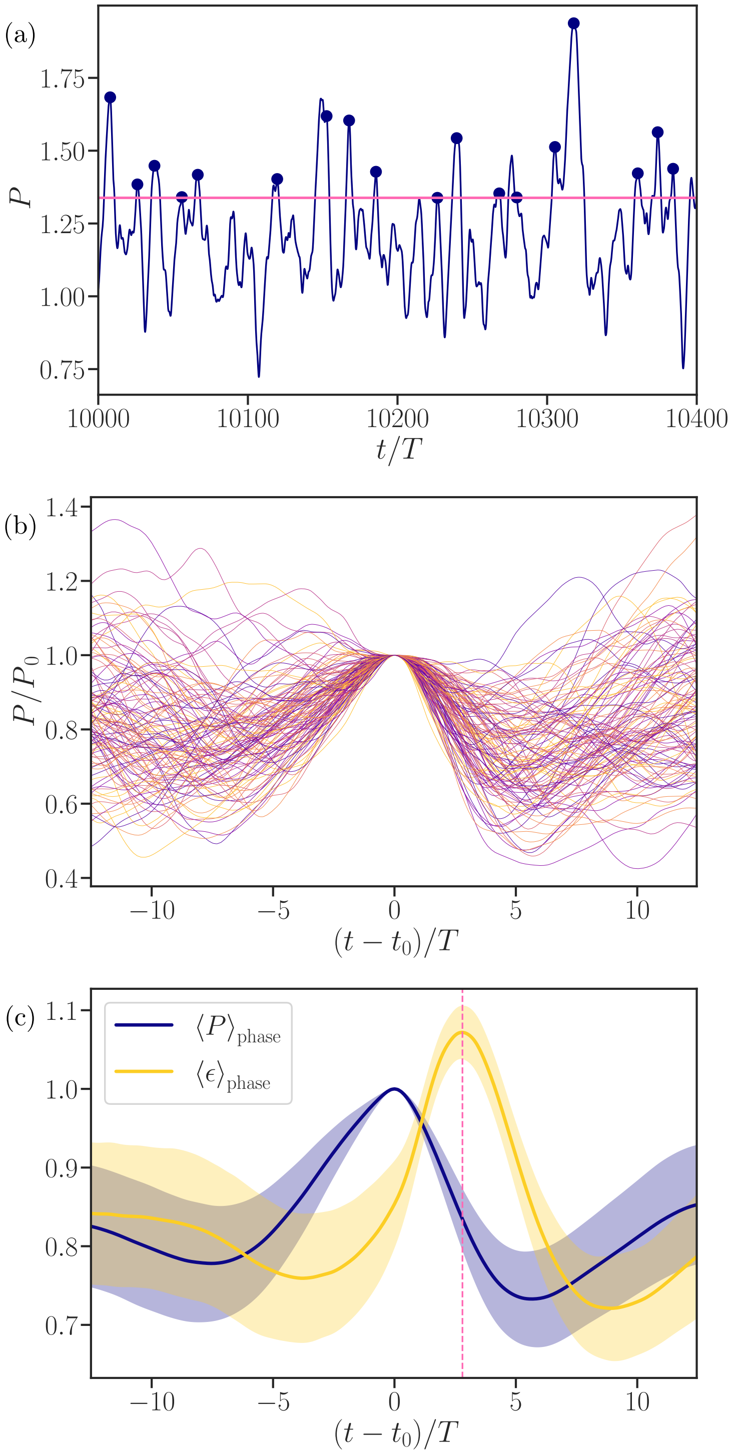

Figure 3.3: (a) Time series of $P(t)$ with its local maxima P_0 denoted by dots. The pink horizontal line corresponds to the threshold of the magnitude $\langle P\rangle_t + \sigma(P)$. (b) Overlapped segments of the time series of $P(t)$ around t_0 and normalised by P_0. (c) Phase averaged time series of $P(t)$ and $\epsilon(t)$. Shaded region represents $\langle f\rangle_t \pm \sigma(f)$ where f is $P(t)$ or $\epsilon(t)$. The pink vertical dashed line indicates the maximum of $\langle\epsilon\rangle_{\text{phase}}$, denoting the average time delay between $P(t)$ and $\epsilon(t)$.

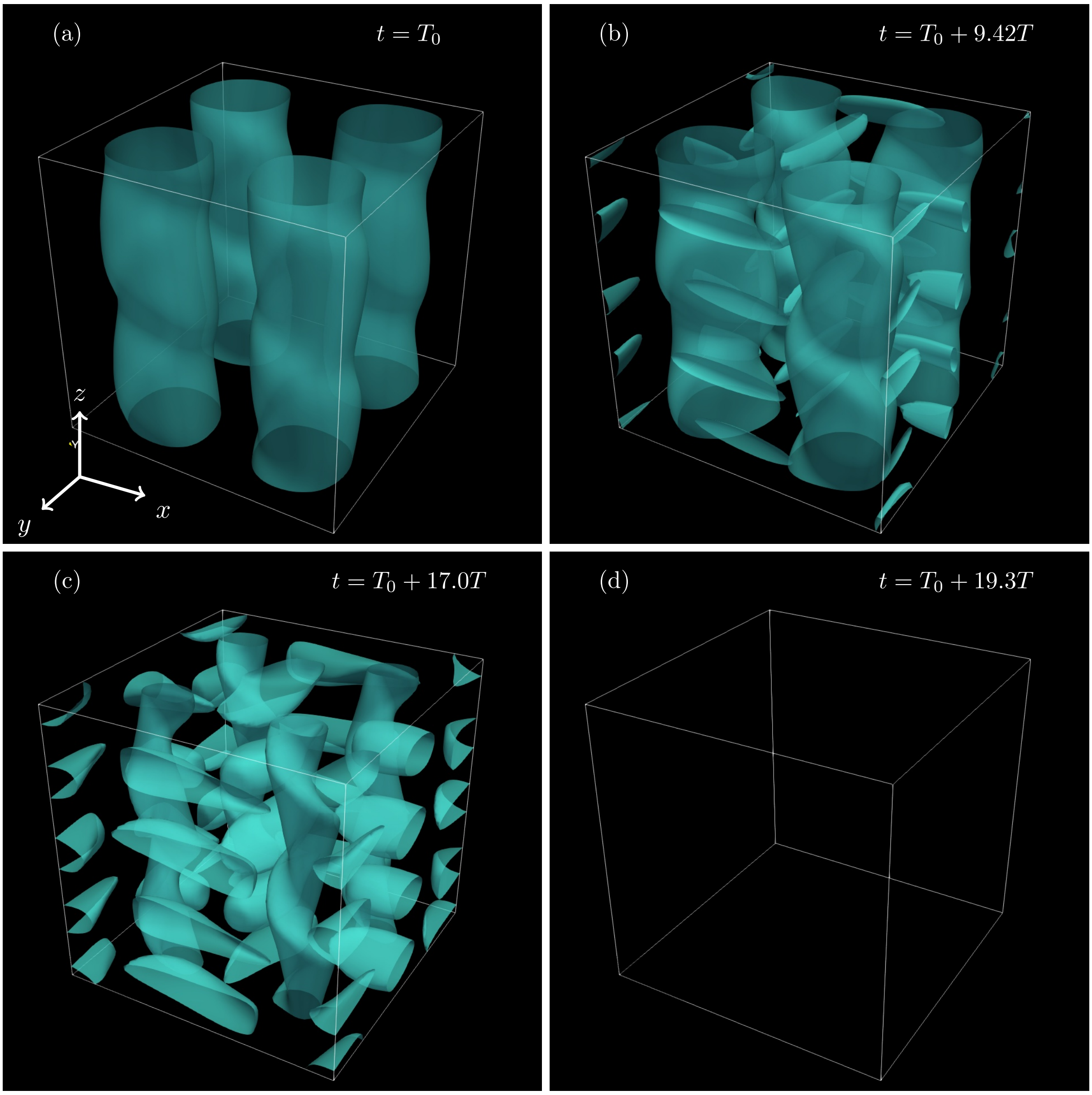

Figure 3.4: Visualisation of vortical structures of the SPO (at Re $= 5.83$) at four instances with isosurface of $|\boldsymbol{\omega}| = 5$. See Fig. 3.1(d) for the corresponding instances.

3.2 Three-equation model of quasi-cyclic behaviour

3.2.1 Construction of the model

Our objective is to construct the simplest possible model capable of reproducing QCB while retaining a close connection with the structure of the Navier–Stokes equations (3.1). For this purpose, we recall that in a Fourier representation of (3.1), the individual modes q_i for the ith wavevector $\boldsymbol{k}_i$ are governed by (Kraichnan 1958; Kraichnan 1988),

$$\left(\frac{\partial}{\partial t} + \nu|\boldsymbol{k}_i|^2\right) q_i = \sum_{j,m} A_{ijm} q_j q_m + f_i, \tag{3.4}$$

where f_i is the forcing applied to the ith mode, and A_{ijm} are the coupling constants resulting from the advection and pressure terms of (3.1). The nonlinear term associated with triad interactions rapidly yields an overwhelming complexity when the number of retained modes increases. Even in our SPO, a large number of modes are dynamically active. In order to develop an analytically tractable model, we use a coarse-graining approach where we group subsets of Fourier modes and represent each group by a single variable, leading to a sort of shell-model (Obukhov 1971; Ditlevsen 2010).

The shells or groups used in our model are not regrouping modes as a function of scale using a rigorous criterion but as a function of the type of nonlinear interactions and energetic content. Indeed, we investigate the Fourier decomposition of the SPO to find that only Fourier modes with wavevectors (k_x, k_y, k_z) of

$$(\pm 1, \pm 1, 0),\ (\pm 1, 0, 0),\ (0, \pm 1, 0),\ (0, 0, \pm 2),\ (\pm 1, \pm 1, \pm 2),\ (\pm 2, 0, \pm 2), \text{ and } (0, \pm 2, \pm 2) \tag{3.5}$$

are responsible for 98 % of its energy.

We now show the detailed behaviour of the seven most energetic modes. Figure 3.5 shows $|\boldsymbol{\omega}|$ distributions of these seven modes. Triangles indicate combinations of different modes where energy transfer via triad interactions is possible. Figure 3.5 also compares isosurfaces of $|\boldsymbol{\omega}|$ of the sum of these seven primary energetic modes and that of all modes. We find similar principal structures: the large columnar vortices and the small counter-rotating pairs of vortices. Here, we denote the velocity field consisting of the forced mode by $\boldsymbol{u}_X$ and the other six primary energetic modes by $\boldsymbol{u}_Y$. The corresponding vorticity fields are denoted by $\boldsymbol{\omega}_X$ and $\boldsymbol{\omega}_Y$, respectively.

We plot the time series of the energy of the forced and six primary modes of the SPO at $\mathrm{Re} = 5.83$ in Fig. 3.6. Although the energy $E_{110}(t)$ of the forced mode dominates, which is approximately equal to the total energy $E(t)$, we observe a distinctive difference between $E(t)$ and $E_{110}(t)$ when the primary scale energies are excited. By summing up the contributions of these seven modes, we obtain E_{X+Y} shown in Fig. 3.7(a). We also note that there are fast oscillations in $E_{100}(t)$ and $E_{010}(t)$. However, these two modes are compensated with each other, and such rapid dynamics are not visible in $E_{X+Y}(t)$ [Fig. 3.7(a)]. This observation explains why there are no fast oscillations in the time series shown in Fig. 3.10(b).

Figure 3.7(a) illustrates that the time evolution of the kinetic energy is closely reproduced, retaining only these modes.

A close inspection of the seven modes shows that all the nonlinear interactions involve the forced mode and two of the six other modes (see Fig. 3.5). In the following, $X \in \mathbb{R}$ denotes the characteristic velocity of the forced modes $\boldsymbol{k} = (\pm 1, \pm 1, 0)$ and $Y \in \mathbb{R}$ corresponds to that of the remaining modes in (3.5). At this point, we suppose that there are only these two classes of modes and that we represent each class by a single, real variable. Furthermore, we assume (3.4) to govern the interaction of these two variables, X and Y, yielding,

$$\begin{aligned} \frac{\mathrm{d}X}{\mathrm{d}t} &= -AY^2 \quad - \nu K_X^2 X + F, \\ \frac{\mathrm{d}Y}{\mathrm{d}t} &= +AXY \quad - \nu K_Y^2 Y, \end{aligned} \tag{3.6}$$

with a coefficient $A > 0$, typical wavenumbers $K_\alpha > 0$ with $\alpha \in \{X, Y\}$, and a steady force $F > 0$. The first term on the RHS of each equation represents the nonlinear coupling between X and Y. This interaction conserves the global energy, $(X^2 + Y^2)/2$. Note that since we model the triadic nonlinear term of (3.4) by regrouping the modes into two families (see Fig. 3.5). For notation, we employ both X and Y as the principal variables of our model and as subscripts to denote quantities associated with these variables.

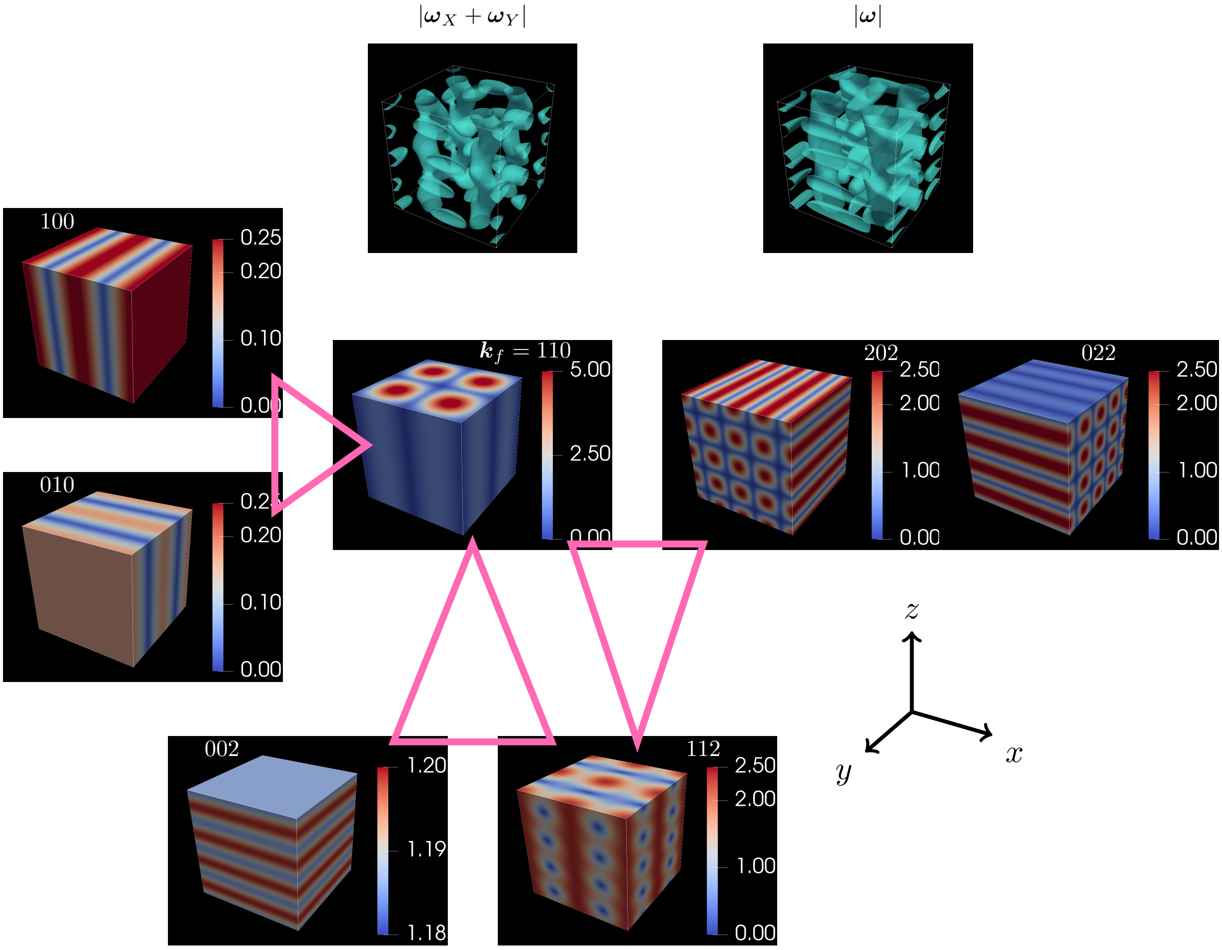

Figure 3.5: Schematic of forced (centre) plus six primary energetic (surrounding) Fourier modes in the SPO at Re = 5.83. Visualisations show distributions of $|\boldsymbol{\omega}|$ at the same instance. The three-digit numbers on the visualisations indicate three components of wavevector $k_x k_y k_z$. Note that all the possible sign combinations $(\pm k_x, \pm k_y, \pm k_z)$ are gathered. Triangles denote the possible triad interactions. On top, we compare the isosurfaces of $|\boldsymbol{\omega}_X + \boldsymbol{\omega}_Y|$ with $|\boldsymbol{\omega}|$ of the full flow. Here, $\boldsymbol{\omega}_X$ and $\boldsymbol{\omega}_Y$ denote the vorticity of the forced and the primary energetic modes, respectively.

An extensive parameter scan of the two-equation model shows that the model always converges to a steady solution, and we do not observe an SPO or QCB. In fact, linear stability analysis of the fixed points of (3.6) shows that there are only stable steady solutions.

Here, we show the results of the linear stability analysis of the fixed points of (3.6). There are two kinds of fixed points: namely,

$$\overline{\boldsymbol{X}}_1 = \left(\frac{F}{\nu K_X^2}, 0\right) \quad \text{and} \quad \overline{\boldsymbol{X}}_2 = \left(\frac{\nu K_Y^2}{A}, \pm\frac{1}{A}\sqrt{AF - \nu^2 K_X^2 K_Y^2}\right), \tag{3.7}$$

where $\overline{\boldsymbol{X}} \equiv (\overline{X}, \overline{Y})$. Note that the fixed points $\overline{\boldsymbol{X}}_2$ exist only for $\nu < \sqrt{AF}/K_X K_Y$. The perturbation (x, y) in the vicinity of the fixed points $(\overline{X}, \overline{Y})$ obeys

$$\frac{\mathrm{d}x}{\mathrm{d}t} = -A\left(\overline{Y}^2 + 2\overline{Y}y\right) \qquad - \nu K_X^2\left(\overline{X} + x\right) + F, \tag{3.8}$$

$$\frac{\mathrm{d}y}{\mathrm{d}t} = +A\left(\overline{X}\,\overline{Y} + \overline{X}y + x\overline{Y}\right) - \nu K_Y^2\left(\overline{Y} + y\right), \tag{3.9}$$

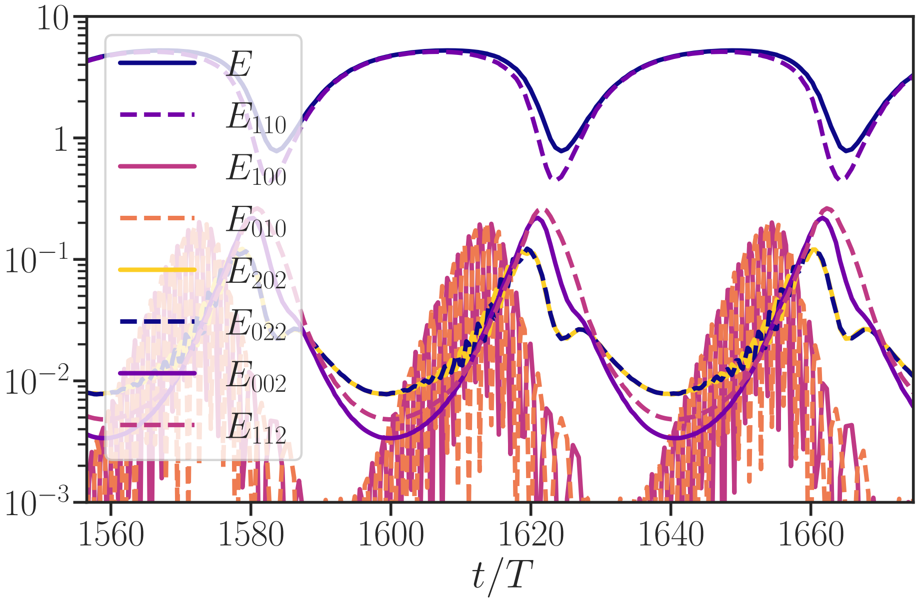

Figure 3.6: Time series of energy of the forced and six primary energetic modes in the SPO. $E_{k_x k_y k_z}$ denotes the energy summed-up for the wavevectors $(\pm k_x, \pm k_y, \pm k_z)$. Total energy $E(t)$ is also shown for reference.

where we have neglected second-order terms x^2, y^2, and xy. The Jacobian matrix is then expressed as

$$\boldsymbol{J} = \begin{pmatrix} -\nu K_X^2 & -2A\overline{Y} \\ A\overline{Y} & A\overline{X} - \nu K_Y^2 \end{pmatrix}, \tag{3.10}$$

whose eigenvalues are

$$\lambda = -\frac{1}{2}\left[-A\overline{X} + \nu\left(K_X^2 + K_Y^2\right)\right] \pm \frac{1}{2}\sqrt{\left[A\overline{X} + \nu\left(K_X^2 - K_Y^2\right)\right]^2 - 8A^2\overline{Y}^2}. \tag{3.11}$$

The eigenvalues for $\boldsymbol{X}_1$ are

$$\lambda_1^{(\boldsymbol{X}_1)} = -\nu K_X^2, \quad \lambda_2^{(\boldsymbol{X}_1)} = \frac{AF}{\nu K_X^2} - \nu K_Y^2, \tag{3.12}$$

which are both negative for $\nu > \sqrt{AF}/K_X K_Y$. Therefore, $\overline{\boldsymbol{X}}_1$ is stable for $\nu > \sqrt{AF}/K_X K_Y$, and a pitchfork bifurcation takes place at $\nu = \sqrt{AF}/K_X K_Y$. Then, for $\nu < \sqrt{AF}/K_X K_Y$, $\overline{\boldsymbol{X}}_2$ exists, which is stable irrespective of ν because the eigenvalues are

$$\lambda_{1,2}^{(\boldsymbol{X}_2)} = -\frac{\nu K_X^2}{2} \pm \frac{\sqrt{-8AF + \nu^2 K_X^2\left(1 + 8K_Y^2\right)}}{2}. \tag{3.13}$$

Thus, retaining only this simple interaction between the forced and most energetic modes seems insufficient to reproduce QCB via supercritical bifurcations. Results of the parameter scan further suggest that the subcritical route to QCB is not present either.

The additional ingredient for QCB turns out to be a small-scale representative and its associated triad interaction terms. Figure 3.7(a) shows the time series of energy $E(t)$ and energy dissipation rate $\epsilon(t)$ in the SPO along with partial energy $E_{X+Y} \equiv \left\langle |\boldsymbol{u}_X|^2 \right\rangle/2 + \left\langle |\boldsymbol{u}_Y|^2 \right\rangle/2$ and partial energy dissipation rate $\epsilon_{X+Y} \equiv \nu\left(\left\langle |\boldsymbol{\omega}_X|^2 \right\rangle + \left\langle |\boldsymbol{\omega}_Y|^2 \right\rangle\right)$ contained by the forced and primary modes. While the energy is almost

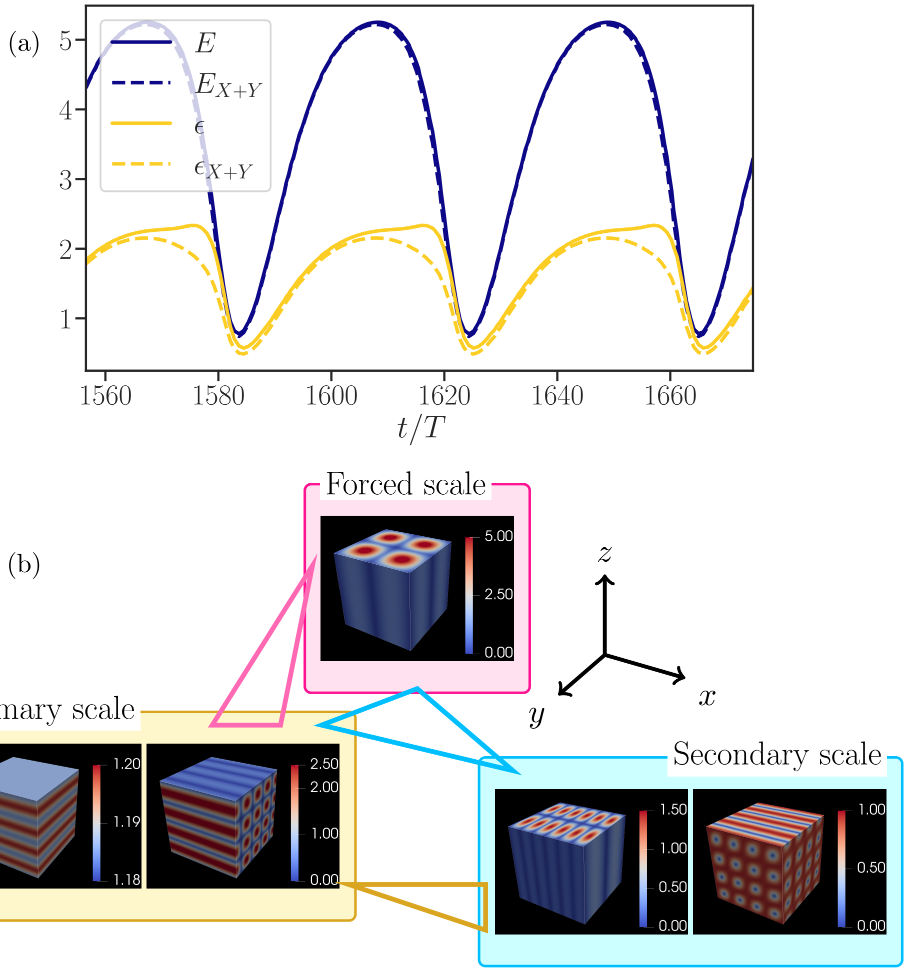

Figure 3.7: (a) Time series of energy $E(t)$ and energy dissipation rate $\epsilon(t)$ computed from all modes (solid lines) and those of the forced plus the primary energetic modes, denoted by $(\cdot)_{X+Y}$ (dashed lines). (b) Schematic of three different scales: "forced", "primary", and "secondary". We visualise $|\boldsymbol{\omega}|$ distributions of typical Fourier modes in each scale. The forced scale corresponds to $\boldsymbol{k}_f = (\pm1, \pm1, 0)$. In the primary scale, we visualise $\boldsymbol{k} = (0, 0, \pm2)$ and $(0, \pm2, \pm2)$ modes. For the secondary scale, we visualise $\boldsymbol{k} = (\pm3, \pm1, 0)$ and $(\pm2, \pm2, \pm2)$ modes for example. Note that the contributions of modes with all the possible sign combinations $(\pm k_x, \pm k_y, \pm k_z)$ are gathered in the visualisations. Triangles denote triad interactions between different scales. For details of interactions between the forced and primary scales, see Fig. 3.5.

entirely contained in E_{X+Y}, there is a visible difference between the full and partial energy dissipation rates. This reveals that the rest of the Fourier modes contribute significantly to the dynamics of the energy dissipation, representing the small scales. We denote the ensemble of these residual modes by Z. The essential nonlinear interactions of Z form triads with one mode of the Y-ensemble and another mode from either the Z-ensemble or the forced mode X. These observations lead to a refined three-equation model,

$$\begin{aligned}\frac{\mathrm{d}X}{\mathrm{d}t} &= -A_1Y^2 \qquad\qquad + A_3YZ \qquad\qquad - \nu K_X^2X + F,\\ \frac{\mathrm{d}Y}{\mathrm{d}t} &= +A_1XY - A_2Z^2 + A_4XZ \qquad\qquad - \nu K_Y^2Y,\\ \frac{\mathrm{d}Z}{\mathrm{d}t} &= \qquad\qquad + A_2YZ - (A_3+A_4)XY - \nu K_Z^2Z,\end{aligned} \tag{3.14}$$

which is represented by a schematic in Fig. 3.7(b). Here, A_1, $A_2 > 0$ and A_3, $A_4 \in \mathbb{R}$ are triad coefficients which retain the discrete Navier–Stokes structure (3.4). We choose the signs and the values of the triad coefficients such that the detailed balance holds in the energy transfer between the three scales. The signs of A_1 and A_2 are defined so that energy cascades towards small scales: from X to Y and Y to Z. This two-step energy cascade (for $A_3 = A_4 = 0$) is similar to the Obukhov two-stage cascade (Obukhov 1971). The triads with coefficients A_3 and A_4 represent the "non-local" interactions involving all three scales. Note that this system is different from, but is of the same level of complexity, as the well-known Lorenz (Lorenz 1963) or Rössler models (Rössler 1976; Rössler 1979). An important difference is that each variable denotes a Fourier mode in the Lorenz model, while in our model, it represents a group of modes.

3.2.2 Determination of the parameters

The model (3.14) is a simplified representation of the SPO, where all Fourier modes are sorted into three scales; the forced mode X, the energetic modes Y directly draining energy from X through the A_1 interaction, and the small scale modes Z which couple through the local direct cascade interaction A_2 with Y. There are also scale non-local interactions represented by A_3 and A_4. Even though such a representation of the flow discards details of the actual flow obtained by the DNS, we will fit the model parameters to the DNS data to assess how the model can reproduce actual flow properties.

We can fit six out of eight model constants in (3.14) by comparing them to the DNS of the periodic flow: A_i with $i = 1, 2, 3, 4$, K_α^2, where $\alpha \in \{X, Y, Z\}$, and F. To do so, we use the energy equations associated with (3.14),

$$\begin{aligned}\frac{\mathrm{d}E_X}{\mathrm{d}t} &= T_X - \epsilon_X + P,\\ \frac{\mathrm{d}E_Y}{\mathrm{d}t} &= T_Y - \epsilon_Y,\\ \frac{\mathrm{d}E_Z}{\mathrm{d}t} &= T_Z - \epsilon_Z.\end{aligned} \tag{3.15}$$

Here, $E_\alpha \equiv \alpha^2/2$ is the energy,

$$\begin{aligned}T_X &\equiv -A_1XY^2 \qquad\qquad + A_3XYZ,\\ T_Y &\equiv +A_1XY^2 - A_2YZ^2 + A_4XYZ,\\ T_Z &\equiv \qquad\qquad + A_2YZ^2 - (A_3+A_4)XYZ\end{aligned} \tag{3.16}$$

are the energy transfer terms, $\epsilon_\alpha \equiv 2\nu K_\alpha^2 E_\alpha$ is the energy dissipation rate, and $P \equiv FX$ is the energy input rate. The model parameters are determined by their corresponding quantities of the SPO obtained by DNS. The resulting values are

$$A_1 = 0.4,\ A_2 = 4,\ F = 0.7,\ K_X^2 = 2,\ K_Y^2 = 5,\ \text{and } K_Z^2 = 15. \tag{3.17}$$

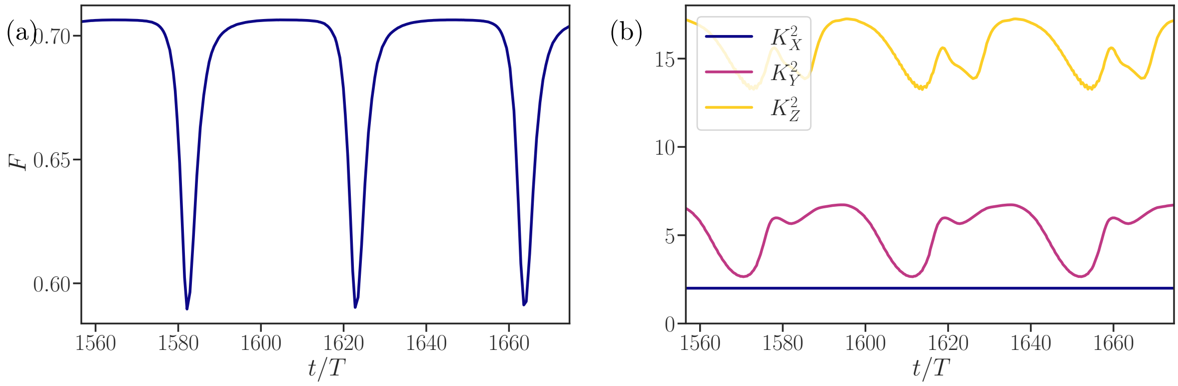

Figure 3.8: Time series of (a) forcing coefficient $F(t)$ and (b) scale coefficients $K_\alpha^2(t)$ in the DNS of the SPO.

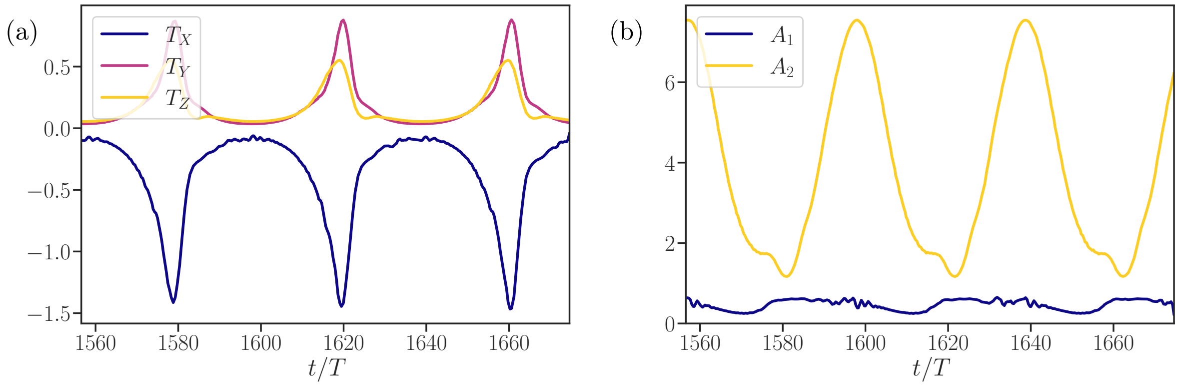

Figure 3.9: Time series of (a) energy transfer terms $T_\alpha(t)$ and (b) transfer coefficients $A_i(t)$ in the DNS of the SPO.

In the following, we discuss the detailed procedure of the parameter fitting (3.17) of the three-equation model (3.14). Figure 3.8(a) shows the time evolution of the forcing coefficient defined by

$$F(t) \equiv \frac{P}{\sqrt{2E_X}}. \tag{3.18}$$

We estimate the model parameter $F = 0.7$, since the time average $\langle F(t) \rangle_t = 0.696$. The periodic drops of $F(t)$ are associated with a phase-desynchronisation between the forcing and the forcing-induced velocity field, $\boldsymbol{u}_X$.

We also compute the scale factors

$$K_\alpha^2(t) \equiv \frac{\epsilon_\alpha}{2\nu E_\alpha} \quad (\alpha \in \{X, Y, Z\}). \tag{3.19}$$

Figure 3.8(b) shows their temporal evolutions. The forced scale factor $K_X^2(t) = 2$ is constant, since it corresponds to $\boldsymbol{k}_f = (\pm 1, \pm 1, 0)$ mode. On the other hand, $K_Y^2(t)$ and $K_Z^2(t)$ fluctuate, reflecting the competition of different Fourier modes in these scales. We estimate the model parameters by $K_Y^2 = 5$ and $K_Z^2 = 15$, since $\langle K_Y^2(t) \rangle_t = 4.97$ and $\langle K_Z^2(t) \rangle_t = 15.4$, respectively.

To obtain rough estimates of the scale local coefficients A_1 and A_2, we compute the average energy transfer rate from X to Y and Y to Z while ignoring the scale non-local interactions by setting $A_3 = A_4 = 0$. In this way, the energy transfer terms (3.16) of the energy equation (3.15) of the model are approximated by

$$\begin{aligned} T_X(t) &\approx -A_1 XY^2, \\ T_Y(t) &\approx +A_1 XY^2 \ - A_2 YZ^2, \\ T_Z(t) &\approx \qquad\qquad\quad + A_2 YZ^2. \end{aligned} \tag{3.20}$$

Figure 3.9(a) shows their time series by the DNS of the SPO. $T_X(t) < 0$ supports the energy cascade picture; the forced scale X is transferring energy to smaller scales (Y, Z) on average. Similarly, $T_Y(t), T_Z(t) > 0$ means that these smaller scales receive energy from the larger scales. We then evaluate the time-dependent coefficients,

$$A_1(t) \approx -\frac{T_X}{XY^2} = -\frac{1}{2\sqrt{2}} \frac{T_X}{\sqrt{E_X E_Y}}, \tag{3.21}$$

$$A_2(t) \approx \frac{T_Z}{YZ^2} \quad = \frac{1}{2\sqrt{2}} \frac{T_Z}{\sqrt{E_Y E_Z}}. \tag{3.22}$$

Again, we neglect the scale non-local interactions ($A_3 = A_4 = 0$) in these expressions. The result is shown in Fig. 3.9(b), and we estimate $A_1 = 0.4$ and $A_2 = 4$ as the model parameters from the time-averaged values $\left\langle A_1(t) \right\rangle_t = 0.440$ and $\left\langle A_1(t) \right\rangle_t = 4.04$, respectively.

The above argument allows us to determine the model parameters in (3.17). The non-local interaction coefficients A_3 and A_4 are left to be determined. In § 3.2.2, we vary these two parameters to investigate the model properties.

The energy flux coefficients A_1 and A_2 are determined by the energy transfer terms T_α in (3.16) while ignoring the nonlocal coefficients A_3 and A_4 (3.21-3.22). The forcing coefficient F is evaluated by P and the X-scale energy E_X (3.18). The squared characteristic wavenumber K_α^2 is set by E_α and ϵ_α in each scale (3.19). Note that $K_X = \sqrt{2}$ of the model parameter can be related to $\left|\boldsymbol{k}_f\right| = \sqrt{2}$ of the forcing (3.2) of the DNS. We remark here that our parameter choice (3.17) supports the energy cascade picture with $T_X(t) < 0$: the forced scale X transfers its energy to smaller scales (Y, Z) on average. And $T_Y(t), T_Z(t) > 0$ means that the smaller scales receive energy from the larger scales. The undetermined parameters of the model are the scale non-local interaction coefficients A_3 and A_4, which can be freely chosen. The only control parameter is $\mathrm{Re} \equiv 1/\nu$. We numerically integrate the model with a fourth-order Runge-Kutta scheme and $\Delta t = 0.01$ starting from random initial conditions. See Rackauckas and Nie (2017) for the solver information. Our numerical simulations seem to indicate that no periodic solutions exist without the complete non-local interactions: $A_3 = 0$, $A_4 = 0$, or $A_3 + A_4 = 0$. Conversely, periodic behaviour is observed for a wide range of values when $A_3 \neq 0$, $A_4 \neq 0$, and $A_3 + A_4 \neq 0$. This observation emphasises the importance of non-local triad interactions for periodic behaviour.

3.2.3 Comparison between the model and the direct numerical simulation result

Figure 3.10 compares the SPO obtained by the model and the DNS. Figure 3.10(a) shows the time series of the model with the parameters (3.17) and $(A_3, A_4) = (0.5, -0.95)$. Since the definitions of Re are different in the model and DNS, we have chosen a Reynolds number in the model, which allows qualitatively reproducing the DNS results. We compute two quantities. One is $E_{X-X_0} \equiv (X - X_0)^2/2$, which is the fluctuating energy of the forced mode around the laminar base flow $X_0 \equiv F\,\mathrm{Re}\,/K_X^2$. The other quantity $E_{Y+Z} \equiv Y^2/2 + Z^2/2$ is the energy of the rest of the modes. We compare them to the corresponding quantities in the DNS of the SPO [Fig. 3.10(b)], where the base flow is $\boldsymbol{u}_0 \equiv \boldsymbol{f}/2\nu\left|\boldsymbol{k}_f\right|^2$, the forced-mode fluctuating energy is $E_{X-X_0} \equiv \left\langle \left|\boldsymbol{u}_X - \boldsymbol{u}_0\right|^2 \right\rangle/2$, and E_{Y+Z} is defined by the energy possessed by the non-forced modes. We can observe similar periodic behaviour of E_{X-X_0} and E_{Y+Z} in the model (3.14) and in the SPO driven by the steady forcing (3.2). In particular, there are predator-prey-like exponential growth and decay in both systems. Although fast oscillations are observed in the model but not in the DNS, a close analysis of the DNS of the SPO reveals the presence of rapid oscillations in specific Fourier modes. These oscillations are compensated by modes that display the same energy oscillations with an opposite phase and do not appear in Fig. 3.10(b). We stress that this SPO is independent of the exact

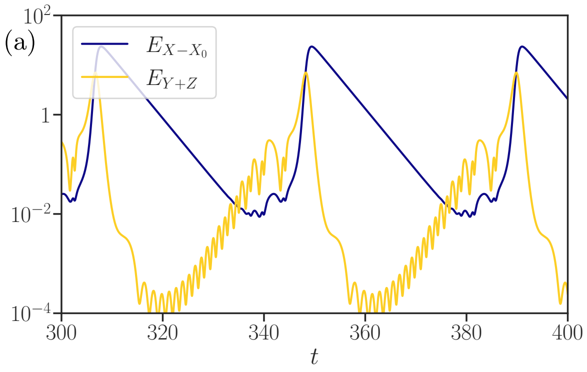

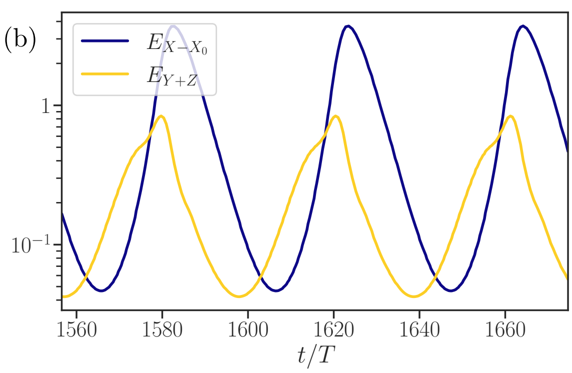

Figure 3.10: Time series of fluctuating energy $E_{X-X_0}(t)$ of the forced scale and residual energy $E_{Y+Z}(t)$ of periodic solutions of (a) model (3.14) at $\mathrm{Re} = 14.05$ and (b) the Navier–Stokes equations (3.1) at $\mathrm{Re} = 5.83$. Parameters of the model are (3.17) and $(A_3, A_4) = (0.5, -0.95)$. Note that time in panel (b) is normalised by T.

amplitude of the initial conditions because the present model is a dissipative system.

3.3 Bifurcation analysis of the model

3.3.1 Bifurcation from stable periodic orbit to chaos with quasi-cyclic behaviour

We observe a chaotic state of the model by varying Re from 14.05 to 14.1 while keeping the model parameters as in Fig. 3.10(a). Figure 3.11(a) shows the orbits in phase space for both the periodic (at Re $=$ 14.05) and chaotic (at Re $=$ 14.1) cases. The chaotic solution remains close to the SPO as it shows chaotic QCB and is permanent as in the turbulence investigated in § 3.1. Thus, the same model reproduces SPO and chaotic QCB. Incidentally, the SPO resembles a Šilnikov homoclinic orbit (Šilnikov 1965). We also plot a simpler periodic orbit at Re $= 12.5$ in this figure. It is almost two-dimensional as opposed to the complex three-dimensional periodic and chaotic orbits, suggesting a possible connection with a two-dimensional periodic orbit in the same forcing configuration (van Veen, Kawahara, et al. 2018, Fig. 4). However, we do not focus on this orbit as it is not directly connected to a chaotic one.

To further assess the behaviour of the system, we draw the bifurcation diagram in Fig. 3.11(b) with the same parameter set as in Fig. 3.10(a) and Fig. 3.11(a). We observe a supercritical transition from periodic to chaotic solutions at a critical Reynolds number $\mathrm{Re}_{\mathrm{cr}} \in [14.060, 14.061]$ [inset of Fig. 3.11(b)], and, as observed in Fig. 3.11(a), the chaotic orbit remains close to the SPO. We note that the solution becomes periodic again when we further increase Re beyond the range of Fig. 3.11(b), probably because the model contains only a small number of degrees of freedom. The inset of Fig. 3.11(b) shows that there is a hysteresis in the range $\mathrm{Re} \in [13.82, 14.03]$, below $\mathrm{Re}_{\mathrm{cr}}$, which corresponds to a subcritical bifurcation from a periodic solution to another periodic solution shown in Fig. 3.10(a). The appearance of the multiplicity of local extrema corresponds to the spiraling behaviour of the orbit in phase space. Thus, although the bifurcations from the trivial steady solution to the SPO are rather complicated, that from the SPO to chaos with QCB is simple. Although there is no clear scenario for the route to turbulence with QCB, the present model results may give us a hint to describe the route in real turbulence.

3.3.2 Subcritical bifurcation to chaos

Since it is well known that, in some cases, turbulence appears via a subcritical transition, here we demonstrate that our model also expresses such a route to chaos. We stress that we cannot use the strategy above to determine the model parameters since there is no SPO in such a system. Instead, by varying the undetermined parameters of the model, we observe transient chaos at $(A_3, A_4) = (0.4, -0.5)$ as shown in Fig. 3.12(a). The corresponding bifurcation diagram in Fig. 3.12(b) shows a subcritical bifurcation between steady and chaotic solutions around $\mathrm{Re} \approx 32.3$. There are bi-stable states for $33 \lesssim \mathrm{Re}(\lesssim 35)$ of steady and chaotic solutions. The inset of Fig. 3.12(b) shows that there are multiple windows of periodic solutions in the chaotic regime, probably due to the limited number of degrees of freedom of the model (3.14).

The transient behaviour in Fig. 3.12(a) reminds us of the sudden relaminarisation observed in a linearly forced turbulence (Linkmann and Morozov 2015), turbulent Kolmogorov flow (van Veen and Goto 2016), pipe flow (Hof et al. 2006), and even in the Lorenz system (Yorke and Yorke 1979; Maslennikov and Nekorkin 2013). We evaluate the survival probability $P_{\mathrm{Re}}(t)$, representing how likely the solution remains in a chaotic regime at a given time t, to investigate this phenomenon. To evaluate $P_{\mathrm{Re}}(t)$, we identify the relaminarisation time t_{r} by the first time when the local maxima of oscillating energy $E_{Y-Y_0} \equiv (Y - Y_0)^2/2$ becomes smaller than a threshold $\delta = 1 \times 10^{-3}$. Here, Y_0 is the stable and steady solution. Then, the probability $P_{\mathrm{Re}}(t)$ for given t can be evaluated by the ratio of a number of samples with $t_{\mathrm{r}} < t$ against the number of the whole sample. We plot $P_{\mathrm{Re}}(t)$ in Fig. 3.13(a) to find that an exponential scaling,

$$P_{\mathrm{Re}}(t) \propto \exp\left[-\frac{t}{\tau(\mathrm{Re})}\right], \tag{3.23}$$

fits the data. The characteristic time scale τ in Fig. 3.13(b) also displays an exponential scaling,

$$\tau(\mathrm{Re}) \propto \exp[a\,\mathrm{Re}], \tag{3.24}$$

against Re. Although the scaling (3.23) of $P_{\mathrm{Re}}(t)$ is consistent with the observations in the previous

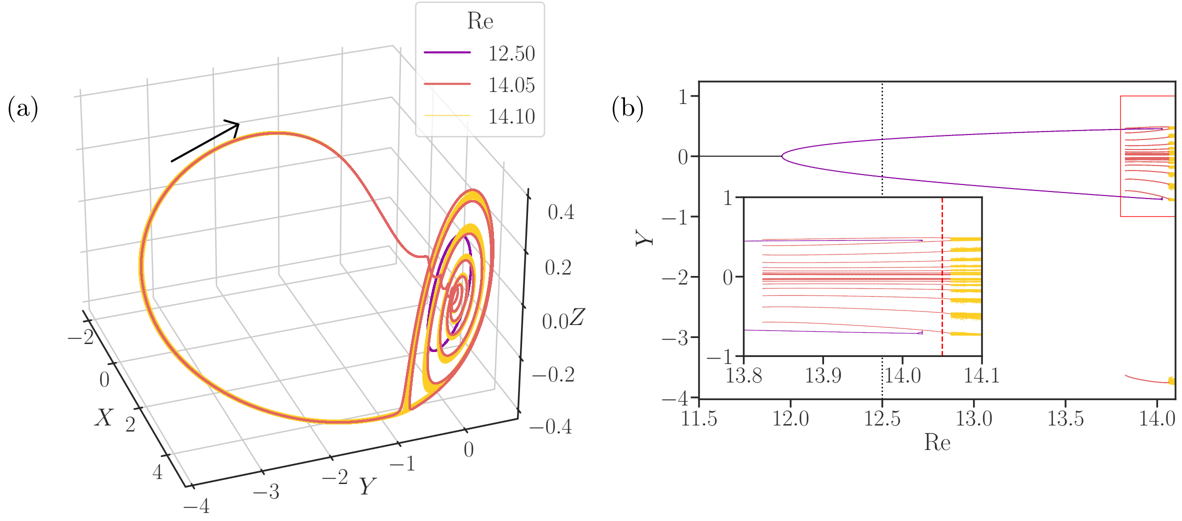

Figure 3.11: (a) Simple periodic (Re = 12.50), complex periodic (Re = 14.05) [Fig. 3.10(a)], and chaotic (Re = 14.1) orbits of the model (3.14). The parameters are the same as in Fig. 3.10(a). The chaotic orbit is tracked over 100 periods. The arrow indicates the direction of the orbit. (b) Bifurcation diagram of the model with changing Re for the same parameters as in Fig. 3.10(a). We plot the local extrema of Y. We have determined the periodicity by Poincaré analysis. The black vertical dotted line corresponds to Re = 12.50 used in panel (a). Inset: close-up in the range shown by the red rectangle in the main plot. The red vertical dashed line corresponds to Re = 14.05 used for panel (a) and Fig. 3.10(a). For both panels, black, purple, orange, and yellow data denote steady, simple periodic, complex periodic, and chaotic solutions, respectively.

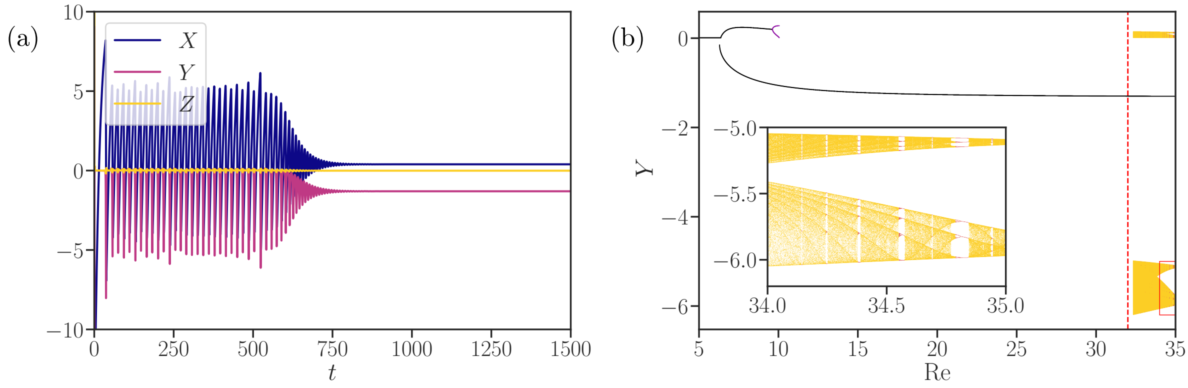

Figure 3.12: (a) Time series of (X, Y, Z) of the model (3.14) with parameters (3.17) and $(A_3, A_4) = (0.4, -0.5)$ at Re = 32. A random initial condition is used. (b) The bifurcation diagram for the same parameter set. The red vertical dashed line denotes Re = 32, which is used for Fig. 3.12(a). Inset: close-up of the diagram in the range shown by the red rectangle in the main plot.

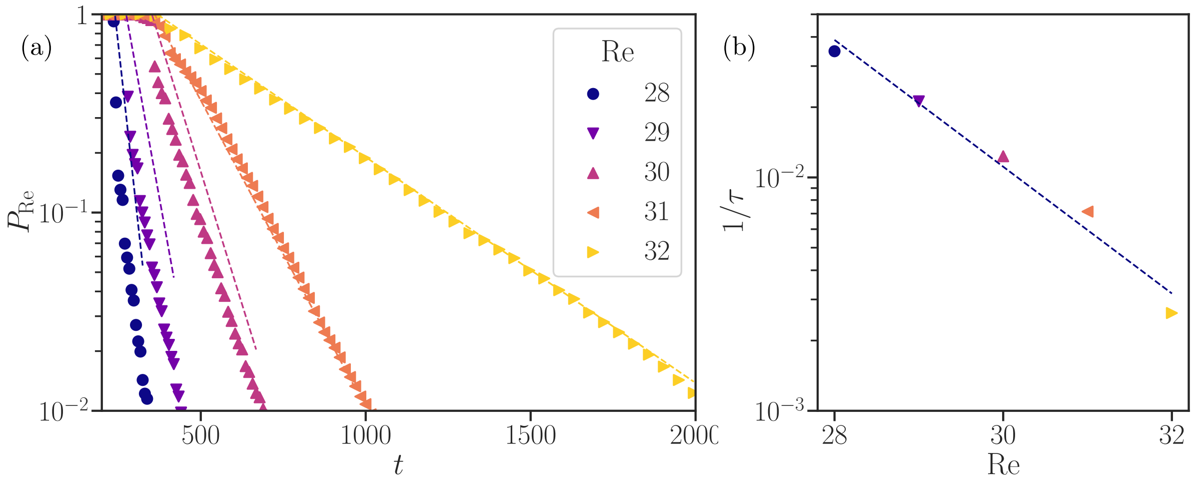

Figure 3.13: (a) Survival probability $P_{\mathrm{Re}}(t)$ of the transient chaos of the model (3.14) evaluated from 10,000 samples for each Re. The parameter set is the same as in Fig. 3.12. Dashed line denotes exponential fitting by (3.23) using $0.01 \leq P_{\mathrm{Re}}(t) \leq 0.9$. (b) The escape rate $1/\tau$ as a function of Re. The dashed line denotes the exponential fitting by (3.24).

studies (Linkmann and Morozov 2015), the exponential scaling (3.24) of $\tau(\mathrm{Re})$ differs from a super-exponential behaviour observed in Linkmann and Morozov (2015). This qualitative difference may also be caused by the minimal number of degrees of freedom in the model.

Note that the Taylor–Green forcing (3.2) in the DNS does not permit such a transition since the laminar base flow $\boldsymbol{u}_0 \equiv \boldsymbol{f}/2\nu|\boldsymbol{k}_f|^2$ is linearly unstable. However, the steady Kolmogorov forcing with a linearly stable laminar base flow exhibits sudden relaminarisations (van Veen and Goto 2016). Thus, we can speculate that the model can reflect different forcing setups applied to the Navier–Stokes equations by varying the parameters (A_3, A_4).

3.4 Concluding remarks

The present investigation attempts to construct a minimal model of turbulence with quasi-cyclic behaviour (QCB) in a steady-force driven flow while keeping the structure of the Navier–Stokes equations. First, through the DNS of Navier–Stokes turbulence, we show that QCB in high-Re turbulence is continuously connected to an SPO at small Re by extracting the intrinsic periodicity of QCB via a phase averaging technique (§ 3.1). Next, we conduct a mode-by-mode analysis of the SPO to identify the flow's forced, primary energetic, and secondary scales. We propose the three-equation model (3.14) describing the evolution of such three distinct scales (§ 3.2.1). By adjusting the model parameters, we observe that the model reproduces an SPO similar to that of the DNS (§ 3.2.2). We emphasise that scale non-local nonlinear interactions (interactions involving three separate scales) are mandatory for reproducing these dynamics. Then, we conduct a bifurcation analysis to show that the model also exhibits chaotic QCB via a supercritical bifurcation, which is continuously connected to the SPO (§ 3.3.1). Thus, we conclude that the proposed model reproduces turbulent QCB and its relation to an SPO using a minimum number of degrees of freedom.

Further analysis of the model by varying the undetermined parameters yields transient chaos with sudden relaminarisation, which is also observed in turbulent flow with different forcing setups (§ 3.3.2). Thus, we speculate that the present model can be a minimal model for certain features of turbulence.

An outstanding open question is how QCB survives in spatially extended flows. How will the global dynamics change when the forcing is applied to scales smaller than the domain size? In other words, how will the modes larger than the forced scale alter QCB turbulence, and how can we model it? Investigating the relation between space and scale locality and temporal dynamics of turbulence is left for further research.

Part II

Space-local Navier–Stokes Turbulence

4 Physical-space Locality of Turbulence

Locality is one of the most fundamental, often implicitly assumed, properties in a number of fields of physics. For example, we do not consider the universal gravitation due to the moon when we compute the velocity of an apple falling from a tree in Cambridge. Generally, we implicitly assume that two nearby objects are more strongly correlated (or affected by each other) than distant ones. Here, the terms *nearby* and *distant* refer to both physical space and scale-space sense; one needs not to consider the effect of the moon on the falling apple, and similarly, one can model the falling apple without being bothered by its $\mathcal{O}(10^{23})$ molecules constituting it. We already discussed the scale-local nature of the energy cascade in § 1.1.2. In this section, we focus on the other locality of turbulence, in the physical space. Although much less attention has been paid to the physical-space locality, this idea may have important implications for the understanding and modelling of turbulence, particularly its physical-space mechanism. In § 4.1, we review previous studies on this subject. In § 4.2, we define the space-local velocity field $\boldsymbol{u}^{\mathrm{L}}$, derived from the Biot–Savart law between the velocity and the vorticity fields. It can be understood as the velocity field *induced* by the neighbouring vorticity field and is the central quantity of interest in this and the next chapter. In § 4.3, we conduct a post-process analysis of a turbulent flow dataset with $\boldsymbol{u}^{\mathrm{L}}$. We investigate how the scale-space property of turbulence is altered by $\boldsymbol{u}^{\mathrm{L}}$. We conclude this chapter in § 4.4.

4.1 Previous studies on physical-space locality

The scale-space locality states that the nonlinear interactions between adjacent scales are responsible for the small-scale universality of turbulence. However, such a discussion on scale space does not explain how local the nonlinear interactions are in physical space. In this section, we review the locality of turbulence in physical space.

The physical-space locality of the energy flux was first considered by Kraichnan (1974). Since then, several formulations of the space-local energy flux have been proposed; Meneveau employed wavelets (Meneveau 1991) and Lagrangian correlation framework to locally track the energy flux in space (Meneveau and Lund 1994). Eyink used a refined similarity hypothesis involving a spatial length scale (Eyink 1995), as well as developing a multi-scale gradient expansion, which decomposes the turbulent stress tensor into multi-scale and multi-order spatial derivatives (Eyink 2005; Eyink 2006; Eyink and Aluie 2009). Tsinober discussed spatially concentrated vorticity and its nonlocal interactions with background turbulence (Tsinober 1998). “Five-dimensional” (three-dimensional space, scale, and time) analysis of energy cascade revealed an emergence and disappearance of fluid structures within the larger- and smaller-scale structures, respectively (Cardesa, Vela-Martín, and Jiménez 2017). Doan et al. (2018) investigated the scale-local energy cascade in terms of vortex stretching in real space. More recent work found a power-law correlation between the filtered strain rate and the space-local energy flux (Alexakis and Chibbaro 2020). In Vela-Martín and Jiménez (2021), the irreversibility of turbulence and preference for direct energy cascade is discussed with its space-local property. We note that these questions are not only of fundamental importance but are also relevant to turbulence modelling, particularly in refining sub-grid scale models (Borue and Orszag 1998).

Recently, the combined analysis of both position in space and scale has been conducted using the Kármán–Howarth–Monin–Hill equation (Valente and Vassilicos 2015; Yasuda and Vassilicos 2018). It is a rigorous equation derived from the Navier–Stokes equation and describes the evolution of “energy” of velocity at two points, $\boldsymbol{x} - \boldsymbol{r}/2$ and $\boldsymbol{x} + \boldsymbol{r}/2$, separated by distance $r = |\boldsymbol{r}|$ centered at $\boldsymbol{x}$. Thus, this equation can

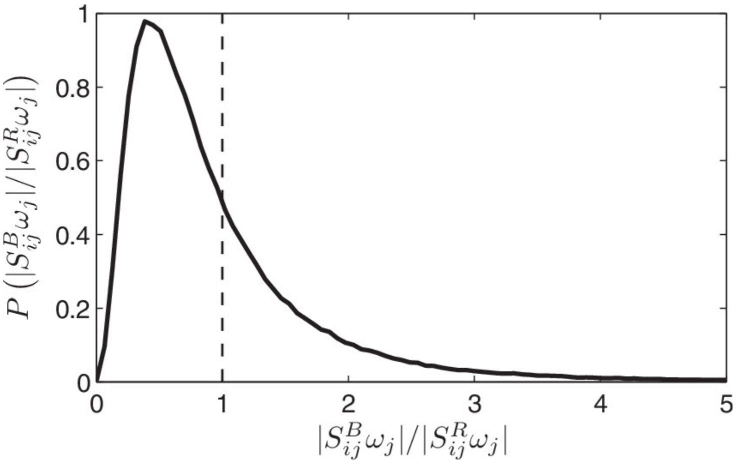

Figure 4.1: Distribution of the vortex stretching contributions from the background strain $S_{ij}^B\omega_j$ against the local strain $S_{ij}^R\omega_j$. Adapted from Hamlington, Schumacher, et al. (2008b, Figure 4).

handle the scale r and space $\boldsymbol{x}$ simultaneously.

Pressure and its Hessian are also important to describe the physical-space nonlocality of turbulence (She, Jackson, et al. 1991). Several investigations report its role in decaying turbulence (Kishiba et al. 1993), relation with finite time blow-up (Ohkitani and Kishiba 1995), rotation (Nomura and Post 1998), and the role of local and nonlocal contributions to the influence of the pressure Hessian (Chevillard, Lévêque, et al. 2011).

In decaying isotropic turbulence, analysis of the spatial local/nonlocal contributions of the strain-rate tensor on the vorticity revealed that considerable (about 40 % for energy dissipation and 50 % for enstrophy production) contributions comes from nonlocal regions in which the separation from the source vorticity is larger than 2λ, where λ is the Taylor microscopic length scale (Kishiba et al. 1993). Geometric analysis of the nonlinear interactions of turbulence was performed in real space to show how purely geometric properties contribute to the forward energy cascade (Ballouz and Ouellette 2020). In the framework of the toy model, Tanogami and Sasa considered an XY spin model with space-local interactions to consider its energy cascade and universal scaling (Tanogami and Sasa 2022).

The most important work regarding our methodology in this study is developed by Hamlington and his colleagues (Hamlington 2009). They proposed the local/nonlocal decomposition of the strain-rate tensor to investigate the alignment between the vorticity and eigenvectors of the strain-rate tensor (Hamlington, Schumacher, et al. 2008a; Hamlington, Schumacher, et al. 2008b). They revealed that the most extensional eigenvector of the nonlocal strain-rate tensor aligns with vorticity. Figure 4.1 shows the distributions of background to local vortex stretching ratio.

Buaria and his colleagues used this local/nonlocal decomposition in Direct Numerical Simulation (DNS) to find the self-attenuation property of the intense vorticity due to the locally induced strain rate (Buaria, Pumir, and Bodenschatz 2020). See Figure 4.2 for the visualisations. They extend the investigation in the eigenvector alignment framework (Buaria and Pumir 2021). In this part of the thesis, we employ the same space-local filtering in the Navier–Stokes equations to investigate the spatial locality of turbulence. Figure 7.7 shows the timeline of research on the spatial locality of turbulence.

In industry-oriented Computational Fluid Dynamics (CFD), assessing the physical space locality of turbulence is important. Industrial CFD often solves flow in/around complex structures such as mixers with rotating blades or aeroplanes. In such a case, the numerical algorithm should be local in space or sparsely connected to a distant fluid element for high scalability. For example, the recent growth of interest in the Lattice Boltzmann Method (LBM) relates to its space-locality (Krüger et al. 2016, §2.4). The LBM considers the temporal evolution of distributions of "particles" in nodes spanning the domain, based on the Boltzmann equation. The nonlinear terms are then evaluated locally (node-wise), and this property contributes to the high scalability of the scheme.

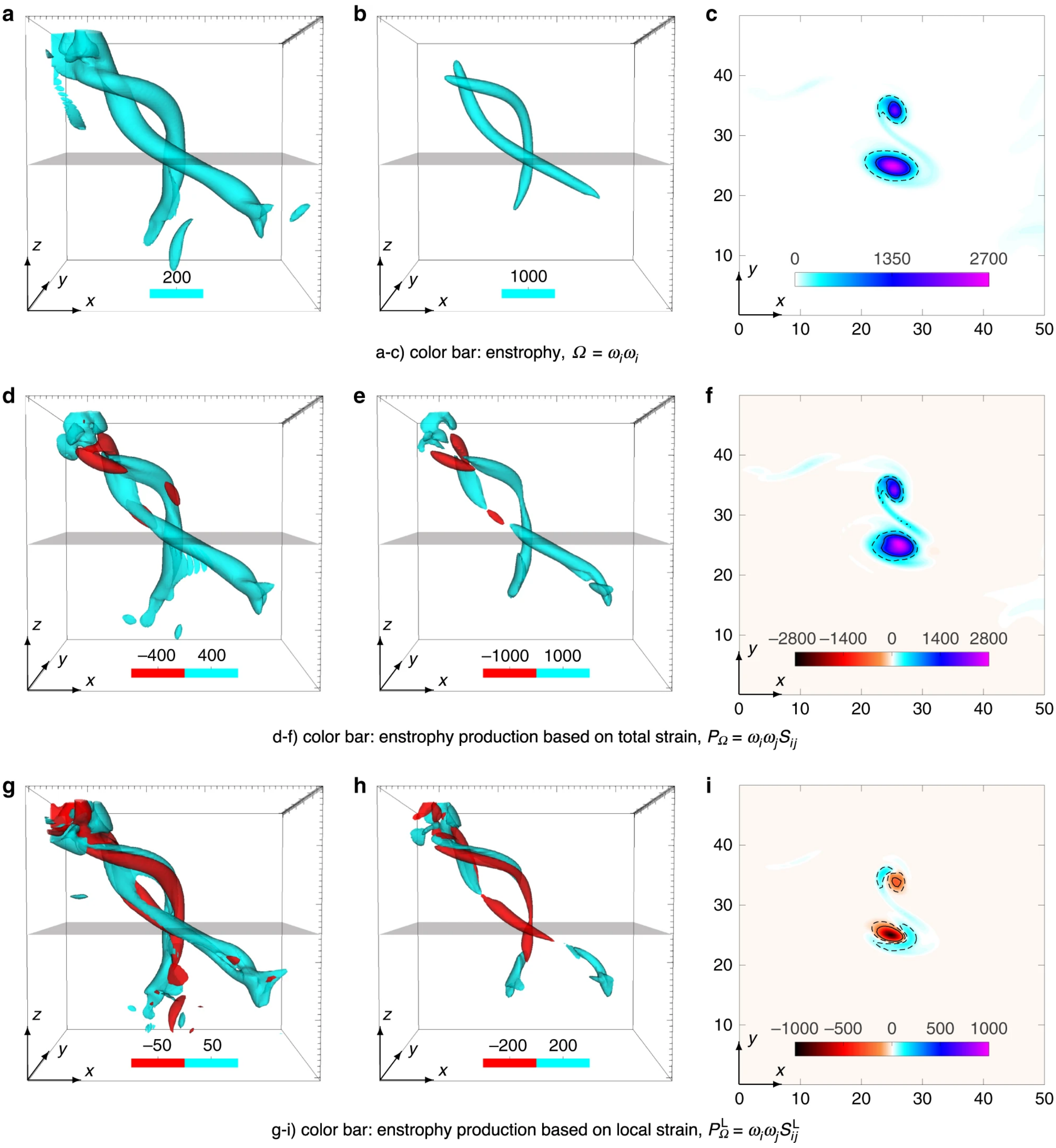

Figure 4.2: Space-local vortex stretching term and the self-attenuation of intense vortex. (a-c) shows the enstrophy. (d-f) shows the positive and negative enstrophy production due to the total strain. (g-i) shows the positive and negative enstrophy production due to the space-local strain. (a, d, g) shows moderate structures with a smaller threshold. (b, e, g) shows the intense structures with a larger threshold. (c, f, i) shows the distributions on the plane denoted by the grey plane in the other panels. Adapted from Buaria, Pumir, and Bodenschatz (2020, Figure 1).

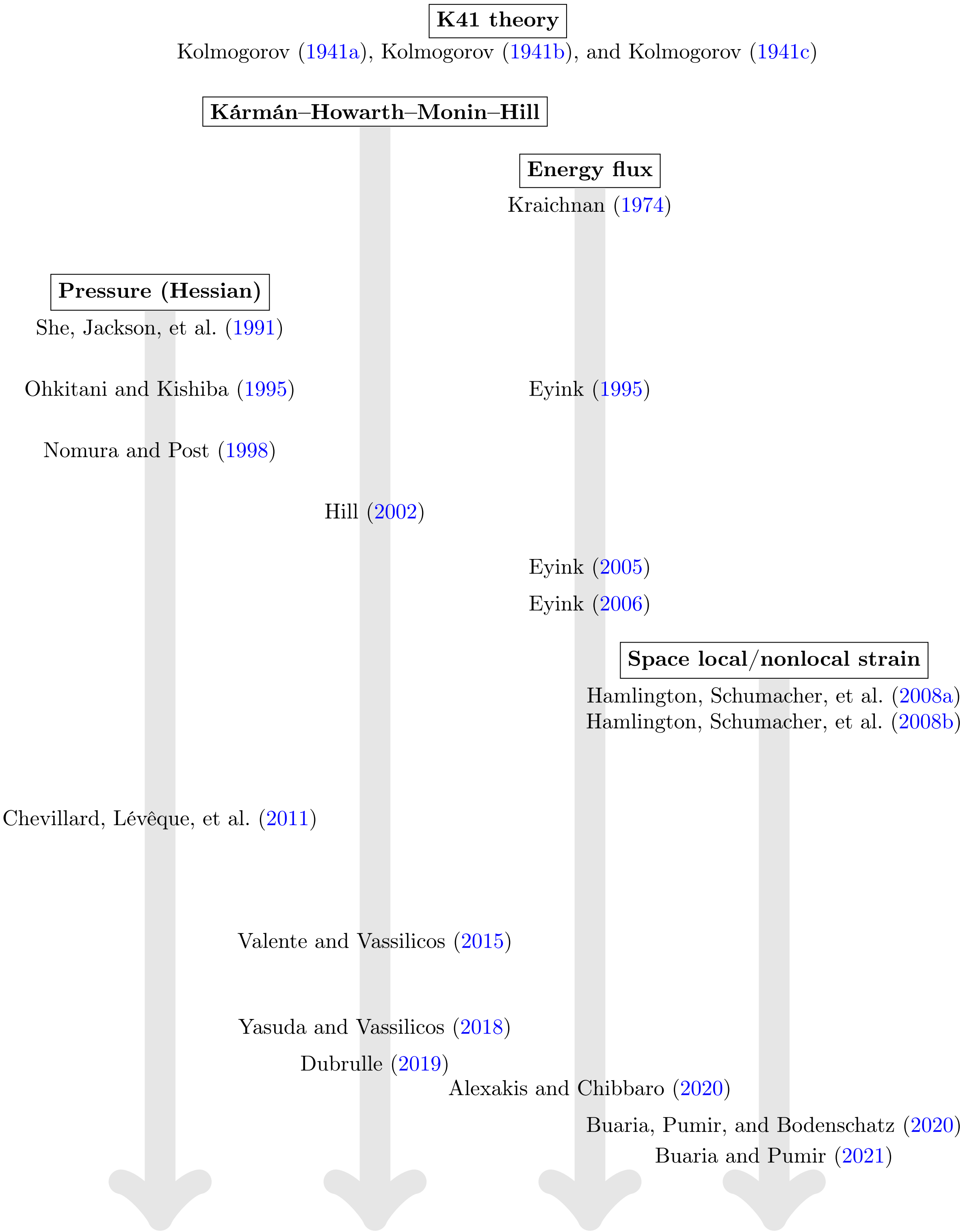

Figure 4.3: Historical timeline of research on the physical-space locality of three-dimensional turbulence.

4.2 Space-local filtering on the velocity field

In this section, we formulate the space-local description we employ in the subsequent investigations. In § 4.2.1, we review the nonlocal relation between vorticity and velocity fields connected by the Biot–Savart law to define the space-local velocity field by truncating the Biot–Savart law in § 4.2.2. In § 4.2.3, we discuss the physical-space locality of the pressure gradient term in the Navier–Stokes equations and how it relates to the space-local velocity field.

4.2.1 Nonlocal relation between vorticity and velocity fields

In this subsection, we consider the physical-space locality in the macroscopic description of fluid. We consider the incompressible three-dimensional Navier–Stokes equations,

$$\begin{cases} \dfrac{\partial \boldsymbol{u}}{\partial t} = -\boldsymbol{\omega} \times \boldsymbol{u} - \boldsymbol{\nabla}\left(p + \dfrac{\boldsymbol{u}^2}{2}\right) + \nu \nabla^2 \boldsymbol{u} + \boldsymbol{f}, & (4.1) \\ \boldsymbol{\nabla} \cdot \boldsymbol{u} = 0. & (4.2) \end{cases}$$

Here, $\boldsymbol{u}$ and $\boldsymbol{\omega} \equiv \boldsymbol{\nabla} \times \boldsymbol{u}$ are velocity and vorticity field, respectively. The forcing field driving the flow is denoted by $\boldsymbol{f}$. The pressure term divided by the constant density is p, and ν is the kinematic viscosity determining the flow property. Except for the pressure gradient term, all the terms on the RHS of (4.1) can be evaluated locally in physical space. By solving the Poisson equation,

$$\nabla^2 p = -\frac{\partial u_i}{\partial x_j}\frac{\partial u_j}{\partial x_i}, \tag{4.3}$$

one obtains the pressure field,

$$p(\boldsymbol{x}, t) = p_0(\boldsymbol{x}, t) + \frac{1}{4\pi}\int_\Omega \left(\frac{\partial u_i}{\partial x_j}\frac{\partial u_j}{\partial x_i}\right)(\boldsymbol{x}', t)\frac{\mathrm{d}\boldsymbol{x}'}{|\boldsymbol{x} - \boldsymbol{x}'|}, \tag{4.4}$$

where Ω denotes the domain. The harmonic part p_0 satisfies $\nabla^2 p_0 = 0$ and depends on the boundary conditions. The pressure field, including the boundary condition and the spatial integral, is thus determined nonlocally in terms of physical space. See § 4.2.3 for a more detailed discussion.

The curl of (4.1) gives the vorticity equation,

$$\frac{\partial \boldsymbol{\omega}}{\partial t} = -\boldsymbol{u} \cdot \boldsymbol{\nabla}\boldsymbol{\omega} + \boldsymbol{\omega} \cdot \boldsymbol{\nabla}\boldsymbol{u} + \nu \nabla^2 \boldsymbol{\omega} + \boldsymbol{\nabla} \times \boldsymbol{f}, \tag{4.5}$$

which gives an alternative point of view on the physical space locality. Since the pressure term vanishes by the identity $\boldsymbol{\nabla} \times \boldsymbol{\nabla} p = \boldsymbol{0}$, the curl operator seems to eliminate the spatial nonlocality. However, there is a spatial nonlocality associated with the curl operator itself. Although one can compute the curl of a given velocity field $\boldsymbol{\nabla} \times \boldsymbol{u}$ locally in space, the opposite procedure requires spatially nonlocal information. Evaluation of $\boldsymbol{u}$ from known $\boldsymbol{\omega}$ can be done by the Biot–Savart law (Majda and Bertozzi 2002, § 2.4),

$$\boldsymbol{u}(\boldsymbol{x}) = \frac{1}{4\pi}\int_\Omega \mathrm{d}^3\boldsymbol{x}' \, \frac{\boldsymbol{\omega}(\boldsymbol{x}') \times (\boldsymbol{x} - \boldsymbol{x}')}{|\boldsymbol{x} - \boldsymbol{x}'|^3}, \tag{4.6}$$

which includes the spatial integral as in the pressure Poisson equation (4.4). It leads us to a new perception of (4.5); temporal evolution of vorticity is described by the advection and stretching due to the velocity induced by the *whole* vorticity field, along with the viscous damping and the forcing. In this sense, we understand that the nonlinear term of the vorticity equation is spatially nonlocal. In § 4.2.3, we discuss the relationship between the two physical-space nonlocalities in pressure (4.4) and velocity (4.6).

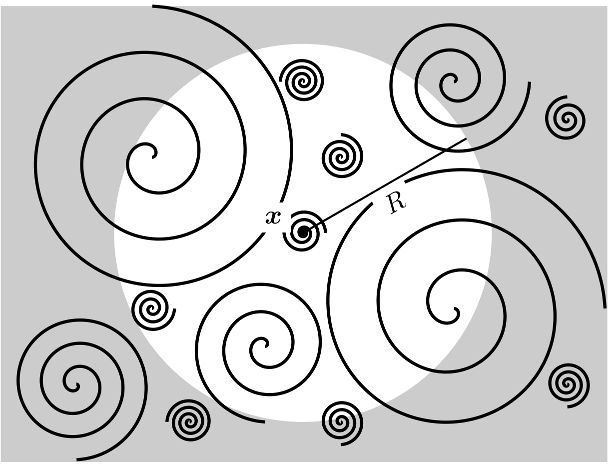

Figure 4.4: Schematic of the space-local velocity field $\boldsymbol{u}^{\mathrm{L}}$, defined by the *local* vorticity field inside the radius R. The shadowed region denotes the *nonlocal* domain outside the radius R.

4.2.2 Space-local velocity field

Here, we define the space-local velocity field with the superscript $\cdot^{\mathrm{L}}$,

$$\boldsymbol{u}^{\mathrm{L}}(\boldsymbol{x}) \equiv \frac{1}{4\pi} \int_{r \leq R} \mathrm{d}^3\boldsymbol{x}' \, \frac{\boldsymbol{\omega}(\boldsymbol{x}') \times (\boldsymbol{x} - \boldsymbol{x}')}{|\boldsymbol{x} - \boldsymbol{x}'|^3}, \tag{4.7}$$

where $r \equiv |\boldsymbol{x} - \boldsymbol{x}'|$. Equation (4.7) involves truncation of the spatial integral of the Biot–Savart law (4.6) at a sphere of radius R centered at $\boldsymbol{x}$. Expression (4.7) was first proposed to investigate the alignment between the vorticity vector and the eigenvectors of the strain-rate tensor (Hamlington, Schumacher, et al. 2008a; Hamlington, Schumacher, et al. 2008b; Hamlington 2009). Figure 4.4 shows the schematic of the space-local velocity field $\boldsymbol{u}^{\mathrm{L}}$.

Next, we consider expressing (4.7) in Fourier space. The procedure below is simpler than the one provided in the Supplemental Note of Buaria, Pumir, and Bodenschatz (2020). To this end, we introduce the three-dimensional top-hat (box) filter with radius R,

$$B(\boldsymbol{r}; R) = \begin{cases} \dfrac{3}{4\pi R^3} & |\boldsymbol{r}| \leq R \\ 0 & |\boldsymbol{r}| > R \end{cases}, \tag{4.8}$$

by using the fact that the volume of the sphere of radius R is $4\pi R^3/3$ and

$$\int B(\boldsymbol{r}; R) \, \mathrm{d}\boldsymbol{r} = 1. \tag{4.9}$$

Here, $\boldsymbol{r} \equiv \boldsymbol{x} - \boldsymbol{x}'$ denotes the vector between two points. We introduce spherical coordinates

$$\boldsymbol{x} = \begin{pmatrix} x \\ y \\ z \end{pmatrix} = \begin{pmatrix} r \sin\theta \cos\phi \\ r \sin\theta \sin\phi \\ r \cos\theta \end{pmatrix}, \tag{4.10}$$

where $r \geq 0$ denotes the radius, $\phi \in [0, 2\pi)$ the angle between the projection of $\boldsymbol{r}$ vector onto the (x, y) plane and the x axis, and $\theta \in [0, \pi]$ the angle between $\boldsymbol{r}$ and the z axis. The Fourier representation of (4.8)

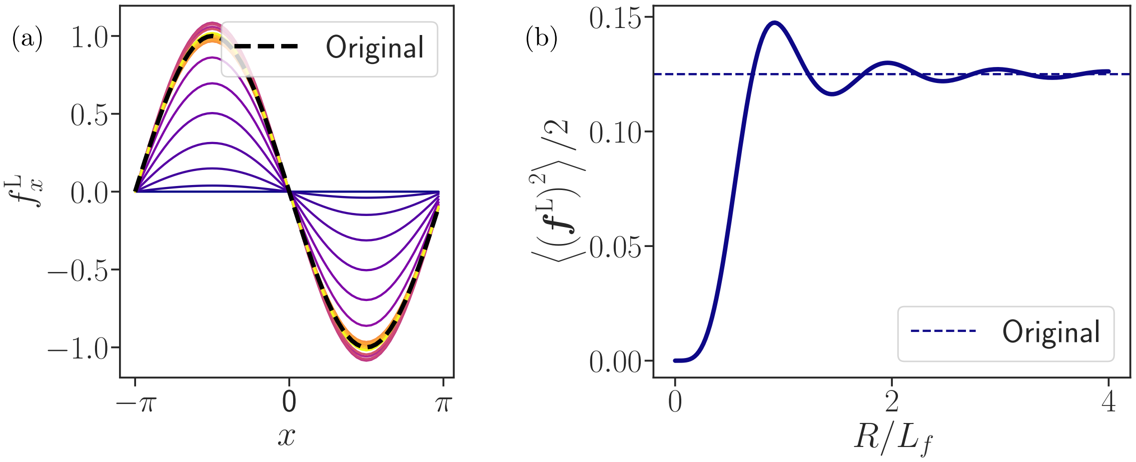

Figure 4.5: (a) Profile of the space-local component of the forcing field f_x^{L} against the x coordinate at the edge of the computational domain, $y = z = -\pi$. Dark (light) colour denotes a small (large) value of R in $0 \leq R \leq 2L_f$. The black dashed line represents the original f_x profile. (b) "Energy" of the space-local forcing field $\left\langle\left(\boldsymbol{f}^{\mathrm{L}}\right)^2\right\rangle/2$ as a function of R/L_f. The black dashed line represents the one of the original forcing field $\left\langle\boldsymbol{f}^2\right\rangle/2$.

can be computed as,

$$\begin{aligned}
B(kR) &= \int B(\boldsymbol{r}; R)\mathrm{e}^{-\mathrm{i}\boldsymbol{k}\cdot\boldsymbol{r}}\,\mathrm{d}\boldsymbol{r} && (4.11)\\
&= \left(\frac{3}{4\pi R^3}\right) \times \int_0^R \mathrm{d}r \int_0^{2\pi} \mathrm{d}\phi \int_0^{\pi} \mathrm{d}\theta \exp(-\mathrm{i}kr\cos\theta) r^2 \sin\theta && (4.12)\\
&= \left(\frac{3}{4\pi R^3}\right) \times 2\pi \int_0^R \mathrm{d}r \int_{-1}^{1} \mathrm{d}\zeta \exp(\mathrm{i}kr\zeta) r^2 && (4.13)\\
&= \left(\frac{3}{4\pi R^3}\right) \times 4\pi \int_0^R \mathrm{d}r\, \frac{r}{k}\sin(kr) && (4.14)\\
&= \left(\frac{3}{4\pi R^3}\right) \times \frac{4\pi}{k^3} \int_0^{kR} \mathrm{d}(kr)\, kr\sin(kr) && (4.15)\\
&= \left(\frac{3}{4\pi R^3}\right) \times 4\pi R^3 \frac{\sin(kR) - kR\cos(kR)}{(kR)^3} && (4.16)\\
&= 3\frac{\sin(kR) - kR\cos(kR)}{(kR)^3}. && (4.17)
\end{aligned}$$

From (4.11) to (4.12), we can choose arbitrary expression for $\boldsymbol{k}$ so that we set $\boldsymbol{k} = (0, 0, k)$. From (4.12) to (4.13), we exchange the variable by $\zeta = -\cos\theta$, then $\mathrm{d}\zeta = \sin\theta\,\mathrm{d}\theta$ and $\theta \in [0, \pi] \to \zeta \in [-1, 1]$. From (4.13) to (4.14), we rewrite using $\sin\theta = \mathrm{i}\left(\mathrm{e}^{-\mathrm{i}\theta} - \mathrm{e}^{\mathrm{i}\theta}\right)/2$. We change the variable from r to kr in (4.15). This integral is solved as $\int_0^X \mathrm{d}x\, x\sin x = \sin X - X\cos X$.
Thus, we obtain the following Fourier-space expression of the space-local velocity field

$$\begin{cases}
\boldsymbol{u}^{\mathrm{L}}(\boldsymbol{k}) \equiv \left[1 - B(kR)\right]\boldsymbol{u}(\boldsymbol{k}), & (4.18)\\
B(kR) = \dfrac{3\left[\sin(kR) - (kR)\cos(kR)\right]}{(kR)^3}, & (4.19)
\end{cases}$$

where $\boldsymbol{u}(\boldsymbol{k})$ denotes the Fourier transform of $\boldsymbol{u}(\boldsymbol{x})$, with $\boldsymbol{k}$ the wavevector and $k = |\boldsymbol{k}|$.

Figure 4.5 shows the validation of the space-local function using the space-local forcing field,

$$f_i^{\mathrm{L}}(\boldsymbol{x};R) = \frac{1}{2\pi}\int \left[1 - B(kR)\right] f_i(\boldsymbol{k})\mathrm{e}^{\mathrm{i}\boldsymbol{k}\cdot\boldsymbol{x}}\,\mathrm{d}\boldsymbol{k}\,, \tag{4.20}$$

with the filter function (4.19). Figure 4.5(a) shows the profile of $f_x^{\mathrm{L}}(\boldsymbol{x};R)$ in x coordinate at the edge of the computational domain, $y = z = -\pi$. The colour gradient from dark to light corresponds to $0 \leq R \leq 2L_f$. At $R = 0$, the profile is zero everywhere, $f_x^{\mathrm{L}}(x;0) = 0$. By increasing R, it converges to the original profile $\lim_{R\to\infty} f_x^{\mathrm{L}}(x;R) = f_x(x)$. However, we note that the convergence is not monotonous as we observe overshoot in the intermediate R values. This property is also depicted in Fig. 4.5(b) with the “energy” of the space-local forcing field $\left\langle \left(\boldsymbol{f}^{\mathrm{L}}\right)^2 \right\rangle/2$ against R. We observe overshoot and eventual convergence to the energy of the original forcing field, $\left\langle \boldsymbol{f}^2 \right\rangle/2$.

4.2.3 Physical-space nonlocality of the pressure field

Here, we consider the physical-space nonlocality associated with the pressure field. Indeed, the solution of the Poisson equation (4.4) contains a spatial integral. When we restrict the integral range, as we have done for the Biot–Savart law between vorticity and velocity fields (4.7), how different are these two fields: space-local pressure field and space-local velocity field? Regarding this problem, it is important to note that the role of the pressure gradient term is to sustain the incompressibility of the fluid. Indeed, the Poisson equation represents the velocity redistribution on the same scale $|\boldsymbol{k}|$ in Fourier space. Thus, it does not directly contribute to the nonlinear interactions involving multiple scales. However, it is possible that the space-local pressure field indirectly affects the nonlinearity or the energy cascade. Theoretical and numerical quantification of its role, including the comparison with a similar analysis through the pressure Hessian (Chevillard, Lévêque, et al. 2011), would constitute an important subject of future research interest.

4.3 Space locality in turbulence spectra

In this section, we investigate the physical-space locality of Navier–Stokes turbulence using Fourier spectra. In § 4.3.1, we address the DNS configurations. In § 4.3.2, we apply the space-local filter, introduced in § 4.2, to re-define space-local contributions of various spectra in Fourier space.

4.3.1 Direct numerical simulation with the three-dimensional Taylor–Green forcing

We conduct DNS of the space-local Navier–Stokes equations (5.2) in a triply periodic cube of size 2π. Throughout this part of the thesis, we report the result of the three-dimensional Taylor–Green forcing

$$\boldsymbol{f} = \begin{pmatrix} -f_0 \sin x \cos y \cos z \\ +f_0 \cos x \sin y \cos z \\ 0 \end{pmatrix}, \tag{4.21}$$

with the forcing coefficient $f_0 = 1$. Figure 4.6(a) visualizes positive and negative isosurfaces of the x-component of the forcing field (4.21). It consists of large-scale spherical objects, which correspond to the vortical structures in the steady flow at low Reynolds numbers as well as the largest vortices in turbulence at high Reynolds numbers. We define the characteristic length scale

$$L_f \equiv 2\pi/\left|\boldsymbol{k}_f\right| = 2\pi/\sqrt{3} \tag{4.22}$$

and the characteristic time scale

$$T_f = 1/\sqrt{\left|\boldsymbol{k}_f\right| f_0} = 1/\sqrt[4]{3} \tag{4.23}$$

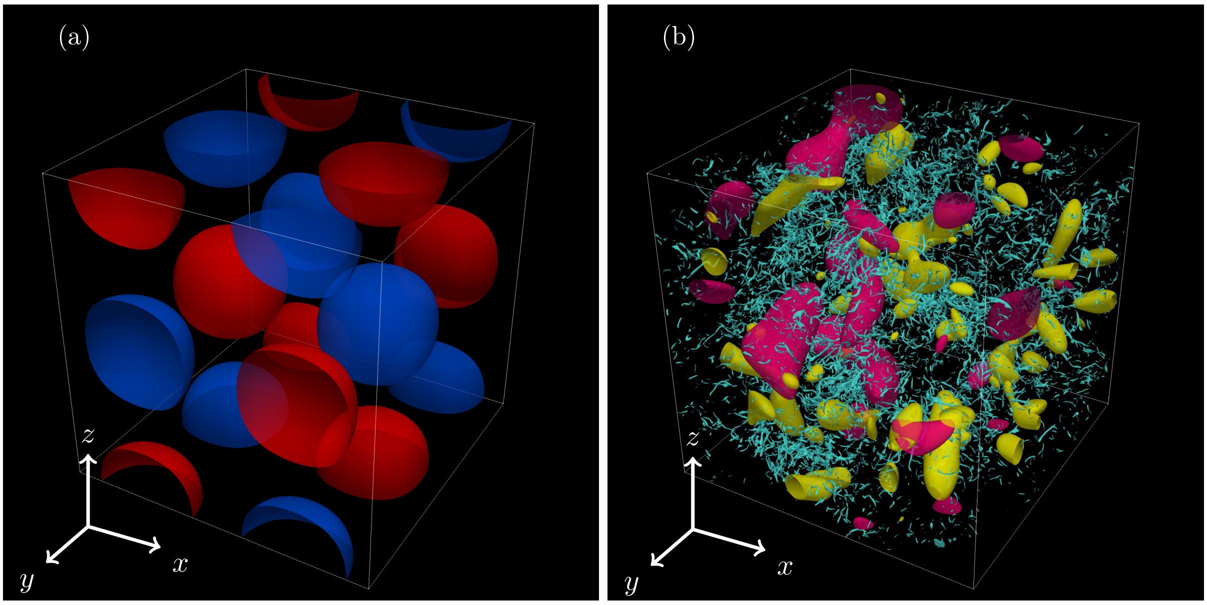

Figure 4.6: (a) Positive (red) and negative (blue) isosurfaces of x-component of the forcing field, $f_x = \pm 0.5$. See (4.21) for the definition. (b) An instantaneous snapshot of vortical structures. Isosurfaces of vorticity magnitude in low-pass filtered $\left|\boldsymbol{\omega}^{<}\right| = 4$ for $k \leq 3$ (red), band-pass filtered $\left|\boldsymbol{\omega}^{\lessgtr}\right| = 6$ for $3 < k \leq 6$ (yellow), and original $|\boldsymbol{\omega}| = 100$ (blue) are shown. Low-pass and band-pass filtering are applied in the Fourier-space velocity field.

N	ν	u'	λ	ϵ	$k_{\max}\eta$	Re_λ	T_{total}/T_f
512	6×10^{-4}	0.783	0.113	0.433	1.14	147	81.6

Table 4.1: DNS setting and statistical quantities of the DNS of the original Navier–Stokes equations. The parameters are the resolution of computational domain N and kinematic viscosity ν. The statistical quantities are evaluated by time average of: the fluctuating isotropic RMS velocity $u'(t) \equiv \sqrt{2K'(t)/3}$, which is defined by the fluctuating energy $K'(t) \equiv \left\langle u_i' u_i' \right\rangle /2$ where $\langle \cdot \rangle$ denotes the spatial average and $u_i'(\boldsymbol{x}, t)$ denotes the temporal fluctuating velocity field; the Taylor microscale $\lambda(t) \equiv u'(t)\sqrt{15\nu/\epsilon(t)}$ where the energy dissipation rate is evaluated by $\epsilon(t) = \nu \langle \omega_i \omega_i \rangle$; the Taylor-length Reynolds number $\mathrm{Re}_\lambda(t) \equiv u'(t)\lambda(t)/\nu$; the simulation time in the statistically steady state T_{total} as a function of T_f.

of the forcing, respectively, where the forced wave vector is $\boldsymbol{k}_f \equiv (\pm 1, \pm 1, \pm 1)^{\mathsf{T}}$.

Table 4.1 summarizes the DNS setting and the statistical quantities, and Fig. 4.6(b) shows the vortical structures in a snapshot of developed turbulence generated by the original Navier–Stokes equations. The observations are consistent with higher Reynolds number turbulence visualizations presented, for example, in Goto, Saito, et al. (2017).

Figure 4.7 shows the time-averaged statistics of turbulent flow. Panel (a) shows the normalized energy spectrum $E(k)$ with the universal scaling $E(k) \propto k^{-5/3}$ for about an order of scale. Panel (b) shows the normalized Probability Distribution Function (PDF) of vorticity components. The figure indicates the small-scale isotropy of the flow, in agreement with the K41 theory discussed in § 1.2.2. Its wide tail represents the intermittency of the small scale of turbulence.

4.3.2 Spectra with the space-local restrictions

In Fig. 4.8(a), we plot the space-local nonlinear energy transfer

$$T^{\mathrm{L}}(k) \equiv \int N_i^{\mathrm{L}}(\boldsymbol{k}) u_i^*(\boldsymbol{k}) \,\mathrm{d}\Omega_k \,, \tag{4.24}$$

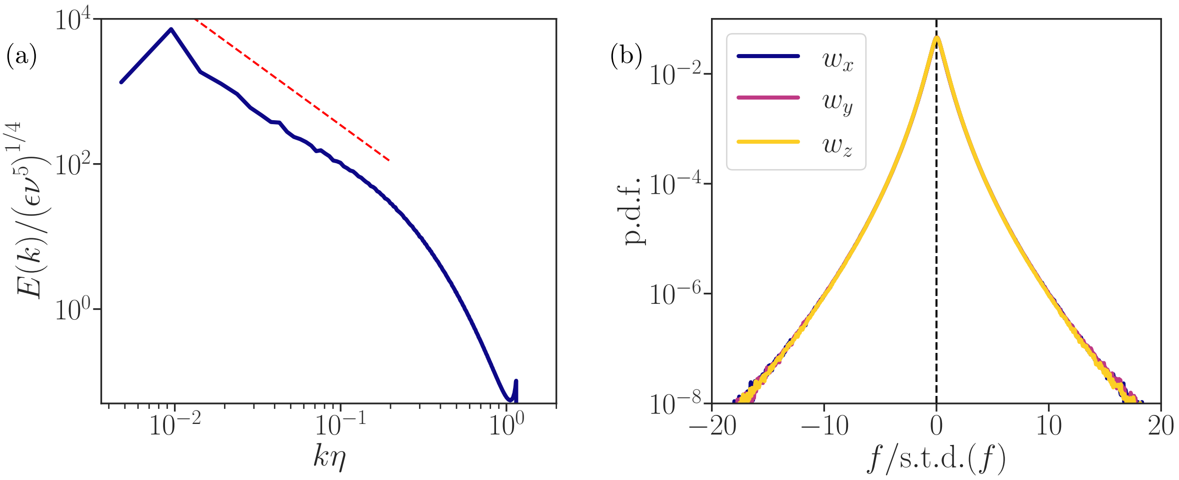

Figure 4.7: Time-averaged statistics of the turbulent flow. (a) Normalized energy spectrum $E(k)$ with the $-5/3$ scaling denoted by the red dashed line. (b) Normalized Probability Distribution Function (PDF) of vorticity components $(\omega_x, \omega_y, \omega_z)$.

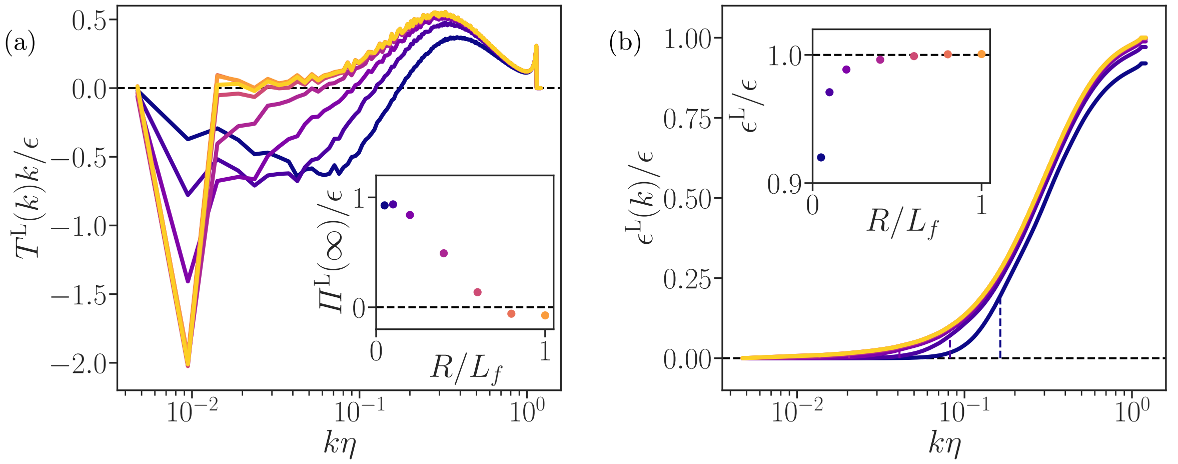

Figure 4.8: (a) Space-local energy transfer spectrum $T^{\mathrm{L}}(k)$ and (b) space-local cumulative energy dissipation spectrum $\epsilon^{\mathrm{L}}(k)$ evaluated in the post-process analysis. For both panels, Dark (light) colour represents small (large) R. The lightest colour represents the spectrum of the original Navier–Stokes turbulence. Both panels are normalised by ϵ. The horizontal axis is normalised by the Kolmogorov length scale η. Vertical dashed lines denote $2\pi/R$ corresponding to the length scale of the radius of the space-local domain. In the inset, the integrals of (a) $\Pi^{\mathrm{L}}(\infty) = -\int_0^\infty T^{\mathrm{L}}(k)\,\mathrm{d}k$ and (b) $\epsilon^{\mathrm{L}} \equiv 2\nu\int_0^\infty k^2 E^{\mathrm{L}}(k)\,\mathrm{d}k$ are plotted against the normalized space-local domain radius R/L_f. Both integrals are normalised by ϵ. The marker colour in the inset matches the curves in the main plot. Note that the original Navier–Stokes turbulence is not shown in the inset since it corresponds to $R = \infty$. They take (a) $\Pi(\infty)/\epsilon = 0$ and (b) $\epsilon/\epsilon = 1$, respectively.

with the space-local nonlinear term,

$$\boldsymbol{N}^{\mathrm{L}}(\boldsymbol{x}) \equiv -\boldsymbol{\omega}(\boldsymbol{x}) \times \boldsymbol{u}^{\mathrm{L}}(\boldsymbol{x}). \tag{4.25}$$

Note that we add the superscript $\cdot^{\mathrm{L}}$ to distinguish the quantity responsible for the space-local contributions of the original governing equation. One immediate finding is a collapse in the small scale, indicating that the small-scale transfer is not affected by the space-local cutoff. On the contrary, there is a strong R dependency on the larger scale. In particular, the large negative regime is different from the original turbulence data, which exhibits a plateau at zero (corresponding to the inertial range) in the same regime. By increasing R, $T^{\mathrm{L}}(k)$ collapses on the original energy transfer spectrum $T(k)$. These observations are consistent with the rough correspondence between large (small) wavenumber and small (large) physical-space scale. By integrating $T^{\mathrm{L}}(k)$, one can evaluate the space-local energy flux $\Pi^{\mathrm{L}}(k) \equiv -\int_0^k T^{\mathrm{L}}(p)\,\mathrm{d}p$. In the original turbulence, the energy transfer is summed up to zero, thus $\Pi(\infty) \equiv \int_0^\infty T(k)\,\mathrm{d}k = 0$. However, the space-local transfer is not a conserved quantity: $\Pi^{\mathrm{L}}(\infty) \equiv \int_0^\infty T^{\mathrm{L}}(k)\,\mathrm{d}k \neq 0$. This is evident in inset of Fig. 4.8(a), which plots $\Pi^{\mathrm{L}}(\infty)/\epsilon$. This quantity approaches unity for small values of R, indicating that almost no energy is transferred by $T^{\mathrm{L}}(k)$. The convergence property $\Pi^{\mathrm{L}}(\infty)/\epsilon \to 0$ as $R \nearrow$ is consistent with the property of the original Navier–Stokes turbulence. Another finding from Fig. 4.8(a) is a trend on the zero-crossing wavenumber $k_0(R)$, defined by $T^{\mathrm{L}}(k_0) = 0$. Since $k_0(R)$ corresponds to the peak of $\Pi^{\mathrm{L}}(k)$, a decreasing trend of $k_0(R)$ indicates that the space-local constraint inhibits the large-scale transfer and flux. Note that the overshoot in $T^{\mathrm{L}}(k)$ against $T(k)$ at large values of R is due to the convergence property of the space-local filter. Overall, the space-local contributions of the energy transfer $T^{\mathrm{L}}(k)$ exhibit a qualitatively different profile against the one in the space-local turbulence $T(k)$, in particular at the large scales $k_f < k < 2\pi/R$. This observation indicates that the space-local system (see next chapter) and the space-local contributions of the original system are not identical.

In Fig. 4.8(b), we plot the space-local energy dissipation rate spectrum

$$\epsilon^{\mathrm{L}}(k) \equiv 2\nu \int_0^k p^2 E^{\mathrm{L}}(p)\,\mathrm{d}p\,. \tag{4.26}$$

Note that its integral defines the space-local contributions of the energy dissipation rate $\epsilon^{\mathrm{L}} \equiv 2\nu \int_0^\infty k^2 E^{\mathrm{L}}(k)\,\mathrm{d}k$. We observe similar properties as in Fig. 4.8(a); while the small-scale profile is preserved, the large-scale profile is affected by R. However, since the small scale primarily defines the energy dissipation rate thanks to the k^2 coefficient, the R dependency on $\epsilon^{\mathrm{L}}(R)$ is small compared to $\Pi^{\mathrm{L}}(R)$, as shown in the inset of Fig. 4.8(b). Thus, we can conclude that energy dissipation is a spatially local phenomenon.

4.4 Concluding remarks

The research question posed in this Part II is the physical-space locality of turbulence, which has not been focused on compared to the locality in scale. In this chapter, we reviewed the physical-space locality of turbulence in the literature (§ 4.1), and we defined the space-local velocity field (§ 4.2) to analyse the turbulence dataset (§ 4.3). Here, the space-local velocity (4.7) is defined by the truncated Biot–Savart law and interpreted as "locally induced velocity by the neighbouring vorticity field".

The main results, summarised in Fig. 4.8, are consistent with our intuition that the space-local structures correspond to small-scale structures. We find that the space-local filter strongly alters the energy transfer rate at large scales. Contrarily, transfer at the small scales and the energy dissipation, dominated by the smallest scales of the flow, remains almost unaltered under the filtering.

Here, we note that the analysis conducted in this chapter examines the space-local contributions in the turbulence dataset. In the next chapter, we will work on the same research question from an alternative point of view. We will modify the governing equations in a space-local sense to see how the *space-local* turbulence driven by such a system behave differently against the *original* turbulence we investigated in this chapter.

5 Space-local Navier–Stokes Turbulence

This chapter analyses the modified Navier–Stokes equations, in which the nonlinear term is restricted in the space-local sense. The content is based on the following:

> Araki, Ryo, Wouter J. T. Bos, and Susumu Goto (2023b). Space-local Navier–Stokes turbulence. *arXiv preprint*. arXiv: `2308.07255 [flu-dyn]`.

In § 5.1, we define a new system called space-local Navier–Stokes equations, in which the nonlinear interactions are restricted locally in physical space. We also discuss some basic properties of the new system, which may differ from the original Navier–Stokes equations. In § 5.2, we review details of direct numerical simulation of the space-local system. In particular, we focus on its temporal dynamics. In § 5.3 and § 5.4, we investigate statistics of the space-local system. We focus on two different scaling regimes, observed in scales larger (§ 5.3) and smaller (§ 5.4) than the space-local filter size, respectively. We conclude this chapter in § 5.5.

5.1 Space-local Navier–Stokes equations

Using the space-local velocity field (4.7–4.19), we here define the modified Navier–Stokes equations with restricted nonlinearity in the space-local sense. The space-local vorticity equation becomes

$$\frac{\partial \boldsymbol{\omega}}{\partial t} + \boldsymbol{u}^{\mathrm{L}} \cdot \boldsymbol{\nabla} \boldsymbol{\omega} = \boldsymbol{\omega} \cdot \boldsymbol{\nabla} \boldsymbol{u}^{\mathrm{L}} + \nu \nabla^2 \boldsymbol{\omega} + \boldsymbol{\nabla} \times \boldsymbol{f}, \tag{5.1}$$

where the velocity $\boldsymbol{u}$ in the nonlinear terms is substituted by the space-local one $\boldsymbol{u}^{\mathrm{L}}$. This equation is space-locally closed, as the evolution of $\boldsymbol{\omega}$ at point $\boldsymbol{x}$ is described by $\boldsymbol{u}^{\mathrm{L}}$, locally determined in the sphere of radius R centered at $\boldsymbol{x}$.

We here examine the basic properties of (5.1). First, we remark that the space-local system remains incompressible; namely, $\boldsymbol{\nabla} \cdot \boldsymbol{u} = 0$. Here, $\boldsymbol{u}$ is governed by the space-local Navier–Stokes equations

$$\frac{\partial \boldsymbol{u}}{\partial t} = -\boldsymbol{\omega} \times \boldsymbol{u}^{\mathrm{L}} - \boldsymbol{\nabla}\left(p + \frac{\boldsymbol{u}^2}{2}\right) + \nu \nabla^2 \boldsymbol{u} + \boldsymbol{f}, \tag{5.2}$$

corresponding to (5.1). The incompressibility of $\boldsymbol{u}$ immediately follows from that of the space-local velocity field,

$$\boldsymbol{\nabla} \cdot \boldsymbol{u}^{\mathrm{L}} = 0 \quad \leftrightarrow \quad \mathrm{i} k_j u_j^{\mathrm{L}} = \mathrm{i}\big[1 - B(kR)\big] k_j u_j = 0. \tag{5.3}$$

Second, the space-local system violates the Galilean invariance of the original Navier–Stokes equations. It follows from the property of the space-local filter function (4.19):

$$\lim_{k \searrow 0} \big[1 - B(kR)\big] = 0, \tag{5.4}$$

stating that the $k = 0$ mode flow is purely nonlocal and is eliminated by filtering.

Third, by taking the inner product of (5.2) and $\boldsymbol{u}$ and integrating over space, we obtain the energy equation,

$$\frac{\mathrm{d}E}{\mathrm{d}t} = P - \epsilon^{\mathrm{NL}} - \epsilon, \tag{5.5}$$

where

$$E \equiv \frac{1}{2}\int \mathrm{d}\boldsymbol{x}\, \boldsymbol{u}^2, \quad P \equiv \int \mathrm{d}\boldsymbol{x}\, \boldsymbol{f}\cdot\boldsymbol{u}, \quad \epsilon \equiv \nu \int \mathrm{d}\boldsymbol{x}\, (\boldsymbol{\nabla}\boldsymbol{u})^2, \tag{5.6}$$

and

$$\epsilon^{\mathrm{NL}} \equiv \int \mathrm{d}\boldsymbol{x}\, \left[\boldsymbol{\omega} \times \boldsymbol{u}^{\mathrm{L}}\right]\cdot\boldsymbol{u}. \tag{5.7}$$

The additional term ϵ^{NL} is associated with the spatially nonlocal contributions of the nonlinear term. It disappears in the $R \nearrow \infty$ limit, since

$$\lim_{R\nearrow\infty} \epsilon^{\mathrm{NL}} = \int \mathrm{d}\boldsymbol{x}\, [\boldsymbol{\omega}\times\boldsymbol{u}]\cdot\boldsymbol{u} = 0. \tag{5.8}$$

See § 4.2.3 for physical-space locality of pressure gradient term in the Navier–Stokes equations and how it relates to the space-local velocity field.

5.2 Direct numerical simulation of the space-local Navier–Stokes equations

In this section, we address details of the DNS of the space-local Navier–Stokes equations. In § 5.2.1, we provide the implementation of the space-local nonlinear term. In § 5.2.2, we report the temporal evolution of the space-local system.

5.2.1 Numerical evaluation of the space-local nonlinear term

Here, we address the numerical implementation of the space-local nonlinear term. The space-local vorticity equation reads, without forcing and damping,

$$\frac{\partial\boldsymbol{\omega}(\boldsymbol{x})}{\partial t} = -\boldsymbol{\nabla}\times\left(\boldsymbol{\omega}\times\boldsymbol{u}^{\mathrm{L}}\right)(\boldsymbol{x}), \tag{5.9}$$

and its Fourier transform is

$$\frac{\partial\boldsymbol{\omega}(\boldsymbol{k})}{\partial t} = -\mathrm{i}\boldsymbol{k}\times\left(\boldsymbol{\omega}\times\boldsymbol{u}^{\mathrm{L}}\right)(\boldsymbol{k}). \tag{5.10}$$

We can retrieve the Euler equations by uncurling (5.10) as,

$$\begin{aligned}\frac{\partial\boldsymbol{u}}{\partial t} &= -\frac{\mathrm{i}\boldsymbol{k}}{k^2}\times\left[\mathrm{i}\boldsymbol{k}\times\left(\boldsymbol{\omega}\times\boldsymbol{u}^{\mathrm{L}}\right)\right], &(5.11)\\ &= -P_{ij}\left(\boldsymbol{\omega}\times\boldsymbol{u}^{\mathrm{L}}\right)_j, &(5.12)\end{aligned}$$

where $P_{ij} = \delta_{ij} - k_i k_j/k^2$. Using this formulation, the space-local nonlinear term in the Fourier domain can be computed using standard pseudo-spectral procedures.

5.2.2 Temporal evolution of space-local Navier–Stokes turbulence

We conduct DNS of the space-local nonlinear term by taking advantage of the Fourier expression of the space-local Navier–Stokes equations. See § 4.3.1 for details of the DNS configurations. We first conduct a DNS of developed turbulent flow governed by the original Navier–Stokes equations. Then, we launch the DNS of flow governed by the space-local Navier–Stokes equations from a snapshot of this developed turbulent flow.

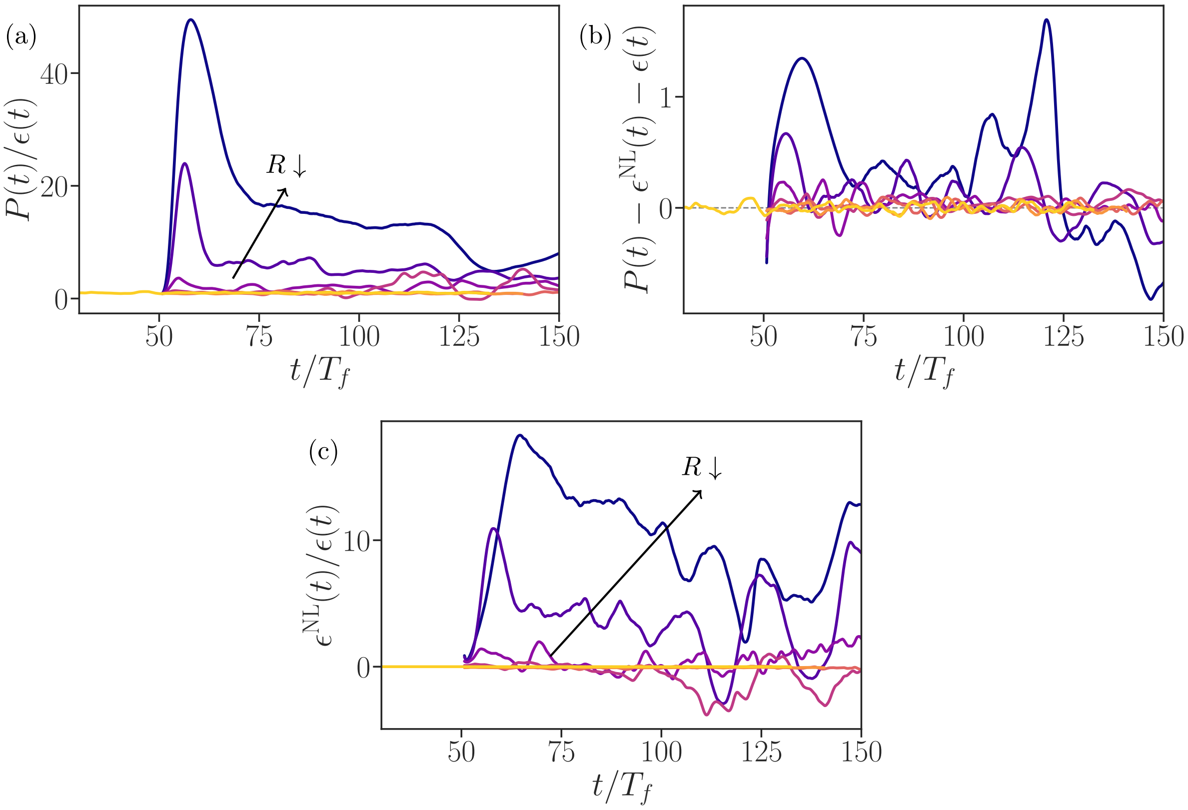

Figure 5.1: Time series of (a) energy input rate $P(t)$, (b) RHS of the energy equation (5.5), and (c) spatially nonlocal nonlinear contributions $\epsilon^{\mathrm{NL}}(t)$ of space-local Navier–Stokes turbulence at different values of R. For all panels, time is normalized by T_f: the characteristic timescale of the forcing (4.23). For panels (a) and (c), both quantities are normalised by the energy dissipation rate $\epsilon(t)$. The horizontal grey dashed line in panel (b) denotes $y = 0$. See the caption of Fig. 5.4 for the parameter list for R corresponding to each curve with a different colour.

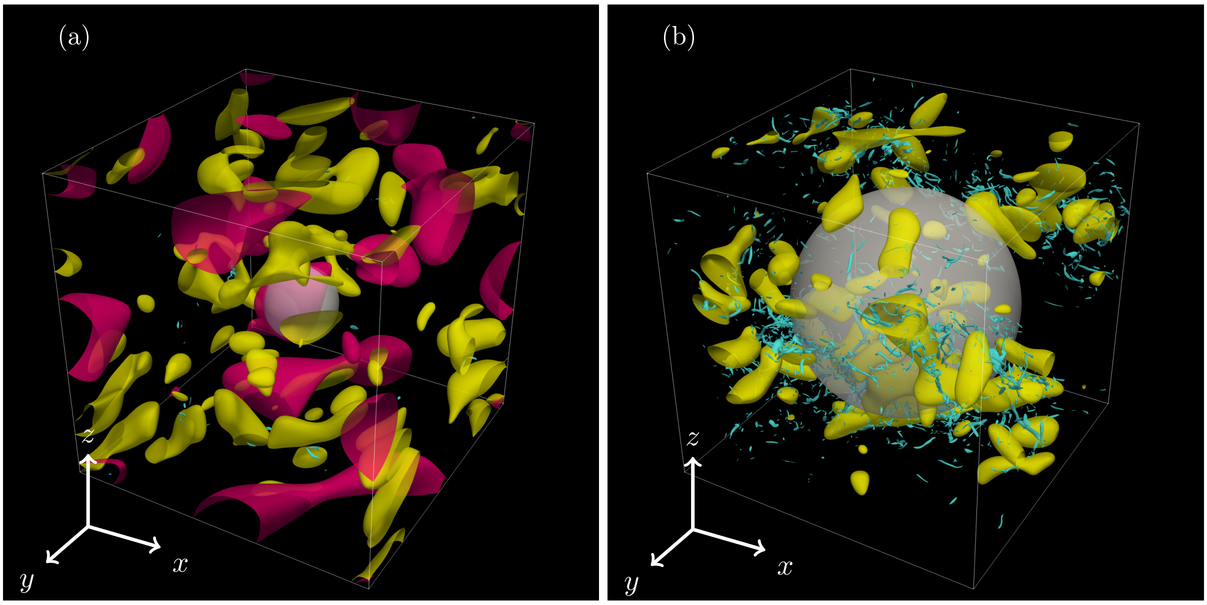

Figure 5.2: Snapshots of vortical structures in space-local Navier–Stokes turbulence at (a) $R = 0.2L_f$ and (b) $R = 0.6L_f$, respectively. Isosurfaces of the magnitude of low-pass filtered vorticity $\left|\boldsymbol{\omega}^{<}\right| = 8$ (red), band-pass filtered one $\left|\boldsymbol{\omega}^{\lessgtr}\right| = 3$ (yellow), and unfiltered one $|\boldsymbol{\omega}| = 50$ (blue) are shown. See the caption of Fig. 4.6(b) for the filtering wavenumber ranges. Note that we employ smaller thresholds compared to the visualization of the original turbulent flow in Fig. 4.6(b), but they are common in the panels (a) and (b) of this figure. The grey spherical domain illustrates the size of the locality parameter R at the centre of the computational domain.

Figure 5.1(a) shows the time series of $P(t)/\epsilon(t)$, the ratio between input and dissipation rates of energy. By switching the governing equation from original to space-local Navier–Stokes equations, the energy input rate surpasses the energy dissipation rate due to the weakened nonlinearity and energy cascade. This transient regime appears as a peak in the time series. We observe a higher peak for flows with smaller values of R because the nonlinearity is more suppressed for small R.

After the transient stage, the flow reaches a state where $P(t)/\epsilon(t)$ seems to fluctuate around a constant value which depends on R. It therefore differs from a statistically steady state of the original Navier–Stokes turbulence, as there is no statistical balance between the injection and the dissipation of energy: $\left\langle P(t)\right\rangle_t \neq \left\langle \epsilon(t)\right\rangle_t$. Here, $\langle\cdot\rangle_t$ denotes the time average. In Fig. 5.1(b), we plot $P(t) - \epsilon^{\mathrm{NL}}(t) - \epsilon(t)$, i.e. the RHS of the energy equation (5.5), to assess the temporal evolution of the space-local Navier–Stokes turbulence. For the original Navier–Stokes turbulence, we observe $\left\langle P(t) - \epsilon^{\mathrm{NL}}(t) - \epsilon(t)\right\rangle_t = 0$ with $\epsilon^{\mathrm{NL}} = 0$ (5.8). When the value of R is finite, we still observe fluctuations around zero after the initial transient regime depicted in Fig. 5.1(a). This observation indicates that the space-local Navier–Stokes turbulence eventually establishes the statistically steady state, as the three terms on the RHS of the energy equation (5.5) attain a statistical balance and thus $\left\langle \mathrm{d}E(t)/\mathrm{d}t\right\rangle_t = 0$.

We note that for the smallest value of $R/L_f = 0.1$, we observe a large fluctuation amplitude indicating a significant instantaneous imbalance between the three terms. However, since there are both positive and negative values, we speculate that there is a statistical balance in the long enough time series. Unfortunately, due to the energy accumulation at large scales, long enough computation to evaluate the statistical convergence is beyond our computational capacity.

Figure 5.1(c) plots the time series of $\epsilon^{\mathrm{NL}}(t)$, illustrating that $\epsilon^{\mathrm{NL}} \to 0$ for $R \nearrow \infty$ as discussed in (5.8) of § 5.1. Note that $\epsilon^{\mathrm{NL}}(t)$ does not always act as an alternative energy dissipation as it can be negative.

Figure 5.2 shows the vortical structures in space-local Navier–Stokes turbulence at $R = 0.2L_f$ and $R = 0.6L_f$. By comparing them with the original Navier–Stokes turbulence in Fig. 4.6(b), we can see that the space-local turbulence has much less fine-scale structures (in blue), even though smaller thresholds are employed for the visualization. It supports our finding that the nonlinear interactions and energy cascade are weakened due to the space-local restrictions in the nonlinear term.

Next, we compare the two panels of Fig. 5.2 with the same isosurface thresholds. For $R = 0.2L_f$ in

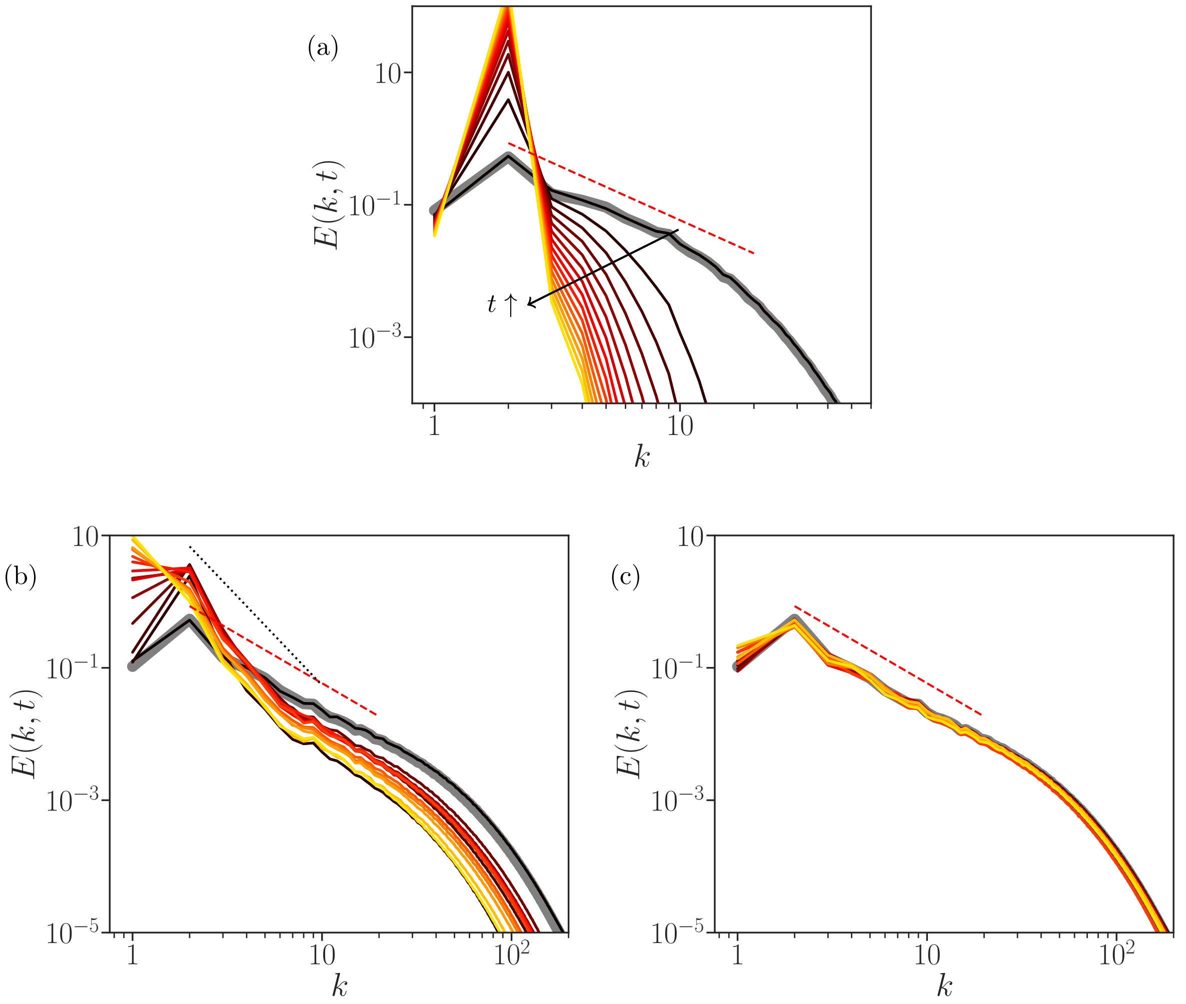

Figure 5.3: Time evolution of energy spectrum $E(k,t;R)$ in the space-local system at different values of R: (a) $R=0$, (b) $R=0.2L_f$, and (c) $R=L_f$. Time evolves from dark to light colours with an interval of $5T$. The thick grey line represents the time-averaged energy spectrum of the original Navier–Stokes turbulence. The red dashed and black dotted lines denote the $k^{-5/3}$ and k^{-3} scalings, respectively. Panel (a) employs the data from 128^3 box simulation while the other panels (b-c) show 512^3 box data.

panel (a), there are distinctive large-scale structures (in red and yellow), while the small-scale structures (in blue) are barely visible. This indicates that more energy remains at these large-scale structures because less energy cascades towards scales smaller than R. For $R=0.6L_f$ in panel (b), we do not observe the strong large-scale structures (in red), whereas the small-scale structures are more active. This is also consistent with the picture that less energy is retained at large scales as the energy cascade becomes more efficient for larger R because the space-local restrictions become less significant. More quantitative arguments are developed in terms of the energy spectrum shown in Fig. 5.4.

Figure 5.3 shows the temporal evolution of the energy spectrum at three different values of R.

First, panel (a) shows the flow at $R=0$, which means that the nonlinear term is zero. Note that this result is obtained in 128^3 box. Thus, the flow exhibits no nonlinear interactions. The flow rapidly loses its energy in $k\neq k_f$ while the energy is accumulated at $k=k_f$. The energy spectrum eventually becomes like the delta function.

Second, the panel (b) shows the result at $R=0.2L_f$. At first, energy accumulates at $k=k_f$, and the small scales ($k\gg k_f$) become less energetic. These changes are due to the sudden reduction of the energy cascade. Another interesting observation is an eventual accumulation of energy in scales larger than the forcing ($k<k_f$), suggesting a possible inverse energy cascade. However, since a further analysis of this property requires a sufficient scale separation between the system size and the forcing scale, we focus

on the smaller-scale ($k > k_f$) scaling regime, which seems to consist of three ranges: a range with the energy spectrum with a power law steeper than $k^{-5/3}$, an $E(k) \propto k^{-5/3}$ scaling range associated with the Kolmogorov similarity, and a dissipation range.

Third, the panel (c) shows the $R = L_f$ result. The flow exhibits almost equivalent statistics against the original turbulence, although we observe a slight energy accumulation in $k < k_f$. We discuss the full statistical recovery and assimilation of the phase-space orbit as future perspectives in Chap. 5.5.

5.3 Space-local nonlinear interactions and robust Kolmogorov's 1941 scaling

In the remainder of this chapter, we focus on the small-scale ($k > k_f$) scaling, which seems to consist of three regions: a range with scaling steeper than $k^{-5/3}$, a $k^{-5/3}$ scaling range associated with the Kolmogorov theory, and a dissipation range. See § 5.2.2 for more DNS details, including the time series and visualization. For the remainder of this chapter, we focus on the first two scaling regimes for $k > k_f$.

To investigate the R-dependence of these regimes, we plot the instantaneous energy spectrum at different values of R in Fig. 5.4. The flows are evaluated after the transient when the energy cascade adapts to the truncation of the nonlinear interactions. We use the same snapshots in the remainder of this chapter. In Fig. 5.4, the spectra are normalized by the high-pass filtered energy dissipation rate

$$\epsilon^{>} \equiv 2\nu \int_{2\pi/R}^{\infty} k^2 E(k) \, \mathrm{d}k \,, \tag{5.13}$$

for which we remove the contributions from the *direct* energy dissipation in wavenumber range $k < 2\pi/R$ without energy cascade. Accordingly, the modified Kolmogorov length

$$\eta^{>} \equiv \left(\nu^3/\epsilon^{>}\right)^{1/4} \tag{5.14}$$

is used to normalize the wavenumber.

In the small scales $2\pi/R \ll k$, the normalized energy spectra collapse onto the Kolmogorov spectrum. We also observe that $E(k) \propto k^{-5/3}$ law in $2\pi/R \ll k \ll k_{\eta^{>}} (= 2\pi/\eta^{>})$ is robust. Here, $2\pi/R$ is the wavenumber corresponding to the space-local domain of radius R. This result indicates that the system with only spatially local nonlinear interactions (parametrized by R) can sustain energy cascade in scales smaller than R.

We stress the nontriviality of this result; the space-local structures in physical space within a sphere of radius R are not equivalent to the small-scale structures in Fourier space for $k \geq 2\pi/R$. Similarly, the space-local domain of radius R contains (partial) information of all the Fourier modes, not only $k \geq 2\pi/R$. Thus, there is no one-to-one correspondence between the space-local and the small-scale structures. Overall, Fig. 5.4 confirms that the observations are consistent with the original space-local assumption in Kolmogorov (1941a).

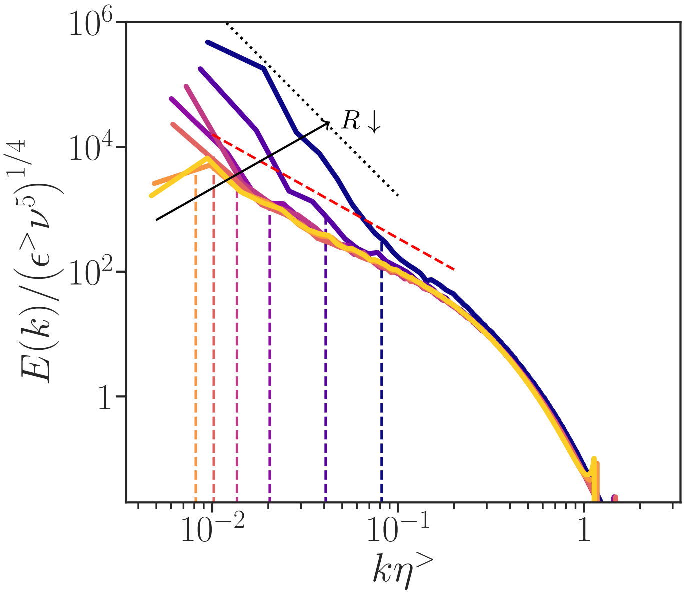

Figure 5.4: Normalized instantaneous energy spectrum $E(k)$ at different values of R. Normalization is performed by the energy dissipation rate $\epsilon^>$ and the Kolmogorov length scale $\eta^>$ (5.13) with high-pass filter. Vertical dashed lines denote $2\pi/R$ and normalized by $\eta \equiv (\nu^3/\epsilon)^{1/4}$ of the original turbulence. The dark (light) colour represents small (large) values of R: $R/L_f = 0.1$, 0.2, 0.4, 0.6, 0.8, 1, and the lightest colour represents the original turbulence. The red dashed and black dotted lines denote the $k^{-5/3}$ and k^{-3} scalings, respectively.

5.4 Space-local nonlinear interactions and enstrophy-conserving scaling

In this section, we investigate the enstrophy scaling to understand the alternative scaling observed in the large scales $k_f \ll k \ll 2\pi/R$ in Fig. 5.4. In § 5.4.1, we first discuss the enstrophy scaling in the Navier–Stokes turbulence. Then, in § 5.4.2, we investigate the enstrophy scaling in the space-local Navier–Stokes turbulence.

5.4.1 Enstrophy balance and its scaling

Here, we investigate the enstrophy balance scaling of the original Navier–Stokes turbulence in Fourier space. We begin with the enstrophy balance equation

$$\frac{\partial}{\partial t} k^2 E(k) = T_\omega(k) + S_\omega(k) - 2\nu k^4 E(k) + F_\omega(k), \tag{5.15}$$

where $k^2 E(k)$ denotes the enstrophy spectrum. There are two nonlinear terms, namely, the enstrophy production

$$S_\omega(k) = \int \big(\omega_j \partial_j u_i\big)(\boldsymbol{k}) \omega_i^*(\boldsymbol{k})\, \mathrm{d}\Omega_k \tag{5.16}$$

and the enstrophy transfer

$$T_\omega(k) = \int -\big(u_j \partial_j \omega_i\big)(\boldsymbol{k}) \omega_i^*(\boldsymbol{k})\, \mathrm{d}\Omega_k\,, \tag{5.17}$$

associated with the stretching and advection term in the vorticity equation (5.1), respectively. Here, $\cdot^*$ and $\int \mathrm{d}\Omega_k$ denote the complex conjugate and the integral over spherical shells of radius k, respectively. The third term on the RHS denotes the enstrophy dissipation, and the fourth term is the enstrophy

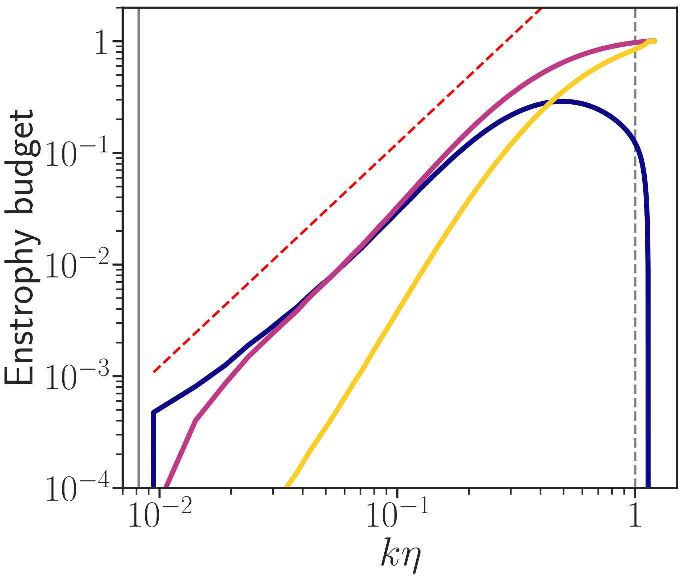

Figure 5.5: Three terms from the enstrophy budget equation (5.19): enstrophy flux $\Pi_\omega(k)$, cumulative enstrophy production $V_\omega^<(k)$, and cumulative enstrophy dissipation rate $\epsilon_\omega(k)$. Each spectrum and the wavenumber are normalized by the enstrophy dissipation rate $\epsilon_\omega^< = 2\nu \int_0^\infty k^4 E(k)\,\mathrm{d}k$ and the Kolmogorov length scale η, respectively. Vertical solid and dashed lines denote k_f and k_η, respectively.

injection

$$F_\omega(k) = \int \left(\epsilon_{ijk}\partial_j f_k\right)(\boldsymbol{k})\omega_i^*(\boldsymbol{k})\,\mathrm{d}\Omega_k\,. \tag{5.18}$$

The large-scale integral of (5.15) defines the enstrophy budget equation

$$\frac{\partial}{\partial t}\int_0^k p^2 E(p)\,\mathrm{d}p + \Pi_\omega(k) = V_\omega^<(k) - \epsilon_\omega^<(k) + \int_0^k F_\omega(p)\,\mathrm{d}p\,, \tag{5.19}$$

which is equivalent to (5.27). Figure 5.5 shows the three terms of (5.19): the cumulative enstrophy production

$$V_\omega^<(k) = \int_0^k S_\omega(p)\,\mathrm{d}p\,, \tag{5.20}$$

the enstrophy flux

$$\Pi_\omega(k) = -\int_0^k T_\omega(p)\,\mathrm{d}p\,, \tag{5.21}$$

and the cumulative enstrophy dissipation

$$\epsilon_\omega^<(k) = 2\nu\int_0^k p^4 E(p)\,\mathrm{d}p\,. \tag{5.22}$$

In the inertial range $k_f \ll k \ll k_\eta (= 2\pi/\eta)$, we observe a balanced scaling of

$$\Pi_\omega(k) = V_\omega^<(k) \propto k^2, \tag{5.23}$$

associated with the plateau in the energy flux $\Pi(k) \propto k^0$ (Davidson et al. 2008; Sadhukhan et al. 2019). Given that $T(k) \propto -\partial\Pi(k)/\partial k$, where $T(k)$ is the energy transfer, $V_\omega^<(k)$ and $\Pi_\omega(k)$ can be expressed as

$$-k^2\frac{\partial\Pi}{\partial k} = -\frac{\partial}{\partial k}\left[k^2\Pi(k)\right] + 2k\Pi(k) = T_\omega(k) + V_\omega^<(k). \tag{5.24}$$

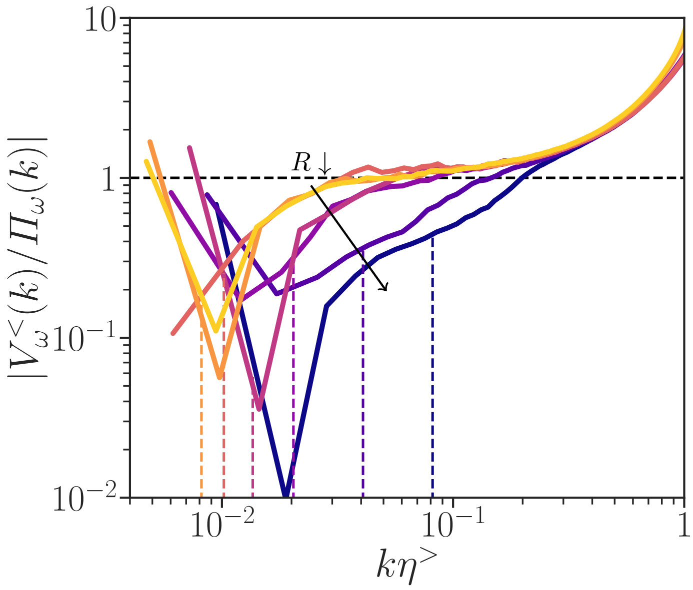

Figure 5.6: Ratio of cumulative enstrophy production $V_\omega^<(k)$ and enstrophy flux $\Pi_\omega(k)$. The horizontal dashed line denotes $V_\omega^<(k) = \Pi_\omega(k)$. The same colourmap and the vertical dashed lines are employed as in Fig. 5.4.

The inertial range of the enstrophy budget equation (5.19), shown in Fig. 5.5, can be understood as the scale-by-scale balance between the cumulative enstrophy production and enstrophy flux (5.23). Although no conservative enstrophy cascade exists, enstrophy is transferred from larger to smaller scales. More precisely, the enstrophy transferred to scale k from a larger scale is further transferred towards a smaller scale, along with the enstrophy generated at that scale.

In Fig. 5.6, we show the balance of $V_\omega^<(k)/\Pi_\omega(k)$ for both the original and space-local Navier–Stokes turbulence. For the latter, the enstrophy production and transfer are defined by

$$\begin{cases} S_\omega(k) = \displaystyle\int \left(\omega_j \partial_j u_i^{\mathrm{L}}\right)(\boldsymbol{k})\omega_i^*(\boldsymbol{k})\,\mathrm{d}\Omega_k\,, & (5.25)\\ T_\omega(k) = \displaystyle\int -\left(u_j^{\mathrm{L}} \partial_j \omega_i\right)(\boldsymbol{k})\omega_i^*(\boldsymbol{k})\,\mathrm{d}\Omega_k\,, & (5.26)\end{cases}$$

where $\boldsymbol{u}$ in (5.16) and (5.17) is substituted by $\boldsymbol{u}^{\mathrm{L}}$.

5.4.2 Enstrophy-conserving scaling in scales larger than the space-local filter size

To understand the steeper scaling of the spectrum in $k_f \ll k \ll 2\pi/R$, we investigate the enstrophy balance in space-local Navier–Stokes turbulence. We consider the large-scale enstrophy budget equation

$$\frac{\partial}{\partial t}\int_0^k p^2 E(p)\,\mathrm{d}p + \Pi_\omega(k) = V_\omega^<(k) - \epsilon_\omega^<(k) + \int_0^k F_\omega(p)\,\mathrm{d}p \tag{5.27}$$

of the Navier–Stokes equations. In three-dimensional isotropic turbulence, there is a balance between the cumulative enstrophy production $V_\omega^<(k)$ and the enstrophy flux $\Pi_\omega(k)$ in the inertial range (Davidson et al. 2008; Sadhukhan et al. 2019). These terms correspond to the vortex stretching and advection terms of the vorticity equation (5.1). For the definition, derivation, and scaling of (5.27), see § 5.4.1.

Figure 5.6 shows the ratio $V_\omega^<(k)/\Pi_\omega(k)$ between the cumulative enstrophy production rate $V_\omega^<(k)$ and the enstrophy flux $\Pi_\omega(k)$. These two terms are balanced in the inertial range of the unmodified Navier–Stokes turbulence (corresponding to the $R \nearrow \infty$ limit), and $V_\omega^<(k)/\Pi_\omega(k)$ should thus be unity. See also

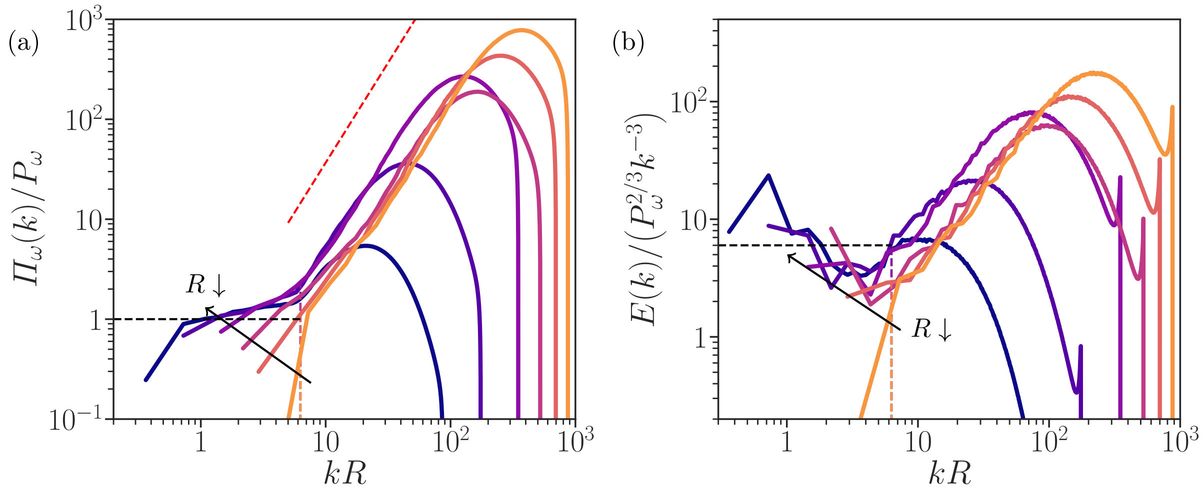

Figure 5.7: (a) Enstrophy flux $\Pi_\omega(k)$ normalized by the enstrophy input rate P_ω. The red dashed line denotes k^2 scaling. (b) Compensated energy spectrum $E(k)$ based on the scaling (5.32). For both panels, the wavenumber is normalized by R so that different $2\pi/R$ collapses onto $kR = 2\pi$. Note that the spectrum of the original turbulence is not shown, since it corresponds to the $R \nearrow \infty$ limit. The horizontal dashed line denotes a plateau. The same colourmap is employed as in Fig. 5.4.

Fig. 5.5. In space-local Navier–Stokes turbulence, the ratio becomes considerably smaller than unity for $k_f \ll k \ll 2\pi/R$ as $R \searrow 0$, which is, as we will argue now, associated with the suppression of enstrophy production.

We consider the global enstrophy production rate,

$$V_\omega = \left\langle \omega_i \frac{\partial u_i^{\mathrm{L}}(\boldsymbol{x})}{\partial x_j} \omega_j \right\rangle = \left\langle \omega_i \omega_j \frac{\partial}{\partial x_j} \mathcal{F}^{-1}\left[u_i^{\mathrm{L}}(\boldsymbol{k})\right] \right\rangle, \tag{5.28}$$

of space-local Navier–Stokes turbulence. Here, $\mathcal{F}^{-1}[\cdot]$ and $\langle\cdot\rangle$ denote the inverse Fourier transform and the spatial average, respectively. In the limit of $kR \ll 1$, a Taylor expansion of the space-local filter function (4.19) yields

$$1 - B(kR) \approx \frac{(kR)^2}{10} + \mathcal{O}\Big((kR)^3\Big). \tag{5.29}$$

Thus, in this limit, the total enstrophy production rate (5.28) scales as

$$V_\omega \approx \frac{R^2}{10} \left\langle \omega_i \omega_j \frac{\partial}{\partial x_j} \mathcal{F}^{-1}\left[k^2 u_i(\boldsymbol{k})\right] \right\rangle \quad \text{for} \quad kR \ll 1. \tag{5.30}$$

This relation states that the enstrophy production at a given scale k is weakened by decreasing the radius of the space-local domain R, and is consistent with Fig. 5.6.

From these numerical and theoretical observations, we conjecture that space-local Navier–Stokes turbulence is asymptotically equivalent to turbulence without vortex stretching (Bos 2021; Wu and Bos 2022) in the $kR \ll 1$ limit. This system has intermediate properties between two- and three-dimensional Navier–Stokes turbulence, as enstrophy and helicity are conserved in the inviscid limit. Note that the nonlinearity of the two-dimensional Navier–Stokes equations conserves energy and enstrophy, while the three-dimensional system conserves energy and helicity.

We numerically verify this speculation in Fig. 5.7. We first show the enstrophy flux $\Pi_\omega(k)$ normalized by the enstrophy injection rate

$$P_\omega \equiv \big\langle (\nabla \times \boldsymbol{f}) \cdot \boldsymbol{\omega} \big\rangle \tag{5.31}$$

in Fig. 5.7(a). The wavenumber is normalized by R so that the flux is horizontally shifted. Under the space-local constraint, we observe shallower scaling in the large scales $k \ll 2\pi/R$, indicating a constant enstrophy flux $\Pi_\omega(k) \propto k^0$ in the asymptotic limit of $R \searrow 0$. Since there is no enstrophy production in this limit, the magnitude of $\Pi_\omega(k)$ in this regime is of the order of the total enstrophy injection P_ω by the forcing (5.31).

In an enstrophy-conserving system, the energy spectrum exhibits an asymptotic scaling of $E(k) \propto k^{-3}$, for example, see Bos (2021, Fig. 1). Figure 5.7(b) shows the compensated energy spectrum according to

$$E(k) \sim P_\omega^{2/3} k^{-3}, \tag{5.32}$$

associated with the conservative enstrophy cascade picture. Although we do not observe a clear plateau even for the smallest value of the $R = 0.1L_f$ snapshot, the large-scale behaviour in $R \searrow 0$ limit is not contradicting the asymptotic enstrophy conservation discussed in Fig. 5.7(a). Plausibly, we may observe clearer k^{-3} scaling with large enough separation between k_f and $2\pi/R$, which would require much larger computational capacity. Furthermore, logarithmic corrections can also affect this scaling (Kraichnan 1971b; Wu and Bos 2022).

5.5 Concluding remarks

The scale locality of nonlinear interactions in three-dimensional turbulence has received considerable attention in the turbulence community, unlike locality in physical space. The present study aims to understand how spatially local and nonlocal nonlinear interactions contribute to the small-scale universality of turbulence. To this end, we considered the space-local velocity field (4.7) induced by the *space-local* vorticity field. Here, *space-local* is defined by the contributions contained in a spherical region of radius R around the considered point in space. We use this velocity to define a variant of the vorticity equation (5.1) in which the nonlinear term is determined in the space-local sense.

We conducted DNS of this space-local flow in a 2π-periodic box driven by the steady forcing (4.21). The wavenumber range of the energy spectrum $E(k)$ of space-local Navier–Stokes turbulence can be decomposed into the following regions: (i) a possible inversely energy cascading range in $k \ll k_f$, (ii) $E(k) \propto k^{-3}$ scaling range associated with a conservative enstrophy cascade in the asymptotic limit of $R \searrow 0$ in $k_f \ll k \ll 2\pi/R$, (iii) $E(k) \propto k^{-5/3}$ scaling range in $2\pi \ll k \ll k_{\eta^>}$, and (iv) a dissipation range. Here, $k_f, 2\pi/R$, and $k_{\eta^>}$ denote the characteristic wavenumbers of the forcing, physical-space locality, and dissipation, respectively. These regimes are schematically summarized in Fig. 5.8.

When we focus on the inertial range $k_f \ll k \ll k_{\eta^>}$ [regions (ii) and (iii)], the space-local Navier–Stokes equations consolidate the robustness of Kolmogorov similarity with energy cascade in its small-scale part [regions (iii) and (iv)]. This finding suggests that the nonlinear interactions of three-dimensional turbulence are local in physical space as well as in scale space. The physical-space locality of the nonlinear interactions is consistent with Kolmogorov (1941a)'s hypothesis, where the spatially local domain was considered. The large-scale part [region (ii)] behaves asymptotically as turbulence without vortex stretching, which is explained by the suppressed enstrophy production and corresponds to a constant enstrophy flux. We note that this spectral shape with two (asymptotic) scaling ranges is similar to the Nastrom–Gage spectrum of atmospheric turbulence (Nastrom et al. 1984). In that case, the enstrophy-conserving range with the k^{-3} scaling corresponds to close to two-dimensional turbulence while the $k^{-5/3}$ scaling is recovered in the small scales.

Extensive investigations with higher resolution and wider scaling range between k_f and $2\pi/R$ are needed to confirm the $E(k) \propto k^{-3}$ scaling and its intersection with the $E(k) \propto k^{-5/3}$ scaling. Furthermore, the nature of a possible inverse cascade of the injected energy with small finite values of R, as in Fig. 5.4, is not investigated in the current study. Indeed, three-dimensional turbulence can exhibit inverse cascades if the nonlinear term is modified (Biferale et al. 2012; Frisch, Pomyalov, et al. 2012; Wu and Bos 2022). An alternative configuration with a much larger scale separation between the system size and the forcing would make it possible to investigate the behaviour of the system in the $k \ll k_f$ regime. Two-dimensional space-local turbulence may exhibit qualitatively different properties compared to the three-dimensional case since the two-dimensional Navier–Stokes equations are governed by long-range (spatially nonlocal) interactions. Recent investigations show that space locality is important in the dynamics of the large-scale condensation in two-dimensional turbulence (Svirsky et al. 2023).

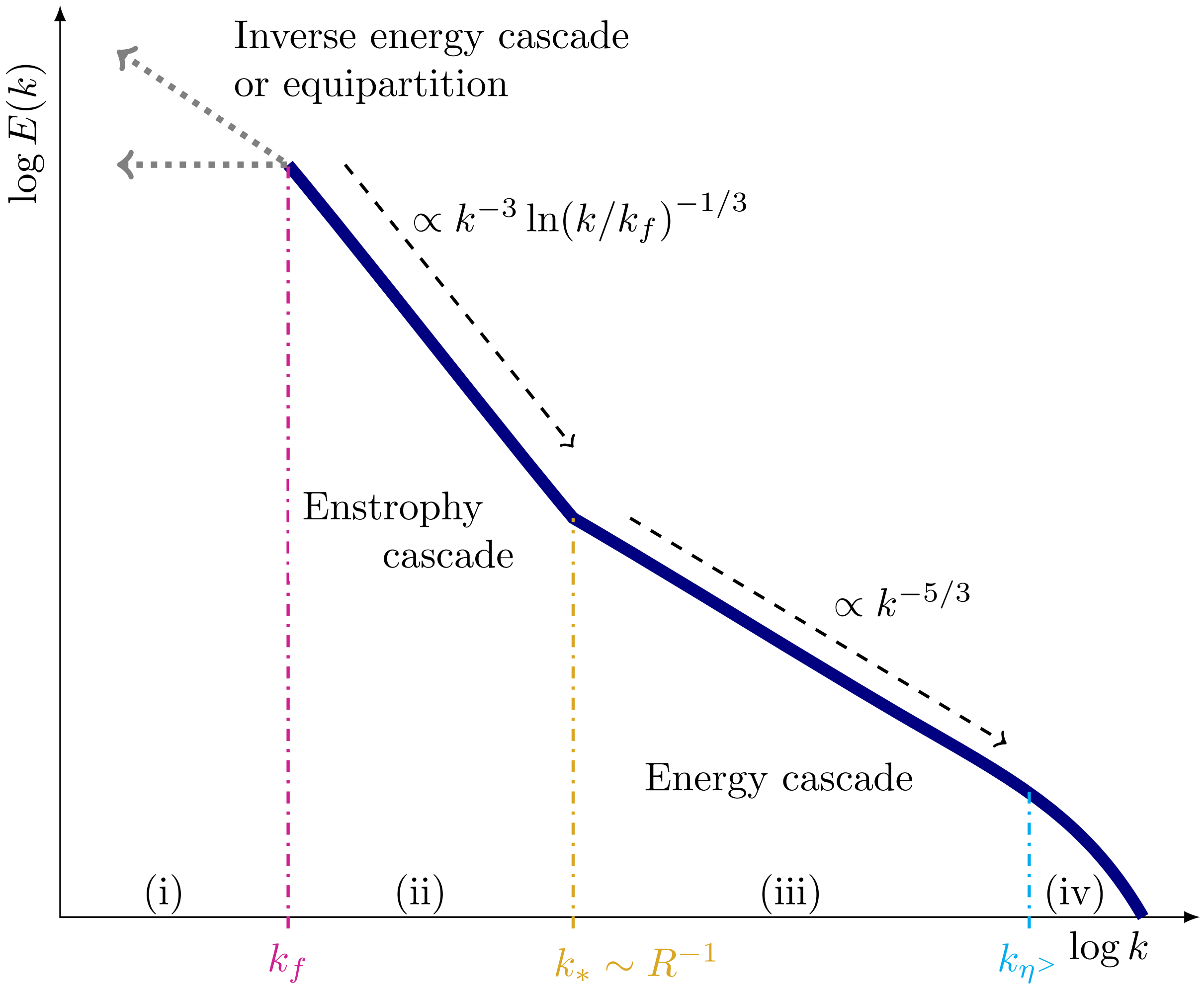

Figure 5.8: A schematic of the energy spectrum associated with space-local Navier–Stokes turbulence. Dashed arrows denote k^{-3} (plus logarithmic correction) and $k^{-5/3}$ scaling, respectively. Vertical dash-dotted lines denote: the forcing wavenumber k_f, the intersecting wavenumber k_* of the two scalings, and the Kolmogorov wavenumber $k_{\eta^>}$, respectively. Annotations (i)-(iv) correspond to different scaling regions divided by the characteristic wavenumbers.

Part III

Nonequilibrium Scaling in Inhomogeneous or Unsteady Turbulence

6 Inhomogeneous Scaling Correction of Energy Spectrum

This chapter investigates scaling correction for energy spectrum of the Navier–Stokes turbulence due to large-scale inhomogeneity. The content is based on the following:

> Araki, Ryo and Wouter J. T. Bos (2022). Inertial range scaling of inhomogeneous turbulence. *arXiv preprint.* arXiv: `2210.14516 [flu-dyn]`.

We begin this chapter by reviewing the effect of large-scale modulation on the energy spectrum in § 6.1. In § 6.2, we discuss the Derivation of the nonequilibrium inhomogeneous scaling correction in a self-contained manner. In § 6.3, we examine the derived scaling correction from the numerical data. We conclude this chapter in § 6.4.

6.1 Nonequilibrium scaling in turbulence with large-scale modulation

As we reviewed in § 1.2, Kolmogorov postulated in 1941 that the small scales of turbulent flows away from boundaries can be considered universal if the Reynolds number is sufficiently large (Kolmogorov 1941a). The small scales are then supposed to be in equilibrium, and the energy spectrum satisfies,

$$E(k, \boldsymbol{x}, t) \sim \epsilon(\boldsymbol{x}, t)^{2/3} k^{-5/3}, \tag{6.1}$$

where ϵ is the average energy dissipation rate. For this expression to hold, the wavenumber k should be sufficiently large compared to $L(\boldsymbol{x}, t)^{-1}$, the inverse of the length scale characterising the largest scales of the flow, and sufficiently small compared to the inverse of the Kolmogorov-scale $\eta(\boldsymbol{x}, t)^{-1}$ (with $\eta = \nu^{3/4}\epsilon^{-1/4}$), associated with the smallest scale of the flow.

In expression (6.1), the time and space dependence of E and ϵ need some particular attention. Theoretically, the most convenient flow type for investigating inertial range scaling is an infinitely large and statistically stationary flow without boundaries. Since all practical flows are limited in size and lifetime, the dissipation rate will be dependent, even on average, on either position $\boldsymbol{x}$ or time t, or both. Expression (6.1) will therefore hold only locally in subdomains of space and time-intervals large enough compared to the considered length and time scales.

Indeed, the assumptions allowing the simple prediction (6.1) are that flow at the scales k can be considered locally isotropic, stationary, and homogeneous. This local equilibrium hypothesis is introduced in § 1.2.1. The criterion $k \gg L^{-1}$ represents the implicit assumption that the influence of anisotropy, instationarity and inhomogeneity decreases as a function of scale.

As an illustration, let us discuss the influence of statistical instationarity on the behaviour of the small scales. This subject was addressed by Yoshizawa (1994), who proposed that the influence of instationarity at large wavenumbers can be described as a perturbation on the energy spectrum as

$$E(k, \boldsymbol{x}, t) = E_0(k, \boldsymbol{x}, t) + E_1(k, \boldsymbol{x}, t), \tag{6.2}$$

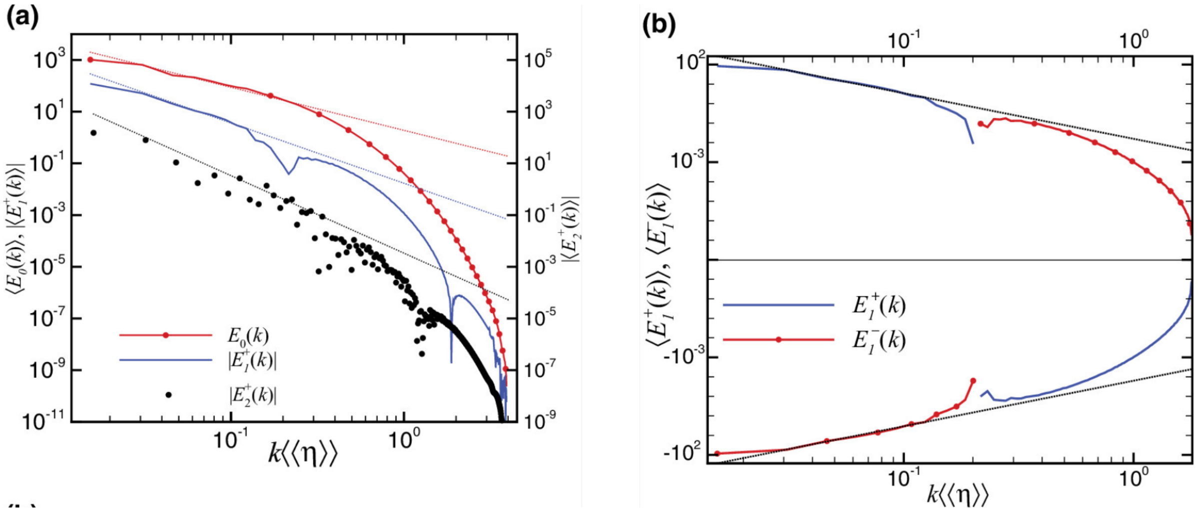

Figure 6.1: (a) The zeroth $E_0(k)$, first $\left|E_1^+(k)\right|$, and second $\left|E_2^+(k)\right|$ order contributions of the energy spectrum. The dotted lines denote the corresponding $k^{-5/3}$, $k^{-7/3}$, and $k^{-9/3}$ scalings, respectively. The superscript $+$ denotes the data associated with the positive sign of the time derivatives of the energy dissipation rate of each order. (b) The first order contributions of the energy spectrum $E_1(k)$. Both the positive (denoted by the superscript $+$) and negative $(-)$ contributions are shown. The dotted lines denote the $k^{-7/3}$ scaling. Adapted from Horiuti and Tamaki (2013, Figure 2).

where the equilibrium part E_0 is given by (6.1) and the perturbation scales as

$$E_1^T(k, \boldsymbol{x}, t) = C_Y \frac{\mathrm{d}\epsilon(\boldsymbol{x}, t)}{\mathrm{d}t} \epsilon(\boldsymbol{x}, t)^{-2/3} k^{-7/3}, \tag{6.3}$$

where the superscript T denotes that we consider perturbations due to instationarity. Numerical evidence of this scaling was first obtained by Horiuti and Ozawa (2011) for the case of homogeneous shear flow and by Horiuti and Tamaki (2013) for statistically isotropic turbulence in a periodic box. Figure 6.1 shows the equilibrium and nonequilibrium energy spectrum in the temporal fluctuations sense (Horiuti and Tamaki 2013). Further theoretical discussion and a more straightforward derivation of (6.3) can be found in Rubinstein and Clark (2005), Woodruff and Rubinstein (2006), and Bos and Rubinstein (2017). The effect of large-scale temporal fluctuations on the kinetic energy spectrum is thus proportional to $k^{-7/3}$, which decays more rapidly than the equilibrium spectrum (6.1) with the $k^{-5/3}$ scaling.

For anisotropic turbulence generated by mean-shear $S = \left\langle \partial u_x / \partial z \right\rangle$ an expression for the shear-stress spectrum similar to (6.3) was predicted by Lumley (1967),

$$E_1^A(k, \boldsymbol{x}, t) = C_L S \epsilon(\boldsymbol{x}, t)^{1/3} k^{-7/3}. \tag{6.4}$$

where the superscript A denotes that we consider perturbations due to anisotropy. This scaling was first confirmed in atmospheric measurements (Wyngaard and Coté 1972), then in closure theory (Leslie and Leith 1975; Bertoglio 1985). Later in wind-tunnel experiments Saddoughi and Veeravalli (1994) and more recently in Direct Numerical simulations and by a perturbative analysis (Ishihara, Yoshida, et al. 2002). This last work also considered other types of anisotropy in shear flow, which were also shown to decay proportionally to $k^{-7/3}$, as shown in Fig. 6.2. These measures concern thus anisotropy induced by velocity gradients on the level of second-order statistics.

In comparison to unsteady or anisotropic effects, the influence of inhomogeneity has received little attention. Historically, sophisticated models are proposed for inhomogeneous spectral dynamics, based on the Test Field Model (Kraichnan 1971a) or the Eddy-Damped Quasi-Normal Approximation (Laporta and Bertoglio 1995; Parpais and Bertoglio 1996). Using Karhunen-Loeve eigenfunctions, it was illustrated that Kolmogorov's equilibrium spectrum can be observed in statistically inhomogeneous flows (Knight and Sirovich 1990; Moser 1994; Liao and Su 2015). By using the SO(3) symmetry group decomposition, Kurien et al. (2000) showed that structure functions contain a subdominant scaling component associated

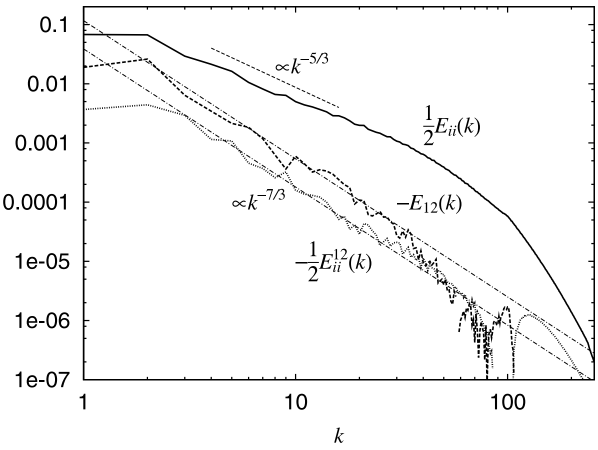

Figure 6.2: Isotropic ($E_{ii}(k)/2$, solid line) and anisotropic ($E_{12}(k)$; dashed line and $-E_{ii}^{12}(k)/2$; dotted line) energy spectra. The dashed anddash-dotted lines show $-5/3$ and $-7/3$ scalings, respectively.

with inhomogeneity. In the remainder of this chapter, we will focus on this inhomogeneity-induced scaling correction.

6.2 Derivation of the nonequilibrium inhomogeneous scaling correction

The main difficulty in the present investigation comes from the fact that we investigate a multi-scale description (the energy spectrum) in an inhomogeneous setting. To simplify as far as possible, we restrict ourselves to a fairly simple setting, where the (statistical) inhomogeneity is periodic in space, and the flow is stationary and far away from boundaries. Before addressing the inhomogeneous multi-scale description, we will first consider the pointwise energy balance of the flow.

6.2.1 Kinetic-energy budget in inhomogeneous turbulence

We consider a statistically inhomogeneous flow kept in a statistically stationary state by a steady forcing $f(z)$. The forcing in the present manuscript consists of a unidirectional steady body force in the x-direction with a sinusoidal dependence in the z-direction. The Navier-Stokes equations for this specific system write

$$\frac{\mathrm{D}\boldsymbol{\mathcal{U}}(\boldsymbol{x},t)}{\mathrm{D}t} = -\boldsymbol{\nabla}\mathcal{P}(\boldsymbol{x},t) + \nu\Delta\boldsymbol{\mathcal{U}}(\boldsymbol{x},t) + f(z)\boldsymbol{e}_x, \tag{6.5}$$

where $\mathrm{D}/\mathrm{D}t$ is the material derivative, $\mathcal{P}$ is the pressure (divided by density) ensuring incompressibility $\boldsymbol{\nabla}\cdot\boldsymbol{\mathcal{U}} = 0$, and $\boldsymbol{e}_x$ denotes the unit vector in the x-direction.

The equations for the mean flow and the kinetic energy of the fluctuations can be derived by introducing the Reynolds decomposition $\boldsymbol{\mathcal{U}} = \langle\boldsymbol{\mathcal{U}}\rangle + \boldsymbol{u}$, where $\langle\boldsymbol{\mathcal{U}}\rangle_{\mathrm{ens}}$ is the ensemble-averaged velocity and $\boldsymbol{u} = (u,v,w)$ the fluctuation. The specific forcing considered in the present investigation leads to a mean flow $\left\langle\boldsymbol{\mathcal{U}}(\boldsymbol{x},t)\right\rangle = U(z)\boldsymbol{e}_x$. Then, the kinetic energy corresponding to the mean flow can be written as

$$K_U(z) = U(z)^2/2, \tag{6.6}$$

and the kinetic energy of the fluctuations is

$$K(z) = \frac{1}{2}\Big[\left\langle u^2\right\rangle(z) + \left\langle w^2\right\rangle(z) + \left\langle w^2\right\rangle(z)\Big]. \tag{6.7}$$

The equation for the mean-velocity $U(z)$ reduces to,

$$\frac{\mathrm{D}U(z)}{\mathrm{D}t} = -\frac{\partial}{\partial z}\left\langle uw\right\rangle(z) + f(z) + \nu\frac{\partial^2 U(z)}{\partial z^2} = 0. \tag{6.8}$$

The details are, for instance, provided in Bos (2020). The equation for the turbulent kinetic energy writes, in a steady state,

$$\frac{\mathrm{D}K(z)}{\mathrm{D}t} = p(z) - \epsilon(z) + d(z) = 0, \tag{6.9}$$

where the production $p(z)$, dissipation $\epsilon(z)$, and diffusion $d(z)$ terms are given by

$$p(z) = -\left\langle uw\right\rangle(z)\frac{\partial U(z)}{\partial z}, \tag{6.10}$$

$$\epsilon(z) = \nu\left\langle\frac{\partial u_i}{\partial x_j}\frac{\partial u_i}{\partial x_j}\right\rangle(z), \tag{6.11}$$

$$d(z) = -\frac{\partial}{\partial z}\left(\left\langle\mathcal{P}w\right\rangle(z) + \left\langle u_i u_i w\right\rangle(z) - \nu\frac{\partial K(z)}{\partial z}\right), \tag{6.12}$$

respectively. The first term $p(z)$ represents the production of turbulent kinetic energy through the interaction of the turbulent fluctuations with the mean-velocity gradient $\partial U(z)/\partial z$. The viscous dissipation term $\epsilon(z)$ involves the gradients of the fluctuating velocity.

In statistically homogeneous flows, production and dissipation are the only terms appearing in the turbulent kinetic energy balance. In statistically *inhomogeneous* flows, we also have spatial diffusion of turbulent kinetic energy $d(z)$. The diffusion contains contributions associated with the turbulent fluctuations of the velocity and pressure (first two terms) and a contribution through viscous diffusion (the last term). This viscous part of the diffusion is generally negligible compared to the contribution of the other two terms and will be dropped in the following.

The main question in the present investigation is how such inhomogeneous redistribution processes $d(z)$ affect the scaling of the kinetic energy spectrum $E(k, \boldsymbol{x})$ in the inertial range of high Reynolds number turbulence.

6.2.2 Fourier-analysis of inhomogeneous turbulence

The use of energy spectra in general turbulent flows needs some justification. In principle, Fourier modes are associated with infinite or periodic domains. This property would exclude using spatial Fourier analysis of any realistic, non-periodic flow. However, a closer look at the lengthscales involved in turbulent flows permits invoking an assumption of scale separation, allowing us to get around this problem. Indeed, the theoretical basis for practical Fourier modelling of non-periodic turbulent flows can be found in various works (see Jeandel et al. 1978; Yoshizawa 1984; Bertoglio and Jeandel 1987; Laporta and Bertoglio 1995; Besnard et al. 1996). In practice, to develop a spectral description of inhomogeneous flows, one needs to introduce a lengthscale L characterising the inhomogeneity of the flow geometry. Then, one can consider Fourier spectra associated with scales $r \sim k^{-1}$ small compared to L.

In the present investigation, we consider a spatially periodic flow without solid boundaries or obstacles to avoid most of these complications. Furthermore, we consider statistically stationary turbulence with a single inhomogeneous direction z to derive corrections due to statistical inhomogeneity. An advantage of the present configuration, where only one inhomogeneous direction is present, is that we can compute energy spectra in planes perpendicular to the z-axis. We thus define

$$E(k_\perp, z) \equiv \frac{1}{2}\int u_i(\boldsymbol{k}_\perp, z)u_i^*(\boldsymbol{k}_\perp, z)\,\mathrm{d}A(k_\perp)\,, \tag{6.13}$$

where $A(k_\perp)$ denotes a wavenumber-shell of radius $k_\perp$ in the k_x, k_y plane. The velocity field in (6.13) is defined by the two-dimensional Fourier transform,

$$u_i(\boldsymbol{k}_\perp, z) \equiv \int e^{-\mathrm{i}\left(k_x x + k_y y\right)} u_i(x, y, z)\,\mathrm{d}x\,\mathrm{d}y\,. \tag{6.14}$$

The resulting energy spectrum $E(k_\perp, z)$ is a function of a perpendicular wavenumber $k_\perp = \sqrt{k_x^2 + k_y^2}$ and a vertical coordinate z. We note that if isotropy is restored in small scales, $E(k_\perp, z)$ is expected to scale like the three-dimensional spectrum $E(k, z)$ (see (6.17) for the definition). In the following subsections in § 6.2, we will keep the notation $E(k, z)$ for the sake of generality, but it should be kept in mind that the scaling of $E(k, z)$ and $E(k_\perp, z)$ should be equivalent in statistically isotropic flow at large k.

6.2.3 Governing equation and modelling

The derivation in this subsection closely follows the rationale used to derive the instationary correction presented in Bos and Rubinstein (2017). This same methodology is here applied to the evolution-equation of the energy spectrum in inhomogeneous turbulence.
The kinetic energy spectrum is associated with the turbulent kinetic energy by the relation

$$\int E(k, z)\,\mathrm{d}k = K(z). \tag{6.15}$$

The evolution equation for $E(k, z)$ is the multi-scale extension of equation (6.9). This equation reads, for the case of a unidirectional mean flow $U(z)\boldsymbol{e}_x$ as in (6.5),

$$\frac{\mathrm{D}E(k,z)}{\mathrm{D}t} = \underbrace{P(k,z)}_{\text{production}} \underbrace{-2\nu k^2 E(k,z)}_{\text{dissipation}} + \underbrace{T(k,z)}_{\text{transfer}} + \underbrace{D(k,z)}_{\text{diffusion}}. \tag{6.16}$$

Next, we define the spectrum and the governing equations for the energy spectrum tensor in inhomogeneous flow (see (6.16)). The generalised spectrum $E(k, \boldsymbol{x}) = E_{ii}(k, \boldsymbol{x})$ is defined by

$$E(k, \boldsymbol{x}) \equiv \frac{1}{2} \iint e^{-\mathrm{i}\boldsymbol{k}\cdot\boldsymbol{r}} \left\langle u_i\left(\boldsymbol{x} + \frac{\boldsymbol{r}}{2}\right) u_i\left(\boldsymbol{x} - \frac{\boldsymbol{r}}{2}\right)\right\rangle \mathrm{d}\boldsymbol{r}\,\mathrm{d}\Omega_k\,, \tag{6.17}$$

where $\int \mathrm{d}\Omega_k$ denotes the integral over spherical shells of radius k. The brackets in this subsection denote the ensemble average. For statistically homogeneous turbulence, this definition is equivalent to the expression

$$E(k) \equiv \int \frac{1}{2} \left\langle u_i(\boldsymbol{k}) u_i^*(\boldsymbol{k})\right\rangle \mathrm{d}\Omega_k\,. \tag{6.18}$$

The evolution equation for $E_{ij}(k, \boldsymbol{x}, t)$ formally reads

$$\frac{\partial E_{ij}(k, \boldsymbol{x}, t)}{\partial t} = \frac{1}{2} \int \left[\int e^{-\mathrm{i}\boldsymbol{k}\cdot\boldsymbol{r}} \Psi_{ij}(\boldsymbol{x} + \boldsymbol{r}/2, \boldsymbol{x} - \boldsymbol{r}/2, t)\,\mathrm{d}\boldsymbol{r}\right] \mathrm{d}\Omega_k\,. \tag{6.19}$$

For the tensor on the RHS, we have

$$\begin{aligned}\Psi_{ij}(\boldsymbol{x}_1, \boldsymbol{x}_2) =& \nu\left(\nabla_1^2 + \nabla_2^2\right) R_{ij}(\boldsymbol{x}_1, \boldsymbol{x}_2)\\ &- \Big[\frac{\partial}{\partial x_{1n}} U_n(\boldsymbol{x}_1) R_{ij}(\boldsymbol{x}_1, \boldsymbol{x}_2) + \frac{\partial}{\partial x_{2n}} U_n(\boldsymbol{x}_2) R_{ij}(\boldsymbol{x}_1, \boldsymbol{x}_2)\\ &+ \frac{\partial}{\partial x_{1n}} U_i(\boldsymbol{x}_1) R_{nj}(\boldsymbol{x}_1, \boldsymbol{x}_2) + \frac{\partial}{\partial x_{2n}} U_j(\boldsymbol{x}_2) R_{ni}(\boldsymbol{x}_1, \boldsymbol{x}_2)\\ &+ \frac{\partial}{\partial x_{1i}} \left\langle \mathcal{P}(\boldsymbol{x}_1) u_j(\boldsymbol{x}_2)\right\rangle + \frac{\partial}{\partial x_{2j}} \left\langle \mathcal{P}(\boldsymbol{x}_2) u_i(\boldsymbol{x}_1)\right\rangle\\ &+ \frac{\partial}{\partial x_{1n}} \left\langle u_i(\boldsymbol{x}_1) u_n(\boldsymbol{x}_1) u_j(\boldsymbol{x}_2)\right\rangle + \frac{\partial}{\partial x_{2n}} \left\langle u_j(\boldsymbol{x}_2) u_n(\boldsymbol{x}_2) u_i(\boldsymbol{x}_1)\right\rangle\Big].\end{aligned} \tag{6.20}$$

In this expression and the following, the argument t for time is omitted for visibility. The two-point velocity tensor is defined by

$$R_{ij}(\boldsymbol{x}_1, \boldsymbol{x}_2) \equiv \left\langle u_i(\boldsymbol{x}_1) u_j(\boldsymbol{x}_2)\right\rangle, \tag{6.21}$$

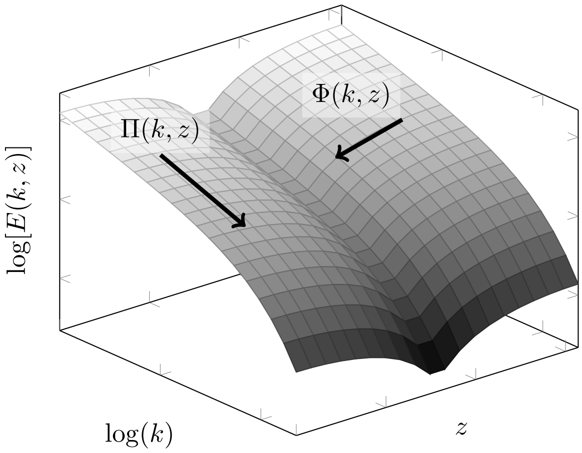

Figure 6.3: A schematic of the energy spectrum in (k, z) coordinates. Two arrows denote the direction of energy fluxes in wavenumber and physical space, respectively.

and the equation (6.20) is completed by incompressibility conditions for the mean field and the fluctuations. Both inhomogeneous turbulence diffusion and spectral transfer are associated with the last two lines of expression (6.20). An assumption of weak inhomogeneity must be invoked to dissociate them to obtain a closed expression. Even retaining only the leading order terms in an expansion about inhomogeneity, the resulting equations become quite cumbersome (see Laporta (1995) and Besnard et al. (1996)).

Subsequently, the different terms in (6.20) need to be modelled to close the triple correlations. We will not proceed in this direction and will directly model them by their physical effects. See (6.22)– (6.25).

Except for the viscous dissipation, all the terms in (6.16) are unclosed. In the following, we discuss the different physics and contributions to propose simple models for them.

Since the flow is statistically stationary and the mean flow is unidirectional, the material derivative on the left-hand side of (6.16) is zero. The first term on the RHS, $P(k, z)$, represents the terms directly proportional to the mean-velocity gradient. It contains two contributions: the production of turbulent kinetic energy and a linear transfer term (Cambon et al. 1981; Briard et al. 2018). These terms are mainly important at large scales and become zero at points in space where the velocity gradient vanishes. The order of magnitude of the production term can be estimated by (Tennekes and Lumley 1972),

$$P(k, z) \sim \left(\frac{\partial U(z)}{\partial z}\right)^2 \tau(k, z) E(k, z), \tag{6.22}$$

with the time scale $\tau(k, z) \sim \epsilon(z)^{-1/3} k^{-2/3}$ in the inertial range. The integral of $P(k, z)$ over wavenumbers yields $p(z)$ in (6.9). Here, $\epsilon(z)$ denotes the profile of the dissipation of kinetic energy through viscous stresses (see (6.11)) and is obtained by the integral of the second term on the RHS of (6.16). At large Reynolds numbers, this term is significant only at large wavenumbers. It is thus this term which is responsible for energy transfer between the mean velocity field $U(z)$ and the turbulent kinetic energy.

The nonlinear transfer $T(k, z)$ represents the energy flux and is a redistributive term in scale space; thus, its integral over all wavenumbers yields zero. The last term $D(k, z)$ represents the diffusion, or transport, through turbulent fluctuations and viscous diffusion. Note that this term is zero in statistically homogeneous turbulence. The term $D(k, z)$ is also a redistribution term like $T(k, z)$, but in physical space. Its integral over wavenumbers corresponds to $d(z)$ in (6.9).

Both $T(k, z)$ and $D(k, z)$ are a function of triple correlations between Fourier modes at different wavelengths. There is no exact expression of these quantities as a closed function of the kinetic energy spectrum $E(k, z)$. At this moment, we will therefore introduce modelling assumptions. Sophisticated models exist for inhomogeneous spectral dynamics, based on the Test Field Model (Kraichnan 1971a) or the Eddy-Damped Quasi-Normal Approximation (Laporta and Bertoglio 1995; Parpais and Bertoglio 1996). However, the resulting closures are quite complicated and do not allow a straightforward analytical perturbation treatment. Therefore, our approach uses simple models that reproduce their main physical features: energy redistribution in scale space for $T(k, z)$ and in physical space for $D(k, z)$, respectively.

We use diffusion approximations for both terms,

$$T(k,z) = -\frac{\partial}{\partial k}\Pi(k,z), \tag{6.23}$$

$$D(k,z) = -\frac{\partial}{\partial z}\Phi(k,z), \tag{6.24}$$

where $\Pi(k,z)$ and $\Phi(k,z)$ are turbulent fluxes in wavenumber and physical space, respectively. Figure 6.3 schematically depicts these two fluxes in (k,z) space. In the absence of inhomogeneity, the flux $\Phi(k,z)$ is zero. In the inhomogeneous case, the presence of this flux will affect the kinetic energy spectrum $E(k,z)$. We model both fluxes using a gradient-diffusion approximation,

$$\Pi(k,z) = -\rho(k,z)\frac{\partial\big(k^{-2}E(k,z)\big)}{\partial k} \tag{6.25}$$

with $\rho(k,z) \sim k^{11/2}E(k,z)^{1/2}$ being a turbulent energy diffusion in Fourier space, and

$$\Phi(k,z) = -\mu(z)\frac{\partial E(k,z)}{\partial z}, \tag{6.26}$$

where $\mu(z)$ is a turbulent diffusivity in real space (see (6.38)). We have effectively decoupled (and simplified) the transfer terms in scale and physical space. Indeed, both $\Phi(k,z)$ and $\Pi(k,z)$ are determined by the same triple velocity and velocity-pressure correlations (see (6.20)). Decomposing the physical space-scale space flux is a major assumption which seems necessary to obtain an analytically tractable model of energy transfer in inhomogeneous turbulence. The model for $\Pi(k,z)$ (6.25) is known as the Leith model (Leith 1967; Rubinstein and Clark 2022). This model tends to homogenise the kinetic energy in spectral space towards equipartition among wave vectors, corresponding to an energy spectrum proportional to k^2. The gradient-diffusion model for the diffusion (6.26) tends to homogenise the energy distribution in physical space and is used in Besnard et al. (1996), Touil et al. (2002), and Cadiou et al. (2004), for instance.

Eddy viscosity models are obviously simplified representations of the real transfer terms. For instance, see Pope (2000, § 10) for extensive discussions. However, we think that this kind of modelling is a useful first step before turning to more sophisticated modelling approaches.

6.2.4 Linear perturbation analysis and scaling predictions

Our goal is to derive a prediction for inertial range scaling at large Reynolds numbers in the limit of weak inhomogeneity, where the influence of inhomogeneity can be treated as a perturbation. In the following, the leading order contributions and perturbations are indicated by a subscript 0 and 1, respectively. We define an inertial range $L^{-1} \ll k \ll \eta^{-1}$ with the length L representing the typical length of the largest and energy-containing scales of the flow. Furthermore, in our description, it is associated with the longest wavelength in our flow domain and is chosen constant. We will define this length scale more precisely later, in § 6.2.5.

We now define the equilibrium about which we expand the equations. To do so, we consider the decomposition

$$E(k,z) = E_0(k,z) + E_1(k,z) \tag{6.27}$$

with $|E_1| \ll |E_0|$. The other quantities, such as $\Pi(k,z)$ and $\Phi(k,z)$, are decomposed in the same manner. We recall here that in addition to these two contributions to the energy spectrum, the flow also contains the time-averaged velocity profile, which consists of a single wave vector in the z-direction in the present case (6.6). This mean flow is not present in the inertial range, on which we will focus in the following. Therefore, in the remainder of this section, we can focus on the contributions $E_0(k,z)$ and $E_1(k,z)$.

For very high Reynolds numbers in the limit of vanishing inhomogeneity, we assume that the equilibrium contributions to the kinetic energy balance (6.16) do not depend on the inhomogeneous turbulent diffusion $D(k,z)$. By integrating the balance between the transfer and dissipation terms in (6.16) from k to ∞, we find

$$\int_k^\infty T(p,z)\,\mathrm{d}p = \int_k^\infty 2\nu p^2 E(p,z)\,\mathrm{d}p \tag{6.28}$$

or, using expression (6.23) and the equilibrium/nonequilibrium decomposition,

$$\Pi_0(k,z)=\epsilon(z). \tag{6.29}$$

Indeed, this corresponds to the equilibrium between the energy flux and the energy dissipation rate, essential to the inertial range description of Kolmogorov (1941a). The constant flux solution of the Leith model is consistent with this framework and is given by

$$E_0(k,z)\sim\epsilon(z)^{2/3}k^{-5/3}. \tag{6.30}$$

This expression defines our equilibrium solution. We now assess the influence of the inhomogeneity of $\epsilon(z)$ on this scaling as a perturbation.

In the following, we consider the terms in the balance equation (6.16) for the nonequilibrium contributions: $E_1(k,z)$ and $\Pi_1(k,z)$. The order of magnitude of the production term (6.22) and the diffusion-gradient modelling with the flux (6.26) leads us to deduce that $D(k,z)\gg P(k,z)$ at $k\gg L^{-1}$. Therefore, the first-order perturbation to the equilibrium scaling in the inertial range is due to the inhomogeneous diffusion $D(k,z)$. Then, in the inertial range, we have

$$T(k,z)=-D(k,z), \tag{6.31}$$

and

$$-\frac{\partial}{\partial k}\Pi_1(k,z)=\frac{\partial}{\partial z}\Phi_0(k,z), \tag{6.32}$$

since $\partial\Pi_0(k,z)/\partial k=0$. Thus, the *first*-order correction of the nonlinear transfer balances the *zeroth*-order contribution of the inhomogeneous diffusion. The first-order perturbation to the nonlinear flux $\Pi_1(k,z)$ is evaluated as (Rubinstein and Clark 2005)

$$\Pi_1(k,z)=E_1(k,z)\left.\frac{\delta\Pi}{\delta E}\right|_{E_0}, \tag{6.33}$$

where $\delta\Pi/\delta E\,\big|_{E_0}$ is the Fréchet derivative of the total flux Π evaluated at $E(k,z)=E_0(k,z)$. In the inertial range, assuming E_1 to scale as a power law, this yields the scaling,

$$\Pi_1(k,z)\sim\epsilon(z)\frac{E_1(k,z)}{E_0(k,z)}. \tag{6.34}$$

Note that we obtain (6.34) not only for the Leith model, but also for most of the other classical closures such as the Kovaznay and Heisenberg model (Rubinstein and Clark 2022). Integrating (6.32) from k to ∞, we have

$$\Pi_1(k,z)=\frac{\partial}{\partial z}\int_k^\infty\Phi_0(k,z)\,\mathrm{d}k\,. \tag{6.35}$$

By combining this with (6.26) and (6.34), we obtain

$$E_1(k,z)\sim-\frac{E_0(k,z)}{\epsilon(z)}\frac{\partial}{\partial z}\left(\mu(z)\frac{\partial\int_k^\infty E_0(p,z)\,\mathrm{d}p}{\partial z}\right). \tag{6.36}$$

Substituting (6.30), the above expression gives

$$E_1(k,z)\sim-\mu(z)\epsilon(z)^{1/3}k^{-7/3}\left[\frac{2}{3}\frac{\epsilon_{zz}(z)}{\epsilon(z)}+\frac{2}{3}\frac{\mu_z(z)}{\mu(z)}\frac{\epsilon_z(z)}{\epsilon(z)}-\frac{2}{9}\left(\frac{\epsilon_z(z)}{\epsilon(z)}\right)\right], \tag{6.37}$$

where the subscripts denote derivatives with respect to z, for example, $\epsilon_{zz}=\partial^2\epsilon(z)/\partial z^2$. We will model the unknown eddy diffusivity in its simplest way,

$$\mu(z) \sim L^{4/3}\epsilon(z)^{1/3}. \tag{6.38}$$

Doing so, we obtain

$$E_1(k,z) \sim -\frac{\epsilon_{zz}(z)L^{4/3}}{\epsilon(z)^{1/3}}k^{-7/3}. \tag{6.39}$$

Note that although all the terms involving ϵ_z and μ_z vanish exactly for the current definition of $\mu(z)$ in (6.38), this might not be the case for arbitrary choices of $\mu(z)$.

6.2.5 Case of a sinusoidal dissipation profile

The comparison of expressions (6.30) and (6.39) indicates that the inhomogeneous contribution ($\propto k^{-7/3}$) is subdominant compared to the equilibrium energy spectrum ($\propto k^{-5/3}$) at large wavenumbers. Furthermore, the expression is proportional to the second spatial derivative of the dissipation rate $\epsilon_{zz}(z)$ and can thus be both positive and negative. Let us illustrate the implication of this expression by considering a large-scale inhomogeneity characterised by a cosine function with a characteristic wavelength of order L,

$$\epsilon(z) = \langle\epsilon\rangle + \tilde{\epsilon}\cos\big(z/L\big), \tag{6.40}$$

with $\langle\epsilon\rangle \gg \tilde{\epsilon}$. We consider L, first introduced in § 6.2.4, to be of the order of and proportional to the characteristic large-scale length of the flow. Substituting this expression for $\epsilon(z)$ in (6.39), we find

$$E_1(k,z) = E_1^X(k)\cos\big(z/L\big) \tag{6.41}$$

with

$$E_1^X(k) = C_A\tilde{\epsilon}\,\langle\epsilon\rangle^{-1/3}L^{-2/3}k^{-7/3}, \tag{6.42}$$

where the superscript X indicates the perturbations due to inhomogeneity.
Let us now assume that both the equilibrium spectrum $E_0(k,z)$ and $E_1(k,z)$ extend from $k = L^{-1}$ to ∞. Integrating the spectra in this range, we find that

$$K_0(z) \sim L^{2/3}\epsilon(z)^{2/3} \tag{6.43}$$

and

$$K_1(z) \sim -\frac{\epsilon_{zz}(z)L^2}{\langle\epsilon\rangle}K_0(z). \tag{6.44}$$

Comparing these last two expressions illustrates that the formal expansion parameter in our system is

$$\gamma = \frac{\epsilon_{zz}(z)L^2}{\langle\epsilon\rangle}. \tag{6.45}$$

The main analytical results of the present investigation [(6.42)–(6.44)] are obtained by phenomenological modelling based on gradient-diffusion assumptions of nonlinear transfer in both physical and scale space. The models and their consequences are, at best, crude approximations of the intricate nonlinear interactions in the actual flow. Therefore, The resulting expressions need verification by experiments or direct numerical simulations.

6.3 Assessment of the inhomogeneous scaling correction

6.3.1 Numerical setup

In order to verify the theoretical predictions, in particular expression (6.42), we carry out DNS of three-dimensional Kolmogorov flow in a triple-periodic box. Such flow has the convenient properties of being

N	ν	u'	λ	Re_λ	T_{total}/T
128	0.07	1.31	0.371	69.6	959
256	0.028	1.35	0.233	113	645
512	0.01	1.33	0.138	184	170

Table 6.1: DNS parameters and statistical quantities. The resolution N and kinematic viscosity ν are the control parameters. The remaining statistical quantities are: the fluctuating isotropic RMS velocity $u' \equiv \sqrt{2K'/3}$ where energy of the temporal fluctuating velocity $K' \equiv \left\langle u_i' u_i' \right\rangle_{\Omega,t}/2$ and $u_i'(\boldsymbol{x},t) \equiv u_i(\boldsymbol{x},t) - \left\langle u_i \right\rangle_t(\boldsymbol{x})$; the Taylor microscale $\lambda \equiv u'\sqrt{15\nu/\epsilon}$ where the energy dissipation rate is evaluated by $\epsilon = \nu\left\langle \omega_i \omega_i \right\rangle_{\Omega,t}$; the Taylor-length Reynolds number $\mathrm{Re}_\lambda \equiv u'\lambda/\nu$; the integral time scale $T \equiv L/u'$ with $L = k_f^{-1} = 1$; the simulation time in the statistically steady state T_{total} as a function of T.

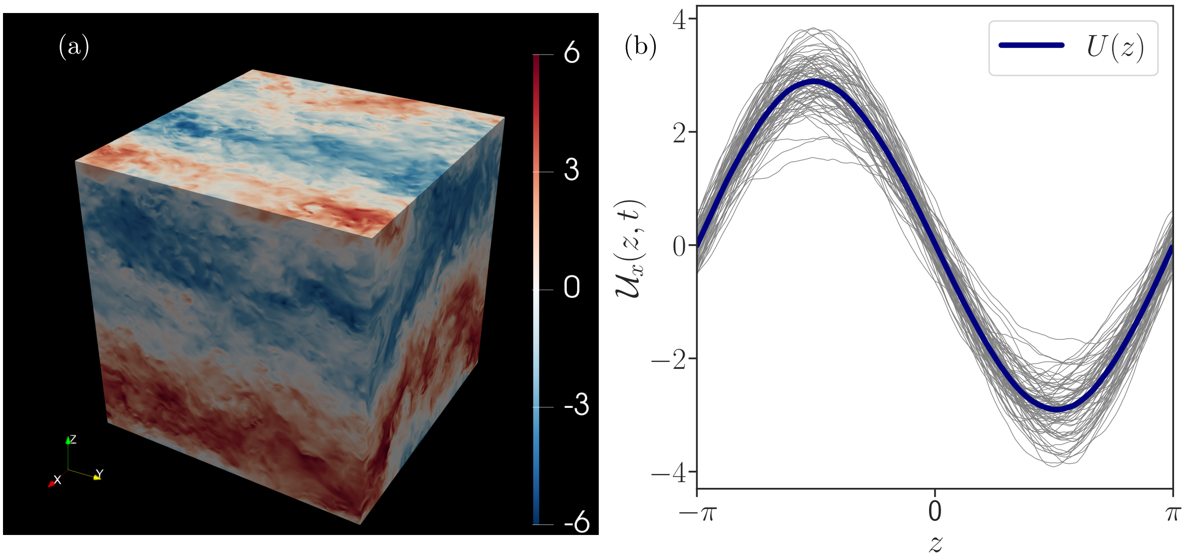

Figure 6.4: (a) Instantaneous distributions of $\mathcal{U}_x(\boldsymbol{x},t)$ at $\mathrm{Re}_\lambda = 184$. Blue (red) corresponds to the negative (positive) value of $\mathcal{U}_x$. (b) Instantaneous profiles of $\mathcal{U}_x(z,t) = \left\langle \mathcal{U}_x(\boldsymbol{x},t) \right\rangle_\perp$ in grey. Time-averaged profile $U(z) = \left\langle \mathcal{U}_x(\boldsymbol{x},t) \right\rangle_{\perp,t}$ is indicated by a thick line.

statistically inhomogeneous in one direction and free of solid boundaries. Furthermore, its properties have been widely investigated numerically (Borue and Orszag 1996; Musacchio and Boffetta 2014; Wu, Schmitt, et al. 2021).

The dynamics of the Kolmogorov flow in the present investigation are governed by (6.5) with

$$f(z) = \sin\left(k_f z\right). \tag{6.46}$$

The numerical domain is a cube of size 2π. These choices imply that the forcing wavelength is equal to the width of the cubic domain, and we set $k_f = L^{-1} = 1$. Simulations are carried out using a standard pseudo-spectral solver (Delache et al. 2014) with a third-order Adams-Bashfort time-integration scheme. The details of the simulations are reported in table 6.1. Since we focus on the effect of inhomogeneity, we attempt to obtain statistics in a steady state over a long-enough time interval to allow the effects of the temporal variations to become as small as possible (see the last column in table 6.1).

6.3.2 Visualisation and dissipation profile

In the following, we will discuss the simulation at the highest considered Reynolds number $\mathrm{Re}_\lambda = 184$. A flow visualisation is shown in figure 6.4(a) with the x-component of the velocity field $\mathcal{U}_x(\boldsymbol{x},t)$. The influence of the large-scale mean flow, proportional to the sinusoidal forcing along the z axis, is distinguishable. Figure 6.4(b) shows the instantaneous profile of $\mathcal{U}_x(z,t) = \left\langle \mathcal{U}_x(\boldsymbol{x},t) \right\rangle_\perp$. The single curve corresponds to

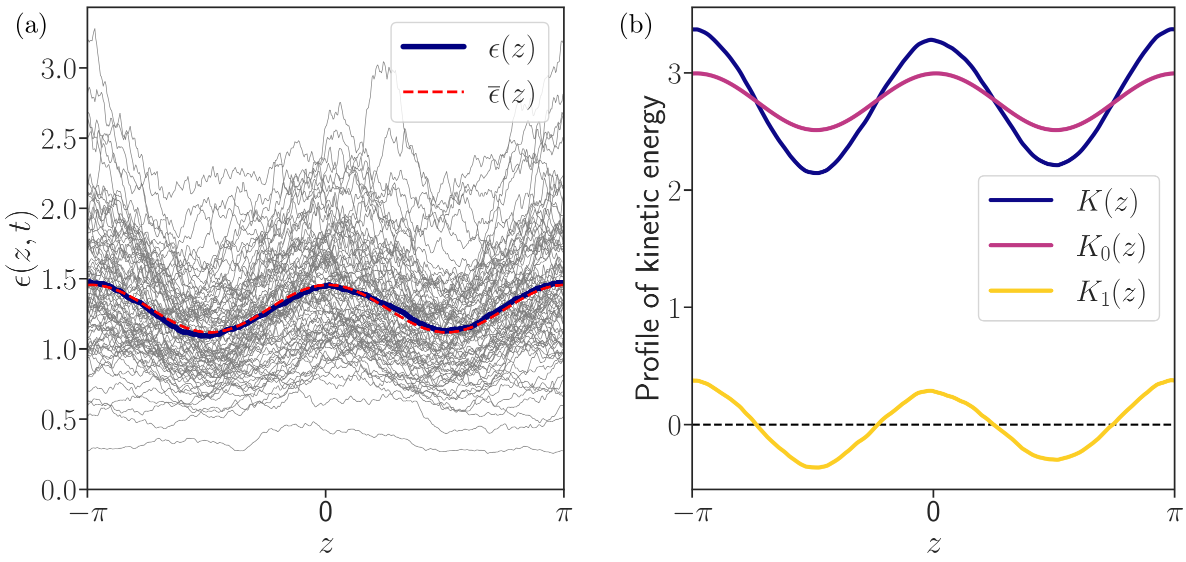

Figure 6.5: (a) Instantaneous profile of $\epsilon(z,t) = \left\langle \epsilon(\boldsymbol{x},t) \right\rangle_{\perp}$. Time-averaged profile $\epsilon(z) = \left\langle \epsilon(\boldsymbol{x},t) \right\rangle_{\perp,t}$ is also shown. The red dashed line denotes $\overline{\epsilon}(z)$, a sinusoidal fitting of $\epsilon(z)$ by (6.40). (b) Time-averaged profile of kinetic energy with fluctuating velocity $K(z)$ and its equilibrium $K_0(z)$ and nonequilibrium $K_1(z)$ contributions. See the main text for the definition.

the horizontal average of a snapshot, as shown in figure 6.4(a). Its time average, $U(z) = \left\langle \mathcal{U}_x(\boldsymbol{x},t) \right\rangle_{\perp,t}$, is also shown in figure 6.4(b) with a smooth sinusoidal profile.

In figure 6.5(a), the instantaneous profile of the energy dissipation rate $\epsilon(z,t) = \left\langle \epsilon(\boldsymbol{x},t) \right\rangle_{\perp}$ is shown along with its time average $\epsilon(z) = \left\langle \epsilon(\boldsymbol{x},t) \right\rangle_{\perp,t}$. The instantaneous profile shows large fluctuations in comparison to the velocity profile (figure 6.4(b)). Its time average, in contrast, shows a smooth sinusoidal profile. This property allows us to use the approximations in § 6.2.5. As expected, the dissipation peaks at values where the mean velocity gradient is strongest (at $z = 0$ and $\pm\pi$). For numerical convenience, we perform a sinusoidal fitting $\overline{\epsilon}(z)$ introduced in (6.40). This profile is also shown in figure 6.5(a).

Figure 6.5 (b) shows the kinetic energy profile of the fluctuating velocity field. The fluctuating energy profile is defined by $K(z,t) = \mathcal{K}(z,t) - K_U(z)$, where the total energy is $\mathcal{K}(z,t) = \mathcal{U}_i(z,t)\mathcal{U}_i(z,t)/2$ and the mean flow energy is $K_U(z) = U(z)^2/2$. We consider the decomposition, see (6.43)–(6.44),

$$K(z,t) = K_0(z,t) + K_1(z,t). \tag{6.47}$$

In figure 6.5 (b), we observe that the equilibrium $K_0(z) = \left\langle K_0(z,t) \right\rangle_t$ and the nonequilibrium $K_1(z) = \left\langle K_1(z,t) \right\rangle_t$ profiles share the same phase, consistent with the prediction that the spectrum $E_1(k,z)$ is proportional to $-\,\partial^2\epsilon(z)/\partial z^2$.

6.3.3 Equilibrium and nonequilibrium spectra

Here, we investigate the different normalisation procedures. We state that the energy spectrum is decomposed into equilibrium (labelled by the subscript 0) and nonequilibrium (labelled by the subscript 1) contributions as

$$E(k,z) = E_0(k,z) + E_1(k,z). \tag{6.48}$$

We further assume that the nonequilibrium contributions are zero-mean,

$$\left\langle E_1(k,z) \right\rangle_z = 0. \tag{6.49}$$

We have therefore

$$\left\langle E(k,z) \right\rangle_z = \left\langle E_0(k,z) \right\rangle_z. \tag{6.50}$$

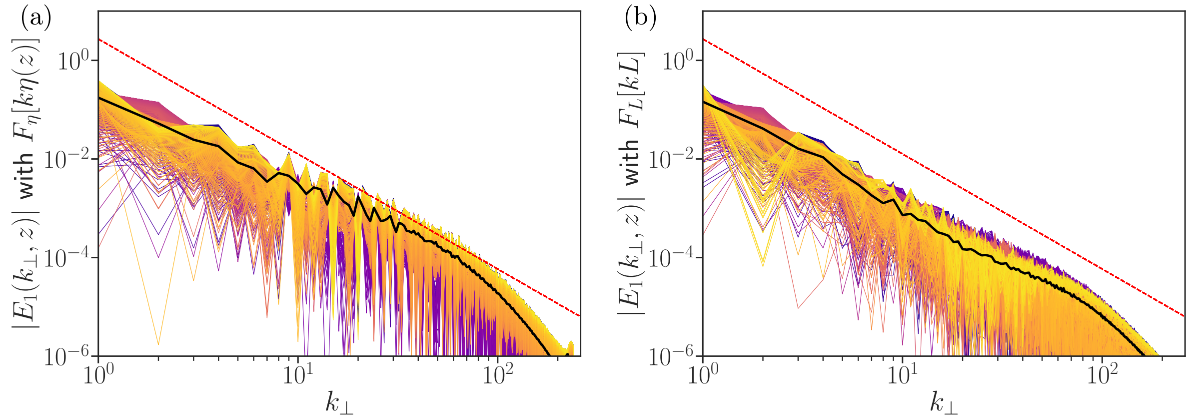

Figure 6.6: Absolute value of the time-averaged nonequilibrium energy spectrum $\left|E_1(k_\perp, z)\right| = \left|\left\langle E_1(k_\perp, z, t)\right\rangle_t\right|$ for the highest Reynolds number dataset. Different nondimensionalised functions are employed to compute the nonequilibrium spectrum; panel (a) with (6.54) and (b) with (6.56), respectively. The black solid and red dashed lines denote the z-average and $k_\perp^{-7/3}$ scaling, respectively.

In order to compute the nonequilibrium contributions $E_1(k, z) = E(k, z) - E_0(k, z)$, we need to know the z-dependence of $E_0(k, z)$. For this purpose, we use self-similarity assumptions and Kolmogorov's equilibrium hypothesis.

Scaling ranges in turbulence spectra appear when scale separation is attained, i.e., at sufficiently high Reynolds numbers. In general, one can write the energy spectrum to scale as,

$$E_0(k, z) \sim \epsilon(z)^{2/3} k^{-5/3} f_L[kL] f_\eta[k\eta(z)], \tag{6.51}$$

at high-Reynolds numbers. We have two nondimensional functions in (6.51); the f_L determines the shape of the spectrum for small k (large-scale) and f_η for large k (small-scale), respectively. These functions satisfy the framework of Kolmogorov (1941a),

$$\lim_{x\to 0} f_\eta[x] = \lim_{x\to\infty} f_L[x] = 1. \tag{6.52}$$

Therefore, we retrieve (6.1) for scales $L^{-1} \ll k \ll \eta^{-1}$ in the limit of $L/\eta \to \infty$. Multiplying both sides of (6.51) by $\eta^{-5/3}$ and dividing by $\epsilon^{2/3}$, we obtain

$$\frac{E_0(k, z)}{\epsilon(z)^{1/4}\nu^{5/4}} = F_\eta[k\eta(z)] f_L[kL], \tag{6.53}$$

with

$$F_\eta[k\eta(z)] = (k\eta)^{-5/3} f_\eta[k\eta(z)]. \tag{6.54}$$

Since $F(kL)$ tends to unity for $k \gg 1/L$, the equilibrium spectra $E_0(k, z)$ should collapse when normalised by (6.53) for any z, for large kL.

Similarly, if the large scales are characterised by a length scale L, we can propose an alternative normalisation for (6.53),

$$\frac{E_0(k, z)}{\epsilon(z)^{2/3} L^{5/3}} \sim F_L[kL] f[k\eta], \tag{6.55}$$

with

$$F_L[kL] = (kL)^{-5/3} f_L[kL]. \tag{6.56}$$

It should scale purely as a function of kL for $k\eta \ll 1$.

There are, therefore, two normalisation possibilities. One focuses on the high wavenumber limit of the inertial range close to the dissipation range (6.53)–(6.54), the other one on the low k range close to the energy-range (6.55)–(6.56). In the limit of infinite Reynolds number, we should find them to be equivalent in the inertial range, since

$$\lim_{x\to\infty} F_L[x] = \lim_{x\to 0} F_\eta[x] = x^{-5/3}. \tag{6.57}$$

Figure 6.6 plots the absolute value of the nonequilibrium energy spectrum $E_1(k_\perp, z)$ for these two normalisations. It is observed that using $F[kL]$ we reveal a larger inertial range. We will therefore use this normalisation in the present investigation.

Since the kinetic energy is dominantly determined by large scales, (6.55) allows us to determine the equilibrium kinetic energy profile,

$$K_0(z) = \int E_0(k,z)\,\mathrm{d}k = C_L \epsilon(z)^{2/3} L^{2/3} \tag{6.58}$$

with $C_L = \int F_L[x]\,\mathrm{d}x$. Then, we define the decomposition

$$K_0(z) = \left\langle K(z)\right\rangle_z + \widetilde{K}_0(z), \tag{6.59}$$

where $\left\langle K_0(z)\right\rangle_z = \left\langle K(z)\right\rangle_z$ follows from the assumption that $\left\langle K_1(z)\right\rangle_z = 0$. By employing the decomposition for the energy dissipation rate profile

$$\epsilon(z)^{2/3} = \left\langle \epsilon(z)^{2/3}\right\rangle_z + \widetilde{\epsilon(z)^{2/3}}, \tag{6.60}$$

it follows from (6.58) that

$$\frac{\widetilde{K}_0(z)}{\left\langle K_0(z)\right\rangle_z} = \frac{\widetilde{\epsilon(z)^{2/3}}}{\left\langle \epsilon(z)^{2/3}\right\rangle_z}, \tag{6.61}$$

and by (6.59),

$$K_0(z) = \left(1 + \frac{\widetilde{\epsilon(z)^{2/3}}}{\left\langle \epsilon(z)^{2/3}\right\rangle_z}\right)\left\langle K(z)\right\rangle_z. \tag{6.62}$$

Since all the terms on the RHS are known, one can evaluate the nonequilibrium kinetic energy profile $K_1(z) = K(z) - K_0(z)$ (see (6.47)).

Figure 6.7 shows the isotropic energy spectrum $E(k,t)$ (see (6.18) for the definition) at three different Taylor-length Reynolds numbers. For simplicity, we denote its time-average by $E(k) = \left\langle E(k,t)\right\rangle_t$. Normalisation using ν and $\epsilon = \left\langle \epsilon(\boldsymbol{x},t)\right\rangle_{\Omega,t}$ allows an excellent collapse for large values of k.

Next, we assess energy spectra in statistically homogeneous planes perpendicular to the z axis, as defined in (6.13). In the following, we analyse the time-averaged inhomogeneous energy spectrum $E(k_\perp, z) = \left\langle E(k_\perp, z, t)\right\rangle_t$ in a statistically steady state (see table 6.1). Figure 6.8(a) shows $E(k_\perp, z)$ nondimensionalised by $\overline{\epsilon}(z)^{2/3} L^{2/3}$. The fluctuations at small scales are small, and variations are barely visible.

In this study, we employ large-scale normalisation in (6.55) and evaluate

$$f_L[k_\perp L] \equiv \left\langle E(k_\perp, z)\overline{\epsilon}(z)^{-2/3} k_\perp^{5/3}\right\rangle_z, \tag{6.63}$$

as shown in figure 6.8(a). Note that this expression is valid for $k_\perp \eta \ll 1$ where $f_\eta(k_\perp \eta)$ tends to a constant value. Then, the equilibrium spectrum can be defined as

$$E_0(k_\perp, z) \equiv \overline{\epsilon}(z)^{2/3} f_L[k_\perp L] k_\perp^{-5/3}. \tag{6.64}$$

Now, we can evaluate the nonequilibrium spectrum by $E_1(k_\perp, z) \equiv E(k_\perp, z) - E_0(k_\perp, z)$. Note that i) this quantity is defined by the time-averaged spectra and ii) since this quantity can be regarded as a perturbation of $E(k_\perp, z)$ around $E_0(k_\perp, z)$, it can be both positive and negative. Figure 6.8(b) shows the z-average of $E(k_\perp, z)$ for specific signs. Similar plots are shown in figure 10 of Horiuti and Ozawa (2011)

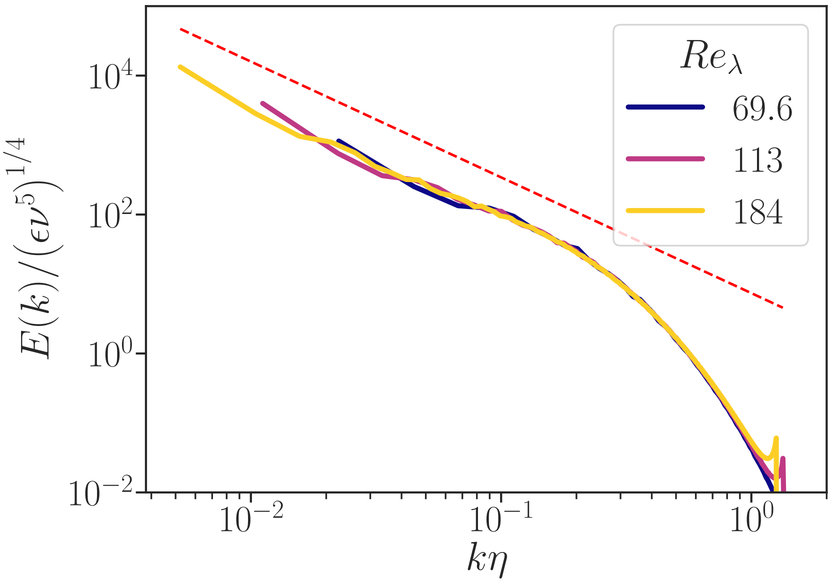

Figure 6.7: Time-averaged three-dimensional isotropic energy spectrum $E(k) = \langle E(k,t)\rangle_t$, normalised by Kolmogorov variables. Results are shown at $\mathrm{Re}_\lambda = 69.6, 113$ and 184 (see table 6.1). The red dashed line denotes the $k^{-5/3}$ scaling for reference.

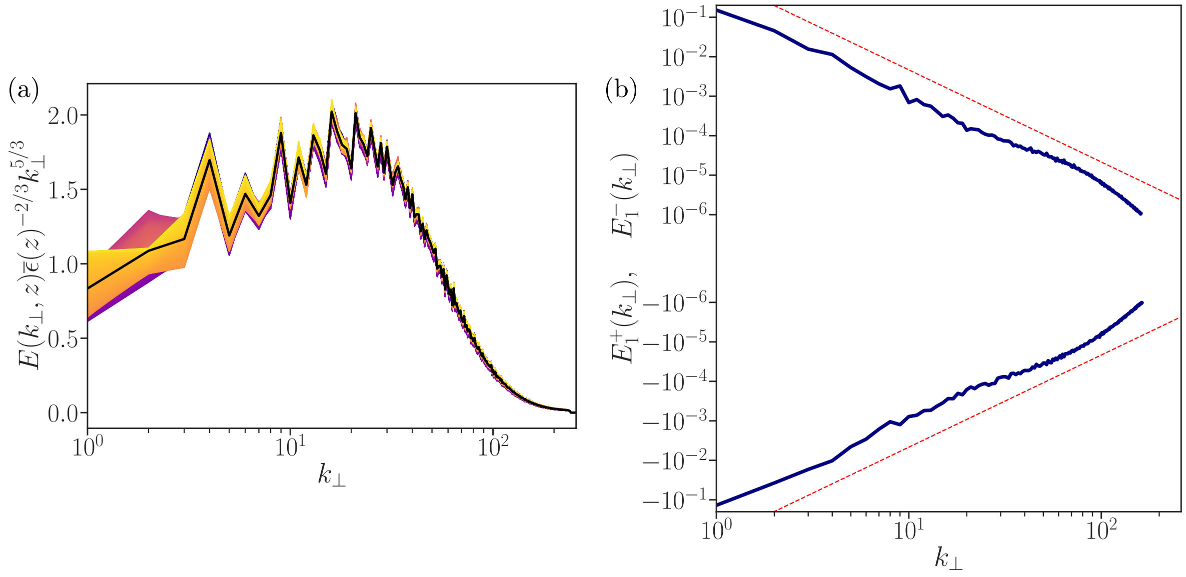

Figure 6.8: (a) Nondimensionalised two-dimensional energy spectrum. Note that $E(k_\perp, z) = \langle E(k_\perp, z, t)\rangle_t$. Dark (light) colour represents the small (large) value of z coordinate. The thick black line denotes (6.63), the average over z coordinate. (b) Time-averaged nonequilibrium energy spectrum with specific signs: $E_1^+(k_\perp) = \langle E_1(k_\perp, z) > 0\rangle_z$ and $E_1^-(k_\perp) = \langle E_1(k_\perp, t) < 0\rangle_z$. Red dashed lines denote the $k_\perp^{-7/3}$ slope.

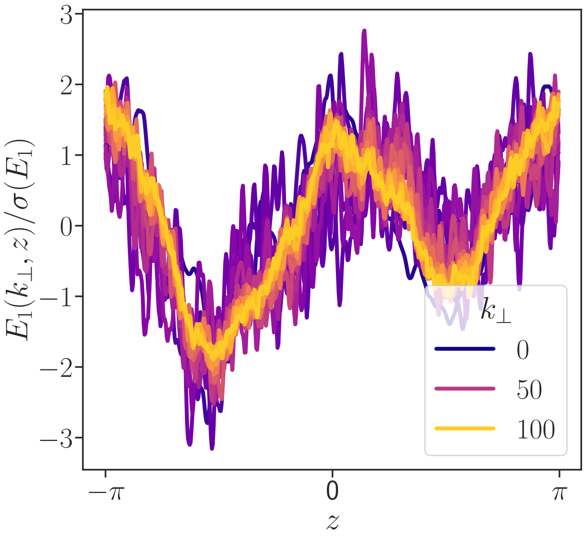

Figure 6.9: z profile of $E_1(k_\perp, z)$ at different $k_\perp$ normalised by their standard deviation $\sigma(E_1)$. The darker (lighter) colour denotes smaller (larger $k_\perp$).

and figure 2 of Horiuti and Tamaki (2013). The scaling is consistent with the one derived in § 6.2.4,

$$\left\langle \left| E_1(k_\perp, z) \right| \right\rangle_z \propto k_\perp^{-7/3}. \tag{6.65}$$

Figure 6.9 shows the z profile of $E_1(k_\perp, z)$ for $0 \leq k_\perp \leq 100$. This profile is in phase with $\epsilon(z)$ shown in Fig. 6.5(a) and thus consistent with the theoretical prediction (6.39).

Figure 6.10(a) compares $\left\langle \left| E_1(k_\perp, z) \right| \right\rangle_z$ for three different Reynolds numbers as in figure 6.7. For smaller values of Re_λ, the spectrum exhibits steeper scaling than $k_\perp^{-7/3}$. At larger Re_λ, the slope approaches the $k_\perp^{-7/3}$ scaling. At the same time, the spectrum in the higher $k_\perp$ range exhibits a bump associated with shallower scaling than $k_\perp^{-7/3}$.

We plot the compensated spectra in figure 6.10(b). Although the scaling range extends for less than a decade, the emergence of the $k_\perp^{-7/3}$ scaling range is well captured using this normalisation. In figure 6.6, we confirm that the bump in the compensated spectra is due to our choice of the nondimensional function (6.51).

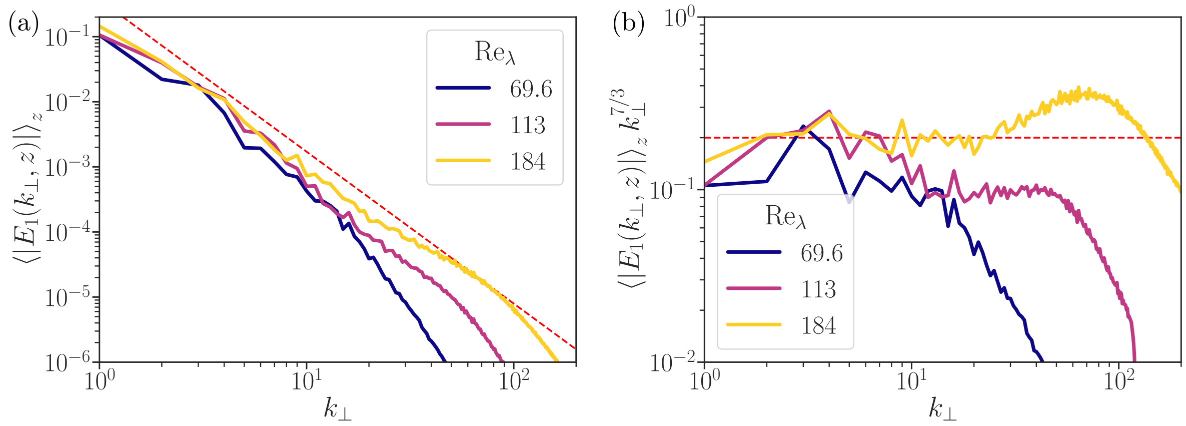

Figure 6.10: (a) Absolute value of the time-averaged nonequilibrium energy spectrum $\left|E_1(k_\perp,z)\right| = \left|\left\langle E_1(k_\perp,z,t)\right\rangle_t\right|$ for three values of the Taylor-length Reynolds numbers. The red dashed line represents the $k_\perp^{-7/3}$ scaling. (b) Compensated spectrum of the panel (a). The red dashed line denotes the compensated $k_\perp^{-7/3}$ scaling.

6.4 Concluding remarks

The numerical simulations in the previous section support our prediction,

$$E(k,z) = C_K \epsilon(z)^{2/3} k^{-5/3} - C_A \frac{\epsilon_{zz}(z) L^{4/3}}{\epsilon(z)^{1/3}} k^{-7/3}, \tag{6.66}$$

of the energy spectrum for turbulence with inhomogeneity in the z direction. This scaling quantifies the influence of spatial inhomogeneity in wavenumber space. In particular, the special case where the dissipation fluctuates as a sinusoidal function around a mean value, discussed in §6.2.5, gives us a useful estimate of the influence of inhomogeneity (6.41)–(6.42). Indeed, introducing an average dissipation $\langle\epsilon\rangle$ and smooth spatial fluctuations $\tilde{\epsilon}$ around $\langle\epsilon\rangle$, so that $\epsilon_{zz}/\tilde{\epsilon} \sim L^{-2}$, we obtain that

$$\frac{E_1^X(k,z)}{E_0(k,z)} \sim \frac{\tilde{\epsilon}}{\langle\epsilon\rangle}(kL)^{-2/3}. \tag{6.67}$$

This expression shows that the influence of large-scale inhomogeneity is negligible for

$$k \gg L^{-1}\left(\frac{\tilde{\epsilon}}{\langle\epsilon\rangle}\right)^{3/2}. \tag{6.68}$$

Therefore, if this requirement is fulfilled in a statistically stationary flow, far enough away from walls, Kolmogorov's equilibrium spectrum is expected to be dominant compared to the contributions associated with spatial inhomogeneity.

7 Dissipation Rate Scaling in Inhomogeneous or Unsteady Turbulence

This chapter investigates the scaling of the normalised energy dissipation rate of spatially inhomogeneous and temporally unsteady turbulence. The content is based on the following:

> Bos, Wouter J. T. and Ryo Araki (in preparation). Analysis of the normalized dissipation rate in inhomogeneous and unsteady turbulence.

First, we define the normalised energy dissipation rate in § 7.1 and discuss its relation with the equilibrium energy spectrum. The derivation of the inhomogeneous or unsteady scaling is provided in § 7.2, followed by their numerical assessment in § 7.3. We further discuss the choice of the length scale and its influence in § 7.4. We then conduct the linearisation of the scaling in § 7.5 to evaluate the scaling exponent. In § 7.6, we remark the influence of the large-scale energy distributions on the dissipation rate scaling, before concluding the chapter in § 7.7.

7.1 Fluctuations of the normalised energy dissipation rate

We begin our discussion, again, with the energy spectrum

$$E_0(k,\boldsymbol{x},t) = C_K \epsilon(\boldsymbol{x},t)^{2/3} k^{-5/3} \tag{7.1}$$

in the equilibrium inertial range of high Reynolds number turbulence. See § 1.2 for more details on the equilibrium description of turbulence. Its integral from L^{-1} to ∞ defines the equilibrium kinetic energy

$$K_0(\boldsymbol{x},t) = \frac{3}{2} C_K \epsilon(\boldsymbol{x},t)^{2/3} L(\boldsymbol{x},t)^{2/3}, \tag{7.2}$$

which is thus a function of ϵ and the characteristic length scale of the largest scales $L(\boldsymbol{x},t)$. Note that $L(\boldsymbol{x},t)$ can be a function of position and time, whereas k is not. For the influence of the large scales $k < L^{-1}$, refer to § 7.6.

By introducing the typical velocity fluctuations $U = \sqrt{2K/3}$, relation (7.2) leads to

$$\epsilon(\boldsymbol{x},t) = C_K^{-3/2} \frac{U(\boldsymbol{x},t)^3}{L(\boldsymbol{x},t)}, \tag{7.3}$$

which is Taylor's dissipation law (Taylor 1935). See § 1.2.3 for an alternative derivation, validation in the statistical sense and violation due to the nonequilibrium nature of turbulence. Now, we define the normalised energy dissipation rate

$$C_\epsilon(\boldsymbol{x},t) \equiv \frac{\epsilon(\boldsymbol{x},t) L(\boldsymbol{x},t)}{U(\boldsymbol{x},t)^3}. \tag{7.4}$$

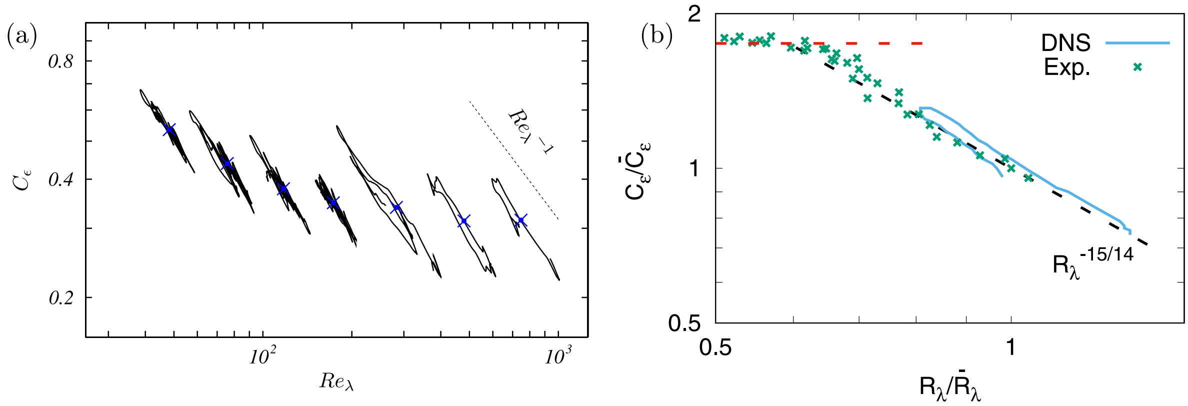

Figure 7.1: Taylor-scale Reynolds number $\mathrm{Re}_\lambda(t)$ dependency of the nondimenional energy dissipation rate $C_\epsilon(t)$. (a) In forced turbulence for different Reynolds numbers. Adapted from Goto and Vassilicos (2015, Figure 3). (b) The theoretical prediction along with numerical and experimental data. The numerical data is taken from panel (a). Adapted from Bos and Rubinstein (2017, Figure 1).

By comparing the expressions (7.3) and (7.4), the normalised dissipation rate should be constant and

$$\langle C_\epsilon(\boldsymbol{x},t)\rangle = C_K^{-3/2}, \tag{7.5}$$

irrespective of the Reynolds number. Note that this relation should hold in the average sense since C_ϵ is a function of space and time by definition (7.4). See § 1.2.3 and Fig. 1.6 for more details.

In the following, we review the scaling of fluctuations of C_ϵ. In Fig. 7.1(a), time series of the nondimenional energy dissipation rate $C_\epsilon(t)$ is plotted against the instantaneous Taylor-scale Reynolds number $\mathrm{Re}_\lambda(t)$ (Goto and Vassilicos 2015). Temporal fluctuations suggest $C_\epsilon(t) \propto \mathrm{Re}_\lambda(t)^{-1}$ scaling. The same quantity is plotted in Fig. 7.1(b), this time based on the equilibrium values denoted by $\bar{\cdot}$ (Bos and Rubinstein 2017). The theoretical investigations claim the refined scaling

$$C_\epsilon(t)/\overline{C_\epsilon} \propto \left(\mathrm{Re}_\lambda(t)/\overline{\mathrm{Re}}_\lambda\right)^{-15/14} \tag{7.6}$$

and very recently, this relation has been confirmed in wind tunnel experiment (Zheng et al. 2023).

Figure 7.2 shows the scaling for inhomogeneous turbulence in the wake of side-by-side square prisms (Chen et al. 2021). Specifically, they computed

$$C'_\epsilon \equiv \frac{\overline{\epsilon'}}{\overline{k'}^{3/2}/L} \quad \text{and} \quad Re'_\lambda \equiv \frac{\overline{k'}^{1/2}\lambda'}{\nu} \tag{7.7}$$

by the kinetic energy k, the integral length scale L, and the Taylor local length scale λ to find a $Re_\lambda'^{-3/2}$ scaling. Here, the prime symbol $\cdot'$ denotes turbulent fluctuations and the overbar $\bar{\cdot}$ denotes the time average. To collapse different datasets, they proposed a refined scaling

$$C'_\epsilon \sim \left(\sqrt{Re_L}/Re'_\lambda\right)^{3/2}. \tag{7.8}$$

Here, Re_L denotes the global Reynolds number, defined by the average over the entire measurement domain.

In (7.6) and (7.8), we have different scalings for temporal and spatial modulations. The objective of this chapter is to provide a unified description for them. To this end, we investigate the scaling of $C_\epsilon(\boldsymbol{x},t)$ against the local Taylor-scale Reynolds number (Valente and Vassilicos 2012; Hearst and Lavoie 2014;

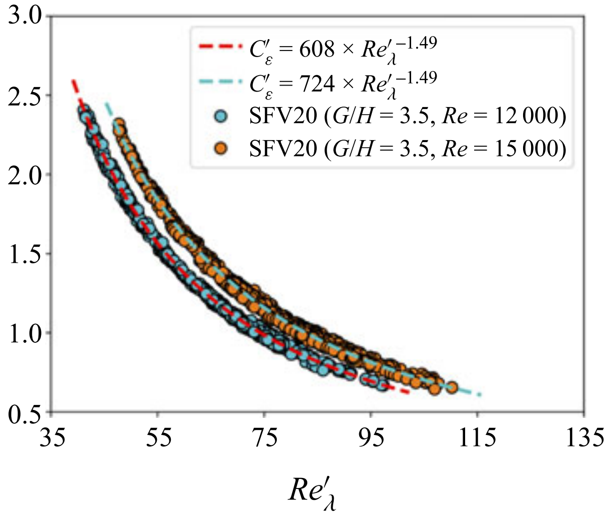

Figure 7.2: Scatter plot of C'_ϵ and Re'_λ for two different inlet Reynolds numbers: $Re = 1.2 \times 10^4$ and $Re = 1.5 \times 10^4$. "SFV" denotes "Small Field of View" and 20 denotes the measurement position. The parameters G and H denote the distance between the prisms and the prism width, respectively. Adapted from Chen et al. (2021, Figure 20(f)).

Goto and Vassilicos 2015)

$$\mathrm{Re}_\lambda(\boldsymbol{x}, t) \equiv \sqrt{\frac{20}{3}} \frac{K(\boldsymbol{x}, t)}{\sqrt{\nu\epsilon(\boldsymbol{x}, t)}}. \tag{7.9}$$

In particular, we consider the effect of statistical inhomogeneity and nonstationarity.

7.2 Derivation of the normalised energy dissipation rate scaling

In this section, we theoretically analyse the normalised energy dissipation rate scaling. We first focus on the corrections to the kinetic energy spectrum in § 7.2.1, then conduct linear perturbation analysis in § 7.2.2. See Fang and Bos (2023) for the same analysis in an EDQNM approach.

7.2.1 Corrections to the kinetic energy spectrum

Here, we introduce several quantities discussed in Chap. 6. We considered the equilibrium/nonequilibrium decomposition of the kinetic energy spectrum

$$E(k, \boldsymbol{x}, t) = E_0(k, \boldsymbol{x}, t) + E_1(k, \boldsymbol{x}, t) = C_K \epsilon(\boldsymbol{x}, t)^{2/3} k^{-5/3} + A(\boldsymbol{x}, t) k^{-7/3}, \tag{7.10}$$

where both spatial and temporal corrections are associated with a steeper scaling $\sim k^{-7/3}$, as discussed in § 6. Here, the coefficient of the perturbation spectrum reads

$$A^T(\boldsymbol{x}, t) = C_Y \frac{\dot{\epsilon}(\boldsymbol{x}, t)}{\epsilon(\boldsymbol{x}, t)^{2/3}} \tag{7.11}$$

for temporal correction (6.3) and

$$A^X(\boldsymbol{x}, t) = -C_A \frac{\epsilon_{zz}(z, t) L(z, t)^{4/3}}{\epsilon(z, t)^{1/3}} \tag{7.12}$$

for spatial correction (6.39), respectively. Note that we employ shorthand notations $\dot{(\cdot)} = \mathrm{d}(\cdot)/\mathrm{d}t$ for the temporal derivative and $(\cdot)_{zz} = \partial^2(\cdot)/\partial z^2$ for the second spatial derivative, respectively. The integral of the energy spectrum yields the decomposition of the kinetic energy

$$K(\boldsymbol{x},t) \equiv \int_{L^{-1}}^{\eta^{-1}} E(k,\boldsymbol{x},t)\,\mathrm{d}k = K_0(\boldsymbol{x},t) + K_1(\boldsymbol{x},t). \tag{7.13}$$

Here, in the limit of high-Reynolds number or $L/\eta \to \infty$, the integral in (7.13) is determined by its lower bound $k \sim L^{-1}$. Thus, the integral to determine the kinetic energy does not depend on the upper bound of the spectrum $k \sim \eta^{-1}$ associated with viscosity. For the influence of the large scales $k < L^{-1}$, refer to § 7.6.

On the contrary, the integral to determine the kinetic energy dissipation rate depends on the viscosity. For example, when we compute the ratio of the nonequilibrium against the equilibrium energy dissipation rate, it yields

$$\begin{aligned}\frac{\epsilon_1}{\epsilon_0} &= \frac{\int_{L^{-1}}^{\eta^{-1}} 2\nu k^2 E_1(k,\boldsymbol{x},t)\,\mathrm{d}k}{\int_{L^{-1}}^{\eta^{-1}} 2\nu k^2 E_0(k,\boldsymbol{x},t)\,\mathrm{d}k} && (7.14)\\ &= \frac{2A\left(\eta^{-2/3} - L^{-2/3}\right)}{C_K \epsilon^{2/3}\left(\eta^{-4/3} - L^{-4/3}\right)} \sim \eta^{2/3} \ll 1. && (7.15)\end{aligned}$$

Note that we consider $L/\eta \to \infty$ limit in the second line. Since $\eta \sim L\,\mathrm{Re}_\lambda^{-3/2} \to 0$ for a large Reynolds number limit, the perturbation component ϵ_1 does not significantly contribute to the total kinetic energy dissipation. In other words, we have

$$\epsilon \approx \epsilon_0 \tag{7.16}$$

for a large Reynolds number limit.

7.2.2 Perturbation analysis of the energy dissipation rate

Since the nonequilibrium energy dissipation rate does not significantly affect the total dissipation, we will consider the following decomposition

$$\epsilon(\boldsymbol{x},t) = \big\langle \epsilon(\boldsymbol{x},t) \big\rangle + \tilde{\epsilon}(\boldsymbol{x},t) \tag{7.17}$$

with $|\tilde{\epsilon}| \,/\, \langle \epsilon \rangle \ll 1$. Here, $\big\langle \epsilon(\boldsymbol{x},t) \big\rangle$ denotes the equilibrium component, and $\tilde{\epsilon}(\boldsymbol{x},t)$ is a small periodic perturbation in both temporal and spatial domains. To that, we assume a spatially homogeneous flow for temporal perturbations and a temporally steady flow for spatial perturbations, respectively. Thus, the bracket $\langle \cdot \rangle$ in (7.17) denotes plane-temporal average for steady flow

$$\langle \epsilon \rangle_{\perp,t}(z) = \langle \epsilon \rangle \left[1 + \alpha_\epsilon \sin(qz)\right] \tag{7.18}$$

and spatial average for homogeneous flow

$$\langle \epsilon \rangle_{\Omega}(t) = \langle \epsilon \rangle \left[1 + \alpha_\epsilon \sin(\omega t)\right], \tag{7.19}$$

respectively. Here, α_ϵ denotes the amplitude of the small perturbations, and we employ a sinusoidal function to express the periodic perturbations. In the following, we employ the general notation $\epsilon(\boldsymbol{x},t)$ for both $\langle \epsilon \rangle_{\Omega}(t)$ and $\langle \epsilon \rangle_{\perp,t}(z)$. We will provide specific expressions for both cases and omit the bracket symbol where there is no ambiguity.

Then, the equilibrium/nonequilibrium kinetic energy profile is expressed by

$$\begin{aligned}K(\boldsymbol{x},t) &\equiv K_0(\boldsymbol{x},t) + K_1(\boldsymbol{x},t) && (7.20)\\ &= \frac{3}{2} C_K \epsilon(\boldsymbol{x},t)^{2/3} L^{2/3} + \frac{3}{4} A(\boldsymbol{x},t) L^{4/3} && (7.21)\\ &= \frac{3}{2} C_K \epsilon(\boldsymbol{x},t)^{2/3} L^{2/3} \left[1 + \Delta(\boldsymbol{x},t)\right] && (7.22)\end{aligned}$$

with

$$\Delta(\boldsymbol{x},t) = \frac{1}{2}\frac{A(\boldsymbol{x},t)L^{2/3}}{C_K\epsilon(\boldsymbol{x},t)^{2/3}}. \tag{7.23}$$

From (7.22), the nondimensional energy dissipation rate can be expressed as

$$C_\epsilon^{k_f}(\boldsymbol{x},t) \equiv \frac{\epsilon(\boldsymbol{x},t)L}{\left[2K(\boldsymbol{x},t)/3\right]^{3/2}} \tag{7.24}$$

$$= C_K^{-3/2}\left[1+\Delta(\boldsymbol{x},t)\right]^{-3/2}. \tag{7.25}$$

Here, we fix the characteristic length scale L to be the inverse of the forced wavenumber: $L = k_f^{-1}$. To explicitly distinguish this choice, we employ the superscript $\cdot^{k_f}$. See § 7.4 for an alternative choice.

Next, we consider the Reynolds number. To obtain a perturbative expression, we introduce a global Reynolds number

$$\mathrm{Re}_0 \equiv \frac{20}{3}\frac{\langle K\rangle}{\sqrt{\nu\langle\epsilon\rangle}}. \tag{7.26}$$

We can express the standard Taylor-scale Reynolds number (7.9) by Re_0 as

$$\mathrm{Re}_\lambda(\boldsymbol{x},t) = \frac{K(\boldsymbol{x},t)}{\langle K\rangle}\left(\frac{\langle\epsilon\rangle}{\epsilon(\boldsymbol{x},t)}\right)^{1/2}\mathrm{Re}_0 \tag{7.27}$$

$$= \left[1+\Delta(\boldsymbol{x},t)\right]\left(\frac{\epsilon(\boldsymbol{x},t)}{\langle\epsilon\rangle}\right)^{1/6}\mathrm{Re}_0\,. \tag{7.28}$$

Now, we have expressions for both $C_\epsilon^{k_f}$ (7.25) and Re_λ (7.28).

For the spatial inhomogeneity scaling, assuming statistical stationarity, we obtain the following expressions:

$$C_\epsilon^{k_f}(z) = C_K^{-3/2}\left[1+\Delta(z)\right]^{-3/2} \quad \text{and} \quad \mathrm{Re}_\lambda(z) = \left[1+\Delta(z)\right]\left(\frac{\epsilon(z)}{\langle\epsilon\rangle}\right)^{1/6}\mathrm{Re}_0 \tag{7.29}$$

with

$$\Delta(z) = (qX)^2\frac{\alpha_\epsilon\sin(qz)}{1+\alpha_\epsilon\sin(qz)} \quad \text{where} \quad X = L\left(\frac{C_A}{2C_K}\right)^{1/2}. \tag{7.30}$$

Similarly, for the temporal unsteady scaling, assuming statistical homogeneity, we obtain the following expressions:

$$C_\epsilon^{k_f}(t) = C_K^{-3/2}\left[1+\Delta(t)\right]^{-3/2} \quad \text{and} \quad \mathrm{Re}_\lambda(t) = \left[1+\Delta(z)\right]\left(\frac{\epsilon(t)}{\langle\epsilon\rangle}\right)^{1/6}\mathrm{Re}_0 \tag{7.31}$$

with

$$\Delta(t) = \omega\mathcal{T}\frac{\alpha_\epsilon\cos(\omega t)}{\left[1+\alpha_\epsilon\sin(\omega t)\right]^{4/3}} \quad \text{where} \quad \mathcal{T} = \frac{C_Y}{2C_K}\frac{L^{2/3}}{\epsilon^{1/3}}. \tag{7.32}$$

Note that the ratios $\epsilon(z)/\langle\epsilon\rangle$ and $\epsilon(t)/\langle\epsilon\rangle$ are evaluated from (7.18) and (7.19), respectively. Furthermore, to complete these expressions, we need to fix the free parameters α_ϵ, qX, and $\omega\mathcal{T}$. Note that the angular velocity ω can be related to the characteristic time scale of temporal fluctuations, as discussed in § 3.1 with Fig. 3.1. However, due to the difference in the external forcing configurations[1], it is not possible to perform direct comparison between the two flows.

---

[1] We employ the two-dimensional Taylor–Green forcing (3.2) in § 3 and the Kolmogorov forcing (6.46) in the following sections of this chapter, respectively.

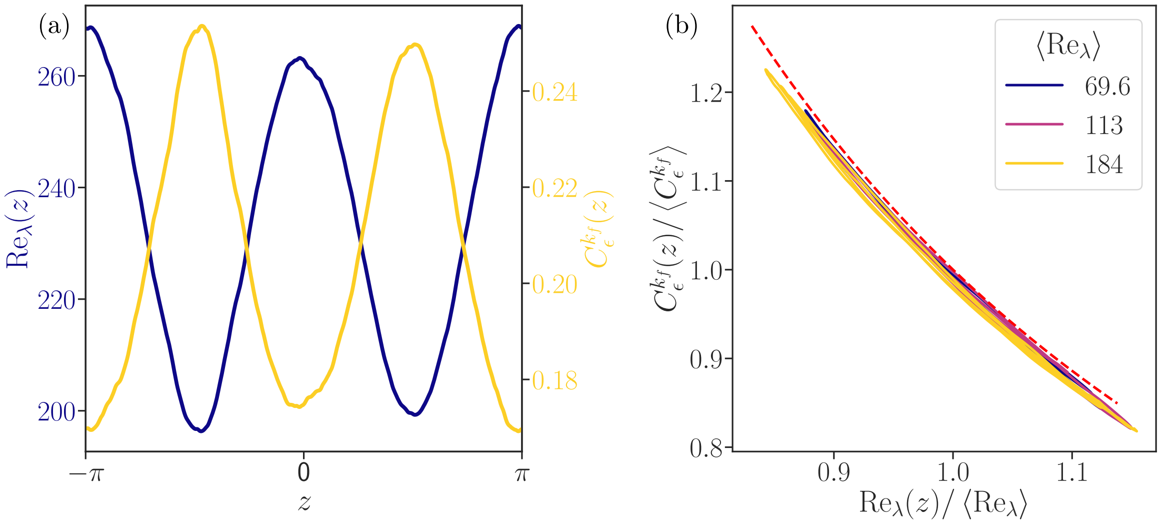

Figure 7.3: (a) z-profile of the normalised energy dissipation rate $C_\epsilon^{k_f}(z)$ and the Reynolds number $\mathrm{Re}_\lambda(z)$. (b) Parametric plot of $C_\epsilon^{k_f}(z)$ as a function of $\mathrm{Re}_\lambda(z)$. Both quantities are divided by their average values: $\left\langle C_\epsilon^{k_f}\right\rangle$ and $\langle \mathrm{Re}_\lambda\rangle$, respectively. Results for three $\langle \mathrm{Re}_\lambda\rangle$ are shown. The red dashed line indicates a theoretical relation (7.29) with $\alpha_\epsilon = 0.13$ and $qX = 1$.

7.3 Numerical assessment of the dissipation rate scaling

To assess the theoretical discussion in the previous section, we employ the same Kolmogorov flow dataset as in Chap. 6. The advantage of this setup is that due to the unidirectional forcing, $f(z) = \sin(k_f z)$ with $k_f = 1$, the dataset is statistically inhomogeneous in this direction. Furthermore, the flow exhibits large-scale quasi-cyclic temporal fluctuations where the time scale is comparable to the integral one, as we have investigated in detail for a different forcing setup in Chap. 3. Thus, we use the Kolmogorov flow dataset to analyse the spatial and temporal scalings simultaneously. For details of the numerical scheme and dataset, refer to § 6.3.1 and Figs. 6.4–6.5.

In this section, we investigate the spatial and temporal fluctuations in § 7.3.1 and § 7.3.2, respectively. Note that in this section, we choose the forcing length $k_f = 1$ as the inverse of the characteristic length scale of the largest scales: $k_f = L^{-1}$. We will discuss an alternative choice of the characteristic length scale in § 7.4.

7.3.1 Spatial fluctuations and their scaling

We have already provided the instantaneous, time-averaged, and trigonometrically fitted energy dissipation rate profile (6.40) in Fig. 6.5. Note that $\epsilon(z)$ is a shortened notation of $\left\langle \epsilon(\boldsymbol{x}, t)\right\rangle_{\perp,t}$, where the subscript denotes the average over (x, y) plane and time. Figure 7.3(a) shows the z-profile of $C_\epsilon^{k_f}(z)$ and $\mathrm{Re}_\lambda(z)$ displaying a clear anti-phase relationship. In Fig. 7.3(b), we overlap parametric plots of $C_\epsilon^{k_f}(z)$–$\mathrm{Re}_\lambda(z)$ for the three datasets by normalising both quantities by their average. The dataset information is summarised in Table 6.1. By overlapping the theoretical relation (7.29), we observe a nice collapse between the theory and the numerical results. Here, we set $\alpha_\epsilon = 0.13$ from the relative amplitude of the fitted energy dissipation rate profile $\bar{\epsilon}(z)$ in Fig. 6.5(a). The other free parameter qX is treated as a fitting parameter and set to be unity.

7.3.2 Temporal fluctuations and their scaling

Figure 7.4(a) shows temporal evolution of $\mathrm{Re}_\lambda(t)$, and $C_\epsilon^{k_f}(t)$. We observe a similar anti-phase trend, as in the inhomogeneous case in Fig. 7.3(a), in complex fluctuations. The normalised parametric plot in Fig. 7.4(b) shows wider distributions than in Fig. 7.3(b). The theoretical relation (7.31) represents an ellipse-like trajectory, which indeed captures the characteristics of the numerical data. Here, we set

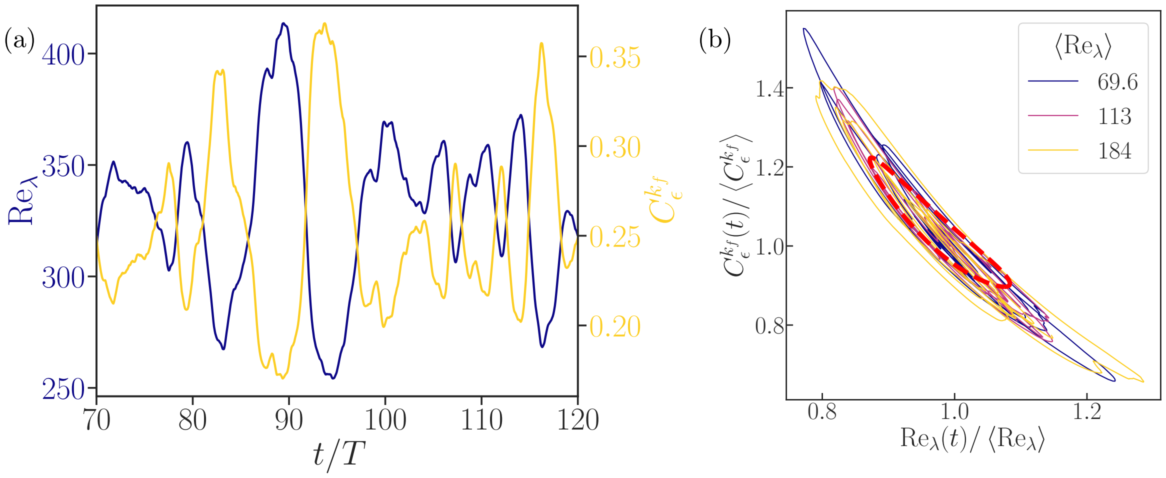

Figure 7.4: Same as Fig. 7.3, but for temporal fluctuations. Panel (b) shows $50T_f$ for three datasets. The red dashed line indicates a theoretical relation (7.31) with $\alpha_\epsilon = 0.19$ and $\omega\mathcal{T} = 0.5$.

$\alpha_\epsilon = 0.19$ from the phase-averaged time series of $C_\epsilon^{k_f}(t)$. See Fig. 7.5 for more details. The other free parameter $\omega\mathcal{T}$ is treated as a fitting parameter and set to be 0.5.

To quantify the ellipse-like trajectory for the temporal scaling, we perform the phase averaging technique introduced in § 3.1. By averaging over segments of time series shifted relative to their local peaks, we can extract a smooth ellipse as shown in Fig. 7.5. Note that we skip the normalisation procedure of the local peak (see Fig. 3.3) to overlap the phase-averaged time series over the original turbulent time series. From the relative amplitude of the phase-averaged time series $\left\langle C_\epsilon^{k_f}\right\rangle_{\text{phase}}$, we set $\alpha_\epsilon = 0.19$. This value is used to draw the theoretical relation in Fig. 7.4(b).

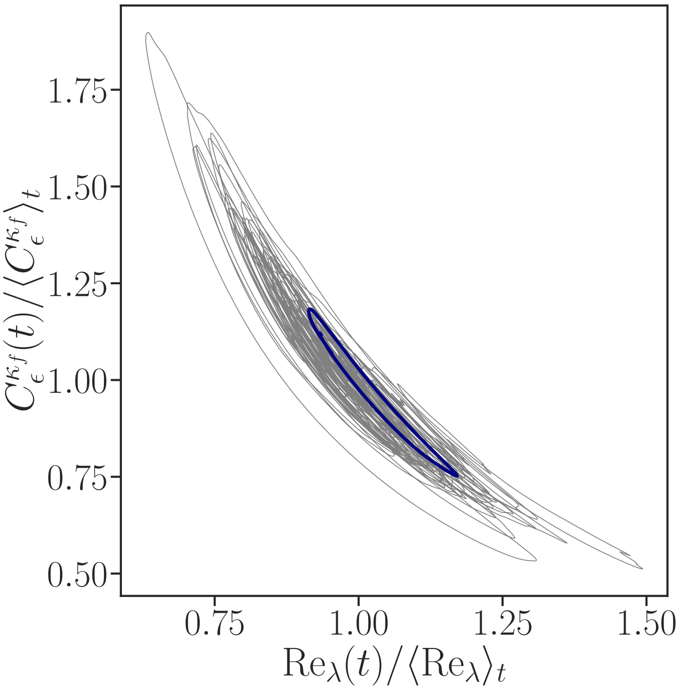

Figure 7.5: A time series of $C_\epsilon^{k_f}(t)$–$\mathrm{Re}_\lambda(t)$ (thin grey) and its phase-averaged time series (thick blue). Both quantities are divided by their time-averaged values.

7.4 Choice of the length scale

In the previous sections, we used the characteristic length scale $L = k_f^{-1}$ associated with the forced wavenumber and the peak of the energy spectrum. In this section, we consider an alternative definition to see how the choice of different length scales affects the scaling. Here, we define the integral length scale

$$\mathcal{L}(\boldsymbol{x},t) = \frac{3\pi}{4}\frac{I(\boldsymbol{x},t)}{K(\boldsymbol{x},t)} \tag{7.33}$$

with

$$I(\boldsymbol{x},t) = \int_{L^{-1}}^{\eta^{-1}} k^{-1}E(k,\boldsymbol{x},t)\,\mathrm{d}k\,, \tag{7.34}$$

and $K(\boldsymbol{x},t)$ defined by (7.13). It is important to note that the alternative choice of the characteristic length scale does not affect the integral range from L^{-1} to η. For the equilibrium/nonequilibrium decomposition, we find that

$$K_0(\boldsymbol{x},t) = \frac{3}{2}C_K\epsilon(\boldsymbol{x},t)^{2/3}L^{2/3}, \quad K_1(\boldsymbol{x},t) = \frac{3}{4}A(\boldsymbol{x},t)L^{4/3}, \tag{7.35}$$

and

$$I_0(\boldsymbol{x},t) = \frac{3}{5}C_K\epsilon(\boldsymbol{x},t)^{2/3}L^{5/3}, \quad I_1(\boldsymbol{x},t) = \frac{3}{7}A(\boldsymbol{x},t)L^{7/3}, \tag{7.36}$$

so that

$$I(\boldsymbol{x},t) = \frac{2}{5}L\left[K_0(\boldsymbol{x},t) + \frac{10}{7}K_1(\boldsymbol{x},t)\right]. \tag{7.37}$$

Thus, we have

$$\begin{aligned}\mathcal{L}(\boldsymbol{x},t) &= L\frac{3\pi}{4}\frac{1+\frac{10}{7}K_1(\boldsymbol{x},t)/K_0(\boldsymbol{x},t)}{1+K_1(\boldsymbol{x},t)/K_0(\boldsymbol{x},t)} &(7.38)\\ &= L\frac{3\pi}{4}\frac{1+\frac{10}{7}\Delta(\boldsymbol{x},t)}{1+\Delta(\boldsymbol{x},t)}, &(7.39)\end{aligned}$$

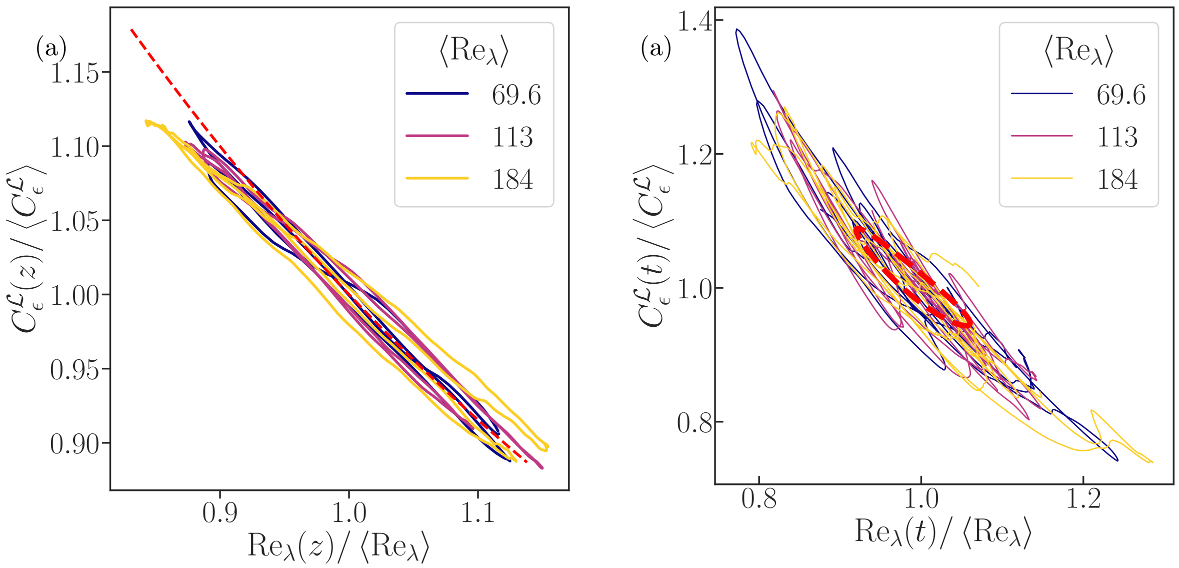

Figure 7.6: $C_\epsilon^{\mathcal{L}}$–Re$_\lambda$ scaling based on the integral length scale $\mathcal{L}$. Panels (a) and (b) corresponds to Fig. 7.3(b) and Fig. 7.4(b), respectively. The fitting parameters for the theoretical relation are: (a) $\alpha_\epsilon = 0.13$ and $qX = 1$ and (b): $\alpha_\epsilon = 0.13$ and $\omega\mathcal{T} = 0.5$.

with $\Delta(\boldsymbol{x}, t)$ defined in (7.23). This relation illustrates that the equilibrium value of $\mathcal{L}(\boldsymbol{x}, t)$, i.e. setting $K_1 = 0$, is proportional to $L = k_f^{-1}$, but the nonequilibrium contributions vary as a function of $\boldsymbol{x}$ and t. By replacing $\mathcal{L}$ in (7.4), the normalised energy dissipation rate reads

$$C_\epsilon^{\mathcal{L}}(\boldsymbol{x}, t) \equiv \frac{\epsilon(\boldsymbol{x}, t)\mathcal{L}(\boldsymbol{x}, t)}{\left[2K(\boldsymbol{x}, t)/3\right]^{3/2}} \tag{7.40}$$

$$= \frac{3\pi}{4} C_K^{-3/2} \left[1 + \frac{10}{7}\Delta(\boldsymbol{x}, t)\right] \left[1 + \Delta(\boldsymbol{x}, t)\right]^{-5/2}. \tag{7.41}$$

To explicitly distinguish this choice, we employ the superscript $\cdot^{\mathcal{L}}$ in the following. Again, our alternative choice of the characteristic length scale does not affect the expression of K (7.22), which is defined by the integral from L^{-1} to η^{-1}. Thus, the normalised energy dissipation (7.25) becomes

$$\frac{C_\epsilon^{\mathcal{L}}(\boldsymbol{x}, t)}{\langle C_\epsilon^{\mathcal{L}} \rangle} = \left[1 + \frac{10}{7}\Delta(\boldsymbol{x}, t)\right] \left[1 + \Delta(\boldsymbol{x}, t)\right]^{-5/2}, \tag{7.42}$$

where $\langle C_\epsilon^{\mathcal{L}} \rangle = 3\pi C_K^{-3/2}/4$ is also modified from (7.5). We can consider $C_\epsilon^{\mathcal{L}}(z)/\langle C_\epsilon^{\mathcal{L}} \rangle$ and $C_\epsilon^{\mathcal{L}}(t)/\langle C_\epsilon^{\mathcal{L}} \rangle$ according to (7.29) and (7.31), respectively.

Figure 7.6 shows the $C_\epsilon^{\mathcal{L}}$–Re$_\lambda$ scaling based on the integral length scale $\mathcal{L}$. A good agreement between the theoretical relation and numerical data is observed for both panels.

7.5 Linearisation of the parametric plots between C_ϵ and Re$_\lambda$

In this section, we conduct linearisation of the dissipation scaling to discuss the scaling coefficient. In § 7.5.1, we consider the scaling derived in § 7.2.2 with the forcing length scale $L = k_f^{-1}$. In § 7.5.2, we consider the scaling of § 7.4, associated with the integral length scale $\mathcal{L}$.

7.5.1 The −3/2 scaling with the forcing length scale

By linearising $C_\epsilon^{k_f}(z)$ (7.25) and $\mathrm{Re}_\lambda(z)$ (7.28), we obtain

$$\begin{aligned} C_\epsilon^{k_f}(\boldsymbol{x},t) &= C_K^{-3/2}\big[1+\Delta(\boldsymbol{x},t)\big]^{-3/2} && (7.43)\\ &= C_K^{-3/2}\left[1-\frac{3}{2}\Delta(\boldsymbol{x},t)\right] \quad \text{and} && (7.44)\\ \mathrm{Re}_\lambda(\boldsymbol{x},t) &= \big[1+\Delta(\boldsymbol{x},t)\big]\left(\frac{\epsilon(\boldsymbol{x},t)}{\langle\epsilon\rangle}\right)^{1/6}\mathrm{Re}_0 && (7.45)\\ &= \big[1+\Delta(\boldsymbol{x},t)\big]\left(1+\frac{\tilde{\epsilon}(\boldsymbol{x},t)}{\langle\epsilon\rangle}\right)^{1/6}\mathrm{Re}_0 && (7.46)\\ &= \big[1+\Delta(\boldsymbol{x},t)\big]\left(1+\frac{1}{6}\frac{\tilde{\epsilon}(\boldsymbol{x},t)}{\langle\epsilon\rangle}\right)\mathrm{Re}_0 && (7.47)\\ &= \left[1+\Delta(\boldsymbol{x},t)+\frac{1}{6}\frac{\tilde{\epsilon}(\boldsymbol{x},t)}{\langle\epsilon\rangle}\right]\mathrm{Re}_0\,. && (7.48) \end{aligned}$$

For the inhomogeneous modulation case, we employ $A^X(\boldsymbol{x},t)$ (7.12) and $\epsilon(z)$ (7.18) to obtain

$$\begin{aligned} \frac{C_\epsilon^{k_f}(z)}{\left\langle C_\epsilon^{k_f}\right\rangle} &= 1-\frac{3}{2}\alpha_\epsilon (qX)^2\sin(qz) \quad \text{and} && (7.49)\\ \frac{\mathrm{Re}_\lambda(z)}{\langle \mathrm{Re}_\lambda\rangle} &= 1+\alpha_\epsilon\left[1+\frac{1}{6(qX)^2}\right](qX)^2\sin(qz). && (7.50) \end{aligned}$$

See (7.30) for the definition of X. Thus, the parametric plot of $C_\epsilon^{k_f}(z)$–$\mathrm{Re}_\lambda(z)$ exhibit a line with its slope close to −3/2 in Fig. 7.3(b). However, the slope should be somewhat steeper than −3/2, since the variations around the equilibrium value exhibit

$$\begin{aligned} \frac{\delta C_\epsilon^{k_f}(z)\big|_0}{\left\langle C_\epsilon^{k_f}\right\rangle} &\equiv \frac{\delta z}{\left\langle C_\epsilon^{k_f}\right\rangle}\left.\frac{\mathrm{d}C_\epsilon^{k_f}(z)}{\mathrm{d}z}\right|_{z=0} = -\frac{3}{2}\alpha_\epsilon q^3X^2, && (7.51)\\ \frac{\delta\,\mathrm{Re}_\lambda(z)\big|_0}{\langle \mathrm{Re}_\lambda\rangle} &\equiv \frac{\delta z}{\langle \mathrm{Re}_\lambda\rangle}\left.\frac{\mathrm{d}\,\mathrm{Re}_\lambda(z)}{\mathrm{d}z}\right|_{z=0} = \alpha_\epsilon\left[1+\frac{1}{6(qX)^2}\right]q^3X^2, && (7.52) \end{aligned}$$

and thus

$$\begin{aligned} \left.\frac{\delta C_\epsilon^{k_f}(z)}{\delta\,\mathrm{Re}_\lambda(z)}\right|_0 &= -\frac{3}{2}\frac{\langle \mathrm{Re}_\lambda\rangle}{\left\langle C_\epsilon^{k_f}\right\rangle}\frac{1}{1+\frac{1}{6(qX)^2}} && (7.53)\\ &\approx -\frac{3}{2}\left[1-\frac{1}{6}(qX)^2\right]. && (7.54) \end{aligned}$$

For the temporal modulation case, we employ $A^T(\boldsymbol{x},t)$ (7.11) and $\epsilon(t)$ (7.19) to obtain

$$\begin{aligned} \frac{C_\epsilon^{k_f}(t)}{\left\langle C_\epsilon^{k_f}\right\rangle} &= 1-\frac{3}{2}\alpha_\epsilon \omega\mathcal{T}\cos(\omega t) \quad \text{and} && (7.55)\\ \frac{\mathrm{Re}_\lambda(t)}{\langle \mathrm{Re}_\lambda\rangle} &= 1+\alpha_\epsilon\left[\omega\mathcal{T}\cos(\omega t)+\frac{1}{6}\sin(\omega t)\right]. && (7.56) \end{aligned}$$

See (7.32) for the definition of $\mathcal{T}$. Thus, the parametric plot of $C_\epsilon^{k_f}(t)$–$\mathrm{Re}_\lambda(t)$ exhibit a ellipse with its major axis have −3/2 slope in Figs. 7.4(b) and 7.5.

7.5.2 The $-15/14$ scaling with the integral length scale

By assuming a small amplitude of K_1 against K_0 or $K_1/K_0 \ll 1$ in (7.39), we can linearise the integral length scale to find

$$\mathcal{L}(\boldsymbol{x},t) = L\frac{3\pi}{4}\frac{1+\frac{10}{7}K_1(\boldsymbol{x},t)/K_0(\boldsymbol{x},t)}{1+K_1(\boldsymbol{x},t)/K_0(\boldsymbol{x},t)} \tag{7.57}$$

$$\sim L\frac{3\pi}{4}\left[1+\frac{3}{7}\Delta(\boldsymbol{x},t)\right]. \tag{7.58}$$

By employing the linearised $\mathcal{L}(\boldsymbol{x},t)$ and $K(\boldsymbol{x},t)$ in the definition of the normalised energy dissipation rate (7.40), we obtain the alternative expressions:

$$C_\epsilon^{\mathcal{L}}(\boldsymbol{x},t) \equiv \frac{\epsilon(\boldsymbol{x},t)\mathcal{L}(\boldsymbol{x},t)}{\left[2K(\boldsymbol{x},t)/3\right]^{3/2}} \tag{7.59}$$

$$\sim \left\langle C_\epsilon^{\mathrm{L}}\right\rangle\left[1-\frac{3}{2}\Delta(\boldsymbol{x},t)\right]\left[1+\frac{3}{7}\Delta(\boldsymbol{x},t)\right], \tag{7.60}$$

$$\frac{C_\epsilon^{\mathcal{L}}(\boldsymbol{x},t)}{\left\langle C_\epsilon^{\mathrm{L}}\right\rangle} \sim 1-\frac{15}{14}\Delta(\boldsymbol{x},t). \tag{7.61}$$

For the temporal modulation case

$$\frac{C_\epsilon^{\mathcal{L}}(t)}{\left\langle C_\epsilon^{\mathcal{L}}\right\rangle} = 1-\frac{15}{14}\alpha_\epsilon\omega\mathcal{T}\cos(\omega t) \tag{7.62}$$

and for the inhomogeneous modulation case

$$\frac{C_\epsilon^{\mathcal{L}}(z)}{\left\langle C_\epsilon^{\mathcal{L}}\right\rangle} = 1-\frac{15}{14}\alpha_\epsilon(qX)^2\sin(qz). \tag{7.63}$$

These new expressions and Re_λ (7.50, 7.56) lead to the $-15/14$ scaling in Fig. 7.6.

7.6 Influence of the large-scale energy distribution

In this section, we discuss the influence of the large-scale energy distribution on the dissipation rate scaling. To this end, we consider the following decomposition of the energy spectrum

$$E(k,\boldsymbol{x},t) = \underbrace{C_K\epsilon(\boldsymbol{x},t)^{2/3}k^{-5/3}F(kL)}_{E_0(k,\boldsymbol{x},t)} + \underbrace{A(\boldsymbol{x},t)k^{-7/3}G(kL)}_{E_1(k,\boldsymbol{x},t)}, \tag{7.64}$$

which is a refined expression of (7.10). Here, two nondimensional functions

$$F(x) = \begin{cases} x^{s+5/3} & \text{for} \quad x<1 & (7.65)\\ 1 & \text{for} \quad x\geq 1 & (7.66)\end{cases}$$

and

$$G(x) = \begin{cases} x^{s'+7/3} & \text{for} \quad x<1 & (7.67)\\ 1 & \text{for} \quad x\geq 1 & (7.68)\end{cases}$$

determine the behaviour of the energy spectrum on large scales as

$$E_0 \propto k^s \quad \text{and} \quad E_1 \propto k^{s'} \quad \text{for} \quad k<L^{-1}. \tag{7.69}$$

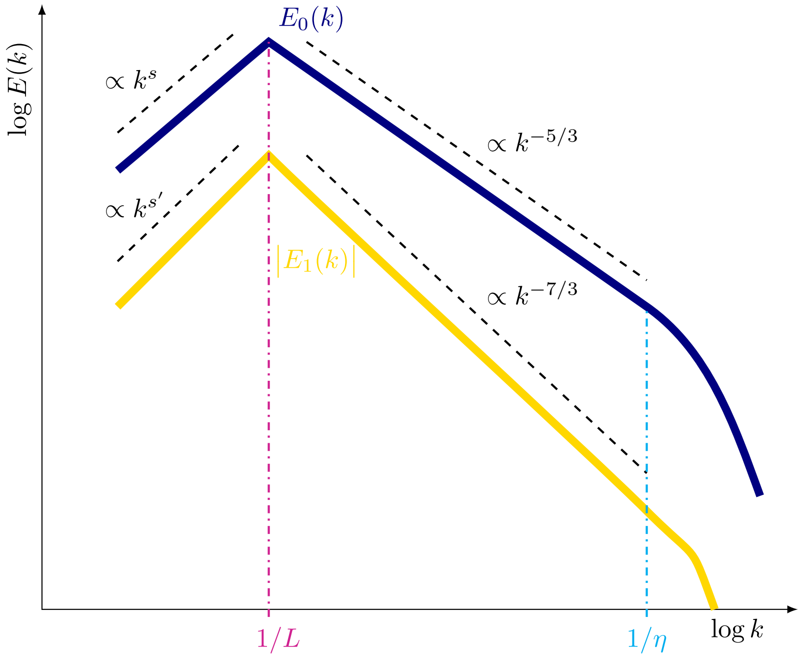

Figure 7.7: Schematic of equilibrium $E_0(k)$ and nonequilibrium $E_1(k)$ energy spectra with their large-scale distribution for $k < L^{-1}$. They exhibit $E_0(k) \propto k^{-5/3}$ and $E_1(k) \propto k^{-7/3}$ scalings for the inertial range $L^{-1} \ll k \ll k_\eta$, respectively. Their large-scale destribution is denoted by $E_0(k) \propto k^s$ and $E_1(k) \propto k^{s'}$, respectively.

Their integral defines

$$K(\boldsymbol{x},t) = \underbrace{\frac{3}{2}C_K\epsilon(\boldsymbol{x},t)^{2/3}L^{2/3}\int F(x)x^{-5/3}\,\mathrm{d}x}_{K_0(\boldsymbol{x},t)} + \underbrace{\frac{3}{4}A(\boldsymbol{x},t)L^{4/3}\int G(x)x^{-7/3}\,\mathrm{d}x}_{K_1(\boldsymbol{x},t)} \tag{7.70}$$

$$= \frac{3}{2}C_K\epsilon(\boldsymbol{x},t)^{2/3}L^{2/3}\int F(x)x^{-5/3}\,\mathrm{d}x\left[1+\Delta(\boldsymbol{x},t)\frac{\int G(x)x^{-7/3}\,\mathrm{d}x}{\int F(x)x^{-5/3}\,\mathrm{d}x}\right], \tag{7.71}$$

and

$$I(\boldsymbol{x},t) = \underbrace{\frac{3}{5}C_K\epsilon(\boldsymbol{x},t)^{2/3}L^{5/3}\int F(x)x^{-8/3}\,\mathrm{d}x}_{I_0(\boldsymbol{x},t)} + \underbrace{\frac{3}{7}A(\boldsymbol{x},t)L^{7/3}\int G(x)x^{-10/3}\,\mathrm{d}x}_{I_1(\boldsymbol{x},t)} \tag{7.72}$$

$$= \frac{3}{5}C_K\epsilon(\boldsymbol{x},t)^{2/3}L^{5/3}\int F(x)x^{-8/3}\,\mathrm{d}x\left[1+\frac{10}{7}\Delta(\boldsymbol{x},t)\frac{\int G(x)x^{-10/3}\,\mathrm{d}x}{\int F(x)x^{-8/3}\,\mathrm{d}x}\right], \tag{7.73}$$

respectively. Note that we consider the case with the integral length scale (§ 7.5.2). By substituting these additional integrals into the normalised energy dissipation rate (7.41), one obtains

$$C_\epsilon^{\mathcal{L}}(\boldsymbol{x},t) \equiv \frac{\epsilon(\boldsymbol{x},t)\mathcal{L}(\boldsymbol{x},t)}{\left[2K(\boldsymbol{x},t)/3\right]^{3/2}} \tag{7.74}$$

$$= \frac{3\pi}{4}\left(\frac{2}{3}\right)^{-3/2}\epsilon(\boldsymbol{x},t)I(\boldsymbol{x},t)K(\boldsymbol{x},t)^{-5/2} \tag{7.75}$$

$$\propto \left[1+\Delta(\boldsymbol{x},t)\right]^{\alpha}. \tag{7.76}$$

The scaling exponent reads

$$\alpha(s,s') = -\frac{5}{2} + \frac{\int G(x)x^{-10/3}\,\mathrm{d}x \int F(x)x^{-5/3}\,\mathrm{d}x}{\int G(x)x^{-7/3}\,\mathrm{d}x \int F(x)x^{-8/3}\,\mathrm{d}x} \tag{7.77}$$

$$= -\frac{5}{2} + \frac{\left(\int_0^1 x^{s'-1}\,\mathrm{d}x + \int_1^\infty x^{-10/3}\,\mathrm{d}x\right)\left(\int_0^1 x^{s}\,\mathrm{d}x + \int_1^\infty x^{-5/3}\,\mathrm{d}x\right)}{\left(\int_0^1 x^{s'}\,\mathrm{d}x + \int_1^\infty x^{-7/3}\,\mathrm{d}x\right)\left(\int_0^1 x^{s-1}\,\mathrm{d}x + \int_1^\infty x^{-8/3}\,\mathrm{d}x\right)} \tag{7.78}$$

$$= -\frac{5}{2} + \frac{\left(\frac{1}{s'} + \frac{3}{7}\right)\left(\frac{1}{s+1} + \frac{3}{2}\right)}{\left(\frac{1}{s'+1} + \frac{3}{4}\right)\left(\frac{1}{s} + \frac{3}{5}\right)}. \tag{7.79}$$

When we assume a sharp cutoff of the energy spectrum for $k < L^{-1}$, it corresponds to $s = s' = \infty$, and we obtain $\alpha(\infty,\infty) = -15/14$. Note that this exponent value is consistent with the linear perturbation analysis in § 7.5.2 and the current numerical configurations where the forcing scale and the box size are comparable. In fact, the above expression reduces to $\alpha(s,s') = -15/14$ when $s = s'$ is assumed. For example, $s = s' = 2$ corresponding to the equipartition of the energy would be a reasonable candidate. However, we can generally consider $s \neq s'$. For this case, the exponent $\alpha(s,s')$ can vary from $-15/14$. Further analysis on this aspect remains in future research.

7.7 Concluding remarks

The scaling of the normalised energy dissipation rate C_ϵ, and its deviations from a constant value, have received a large amount of attention. Our objective in this chapter was to propose a unified view on spatial and temporal scaling, where different behaviour has been reported. We begin from the equilibrium energy spectrum, observed in a wide range of turbulent flows, even when the large scales are in nonequilibrium. We consider perturbations to the equilibrium spectrum and derive the nonequilibrium scaling of C_ϵ for both inhomogeneous and unsteady flow configurations. These theoretical predictions are tested against a high Reynolds number Kolmogorov flow, where the large scales have both statistical inhomogeneity and unsteadiness. The comparison shows that the theoretical results are consistent with the numerical data. We test two different length scales characterising the macroscopic properties of the flow and discuss the difference in the resulting scaling exponent, as well as the influence of the large-scale energy distribution.

8 Conclusions and Perspectives

This chapter summarises the thesis and discusses perspectives for future research.

Intrinsic quasi-cyclic temporal nature of turbulence

The main topic of Part I of the thesis is quasi-cyclic temporal fluctuations (QCB: Quasi-Cyclic Behaviour) observed in turbulence. These dynamics are driven by the energy cascade and resulting imbalance between large- and small-scales. This phenomenon seems to be robust in a number of flow configurations. In particular, we focus on the energy cycle in the von Kármán flow (§ 2.1) and the minimal model of QCB in box turbulence maintained by the steady forcing (Chap. 3). In fact, the von Kármán flow can be considered to be a physical realisation of a steady force-driven box turbulence. Thus, it is tempting to relate the bulk of the von Kármán flow to the dynamics of box turbulence.

The minimal model involves three variables representing the forcing, energy-containing, and small scales representing the energy dissipation rate of the actual flow. This model reproduces several properties of the actual flow, including similar periodic (laminar) and quasi-cyclic chaotic (turbulent) solutions. Here, a new question arises for the robustness of the QCB in different flow configurations, particularly for spatially extended flows. Since the QCB considered in this thesis are excited in minimal flow domains: between a pair of rotating disks or $(k_x, k_y) = (\pm 1, \pm 1)$ forcing Fourier mode in the $(2\pi)^3$ box. What would happen in a much larger flow domain with many large-scale structures? How do the nearby and far away large-scale structures interact with each other regarding QCB? In fact, this question is related to Part II of the thesis.

We also investigate the bifurcation property of the model to discuss its similarity with the real laminar-turbulent transition. Here, we observe a model trajectory as in Fig. 3.11(a), which looks like the Šilnikov bifurcation shown in Fig. 2.6(b). Although this type of bifurcation can be observed in various fields, it has not been observed in laminar-turbulent transition. It would be interesting to assess the flow further to find such a bifurcation.

Localities of turbulence

The main topic of Part II is the physical-space locality of turbulence. Although it is common to discuss the locality in scale space for turbulence research, the physical space locality should not be overlooked; Kolmogorov developed his 1941 theory in “sufficiently small” four-dimensional domain in space and time (Kolmogorov 1941a). There are multiple approaches to investigating the physical-space locality of turbulence, and we employ the space-local velocity field (§ 4.2) in this thesis. It is defined by truncating the Biot–Savart law between the velocity and vorticity fields (Hamlington, Schumacher, et al. 2008a). We conduct both post-process (Chap. 4) and in-situ (Chap. 5) analysis, and the novelty is in the latter where we define the space-local Navier–Stokes equations.

The main findings of the spatially restricted system are two fold. First, we confirm that the nonlinear interactions of the Navier–Stokes turbulence are spatially local. In other words, when the nonlinearity is restricted by a parameter R (radius of the space-local domain), the energy spectrum in $k \gg 2\pi/R$ obeys $E(k) \propto k^{-5/3}$ of Kolmogorov's 1941 theory. This result validates his idea of the “sufficiently small” domain in physical space. Second, due to the suppressed enstrophy production in the large scales, the space-local

Navier–Stokes turbulence can be asymptotically equivalent to turbulence without vortex stretching (Bos 2021; Wu and Bos 2022). Thus, in $k \ll 2\pi/R$, we asymptotically observe conserved enstrophy flux and the corresponding scaling.

Since the space-local Navier–Stokes equations is an original approach, many questions must be explored. First, the comparison with different approaches on the physical-space locality should be further investigated. See § 4.2.3 for more details on the relation with the nonlocality of the pressure field. Second, the multi-scale nonlinear interactions under the space-local restriction can differ greatly from original Navier–Stokes turbulence. In particular, the energy cascade mechanisms reviewed in § 1.3 and their spatial local/nonlocal properties would be important to improve our understanding of the energy cascade. Third, it is interesting to look at the problem of chaos synchronisation from the space-local point of view. In past works (Yoshida et al. 2005; Lalescu et al. 2013), synchronisation of two turbulent trajectories was investigated by varying the characteristic wavenumber below which the velocity field is assimilated. How do we observe synchronisation when translating this setup and assimilating the space-local velocity field? Last, the same space-local formulation of the two-dimensional Navier–Stokes equations, where the spatially nonlocal interactions dominate the flow, would be of interest to quantify the importance of its space-local nonlinear interactions. Furthermore, the large-scale condensation in two- and three-dimensional space-local Navier–Stokes turbulence should be compared and quantified.

Nonequilibrium scalings in turbulence

The main topic of Part III is nonequilibrium scaling of the energy spectrum and energy dissipation rate. Here, equilibrium and nonequilibrium of turbulence are defined by the instantaneous balance between the energy flux and energy dissipation rate. Indeed, the energy arrived at the smallest scales by the forward energy cascade is instantly dissipated. On the contrary, this balance is broken at large scales, and thus, turbulence is in a strong nonequilibrium state. In this thesis, we treat such large-scale nonequilibrium contributions by a perturbation to the equilibrium component of the flow.

We analyse the effect of large-scale statistical inhomogeneity on the inertial range scaling to reveal the presence of corrections to the equilibrium spectrum, proportional to $k^{-7/3}$ (Chap. 6). Since the correction is steeper than the equilibrium $k^{-5/3}$ scaling, the nonequilibrium scaling decays faster than the equilibrium scaling towards the smaller scales. This result indeed confirms the equilibrium nature (local homogeneity) of the small scales of turbulence. For the perspectives, the universality of the nonequilibrium $k^{-7/3}$ scaling should be further investigated. Here, the term universality refers to the origin of the large-scale nonequilibrium. In fact, it has been reported that the large-scale unsteadiness (Yoshizawa 1994) and anisotropy (Ishihara, Yoshida, et al. 2002) results in the same $k^{-7/3}$ scaling in their nonequilibrium component.

We apply the same methodology to the normalised energy dissipation rate C_ϵ and the Reynolds number Re_λ (Chap. 7). Here, we extend our target to unsteady flow configurations along with the inhomogeneous flow, and our analysis reveals the same scaling for both cases. The crucial difference is that the inhomogeneous $C_\epsilon(z)$–$\mathrm{Re}_\lambda(z)$ scaling consists a line-like profile, while the unsteady $C_\epsilon(t)$–$\mathrm{Re}_\lambda(t)$ scaling forms an ellipse-like shape (§ 7.2). These theoretical results are tested against the high Reynolds number turbulence dataset (§ 7.3) as well as alternative formulation using the different macroscopic length scale (§ 7.4). These results can be extended to more complex flow geometries, for example, in the presence of the wall. The simple parametric expressions for the unsteady and inhomogeneous corrections to the normalised energy dissipation rate allow the improvement of turbulence models, where C_ϵ is generally assumed to be constant.

Appendix

A *Pseudo*-energy dissipation rate

In this section, we consider the so-called *pseudo*-energy dissipation rate

$$\epsilon^{\text{pseudo}} = \nu \left\langle \boldsymbol{A}^2 \right\rangle = \nu \left\langle \frac{\partial u_i}{\partial x_j} \frac{\partial u_i}{\partial x_j} \right\rangle \tag{A.1}$$

and how it is different from the proper energy dissipation rate

$$\epsilon = 2\nu \left\langle \boldsymbol{S}^2 \right\rangle = 2\nu \left\langle S_{ij} S_{ij} \right\rangle . \tag{A.2}$$

Note that we omit the subscript $\boldsymbol{x}$ from the bracket symbol for readability.

First, we rewrite the Navier–Stokes equations (1.1) in the index notation

$$\frac{\partial u_i}{\partial t} = -\frac{\partial}{\partial x_j} \left(p\delta_{ij} + u_i u_j \right) + \nu \frac{\partial^2 u_i}{\partial x_j \partial x_j} + f_i . \tag{A.3}$$

Note that we do not nondimensionalise the system ($\nu \to 1/\,\mathrm{Re}$). By taking the inner product with u_i and integrate over space, one obtains

$$\frac{\partial}{\partial t} \int_\Omega \frac{1}{2} u_i^2 \,\mathrm{d}\boldsymbol{x} = -\int_\Omega \frac{\partial}{\partial x_j} \left(p u_i \delta_{ij} + \frac{1}{2} u_i^2 u_j \right) \mathrm{d}\boldsymbol{x} + \nu \int_\Omega \left[\frac{\partial}{\partial x_j} \left(u_i \frac{\partial u_i}{\partial x_j} \right) - \frac{\partial u_i}{\partial x_j} \frac{\partial u_i}{\partial x_j} \right] \mathrm{d}\boldsymbol{x} + \int_\Omega f_i u_i \,\mathrm{d}\boldsymbol{x} \, . \tag{A.4}$$

The integral of the nonlinear term and the first part of the viscous term become zero, thanks to the divergence theorem. In other words, they are conservative terms. Thus, the integrated energy equation can be written as

$$\frac{\partial}{\partial t} \left\langle \frac{1}{2} u_i^2 \right\rangle = \left\langle f_i u_i \right\rangle - \nu \left\langle \frac{\partial u_i}{\partial x_j} \frac{\partial u_i}{\partial x_j} \right\rangle , \tag{A.5}$$

yielding the pseudo energy dissipation rate (A.1). However, this is not the correct expression of the energy dissipation rate since (A.1) contains the conservative contributions. The objective of this section is to derive the correct expression (A.2) from (A.3) and highlight the difference against the pseudo expression (A.1). The contents of this section heavily rely on Mortensen (2020, Chapter 6), while notations and configurations are simplified.

In the following, we consider the viscous term in (A.3):

$$\nu \frac{\partial^2 u_i}{\partial x_j \partial x_j} . \tag{A.6}$$

First, we multiply it with u_k as well as consider its counterpart (equation of u_k multiplied by u_i). Their sum yields the viscous term of the equation of $u_i u_k$:

$$\nu \left(u_i \frac{\partial^2 u_k}{\partial x_j \partial x_j} + u_k \frac{\partial^2 u_i}{\partial x_j \partial x_j} \right). \tag{A.7}$$

Then, we take advantage of the following two identities

$$u_i \frac{\partial^2 u_k}{\partial x_j \partial x_j} = \frac{\partial}{\partial x_j} \left(\frac{\partial u_i u_k}{\partial x_j} - u_k \frac{\partial u_i}{\partial x_j} \right) - \frac{\partial u_i}{\partial x_j} \frac{\partial u_k}{\partial x_j}, \tag{A.8}$$

$$u_k \frac{\partial^2 u_i}{\partial x_j \partial x_j} = \frac{\partial}{\partial x_j} \left(u_k \frac{\partial u_i}{\partial x_j} \right) - \frac{\partial u_i}{\partial x_j} \frac{\partial u_k}{\partial x_j}. \tag{A.9}$$

Then, (A.7) becomes

$$\nu \left[\frac{\partial}{\partial x_j} \left(\frac{\partial u_i u_k}{\partial x_j} \right) - 2 \frac{\partial u_i}{\partial x_j} \frac{\partial u_k}{\partial x_j} \right] \to \nu \left[\frac{\partial}{\partial x_j} \left(\frac{1}{2} \frac{\partial u_i u_i}{\partial x_j} \right) - \frac{\partial u_i}{\partial x_j} \frac{\partial u_i}{\partial x_j} \right], \tag{A.10}$$

where on the RHS, we take $k \to i$ and divide by 2 to make it the viscous term of the energy equation, $K = u_i u_i / 2$. Another relation

$$\frac{\partial^2 u_i u_i}{\partial x_j \partial x_j} = 4 \frac{\partial}{\partial x_j} (S_{ij} u_i) - 2 \frac{\partial u_i}{\partial x_j} \frac{\partial u_j}{\partial x_i} \tag{A.11}$$

turns (A.10) into

$$\nu \left[2 \frac{\partial}{\partial x_j} (S_{ij} u_i) - \frac{\partial u_i}{\partial x_j} \left(\frac{\partial u_j}{\partial x_i} + \frac{\partial u_i}{\partial x_j} \right) \right]. \tag{A.12}$$

Here, the first term can be combined into the nonlinear term in the divergence form. The second term becomes

$$-2\nu \frac{\partial u_i}{\partial x_j} S_{ij} = -2\nu \big(S_{ij} + \Omega_{ij} \big) S_{ij} = -2\nu S_{ij} S_{ij}, \tag{A.13}$$

due to the identity between the symmetric and antisymmetric tensor

$$S_{ij} \Omega_{ij} = 0. \tag{A.14}$$

The rightmost-hand side of (A.13) is equivalent to the proper definition of the energy dissipation rate (A.2).

B Betchov's relation

In this section, we derive the Betchov's relation (Betchov (1956); Davidson (2015, § 5.3.6)):

$$\langle \omega_i S_{ij} \omega_j \rangle = -\frac{4}{3} \langle S_{ij} S_{jk} S_{ki} \rangle . \tag{B.1}$$

We start with the velocity gradient tensor and its symmetric/anti-symmetric decomposition,

$$A_{ij} = \frac{\partial u_i}{\partial x_j} = S_{ij} + \Omega_{ij} = \begin{pmatrix} a & 0 & 0 \\ 0 & b & 0 \\ 0 & 0 & c \end{pmatrix} + \frac{1}{2} \begin{pmatrix} 0 & -\omega_c & \omega_b \\ \omega_c & 0 & -\omega_a \\ -\omega_b & \omega_a & 0 \end{pmatrix}, \tag{B.2}$$

which is obtained by aligning the coordinate to the principal axes of the strain-rate tensor S_{ij} and by using $\boldsymbol{\omega} = (\omega_a, \omega_b, \omega_c)$. We set $a \geq b \geq c$. Note that the incompressibility reads

$$A_{ii} = S_{ii} = a + b + c = 0, \tag{B.3}$$

and we denote the three eigenvalues of $\boldsymbol{A}$ by λ_1, λ_2, and λ_3. The characteristic equation of $\boldsymbol{A}$ reads

$$\boldsymbol{A} - P\boldsymbol{A}^2 + Q\boldsymbol{A} - R\boldsymbol{I} = 0, \tag{B.4}$$

where P, Q, and R are three invariants of $\boldsymbol{A}$ with

$$P = \lambda_1 + \lambda_2 + \lambda_3 = A_{ii} = 0, \tag{B.5}$$

$$Q = \lambda_1\lambda_2 + \lambda_2\lambda_3 + \lambda_3\lambda_1 = \frac{1}{2}P^2 - \frac{1}{2}A_{ji}A_{ij} = -\frac{1}{2}A_{ji}A_{ij}, \tag{B.6}$$

$$R = \lambda_1\lambda_2\lambda_3 = \det\left(A_{ij}\right) = \frac{1}{3}A_{ij}A_{jk}A_{ki}. \tag{B.7}$$

Note that the RHS of R obeys from the trace of (B.4). By substituting (B.2) into (B.6, B.7), we obtain

$$Q = -\frac{1}{2}\left(a^2 + b^2 + c^2\right) + \frac{1}{4}\left(\omega_a^2 + \omega_b^2 + \omega_c^2\right) \tag{B.8}$$

$$= -\frac{1}{2}S_{ij}S_{ji} + \frac{1}{4}\boldsymbol{\omega}^2 \tag{B.9}$$

and

$$R = \frac{1}{3}\left(a^3 + b^3 + c^3\right) - \frac{1}{4}\left[(b+c)\omega_a^2 + (a+c)\omega_b^2 + (a+b)\omega_c^2\right] \tag{B.10}$$

$$= \frac{1}{3}\left(a^3 + b^3 + c^3\right) + \frac{1}{4}\left(a\omega_a^2 + b\omega_b^2 + c\omega_c^2\right) \tag{B.11}$$

$$= \frac{1}{3}S_{ij}S_{jk}S_{ki} + \frac{1}{4}\omega_i S_{ij}\omega_j. \tag{B.12}$$

Note that we use the identity (B.3) from the first to the second line.

Betchov derived the divergence expressions

$$Q = -\frac{1}{2}\frac{\partial}{\partial x_j}\left[u_i\frac{\partial u_j}{\partial x_i}\right], \tag{B.13}$$

$$R = \frac{1}{3}\frac{\partial}{\partial x_i}\left[\frac{\partial u_i}{\partial x_j}\frac{\partial u_j}{\partial x_k}u_k - \frac{1}{2}u_i\frac{\partial u_k}{\partial x_j}\frac{\partial u_j}{\partial x_k}\right]. \tag{B.14}$$

One can assume the divergence free in homogeneous turbulence: $\langle Q\rangle = 0$ and $\langle R\rangle = 0$. Thus, (B.9, B.12) becomes, in the average sense,

$$\left\langle\boldsymbol{\omega}^2\right\rangle = 2\left\langle S_{ij}S_{ij}\right\rangle, \tag{B.15}$$

$$\left\langle\omega_i S_{ij}\omega_j\right\rangle = -\frac{4}{3}\left\langle S_{ij}S_{jk}S_{ji}\right\rangle. \tag{B.16}$$

The importance of these two equations cannot be overestimated; Equation (B.15) leads to the estimation of the kinetic energy dissipation rate

$$\langle\epsilon\rangle \equiv 2\nu\left\langle S_{ij}S_{ij}\right\rangle = \nu\left\langle\boldsymbol{\omega}^2\right\rangle, \tag{B.17}$$

and (B.16) connects the enstrophy production (LHS) and the strain self-amplification (RHS).

C Other candidates for energy cascade mechanism

In § 1.3, we reviewed two main candidates for the energy cascade mechanism: vortex stretching and strain self-amplification. However, turbulence researchers have been proposing various energy cascade scenarios. In this Appendix, we review several of them, including instability (§ C.1), vortex reconnection (§ C.2), and Lundgren's spiral vortex scenario (§ C.3). Figure C.1 shows the timeline of important works on these topics.

C.1 Instability

Although vortex stretching (§ 1.3.1) and the strain self-amplification (§ 1.3.2) are the main contenders for the energy cascade mechanism, there are several other candidates. In this subsection, we focus on the "instability-driven cascade" picture. To begin our discussion, we quote the full paragraph in which Richardson wrote down his poem (Richardson 1922, p. 66):

> On the other hand we find that convectional motions are hindered by the formation of small eddies resembling those due to dynamical instability. Thus C. K. M. Douglas writing of observations from aeroplanes remarks: "The upward currents of large cumuli give rise to much turbulence within, below, and around the clouds, and the structure of the clouds is often very complex." One gets a similar impression when making a drawing of a rising cumulus from a fixed point; the details change before the sketch can be completed. We realize thus that: big whirls have little whirls that feed on their velocity, and little whirls have lesser whirls and so on to viscosity — in the molecular sense.

Here, he referred to "dynamical instability" as the generation mechanism of the small eddies.

In Vincent and Meneguzzi (1994), instability was claimed as the key energy cascade mechanism. In this study, the authors investigated the early-days DNS result of both statistically steady homogeneous and decaying turbulence from visualisations. They claimed that the roll-up of the vortex sheet forming the vortex tube is the essential mechanism of the energy cascade. Although this process contradicts Richardson's step-by-step cascade picture, the authors describe the vortex sheet roll-up as "a one-step process, with a strong correlation between small and large scales" (Vincent and Meneguzzi 1994). However, note that this study is based on the visualisation of DNS, and no quantitative evidence was presented. Furthermore, it seems that this paper is referred to as one of the first numerical pieces of evidence of the strong fine-scale vortex filaments in turbulence and not in the context of the physical mechanism of the energy cascade.

In Brenner et al. (2016), the iterative vortex mechanism between a pair of vortex tubes and sheets are discussed. As schematically shown in Fig. C.2(a), this process is a candidate of the singular solution of the Euler equation[1]. This instability process in the inviscid situation can be related to vortex reconnection in a viscous fluid (see § C.2).

Recently, another mechanism driven by the instability has been reported as a candidate for the energy cascade (McKeown, Ostilla-Mónico, et al. 2018; McKeown, Ostilla-Mónico, et al. 2020); It is the elliptical instability observed in the secondary (and beyond) vortex structures of the face-to-face vortex ring collision. Figure C.2(b) visualises the development of the finer vortex structures in a pair of interacting vortex tubes. The collided vortex rings instantaneously break down into secondary filaments; their interactions lead to tertiary fine-scale structures. This cascade of energy from the large vortex rings to the fine-scale vortex filaments. The authors reminded the similarity of this process with the scale-by-scale vortex stretching (see § 1.3.1). However, they simultaneously remark that this process is "reminiscent of, but perhaps different from, Richardson's initial proposal (Richardson 1922)" (McKeown, Ostilla-Mónico, et al. 2018).

C.2 Vortex reconnection

In this subsection, we focus on the vortex reconnection (Kida and Takaoka 1994; Yao and Hussain 2022) and its contribution to the energy cascade. The vortex reconnection event, shown in Fig. C.3, can be decomposed into several steps. Two antiparallel vortex tubes [Fig. C.3(a)] are curved to approach each other and collapse [Fig. C.3(b-c)]. Then, the reconnection of the vortex axis forms transverse vortex

---

[1] This study is inspired by the one investigating the global singularity of the three-dimensional Navier–Stokes equations by a kind of shell model and its energy-conserving iterative cascades (Tao 2016).

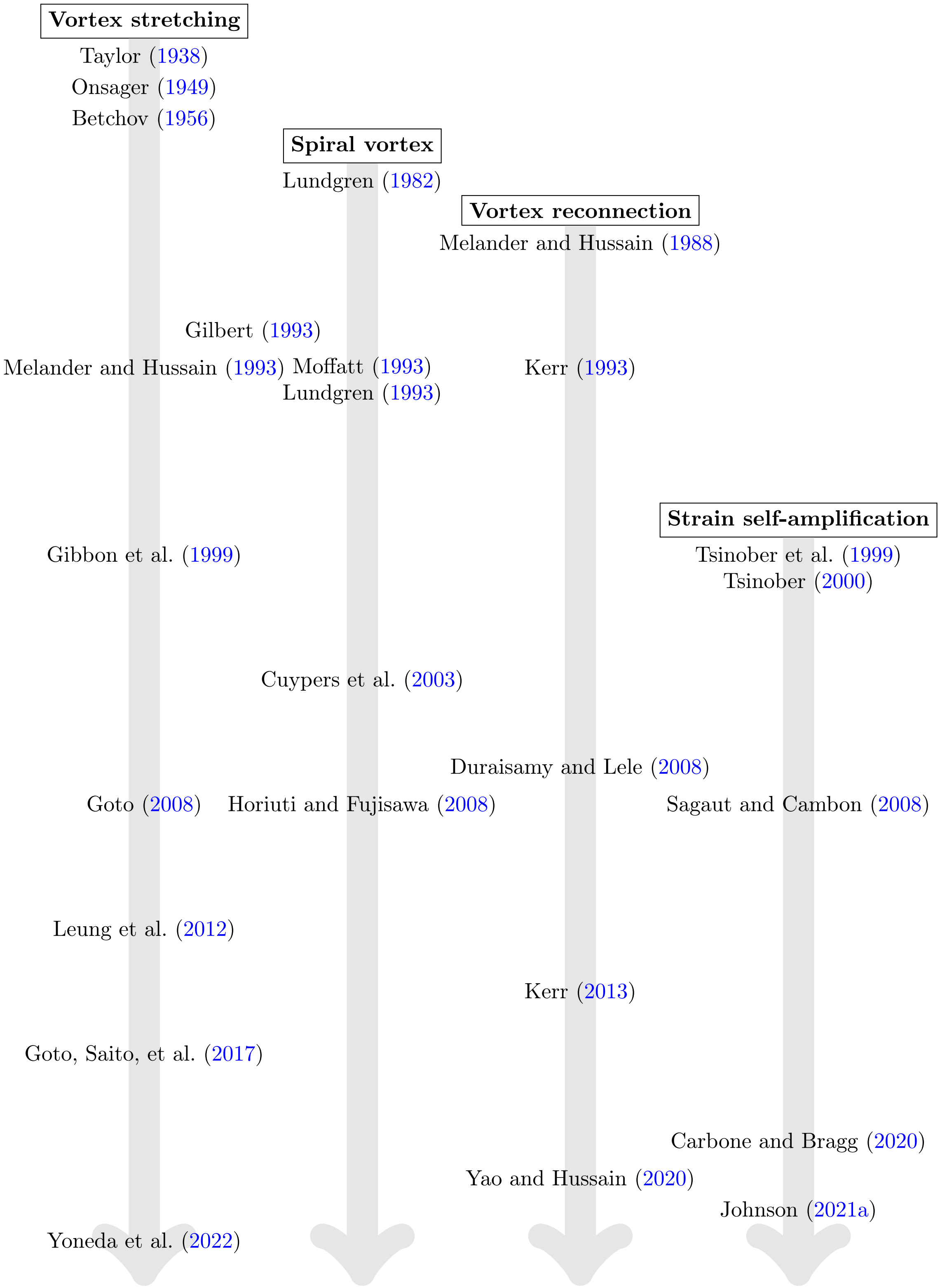

Figure C.1: Historical timeline of research on the physical-space mechanism of energy cascade in three-dimensional turbulence.

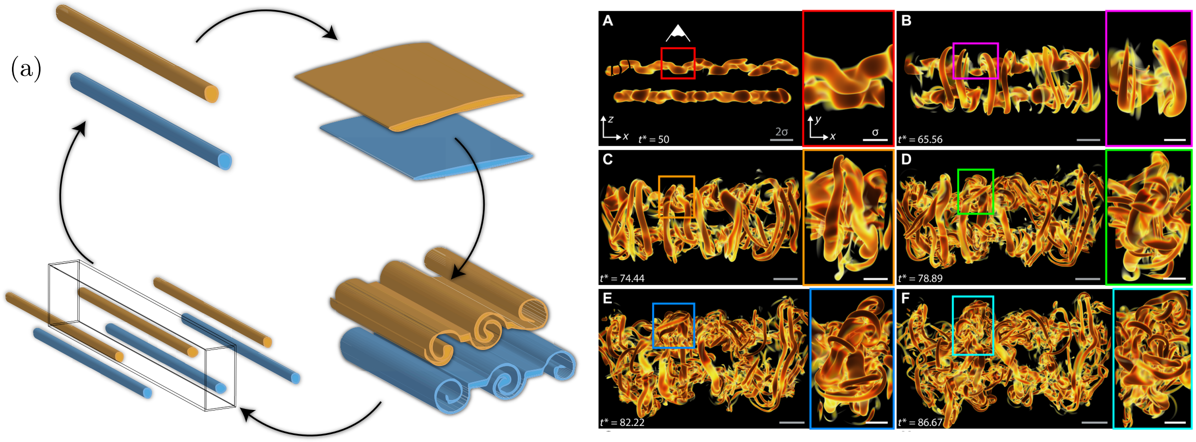

Figure C.2: (a) Schematic of the iterative mechanism of vortex interactions. A pair of anti-parallel vortex tubes (top left) becomes a pair of vortex sheets (top right) by the collision, and then the Kelvin–Helmholtz instability (bottom right) drives them to two arrays of vortex tubes (bottom left) on a smaller scale. Adapted from Brenner et al. (2016, Figure 1). (b) Development of turbulent cascade in interacting vortex tubes. Time evolves from A to F. The full view (left) and a close-up top view (right) are shown in each panel. Adapted from McKeown, Ostilla-Mónico, et al. (2020, Figure 5).

structures called a bridge [Fig. C.3(d-e)]. The remaining part of the original vortex tubes first form sheet-like structures called a thread [Fig. C.3(c)], which result in fine-scale structures spanning the reconnected vortex tubes.

There are several different energy cascade scenarios based on the vortex reconnection. The following review heavily depends upon Yao and Hussain (2022, § 2.2.4). Melander and Hussain (1988) proposed an energy cascade scenario based on the successive vortex reconnection. When we zoom up the threads between the reconnected vortex tubes in Fig. C.3(f), it is equivalent to the original anti-parallel vortex tubes in Fig. C.3(a). Thus, when the Reynolds number is large enough, successive vortex reconnection events can occur at smaller and smaller scales and cascade the energy down towards the smallest scales. Recently, Yao and Hussain (2020) reported the first numerical evidence of the vortex reconnection cascade scenario and the corresponding $k^{-5/3}$ scaling of the energy spectrum. They investigated the multi-generation vortex reconnection event and observed the formation of a "turbulent cloud avalanche" consisting of fine-scale vortices. Note that the late stage of the vortex reconnection event at high Re captures a phenomenon similar to vortex stretching.

An alternative picture proposed in Melander and Hussain (1993) is that the large-scale vortex tube generates the secondary small-scale anti-parallel pairs around it. This process can also be iterative at a large enough Reynolds number and further investigated in Goto (2008). The latest development of this mechanism can be found in a review article (Yao and Hussain 2022).

C.3 Lundgren's spiral vortex scenario

In 1982, Lundgren proposed an innovative energy cascade model. This is Lundgren's spiral vortex scenario (model), which we review in this subsection. This model is schematically described as (Davidson 2015, § 6.4.3 (p. 357)):

> He considered an unsteady, stretched, Burgers-like vortex filament whose internal structure is not axisymmetric but spiralled, like a sheet of paper rolled up into a scroll [...].

The schematic is shown in Fig. C.4. A similar schematic can be found in, for example, Horiuti and Ozawa (2011, Figure 2) and Davidson (2015, Figure 6.32). This model is first proposed as a purely mathematical model. In the same year, when Lundgren proposed his refined model (Lundgren 1993), Pullin and Saffman investigated the vorticity and the moments of velocity gradient by the Lundgren's model (Pullin and Saffman 1993). Also, in the same year, Moffatt discussed that the spiral vortex could explain the K41 scaling without the hierarchical structures of different scales (Moffatt 1993). The review article (Pullin and Saffman 1998, § 6) summarises the importance of Lundgren's model as:

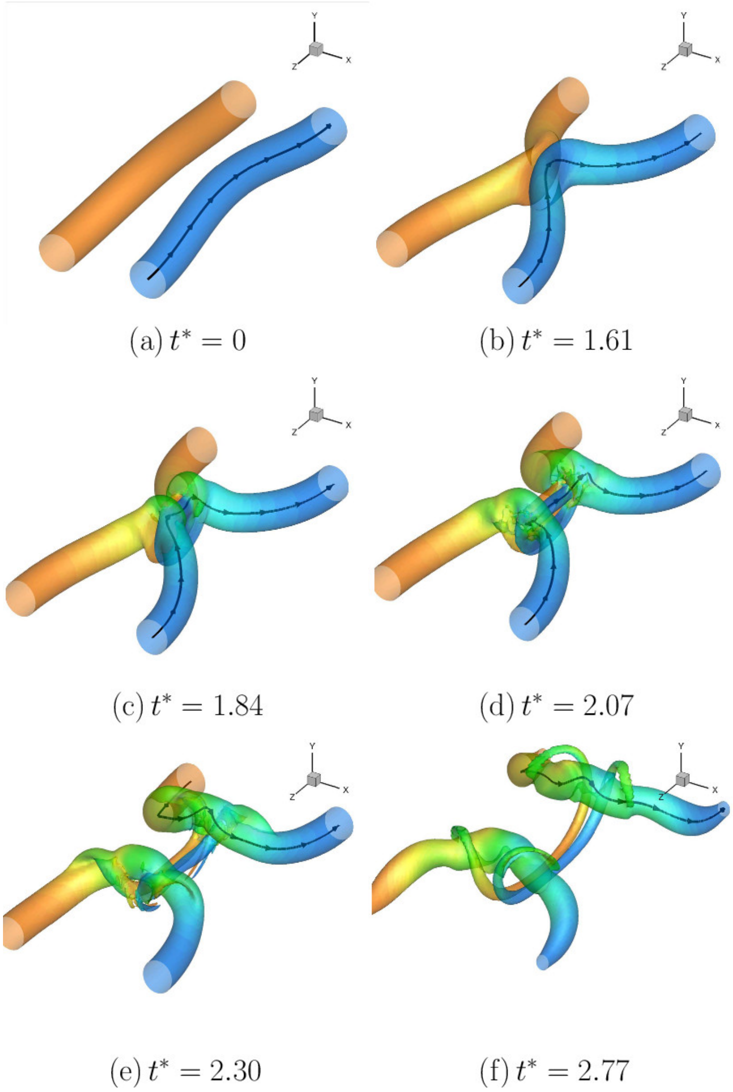

(a) $t^* = 0$ (b) $t^* = 1.61$

(c) $t^* = 1.84$ (d) $t^* = 2.07$

(e) $t^* = 2.30$ (f) $t^* = 2.77$

Figure C.3: Visualisation of vorticity magnitude isosurface during the vortex reconnection event at Re = 2000. Colours denote the axial vorticity magnitude. Sublabels denote the nondimensional time t^*. Adapted from Hussain and Duraisamy (2011, Figure 2).

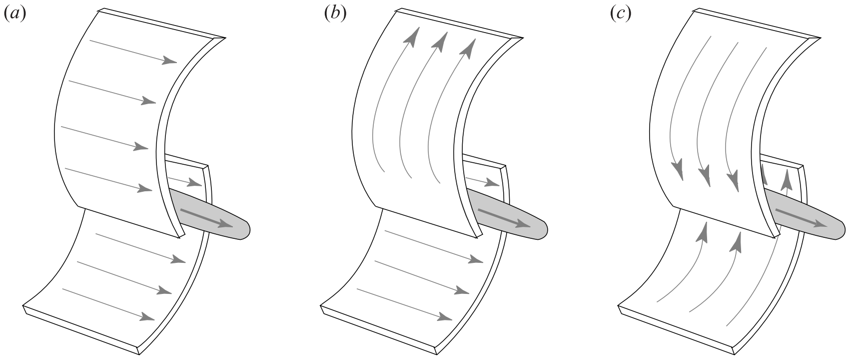

Figure C.4: Schematic of (generalised) Lundgren's spiral vortex model. A pair of vortex sheets wrap around a vortex tube. The arrows denote the vorticity vectors: (a) Mode 1 investigated by Lundgren (1982), (b) Mode 2 by Horiuti and Takagi (2005), (c) Mode 3 by Pearson and Abernathy (1984), Moore (1985), and Kawahara, Kida, et al. (1997). Adapted from Horiuti and Fujisawa (2008, Figure 1). See Hino (2020, § 4.11.1) for a review (in Japanese).

> It appears to be the only known repeatable result making a definite analytical connection between a $k^{-5/3}$-type spectrum and an approximate solution of the Navier–Stokes equations [...].

The first experimental evidence of spiral vortex and corresponding $E(k) \propto k^{-5/3}$ scaling is reported two decades after the first paper (Cuypers et al. 2003). Japanese researchers investigated the spiral vortex in DNS with HIT and homogeneous shear flows (Horiuti and Fujisawa 2008; Horiuti and Ozawa 2011). Kerr (2013) discussed that a chain of spiral vortex rings generated from anti-parallel vortex tubes exhibits the 3D turbulence statistics.

D Quantitative comparison of different cascade mechanisms

We have reviewed many (but not all) candidates for forward energy cascade mechanisms in three-dimensional turbulence in § 1.3 and Appendix C. However, our discussion was limited on a phenomenological level. Now, we would ask a question:

What is *the* physical mechanism of energy cascade driving turbulence?

The difficulties regarding this problem are twofold, as summarised by Vela-Martín (2019, § 1.1.3). First, "eddy" cannot be locally determined regarding space and scale. For example, applying a bandpass filter isolates vortex structures of a given scale (see Fig. 1.11) distributed in the entire domain. The opposite procedure of extracting the subspace of the flow domain can isolate the spatially local vortex structures, but their size spans a wide range of scales. Second, there is no definitive way of determining energy flux. One can define one's energy flux by focusing on different quantities, terms in the governing equations, and types of nonlinear interactions. Indeed, as Tsinober stated (Tsinober 2009, § 5.4.2):

> [...] the energy exchange/transfer is decomposition dependent.

In this subsection, we review several recent articles:

- Goto, Susumu, Yuta Saito, and Genta Kawahara (2017). Hierarchy of antiparallel vortex tubes in spatially periodic turbulence at high Reynolds numbers. *Physical Review Fluids* **2** (6), p. 064603; Yoneda, Tsuyoshi, Susumu Goto, and Tomonori Tsuruhashi (2022). Mathematical reformulation of the Kolmogorov–Richardson energy cascade in terms of vortex stretching. *Nonlinearity* **35** (3), p. 1380
- Carbone, Maurizio and Andrew D. Bragg (2020). Is vortex stretching the main cause of the turbulent energy cascade? *Journal of Fluid Mechanics* **883**, R2
- Johnson, Perry L. (2020). Energy transfer from large to small scales in turbulence by multiscale nonlinear strain and vorticity interactions. *Physical Review Letters* **124** (10), p. 104501; Johnson, Perry L. (2021a). On the role of vorticity stretching and strain self-amplification in the turbulence energy cascade. *Journal of Fluid Mechanics* **922**, A3
- McKeown, Ryan, Alain Pumir, Shmuel M. Rubinstein, Michael P. Brenner, and Rodolfo Ostilla-Mónico (2022). Energy transfer and vortex structures: Visualizing the incompressible turbulent energy cascade. *arXiv preprint*. arXiv: `2204.09023 [flu-dyn]`

In fact, we would encounter several different definitions of energy flux in this subsection. Thus, our objective in this subsection is *not* to claim the answer to the question but to pause a current picture of our understanding. Note that we maintain the notations in the original articles.

Goto, Saito, et al. (2017) and Yoneda et al. (2022)

The hierarchical vortex structures in anti-parallel configurations (see Fig. 1.11) reported in Goto, Saito, et al. (2017) suggests that the vortex structures at scale ℓ are generated by the strain-rate field induced by the large-scale (for example, 2ℓ) vortex structures. In contrast, they induce the strain-rate field by themselves, which leads to finer-scale vortices (at scale $\ell/2$). The scale-local nature of vortex stretching is consistent with the scale-local energy cascade picture. In Yoneda et al. (2022), a new mathematical derivation of the Kolmogorov's $-5/3$ law was presented based on the hierarchical vortex structures and

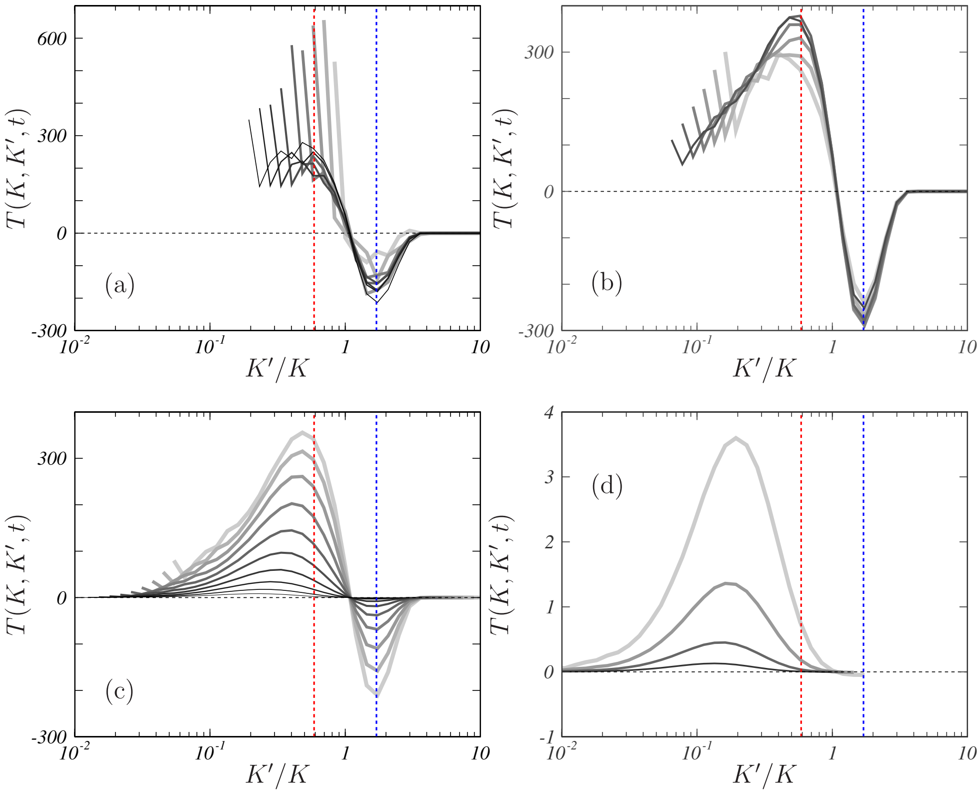

Figure D.1: Scale-by-scale energy transfer $T(K, K', t)$ from wavenumber K to K' due to the vortex stretching term. In each panel, darker and thinner curves correspond to larger K, and lighter and thicker curves denote smaller values of K. From panel (a) to (d), the different ranges of K are shown; Panels (a) show the smallest values of K and represent the energy transfer in the forcing region. The range of K successively increases: (b) represents the inertial range, (c) the dissipation range, and (d) the far-dissipation range. The red and blue dotted lines denote the characteristic wavenumber for the dominant energy loss and gain, respectively. Adapted from Yoneda et al. (2022, Figure 1).

the scale-local interactions between them. The novelty of this study is that they reformulate the universal scaling without directly using the similarity hypotheses.

To quantify the scale-space property of energy transfer associated with vortex stretching, they defined

$$T(K,K') \equiv \frac{1}{K^2}\int \omega_i(K)\frac{\partial u_i(K')}{\partial x_j}\omega_j(K)\,\mathrm{d}\Omega\,. \tag{D.1}$$

Here, the argument K and K' denote the bandpass-filter defined by

$$u_i(K) \equiv \mathcal{F}^{-1}\left[\chi_{\left[K/\sqrt{2},\sqrt{2}K\right)}\mathcal{F}[u_i]\right], \quad \text{and} \quad \omega_i(K) \equiv \mathcal{F}^{-1}\left[\chi_{\left[K/\sqrt{2},\sqrt{2}K\right)}\mathcal{F}[\omega_i]\right], \tag{D.2}$$

where $\mathcal{F}$ and $\mathcal{F}^{-1}$ denote forward and inverse Fourier transformation, respectively. The bandpass-filter in $k \in \left[K/\sqrt{2}, \sqrt{2}K\right)$ is denoted by $\chi_{\left[K/\sqrt{2},\sqrt{2}K\right)}$. Since $\int \omega_i(K)\,\partial u_i(K')/\partial x_j\,\omega_j(K)\,\mathrm{d}\Omega$ represents the enstrophy production rate at scale K due to velocity gradient at K', (D.1) with the coefficient K^{-2} denotes the energy transfer due to vortex stretching from scale K' to K. Figure D.1 shows this energy transfer spectrum in high-Reynolds-number turbulence (Taylor-scale Reynolds number $\mathrm{Re}_\lambda \approx 280$) snapshot as a function of K'/K. Four panels of Fig. D.1 correspond to different spectral regimes in turbulence, and we focus on panel (b): inertial range. The collapsed curves in this panel indicate that the energy transfer profile is self-similar irrespective of K (receives energy). This observation is consistent with the inertial range statistics of the K41 theory. Furthermore, the positive peak of the spectrum at $K'/K \approx 0.5$ (where the red dashed line denotes $K'/K = 0.58$) states that the most significant energy transfer is from as twice as large scales. At the same time, the energy transfer to the smaller scale is most significant at the negative peak around $K'/K \approx 2$ (where the blue dashed line denotes $K'/K = 1.7$), corresponds to scales as half as small as the original scale K. These properties also support the scale-local nature of the energy cascade.

Carbone and Bragg (2020)

They investigated the Kármán–Howarth equation

$$\partial_t \mathcal{K} = -\boldsymbol{\partial_r} \cdot \boldsymbol{T} + 2\nu \boldsymbol{\partial}_{\boldsymbol{r}}^2 K - 2\left\langle \epsilon \right\rangle + W, \tag{D.3}$$

which governs the ensemble-averaged turbulent kinetic energy

$$\mathcal{K}(\boldsymbol{x}, \boldsymbol{r}, t) \equiv \left\langle \left\| \Delta \boldsymbol{u}(\boldsymbol{x}, \boldsymbol{r}, t) \right\|^2 \right\rangle / 2 \tag{D.4}$$

of the velocity increment $\Delta \boldsymbol{u}(\boldsymbol{x}, \boldsymbol{r}, t) \equiv \boldsymbol{u}(\boldsymbol{x} + \boldsymbol{r}/2, t) - \boldsymbol{u}(\boldsymbol{x} - \boldsymbol{r}/2, t)$. Here, the nonlinear energy flux term is defined by

$$\boldsymbol{\partial_r} \cdot \boldsymbol{T} \equiv \frac{1}{2} \boldsymbol{\partial_r} \cdot \left\langle \left\| \Delta \boldsymbol{u} \right\|^2 \Delta \boldsymbol{u} \right\rangle . \tag{D.5}$$

The other terms of (D.3) are the average kinetic energy dissipation rate $\left\langle \epsilon \right\rangle$ and the power input W, respectively.
To investigate the energy flux $\boldsymbol{\partial_r} \cdot \boldsymbol{T}$ for different scales, they introduced the coarse-graining

$$\begin{cases} \boldsymbol{u} = \widetilde{\boldsymbol{u}} + \boldsymbol{u}', & \text{(D.6)} \\ \widetilde{\boldsymbol{u}}(\boldsymbol{x}, t) \equiv \displaystyle\int_{\mathbb{R}} \mathcal{G}\left(\left\| \boldsymbol{y} \right\|\right) \boldsymbol{u}(\boldsymbol{x} - \boldsymbol{y}, t) \, \mathrm{d}\boldsymbol{y} \, , & \text{(D.7)} \end{cases}$$

where $\mathcal{G}$ denotes an isotropic filter kernel with length scale r. With this decomposition and assuming isotropy, one can define the energy flux at scale r:

$$\boldsymbol{\partial_r} \cdot \boldsymbol{T} = \mathcal{L}\left\{ \left\langle \left(\widetilde{\boldsymbol{S}} \cdot \widetilde{\boldsymbol{S}} \right) : \widetilde{\boldsymbol{S}} \right\rangle - \frac{1}{4} \left\langle \widetilde{\boldsymbol{\omega}} \widetilde{\boldsymbol{\omega}} : \widetilde{\boldsymbol{S}} \right\rangle \right\} + \mathcal{F}, \tag{D.8}$$

$$\mathcal{L}\{\cdot\} \equiv \left(\frac{\partial}{\partial r} + \frac{2}{r} \right) \left[\frac{r^4}{105} \left(\frac{\partial}{\partial r} + \frac{7}{r} \right) \{\cdot\} \right]. \tag{D.9}$$

Here, $\widetilde{\boldsymbol{S}} \equiv \left(\boldsymbol{\nabla} \widetilde{\boldsymbol{u}} + \boldsymbol{\nabla} \widetilde{\boldsymbol{u}}^{\intercal} \right)/2$ and $\widetilde{\boldsymbol{\omega}} \equiv \boldsymbol{\nabla} \times \widetilde{\boldsymbol{u}}$ are filtered strain-rate tensor and vorticity, respectively, and Eq. (D.9) is an operator in isotropic configuration and $\mathcal{F}$ denotes the residual contributions. The $\left(\widetilde{\boldsymbol{S}} \cdot \widetilde{\boldsymbol{S}} \right) : \widetilde{\boldsymbol{S}}$ and $\widetilde{\boldsymbol{\omega}} \widetilde{\boldsymbol{\omega}} : \widetilde{\boldsymbol{S}}$ are the strain self-amplification (SSA) and the vortex stretching (VS) terms, respectively.
Figure D.2(a) shows the energy flux with its contributions. The important conclusion drawn from this figure is that regardless of the scale, the flux magnitude is always SSA > VS. However, the authors remarked that this result claims the dominance of SSA over VS in terms of the average energy cascade. They also computed the exponent

$$\zeta_n(r) \equiv \frac{\left\langle \left[(-3/4) \widetilde{\boldsymbol{\omega}} \widetilde{\boldsymbol{\omega}} : \widetilde{\boldsymbol{S}} \right]^n \right\rangle}{\left\langle \left[\left(\widetilde{\boldsymbol{S}} \cdot \widetilde{\boldsymbol{S}} \right) : \widetilde{\boldsymbol{S}} \right]^n \right\rangle} \tag{D.10}$$

to evaluate the balance of these two contributions in fluctuations. Note that for $n = 1$, the exponent is unity: $\zeta_1(r) = 1$ as it is the Betchov's relation (see Appendix B). The result (Carbone and Bragg 2020, Fig. 3(c)) reveled that for $n > 1$, it is $\zeta_n(r) > 1$ regardless of r. This means that the VS becomes more

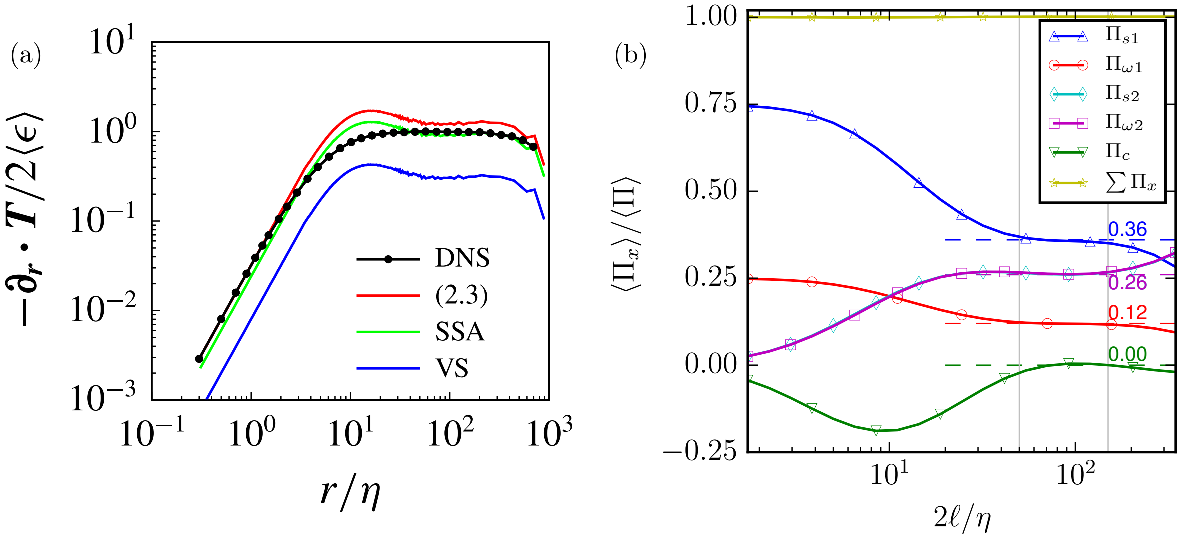

Figure D.2: (a) Nonlinear energy flux with its different contributions: DNS result (black line with dots), $\boldsymbol{\partial_r} \cdot \boldsymbol{T}$ defined in (D.8) (red line), SSA (green line) and VS (blue line) contributions. The difference between the DNS result (black line with dots) and $\boldsymbol{\partial_r} \cdot \boldsymbol{T}$ (red line) denotes the residual $\mathcal{F}$ in (D.8). Adapted from Carbone and Bragg (2020, Figure 1(a)). (b) The mean contributions to the energy cascade rate $\langle\Pi_x\rangle$ for different contributions against the filter size. See the main text for the definition and interpretation of each term. The total energy cascade rate is denoted by $\sum \Pi_x$ and equals one after the normalisation. The grey lines denote the approximate range of the inertial range. The horizontal dashed lines denote the magnitude of each contribution in the inertial range. Adapted from Johnson (2021a, Figure 8(b)).

important than SSA for the strong fluctuations of the energy cascade. The authors mentioned that:

> [This property] may in part be associated with the known fact that the vorticity field is more intermittent that the strain-rate field in turbulent flows [...].

Johnson (2020) and Johnson (2021a)

They investigate the energy flux at scale ℓ:

$$\mathit{\Pi}^\ell = -\left[\tau_\ell(u_i, u_j) - \frac{1}{3}\tau_\ell(u_k, u_k)\delta_{ij}\right]\bar{S}^\ell_{ij}, \tag{D.11}$$

where the Reynolds stress tensor is

$$\tau_\ell(a, b) = \overline{ab}^\ell - \bar{a}^\ell \bar{b}^\ell, \tag{D.12}$$

and the strain-rate tensor is

$$\bar{S}^\ell_{ij} = \frac{1}{2}\left[\bar{A}^\ell_{ij} + \bar{S}^\ell_{ji}\right]. \tag{D.13}$$

The low-pass filtered quantity is defined by

$$\bar{a}^\ell(\boldsymbol{x}) = \iiint_{-\infty}^{\infty} G_\ell(\boldsymbol{r}) a(\boldsymbol{x} + \boldsymbol{r})\, \mathrm{d}\boldsymbol{r}\,, \tag{D.14}$$

with an appropriate filterkernel function $G_\ell(\boldsymbol{r})$.
They decompose the energy flux (D.11) as

$$\mathit{\Pi}^\ell = \mathit{\Pi}^\ell_{s1} + \mathit{\Pi}^\ell_{\omega 1} + \mathit{\Pi}^\ell_{s2} + \mathit{\Pi}^\ell_{\omega 2} + \mathit{\Pi}^\ell_{c}, \tag{D.15}$$

where each term is defined by:

$$\mathit{\Pi}^{\ell}_{s1} = -\ell^2 \bar{S}^{\ell}_{ij}\bar{S}^{\ell}_{jk}\bar{S}^{\ell}_{ki} \tag{D.16}$$

$$\mathit{\Pi}^{\ell}_{\omega 1} = \frac{1}{4}\ell^2 \bar{S}^{\ell}_{ij}\bar{\omega}^{\ell}_{i}\bar{\omega}^{\ell}_{j} \tag{D.17}$$

$$\mathit{\Pi}^{\ell}_{s2} = -\int_0^{\ell^2} \mathrm{d}\alpha\, \bar{S}^{\ell}_{ij}\tau_\beta\left(\bar{S}^{\sqrt{\alpha}}_{jk}, \bar{S}^{\sqrt{\alpha}}_{ki}\right), \tag{D.18}$$

$$\mathit{\Pi}^{\ell}_{\omega 2} = -\int_0^{\ell^2} \mathrm{d}\alpha\, \bar{S}^{\ell}_{ij}\tau_\beta\left(\bar{\omega}^{\sqrt{\alpha}}_{i}, \bar{\omega}^{\sqrt{\alpha}}_{j}\right), \tag{D.19}$$

$$\mathit{\Pi}^{\ell}_{c} = \bar{S}^{\ell}_{ij}\int_0^{\ell^2} \mathrm{d}\alpha\left[\tau_\beta\left(\bar{S}^{\sqrt{\alpha}}_{jk}, \bar{\mathit{\Omega}}^{\sqrt{\alpha}}_{ki}\right) - \tau_\beta\left(\bar{\mathit{\Omega}}^{\sqrt{\alpha}}_{jk}, \bar{S}^{\sqrt{\alpha}}_{ki}\right)\right]. \tag{D.20}$$

The terms with subscript "1" involve quantities at a single scale: the filter length scale ℓ. The above $\mathit{\Pi}^{\ell}_{s1}$ (D.16) and $\mathit{\Pi}^{\ell}_{\omega 1}$ (D.17) are strain self-amplification and vortex stretching due to strain at ℓ. Note that these terms also appear in the restricted Euler equation for the magnitude of the filtered velocity gradient tensor

$$\frac{\mathrm{D}}{\mathrm{D}t}\left(\frac{1}{2}\left\|\bar{\boldsymbol{A}}^{\ell}\right\|^2\right) = \frac{1}{4}\bar{\omega}^{\ell}_{i}\bar{S}^{\ell}_{ij}\bar{\omega}^{\ell}_{j} - \bar{S}^{\ell}_{ij}\bar{S}^{\ell}_{jk}\bar{S}^{\ell}_{ki}. \tag{D.21}$$

Thus, the author discussed that:

> The same processes responsible for increasing the filtered velocity gradient magnitude also redistribute energy to sub-filter scales, thus connecting the restricted Euler singularity with the energy cascade.

The subscript "2" in the third and fourth term on the RHS of (D.15) represents the nonlinear interactions between the strain rate filtered at ℓ and velocity gradient at scales smaller than ℓ. Similar to those with subscript "1", $\mathit{\Pi}^{\ell}_{s2}$ (D.18) denotes the strain self-amplification, but this time the amplification of the small-scale strain by the larger-scale strain. The other term, $\mathit{\Pi}^{\ell}_{\omega 2}$ (D.19), represents the stretching of the small-scale vorticity by the large-scale strain. The final term $\mathit{\Pi}^{\ell}_{c}$ denotes the interactions between the larger-scale strain and smaller-scale strain–vorticity covariance.

Figure D.2(b) shows the distribution of (D.16–D.20) against the filter length scale size. In the inertial range, we observe each contribution takes a plateau, supporting the statistically self-similar nature of turbulence. The most important indication of the figure is that $\mathit{\Pi}_{s1}$ takes the largest value among the five contributions, roughly one-third of the total energy flux. This claims that the single-scale strain self-amplification is the most significant in the energy cascade. Then, almost indistinguishable multi-scale strain self-amplification and vortex stretching follow. The single-scale vortex stretching has weaker contributions than these three terms. The covariance term does not play a role in the inertial range.

McKeown, Pumir, et al. (2022)

They defined the Fourier band

$$I_P = \left\{\left(k_x, k_y, k_z\right), \quad \text{such that} \quad 2^{P-1}k_f/\sqrt{2} \leq |\boldsymbol{k}| \leq 2^{P-1}k_f \times \sqrt{2}\right\}, \tag{D.22}$$

where k_f is the forcing wavenumber, to evaluate the physical-space velocity corresponds to the band P:

$$\boldsymbol{u}_P(\boldsymbol{x}, t) = \sum_{\left(k_x, k_y, k_z\right)\in I_P} \hat{\boldsymbol{u}}\left(k_x, k_y, k_z\right)\exp\left[\mathrm{i}\left(k_x x + k_y y + k_z z\right)\right]. \tag{D.23}$$

Here, a larger value of P corresponds to a larger Fourier shell or small scale. Now, one can define the energy transfer from shell (Fourier band) K to shell Q due to the interaction with the shell P:

$$\mathcal{T}_3(K, P, Q, \boldsymbol{x}) = -\boldsymbol{u}_K \cdot (\boldsymbol{u}_P \cdot \boldsymbol{\nabla})\boldsymbol{u}_Q. \tag{D.24}$$

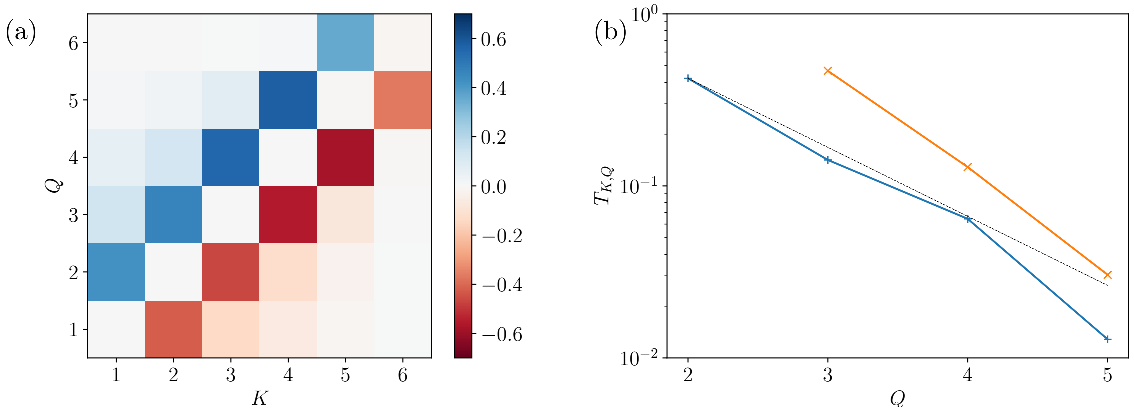

Figure D.3: (a) Two-dimensional instantaneous energy transfer spectrum normalised by the average energy dissipation rate $T_2(K,Q)/\langle\epsilon\rangle$ in homogeneous isotropic turbulence at $Re_\lambda = 210$. Adapted from McKeown, Pumir, et al. (2022, Figure 2(a)). (b) The integrated energy transfer scaling $T_{1,Q} = T_2(1,Q)$ (blue plus symbols) and $T_{2,Q} = T_2(2,Q)$ (red cross symbols). Note that the shortened notation $T_{K,Q} = T_2(K,Q)$ is employed in the paper. The straight dashed line shows the theoretical prediction $T_{K,Q} \propto 2^{-4Q/3}$. Adapted from McKeown, Pumir, et al. (2022, Figure 2(b)).

Note that this quantity also depends on $\boldsymbol{x}$, allowing one to investigate the distribution of the energy transfer rate in physical space. By integrating $\mathcal{T}_3$ in space, scale-to-scale energy transfer (with a specific mediator scale) can be evaluated in the global sense:

$$T_3(K,P,Q) = \int \mathcal{T}_3(K,P,Q,\boldsymbol{x})\,\mathrm{d}\boldsymbol{x}\,. \tag{D.25}$$

From the space-dependent $\mathcal{T}_3(K,P,Q,\boldsymbol{x})$ (D.24) The “mediator” shell P can be averaged out to define

$$\mathcal{T}_2(K,Q,\boldsymbol{x}) = \sum_P \mathcal{T}_3(K,P,Q,\boldsymbol{x}) = -\boldsymbol{u}_K\cdot(\boldsymbol{u}\cdot\boldsymbol{\nabla})\boldsymbol{u}_Q, \tag{D.26}$$

corresponds to the energy transfer from shell K to Q with the aid of the whole velocity field. By further integrating over the “receiver” shell Q, one obtains the energy transferred from shell K:

$$\mathcal{T}_1(K,\boldsymbol{x}) = \sum_Q \mathcal{T}_2(K,Q,\boldsymbol{x}) = -\boldsymbol{u}_K\cdot(\boldsymbol{u}\cdot\boldsymbol{\nabla})\boldsymbol{u}. \tag{D.27}$$

Note that the space-averaged $T_2(K,Q)$ and $T_1(K)$ can be defined accordingly. The energy flux through the shell k can then be obtained by

$$\Pi(k) = -\sum_{K=0}^{k} T_1(K). \tag{D.28}$$

Figure D.3(a) shows the two-dimensional energy transfer spectrum $T_2(K,Q)$ and its scaling in terms of the receiving wavenumber scale Q. First, we notice that $T_2(K,Q) > 0$ for $K < Q$ and $T_2(K,Q) < 0$ for $K > Q$. Since the shell K is the “giver” and Q is the “receiver”, they correspond to forward energy transfer, positive energy transfer from larger to smaller scales and negative energy transfer from smaller to larger scales[2]. In the following, we focus on the upper triangle of Fig. D.3(a) or $Q > K$. For the magnitude of transfer, the local interactions $T_2(K,K+1)$ tend to take large values and the decay of $T_2(K,Q)$ for fixed K and increased Q is fast. These properties are consistent with the scale-local nature of the energy

---

[2] Note that there is a relation $T_2(K,Q) + T_2(Q,K) = 0$ for spatially integrated spectrum. For space-dependent spectrum, $\mathcal{T}_2(K,Q,\boldsymbol{x}) + \mathcal{T}_2(Q,K,\boldsymbol{x}) \neq 0$.

cascade. Figure D.3(b) shows the scaling of $T_2(1, Q)$ and $T_2(2, Q)$ along with the theoretically predicted

$$T_{K,Q} \propto 2^{-4Q/3}, \tag{D.29}$$

derived in Kraichnan (1971b, Eq. (2.19)). Also see Kraichnan (1966), Zhou (1993), and Aluie and Eyink (2009).

The authors investigated the possible energy cascade mechanism based on the visual observation and correlation of the space-dependent energy transfer spectrum $\mathcal{T}_2(K, Q)$ with the magnitude of vorticity and strain. They compared i) Homogeneous Isotropic Turbulence (HIT) driven by a stochastic forcing, ii) anti-parallel and perpendicular vortex tubes, and iii) turbulence driven by a deterministic forcing, also used in Goto, Saito, et al. (2017). From the HIT results, they concluded that:

> [...] the enticing energy cascade proposed by Tennekes and Lumley (1972), resting on a description of the action of strain and vorticity at neighbouring scales, is oversimplified; [...].

Furthermore, they claimed that in the simplified setup, such as anti-parallel vortex tubes or even turbulence driven by a columnar forcing (two-dimensional Taylor–Green forcing), one cannot correctly capture the energy transfer in HIT:

> [...] the remarkably simple picture, observed in the interaction of antiparallel vortex tubes and in the configuration studied by Goto, Saito, et al. (2017), appears to be the result of a strong influence of the large-scale forcing (or initial conditions), [...]. This makes both flows ideal for the study of the energy transfer associated to vortex stretching, but less applicable to the general case of the turbulent cascade.

Bibliography

Ahmed, Shady E., Suraj Pawar, Omer San, Adil Rasheed, Traian Iliescu, and Bernd R. Noack (2021). On closures for reduced order models—A spectrum of first-principle to machine-learned avenues. *Physics of Fluids* **33** (9), p. 091301 (cited on page 34).

Alexakis, Alexandros and Luca Biferale (2018). Cascades and transitions in turbulent flows. *Physics Reports* **767**, pp. 1–101 (cited on page 19).

Alexakis, Alexandros and Sergio Chibbaro (2020). Local energy flux of turbulent flows. *Physical Review Fluids* **5** (9), p. 094604 (cited on pages 57, 60).

Aluie, Hussein and Gregory L. Eyink (2009). Localness of energy cascade in hydrodynamic turbulence. II. Sharp spectral filter. *Physics of Fluids* **21** (11), p. 115108 (cited on page 128).

Anselmet, Fabien, Yves Gagne, Emil J. Hopfinger, and Robert A. Antonia (1984). High-order velocity structure functions in turbulent shear flows. *Journal of Fluid Mechanics* **140**, pp. 63–89 (cited on page 24).

Aoyama, Tomohiro, Takashi Ishihara, Yukio Kaneda, Mitsuo Yokokawa, Ken'ichi Itakura, and Atsuya Uno (2005). Statistics of energy transfer in high-resolution direct numerical simulation of turbulence in a periodic box. *Journal of the Physical Society of Japan* **74** (12), pp. 3202–3212 (cited on page 7).

Aragón, José Luis, Gerardo G Naumis, Ming Bai, Manuel Torres, and Philip K. Maini (2008). Turbulent luminance in impassioned van Gogh paintings. *Journal of Mathematical Imaging and Vision* **30** (3), pp. 275–283 (cited on page 6).

Araki, Ryo and Wouter J. T. Bos (2022). Inertial range scaling of inhomogeneous turbulence. *arXiv preprint.* arXiv: `2210.14516 [flu-dyn]` (cited on pages v, 3, 83).

Araki, Ryo, Wouter J. T. Bos, and Susumu Goto (2023a). Minimal model of quasi-cyclic behaviour in turbulence driven by Taylor–Green forcing. *Fluid Dynamics Research* **55** (3), p. 035507. arXiv: `2112.03417 [flu-dyn]` (cited on pages v, 3, 37).

—— (2023b). Space-local Navier–Stokes turbulence. *arXiv preprint.* arXiv: `2308.07255 [flu-dyn]` (cited on pages v, 3, 69).

Araki, Ryo and Susumu Goto (2021). Quasiperiodic fluctuations of von Kármán turbulence driven by viscous stirring. *Physical Review Fluids* **6** (8), p. 084603 (cited on pages v, 3, 30, 31).

Arndt, Roger E. A., D. F. Long, and Mark N. Glauser (1997). The proper orthogonal decomposition of pressure fluctuations surrounding a turbulent jet. *Journal of Fluid Mechanics* **340**, pp. 1–33 (cited on page 34).

Avila, Marc, Dwight Barkley, and Björn Hof (2023). Transition to turbulence in pipe flow. *Annual Review of Fluid Mechanics* **55** (1), pp. 575–602 (cited on page 35).

Bakewell Jr, Henry P. and John L. Lumley (1967). Viscous sublayer and adjacent wall region in turbulent pipe flow. *The Physics of Fluids* **10** (9), pp. 1880–1889 (cited on page 34).

Ballouz, Joseph G. and Nicholas T. Ouellette (2020). Geometric constraints on energy transfer in the turbulent cascade. *Physical Review Fluids* **5** (3), p. 034603 (cited on page 58).

Beattie, James and Neco Kriel (2019). Is the Starry Night turbulent? *arXiv preprint*. arXiv: `1902.03381 [pop-ph]` (cited on page 6).

Bergmann, Michel, Laurent Cordier, and Jean-Pierre Brancher (2005). Optimal rotary control of the cylinder wake using proper orthogonal decomposition reduced-order model. *Physics of Fluids* **17** (9), p. 097101 (cited on page 34).

Berkooz, Gal, Philip Holmes, and John L. Lumley (1993). The proper orthogonal decomposition in the analysis of turbulent flows. *Annual Review of Fluid Mechanics* **25** (1), pp. 539–575 (cited on page 34).

Bertoglio, Jean-Pierre (1985). A stochastic subgrid model for sheared turbulence. In: *Macroscopic Modelling of Turbulent Flows*. Springer, pp. 100–119 (cited on page 84).

Bertoglio, Jean-Pierre and Denis Jeandel (1987). A simplified spectral closure for inhomogeneous turbulence: application to the boundary layer. In: *Turbulent Shear Flows 5*. Springer, pp. 19–30 (cited on page 86).

Besnard, Didier C., Francis H. Harlow, Rick M. Rauenzahn, and Charles Zemach (1996). Spectral transport model for turbulence. *Theoretical and Computational Fluid Dynamics* **8** (1), pp. 1–35 (cited on pages 86, 88, 89).

Betchov, Robert (1956). An inequality concerning the production of vorticity in isotropic turbulence. *Journal of Fluid Mechanics* **1** (5), pp. 497–504 (cited on pages 116, 117, 119).

Biferale, Luca (2003). Shell models of energy cascade in turbulence. *Annual Review of Fluid Mechanics* **35** (1), pp. 441–468 (cited on page 35).

Biferale, Luca, Stefano Musacchio, and Federico Toschi (2012). Inverse energy cascade in three-dimensional isotropic turbulence. *Physical Review Letters* **108** (16), p. 164501 (cited on pages 11, 79).

Boffetta, Guido and Robert E. Ecke (2012). Two-dimensional turbulence. *Annual Review of Fluid Mechanics* **44**, pp. 427–451 (cited on page 19).

Borggaard, Jeff, Traian Iliescu, and Zhu Wang (2011). Artificial viscosity proper orthogonal decomposition. *Mathematical and Computer Modelling* **53** (1-2), pp. 269–279 (cited on page 34).

Borue, Vadim and Steven A. Orszag (1996). Numerical study of three-dimensional Kolmogorov flow at high Reynolds numbers. *Journal of Fluid Mechanics* **306**, pp. 293–323 (cited on page 92).

—— (1998). Local energy flux and subgrid-scale statistics in three-dimensional turbulence. *Journal of Fluid Mechanics* **366**, pp. 1–31 (cited on page 57).

Bos, Wouter J. T. (2020). Production and dissipation of kinetic energy in grid turbulence. *Physical Review Fluids* **5** (10), p. 104607 (cited on pages 18, 86).

—— (2021). Three-dimensional turbulence without vortex stretching. *Journal of Fluid Mechanics* **915**, A121 (cited on pages 22, 78, 79, 114).

Bos, Wouter J. T. and Ryo Araki (in preparation). Analysis of the normalized dissipation rate in inhomogeneous and unsteady turbulence (cited on pages v, 3, 99).

Bos, Wouter J. T., Laurent Chevillard, Julian F. Scott, and Robert Rubinstein (2012). Reynolds number effect on the velocity increment skewness in isotropic turbulence. *Physics of Fluids* **24** (1) (cited on page 24).

Bos, Wouter J. T. and Robert Rubinstein (2017). Dissipation in unsteady turbulence. *Physical Review Fluids* **2** (2), p. 022601 (cited on pages 84, 87, 100).

Bos, Wouter J. T., Liang Shao, and Jean-Pierre Bertoglio (2007). Spectral imbalance and the normalized dissipation rate of turbulence. *Physics of Fluids* **19** (4), p. 045101 (cited on pages 16, 27).

Brenner, Michael P., Sahand Hormoz, and Alain Pumir (2016). Potential singularity mechanism for the Euler equations. *Physical Review Fluids* **1** (8), p. 084503 (cited on pages 118, 120).

Briard, Antoine, Benoît-Joseph Gréa, Vincent Mons, Claude Cambon, Thomas Gomez, and Pierre Sagaut (2018). Advanced spectral anisotropic modelling for shear flows. *Journal of Turbulence* **19** (7), pp. 570–599 (cited on page 88).

Brunton, Steven L. and J Nathan Kutz (2022). *Data-driven Science and Engineering: Machine Learning, Dynamical Systems, and Control.* 2nd ed. Cambridge University Press (cited on page 34).

Brunton, Steven L., Joshua L. Proctor, and J. Nathan Kutz (2016). Discovering governing equations from data by sparse identification of nonlinear dynamical systems. *Proceedings of the National Academy of Sciences* **113** (15), pp. 3932–3937 (cited on page 34).

Buaria, Dhawal, Eberhard Bodenschatz, and Alain Pumir (2020). Vortex stretching and enstrophy production in high Reynolds number turbulence. *Physical Review Fluids* **5** (10), p. 104602 (cited on page 22).

Buaria, Dhawal and Alain Pumir (2021). Nonlocal amplification of intense vorticity in turbulent flows. *Physical Review Research* **3** (4), p. L042020 (cited on pages 58, 60).

Buaria, Dhawal, Alain Pumir, and Eberhard Bodenschatz (2020). Self-attenuation of extreme events in Navier–Stokes turbulence. *Nature Communications* **11** (1), pp. 1–7 (cited on pages 58–60, 62).

Buaria, Dhawal, Alain Pumir, Eberhard Bodenschatz, and Pui-Keun Yeung (2019). Extreme velocity gradients in turbulent flows. *New Journal of Physics* **21** (4), p. 043004 (cited on pages 7, 8).

Cadiou, Anne, Kemal Hanjalić, and K Stawiarski (2004). A two-scale second-moment turbulence closure based on weighted spectrum integration. *Theoretical and Computational Fluid Dynamics* **18** (1), pp. 1–26 (cited on page 89).

Cadot, Olivier, Yves Couder, Adrian Daerr, Stephane Douady, and Arkady Tsinober (1997). Energy injection in closed turbulent flows: Stirring through boundary layers versus inertial stirring. *Physical Review E* **56** (1), p. 427 (cited on pages 16, 30, 32).

Cambon, Claude, Denis Jeandel, and Jean Mathieu (1981). Spectral modelling of homogeneous non-isotropic turbulence. *Journal of Fluid Mechanics* **104**, pp. 247–262 (cited on page 88).

Carbone, Francesco, Daniele Telloni, Gary Zank, and Luca Sorriso-Valvo (2021). Transition to turbulence in a five-mode Galerkin truncation of two-dimensional magnetohydrodynamics. *Physical Review E* **104** (2), p. 025201 (cited on page 34).

Carbone, Maurizio and Andrew D. Bragg (2020). Is vortex stretching the main cause of the turbulent energy cascade? *Journal of Fluid Mechanics* **883**, R2 (cited on pages 23, 119, 122, 124, 125).

Cardesa, José I., Alberto Vela-Martín, Siwei Dong, and Javier Jiménez (2015). The temporal evolution of the energy flux across scales in homogeneous turbulence. *Physics of Fluids* **27** (11), p. 111702 (cited on page 27).

Cardesa, José I., Alberto Vela-Martín, and Javier Jiménez (2017). The turbulent cascade in five dimensions. *Science* **357** (6353), pp. 782–784 (cited on pages 11, 57).

Chantry, Matthew, Laurette S. Tuckerman, and Dwight Barkley (2016). Turbulent–laminar patterns in shear flows without walls. *Journal of Fluid Mechanics* **791**, R8 (cited on page 36).

Chen, Jiangang G., Christophe Cuvier, Jean-Marc Foucaut, Yasar Ostovan, and John C. Vassilicos (2021). A turbulence dissipation inhomogeneity scaling in the wake of two side-by-side square prisms. *Journal of Fluid Mechanics* **924**, A4 (cited on pages 100, 101).

Chevillard, Laurent, Bernard Castaing, Emmanuel Lévêque, and Alain Arnéodo (2006). Unified multifractal description of velocity increments statistics in turbulence: Intermittency and skewness. *Physica D: Nonlinear Phenomena* **218** (1), pp. 77–82 (cited on page 24).

Chevillard, Laurent, Emmanuel Lévêque, Francesco Taddia, Charles Meneveau, Huidan Yu, and Carlos Rosales (2011). Local and nonlocal pressure Hessian effects in real and synthetic fluid turbulence. *Physics of Fluids* **23** (9), p. 095108 (cited on pages 58, 60, 64).

Chevillard, Laurent and Charles Meneveau (2006). Lagrangian dynamics and statistical geometric structure of turbulence. *Physical Review Letters* **97** (17), p. 174501 (cited on page 34).

Couplet, M., Pierre Sagaut, and Claude Basdevant (2003). Intermodal energy transfers in a proper orthogonal decomposition–Galerkin representation of a turbulent separated flow. *Journal of Fluid Mechanics* **491**, pp. 275–284 (cited on page 34).

Cuypers, Yannis, Agnes Maurel, and Philippe Petitjeans (2003). Vortex burst as a source of turbulence. *Physical Review Letters* **91** (19), p. 194502 (cited on pages 119, 122).

Davidson, Peter A. (2015). *Turbulence: An Introduction for Scientists and Engineers*. 2nd ed. Oxford University Press (cited on pages 14, 19, 116, 120).

Davidson, Peter A., Koji Morishita, and Yukio Kaneda (2008). On the generation and flux of enstrophy in isotropic turbulence. *Journal of Turbulence* **9**, N42 (cited on pages 76, 77).

De Morgan, Augustus (1872). *A Budget of Paradoxes*. (Available at `https://archive.org/details/abudgetparadoxe03morggoog`). Longmans, Green (cited on page 5).

Delache, Alexandre, Claude Cambon, and Fabien Godeferd (2014). Scale by scale anisotropy in freely decaying rotating turbulence. *Physics of Fluids* **26** (2), p. 025104 (cited on pages 37, 92).

Ditlevsen, Peter D. (2010). *Turbulence and Shell Models*. Cambridge University Press (cited on pages 35, 43).

Doan, Nguyen A. K., Nithya Swaminathan, Peter A. Davidson, and Mamoru Tanahashi (2018). Scale locality of the energy cascade using real space quantities. *Physical Review Fluids* **3** (8), p. 084601 (cited on pages 22, 57).

Domaradzki, J. Andrzej and Daniele Carati (2007). An analysis of the energy transfer and the locality of nonlinear interactions in turbulence. *Physics of Fluids* **19** (8), p. 085112 (cited on page 11).

Domaradzki, J. Andrzej and Robert S. Rogallo (1990). Local energy transfer and nonlocal interactions in homogeneous, isotropic turbulence. *Physics of Fluids A: Fluid Dynamics* **2** (3), pp. 413–426 (cited on pages 10, 11).

Dubrulle, Bérengère (1994). Intermittency in fully developed turbulence: Log-Poisson statistics and generalized scale covariance. *Physical Review Letters* **73** (7), p. 959 (cited on page 24).

—— (2019). Beyond Kolmogorov cascades. *Journal of Fluid Mechanics* **867**, P1 (cited on pages 14, 30, 60).

Duguet, Yohann, Philipp Schlatter, Dan S. Henningson, and Bruno Eckhardt (2012). Self-sustained localized structures in a boundary-layer flow. *Physical Review Letters* **108** (4), p. 044501 (cited on page 36).

Duraisamy, Karthik, Gianluca Iaccarino, and Heng Xiao (2019). Turbulence modeling in the age of data. *Annual Review of Fluid Mechanics* **51**, pp. 357–377 (cited on page 18).

Duraisamy, Karthik and Sanjiva K. Lele (2008). Evolution of isolated turbulent trailing vortices. *Physics of Fluids* **20** (3), p. 035102 (cited on page 119).

Eckhardt, Bruno and Alois Mersmann (1999). Transition to turbulence in a shear flow. *Physical Review E* **60** (1), p. 509 (cited on page 34).

Edeling, Wouter Nico, Gianluca Iaccarino, and Paola Cinnella (2018). Data-free and data-driven RANS predictions with quantified uncertainty. *Flow, Turbulence and Combustion* **100** (3), pp. 593–616 (cited on page 18).

Eyink, Gregory L. (1995). Local energy flux and the refined similarity hypothesis. *Journal of Statistical Physics* **78** (1), pp. 335–351 (cited on pages 57, 60).

—— (2005). Locality of turbulent cascades. *Physica D: Nonlinear Phenomena* **207** (1-2), pp. 91–116 (cited on pages 11, 57, 60).

—— (2006). Multi-scale gradient expansion of the turbulent stress tensor. *Journal of Fluid Mechanics* **549**, pp. 159–190 (cited on pages 22, 57, 60).

—— (2007-2008). *"Turbulence Theory" course notes.* (The Johns Hopkins University). URL: `https://www.ams.jhu.edu/~eyink/Turbulence/notes.html` (visited on 02/17/2023) (cited on pages 14, 20).

Eyink, Gregory L. and Hussein Aluie (2009). Localness of energy cascade in hydrodynamic turbulence. I. Smooth coarse graining. *Physics of Fluids* **21** (11), p. 115107 (cited on page 57).

Eyink, Gregory L. and Katepalli R. Sreenivasan (2006). Onsager and the theory of hydrodynamic turbulence. *Reviews of Modern Physics* **78** (1), p. 87 (cited on pages 9, 14, 21).

Fang, Le and Wouter J. T. Bos (2023). An EDQNM study of the dissipation rate in isotropic non-equilibrium turbulence. *Journal of Turbulence*, pp. 1–18 (cited on pages 16, 101).

Fjørtoft, Ragnar (1953). On the changes in the spectral distribution of kinetic energy for twodimensional, nondivergent flow. *Tellus* **5** (3), pp. 225–230 (cited on page 19).

Frisch, Uriel (1995). *Turbulence: The Legacy of A. N. Kolmogorov.* Cambridge University Press (cited on pages 14, 16, 20, 24, 28).

Frisch, Uriel, Anna Pomyalov, Itamar Procaccia, and Samriddhi Sankar Ray (2012). Turbulence in non-integer dimensions by fractal Fourier decimation. *Physical Review Letters* **108** (7), p. 074501 (cited on page 79).

Frisch, Uriel, Pierre-Louis Sulem, and Mark Nelkin (1978). A simple dynamical model of intermittent fully developed turbulence. *Journal of Fluid Mechanics* **87** (4), pp. 719–736 (cited on page 20).

Galanti, Barak and Arkady Tsinober (2000). Self-amplification of the field of velocity derivatives in quasi-isotropic turbulence. *Physics of Fluids* **12** (12), pp. 3097–3099 (cited on page 22).

Galletti, Bernardo, Charles-Henri Bruneau, Luca Zannetti, and Angelo Iollo (2004). Low-order modelling of laminar flow regimes past a confined square cylinder. *Journal of Fluid Mechanics* **503**, pp. 161–170 (cited on page 34).

George, William K. (2013). *Lectures in Turbulence for the 21st Century.* URL: `http://www.turbulence-online.com/Publications/Lecture_Notes/Turbulence_Lille/TB_16January2013.pdf` (cited on page 14).

—— (2014). Reconsidering the 'local equilibrium' hypothesis for small scale turbulence. In: *Turbulence Colloquium Marseille TCM2011: Fundamental Problems of Turbulence: 50 Years After the Colloquium Marseille of 1961.* Ed. by Marie Farge, Keith Moffatt, and Kai Schneider. EDP Sciences, pp. 456–477 (cited on page 16).

Gibbon, Jhon D., Athanassios S. Fokas, and Charles R. Doering (1999). Dynamically stretched vortices as solutions of the 3D Navier–Stokes equations. *Physica D: Nonlinear Phenomena* **132** (4), pp. 497–510 (cited on pages 22, 119).

Gilbert, Andrew D. (1993). A cascade interpretation of Lundgren's stretched spiral vortex model for turbulent fine structure. *Physics of Fluids A: Fluid Dynamics* **5** (11), pp. 2831–2834 (cited on page 119).

Gledzer, Evgenii Borisovich (1973). System of hydrodynamic type admitting two quadratic integrals of motion. In: *Soviet Physics - Doklady*. Vol. 18, pp. 216–217 (cited on page 34).

Goldenfeld, Nigel and Hong-Yan Shih (2017). Turbulence as a problem in non-equilibrium statistical mechanics. *Journal of Statistical Physics* **167** (3), pp. 575–594 (cited on page 36).

Goto, Susumu (2008). A physical mechanism of the energy cascade in homogeneous isotropic turbulence. *Journal of Fluid Mechanics* **605**, pp. 355–366 (cited on pages 22, 119, 120).

—— (2012). Coherent structures and energy cascade in homogeneous turbulence. *Progress of Theoretical Physics Supplement* **195**, pp. 139–156 (cited on page 22).

—— (2018). Developed turbulence: On the energy cascade. Japanese. *Butsuri* **73** (7). (後藤 晋，発達した乱流—エネルギーカスケードをめぐって，日本物理学会誌), pp. 457–462 (cited on page 15).

Goto, Susumu, Yuta Saito, and Genta Kawahara (2017). Hierarchy of antiparallel vortex tubes in spatially periodic turbulence at high Reynolds numbers. *Physical Review Fluids* **2** (6), p. 064603 (cited on pages 22, 28, 30, 32, 37, 38, 65, 119, 122, 128).

Goto, Susumu and John C. Vassilicos (2015). Energy dissipation and flux laws for unsteady turbulence. *Physics Letters A* **379** (16-17), pp. 1144–1148 (cited on pages 27, 100, 101).

—— (2016a). Local equilibrium hypothesis and Taylor's dissipation law. *Fluid Dynamics Research* **48** (2), p. 021402 (cited on pages 12, 16, 17, 27, 28, 32).

—— (2016b). Unsteady turbulence cascades. *Physical Review E* **94** (5), p. 053108 (cited on page 16).

Graham, Michael D. and Daniel Floryan (2021). Exact coherent states and the nonlinear dynamics of wall-bounded turbulent flows. *Annual Review of Fluid Mechanics* **53**, pp. 227–253 (cited on page 35).

Guckenheimer, John and Philip Holmes (2013). *Nonlinear Oscillations, Dynamical Systems, and Bifurcations of Vector Fields*. Applied Mathematical Sciences. Springer New York (cited on pages 33, 34).

Hall, Kenneth, Jeffrey Thomas, and Earl Dowell (1999). Reduced-order modelling of unsteady small-disturbance flows using a frequency-domain proper orthogonal decomposition technique. In: *37th Aerospace Sciences Meeting and Exhibit*, p. 655 (cited on page 34).

Hamilton, James M., John Kim, and Fabian Waleffe (1995). Regeneration mechanisms of near-wall turbulence structures. *Journal of Fluid Mechanics* **287**, pp. 317–348 (cited on page 28).

Hamlington, Peter E. (2009). Physics-Based Turbulence Anisotropy Closure Including Nonlocal and Nonequilibrium Effects in Turbulent Flows. PhD thesis. University of Michigan (cited on pages 58, 62).

Hamlington, Peter E., Jörg Schumacher, and Werner J. A. Dahm (2008a). Local and nonlocal strain rate fields and vorticity alignment in turbulent flows. *Physical Review E* **77** (2), p. 026303 (cited on pages 58, 60, 62, 113).

—— (2008b). Direct assessment of vorticity alignment with local and nonlocal strain rates in turbulent flows. *Physics of Fluids* **20** (11), p. 111703 (cited on pages 58, 60, 62).

Hearst, R. Jason and Philippe Lavoie (2014). Decay of turbulence generated by a square-fractal-element grid. *Journal of Fluid Mechanics* **741**, pp. 567–584 (cited on page 100).

Heisenberg, Werner Karl (1948). Zur statistischen Theorie der Turbulenz. *Zeitschrift für Physik* **124**, pp. 628–657 (cited on page 14).

Hill, Reginald J. (2002). Exact second-order structure-function relationships. *Journal of Fluid Mechanics* **468**, pp. 317–326 (cited on page 60).

Hino, Mikio (2020). *Science of Turbulence: Structure and Control.* Japanese. (日野 幹雄，乱流の科学: 構造と制御，朝倉書店). Asakura Publishing (cited on page 121).

Hirsch, Morris W., Stephen Smale, and Robert L. Devaney (2012). *Differential Equations, Dynamical Systems, and an Introduction to Chaos.* Academic press (cited on pages 33, 34).

Hof, Björn, Jerry Westerweel, Tobias M. Schneider, and Bruno Eckhardt (2006). Finite lifetime of turbulence in shear flows. *Nature* **443** (7107), pp. 59–62 (cited on page 51).

Holmes, Philip, John L. Lumley, and Gahl Berkooz (1996). *Turbulence, Coherent Structures, Dynamical Systems and Symmetry.* Cambridge University Press (cited on page 34).

Horiuti, Kiyosi and Takeharu Fujisawa (2008). The multi-mode stretched spiral vortex in homogeneous isotropic turbulence. *Journal of Fluid Mechanics* **595**, pp. 341–366 (cited on pages 119, 121, 122).

Horiuti, Kiyosi and Tetsuya Ozawa (2011). Multimode stretched spiral vortex and nonequilibrium energy spectrum in homogeneous shear flow turbulence. *Physics of Fluids* **23** (3), p. 035107 (cited on pages 84, 95, 120, 122).

Horiuti, Kiyosi and Youhei Takagi (2005). Identification method for vortex sheet structures in turbulent flows. *Physics of Fluids* **17** (12), p. 121703 (cited on page 121).

Horiuti, Kiyosi and Takahiro Tamaki (2013). Nonequilibrium energy spectrum in the subgrid-scale one-equation model in large-eddy simulation. *Physics of Fluids* **25** (12), p. 125104 (cited on pages 18, 84, 97).

Hunt, Julian C. R., Ian Eames, Jerry Westerweel, Peter A. Davidson, Sergey Voropayev, Harindra J. Fernando, and Marianna Braza (2010). Thin shear layers–the key to turbulence structure? *Journal of Hydro-Environment Research* **4** (2), pp. 75–82 (cited on page 5).

Hunt, Julian C. R., Neil D. Sandham, John C. Vassilicos, Brian Edward Launder, Peter A. Monkewitz, and Geoffrey F. Hewitt (2001). Developments in turbulence research: a review based on the 1999 Programme of the Isaac Newton Institute, Cambridge. *Journal of Fluid Mechanics* **436**, pp. 353–391 (cited on page 14).

Hunt, Julian C. R. and John C. Vassilicos (1991). Kolmogorov's contributions to the physical and geometrical understanding of small-scale turbulence and recent developments. *Proceedings of the Royal Society of London. Series A: Mathematical and Physical Sciences* **434** (1890), pp. 183–210 (cited on page 14).

Hussain, Fazle and Karthik Duraisamy (2011). Mechanics of viscous vortex reconnection. *Physics of Fluids* **23** (2), p. 021701 (cited on page 121).

Hwang, Yongyun and Carlo Cossu (2010). Self-sustained process at large scales in turbulent channel flow. *Physical Review Letters* **105** (4), p. 044505 (cited on page 28).

Ilak, Miloš and Clarence W. Rowley (2008). Modeling of transitional channel flow using balanced proper orthogonal decomposition. *Physics of Fluids* **20** (3), p. 034103 (cited on page 34).

Ishihara, Takashi, Toshiyuki Gotoh, and Yukio Kaneda (2009). Study of high-Reynolds number isotropic turbulence by direct numerical simulation. *Annual Review of Fluid Mechanics* **41** (1), pp. 165–180 (cited on page 7).

Ishihara, Takashi, Yukio Kaneda, and Julian C. R. Hunt (2013). Thin shear layers in high Reynolds number turbulence—DNS results. *Flow, Turbulence and Combustion* **91** (4), pp. 895–929 (cited on page 7).

Ishihara, Takashi, Kyo Yoshida, and Yukio Kaneda (2002). Anisotropic velocity correlation spectrum at small scales in a homogeneous turbulent shear flow. *Physical Review Letters* **88** (15), p. 154501 (cited on pages 84, 114).

Jeandel, Denis, J. F. Brison, and Jean Mathieu (1978). Modeling methods in physical and spectral space. *The Physics of Fluids* **21** (2), pp. 169–182 (cited on page 86).

Jiménez, Javier (2012). Cascades in wall-bounded turbulence. *Annual Review of Fluid Mechanics* **44**, pp. 27–45 (cited on pages 5, 16).

Jiménez, Javier and Parviz Moin (1991). The minimal flow unit in near-wall turbulence. *Journal of Fluid Mechanics* **225**, pp. 213–240 (cited on page 28).

Jiménez, Javier, Alan A. Wray, Philip G. Saffman, and Robert S. Rogallo (1993). The structure of intense vorticity in isotropic turbulence. *Journal of Fluid Mechanics* **255**, pp. 65–90 (cited on page 22).

Johansson, Arne V. and P. Henrik Alfredsson (1982). On the structure of turbulent channel flow. *Journal of Fluid Mechanics* **122**, pp. 295–314 (cited on page 28).

Johnson, Perry L. (2020). Energy transfer from large to small scales in turbulence by multiscale nonlinear strain and vorticity interactions. *Physical Review Letters* **124** (10), p. 104501 (cited on pages 23, 122, 125).

—— (2021a). On the role of vorticity stretching and strain self-amplification in the turbulence energy cascade. *Journal of Fluid Mechanics* **922**, A3 (cited on pages 20, 23, 119, 122, 125).

—— (2021b). The squeezes, stretches, and whirls of turbulence. *Physics Today* **74**, pp. 4–46 (cited on page 23).

Johnson, Perry L. and Charles Meneveau (2016). Large-deviation statistics of vorticity stretching in isotropic turbulence. *Physical Review E* **93** (3), p. 033118 (cited on page 22).

Kaneda, Yukio, Takashi Ishihara, Mitsuo Yokokawa, Ken'ichi Itakura, and Atsuya Uno (2003). Energy dissipation rate and energy spectrum in high resolution direct numerical simulations of turbulence in a periodic box. *Physics of Fluids* **15** (2), pp. L21–L24 (cited on page 16).

Kaneda, Yukio and Yoshinobu Yamamoto (2021). Velocity gradient statistics in turbulent shear flow: an extension of Kolmogorov's local equilibrium theory. *Journal of Fluid Mechanics* **929** (cited on page 16).

Kawahara, Genta and Shigeo Kida (2001). Periodic motion embedded in plane Couette turbulence: regeneration cycle and burst. *Journal of Fluid Mechanics* **449**, pp. 291–300 (cited on pages 28, 29).

Kawahara, Genta, Shigeo Kida, Mitsuru Tanaka, and Shinichiro Yanase (1997). Wrap, tilt and stretch of vorticity lines around a strong thin straight vortex tube in a simple shear flow. *Journal of Fluid Mechanics* **353**, pp. 115–162 (cited on page 121).

Kawahara, Genta, Markus Uhlmann, and Lennaert van Veen (2012). The significance of simple invariant solutions in turbulent flows. *Annual Review of Fluid Mechanics* **44**, pp. 203–225 (cited on page 28).

Kellay, Hamid and Walter I. Goldburg (2002). Two-dimensional turbulence: a review of some recent experiments. *Reports on Progress in Physics* **65** (5), p. 845 (cited on page 19).

Kerr, Robert M. (1993). Evidence for a singularity of the three-dimensional, incompressible Euler equations. *Physics of Fluids A: Fluid Dynamics* **5** (7), pp. 1725–1746 (cited on page 119).

—— (2013). Swirling, turbulent vortex rings formed from a chain reaction of reconnection events. *Physics of Fluids* **25** (6), p. 065101 (cited on pages 119, 122).

Kida, Shigeo and Masanori Takaoka (1994). Vortex reconnection. *Annual Review of Fluid Mechanics* **26** (1), pp. 169–177 (cited on page 118).

Kishiba, Seigo, Koji Ohkitani, and Shigeo Kida (1993). Physical-space nonlocality in decaying isotropic turbulence. *Journal of the Physical Society of Japan* **62** (11), pp. 3783–3787 (cited on page 58).

Klotz, Lukasz, Grégoire Lemoult, Kerstin Avila, and Björn Hof (2022). Phase transition to turbulence in spatially extended shear flows. *Physical Review Letters* **128** (1), p. 014502 (cited on page 36).

Knight, Bruce and Lawrence Sirovich (1990). Kolmogorov inertial range for inhomogeneous turbulent flows. *Physical Review Letters* **65** (11), p. 1356 (cited on page 84).

Knutsen, Anna N., Pawel Baj, John M. Lawson, Eberhard Bodenschatz, James R. Dawson, and Nicholas A. Worth (2020). The inter-scale energy budget in a von Kármán mixing flow. *Journal of Fluid Mechanics* **895**, A11 (cited on page 30).

Kolmogorov, Andrey Nikolaevich (1941a). The local structure of turbulence in incompressible viscous fluid for very large Reynolds numbers. *Doklady Akademii Nauk SSSR* **30** (4). (Reprinted in Proc. R. Soc. Lond. A, **434**, pp. 9–13 (1991) and Selected Works of A. N. Kolmogorov, Vol. I: Mathematics and Mechanics, Kluwer Academic Publishers, pp. 312–318 (1991)), pp. 299–303 (cited on pages 13, 14, 60, 74, 79, 83, 90, 94, 113).

—— (1941b). On the degeneration of isotropic turbulence in an incompressible viscous fluid. *Doklady Akademii Nauk SSSR* **31** (6). (Reprinted in Selected Works of A. N. Kolmogorov, Vol. I: Mathematics and Mechanics, Kluwer Academic Publishers, pp. 319–323 (1991)), pp. 538–540 (cited on pages 14, 16, 60).

—— (1941c). Dissipation of energy in locally isotropic turbulence. *Doklady Akademii Nauk SSSR* **32** (1). (Reprinted in Proc. R. Soc. Lond. A, **434**, pp. 16–18 (1991) and Selected Works of A. N. Kolmogorov, Vol. I: Mathematics and Mechanics, Kluwer Academic Publishers, pp. 324–327 (1991)), pp. 16–18 (cited on pages 14, 60).

—— (1962). A refinement of previous hypotheses concerning the local structure of turbulence in a viscous incompressible fluid at high Reynolds number. *Journal of Fluid Mechanics* **13** (1), pp. 82–85 (cited on page 24).

Kraichnan, Robert H. (1958). Irreversible statistical mechanics of incompressible hydromagnetic turbulence. *Physical Review* **109** (5), p. 1407 (cited on page 43).

—— (1966). Isotropic Turbulence and Inertial-Range Structure. *The Physics of Fluids* **9** (9), pp. 1728–1752 (cited on page 128).

—— (1967). Inertial ranges in two-dimensional turbulence. *The Physics of Fluids* **10** (7), pp. 1417–1423 (cited on page 19).

—— (1971a). An almost-Markovian Galilean-invariant turbulence model. *Journal of Fluid Mechanics* **47** (3), pp. 513–524 (cited on pages 84, 88).

—— (1971b). Inertial-range transfer in two-and three-dimensional turbulence. *Journal of Fluid Mechanics* **47** (3), pp. 525–535 (cited on pages 11, 19, 79, 128).

—— (1974). On Kolmogorov's inertial-range theories. *Journal of Fluid Mechanics* **62** (2), pp. 305–330 (cited on pages 57, 60).

—— (1988). Reduced descriptions of hydrodynamic turbulence. *Journal of Statistical Physics* **51** (5), pp. 949–963 (cited on pages 34, 43).

Kraichnan, Robert H. and David Montgomery (1980). Two-dimensional turbulence. *Reports on Progress in Physics* **43** (5), p. 547 (cited on page 19).

Krüger, T., H. Kusumaatmaja, A. Kuzmin, O. Shardt, G. Silva, and E.M. Viggen (2016). *The Lattice Boltzmann Method: Principles and Practice*. Graduate Texts in Physics. Springer International Publishing (cited on page 58).

Kurien, Susan, Victor S. L'vov, Itamar Procaccia, and Katepalli R. Sreenivasan (2000). Scaling structure of the velocity statistics in atmospheric boundary layers. *Physical Review E* **61** (1), p. 407 (cited on page 84).

L'vov, Victor S., Evgenii Podivilov, Anna Pomyalov, Itamar Procaccia, and Damien Vandembroucq (1998). Improved shell model of turbulence. *Physical Review E* **58** (2), p. 1811 (cited on page 35).

Labbé, Raúl, Jean-François Pinton, and Stephan Fauve (1996). Study of the von Kármán flow between coaxial corotating disks. *Physics of Fluids* **8** (4), pp. 914–922 (cited on page 30).

Lalescu, Cristian C., Charles Meneveau, and Gregory L. Eyink (2013). Synchronization of chaos in fully developed turbulence. *Physical Review Letters* **110** (8), p. 084102 (cited on page 114).

Laporta, André (1995). Etude spectrale et modélisation de la turbulence inhomogène. PhD thesis. École Centrale de Lyon (cited on page 88).

Laporta, André and Jean-Pierre Bertoglio (1995). A model for inhomogeneous turbulence based on two-point correlations. In: *Advances in Turbulence V*. Springer, pp. 286–297 (cited on pages 84, 86, 88).

Leith, Cecil E. (1967). Diffusion approximation to inertial energy transfer in isotropic turbulence. *The Physics of Fluids* **10** (7), pp. 1409–1416 (cited on page 89).

—— (1968). Diffusion approximation for two-dimensional turbulence. *The Physics of Fluids* **11** (3), pp. 671–672 (cited on page 19).

Lemoult, Grégoire, Liang Shi, Kerstin Avila, Shreyas V Jalikop, Marc Avila, and Björn Hof (2016). Directed percolation phase transition to sustained turbulence in Couette flow. *Nature Physics* **12** (3), pp. 254–258 (cited on page 36).

Lesieur, Marcel (2008). *Turbulence in Fluids.* Fluid Mechanics and Its Applications. (Fourth revised and enlarged edition). Springer Dordrecht (cited on pages 9, 14, 19).

Leslie, D. C. and Cecil E. Leith (1975). Developments in the theory of turbulence. *Physics Today* **28** (6), p. 59 (cited on page 84).

Leung, Teresa, Nedunchezhian Swaminathan, and Peter A. Davidson (2012). Geometry and interaction of structures in homogeneous isotropic turbulence. *Journal of Fluid Mechanics* **710**, pp. 453–481 (cited on pages 22, 119).

Liao, Zi-Ju and Wei-Dong Su (2015). Kolmogorov's hypotheses and global energy spectrum of turbulence. *Physics of Fluids* **27** (4), p. 041701 (cited on page 84).

Liberge, Erwan and Aziz Hamdouni (2010). Reduced order modelling method via proper orthogonal decomposition (POD) for flow around an oscillating cylinder. *Journal of Fluids and Structures* **26** (2), pp. 292–311 (cited on page 34).

Linkmann, Moritz F. and Alexander Morozov (2015). Sudden relaminarization and lifetimes in forced isotropic turbulence. *Physical Review Letters* **115** (13), p. 134502 (cited on pages 51, 53).

Lorenz, Edward N. (1963). Deterministic nonperiodic flow. *Journal of Atmospheric Sciences* **20** (2), pp. 130–141 (cited on pages 33, 47).

Lotka, Alfred J. (1920). Analytical note on certain rhythmic relations in organic systems. *Proceedings of the National Academy of Sciences* **6** (7), pp. 410–415 (cited on page 33).

Lozano-Durán, Adrián, Markus Holzner, and Javier Jiménez (2016). Multiscale analysis of the topological invariants in the logarithmic region of turbulent channels at a friction Reynolds number of 932. *Journal of Fluid Mechanics* **803**, pp. 356–394 (cited on page 22).

Lucas, Dan and Rich R. Kerswell (2017). Sustaining processes from recurrent flows in body-forced turbulence. *Journal of Fluid Mechanics* **817**, R3 (cited on page 22).

Luchik, Thomas S. and William G. Tiederman (1987). Timescale and structure of ejections and bursts in turbulent channel flows. *Journal of Fluid Mechanics* **174**, pp. 529–552 (cited on page 28).

Lumley, John L. (1967). Similarity and the turbulent energy spectrum. *The Physics of Fluids* **10** (4), pp. 855–858 (cited on page 84).

—— (1992). Some comments on turbulence. *Physics of Fluids A: Fluid Dynamics* **4** (2), pp. 203–211 (cited on pages 14, 16, 27).

Lundgren, Thomas S. (1982). Strained spiral vortex model for turbulent fine structure. *The Physics of Fluids* **25** (12), pp. 2193–2203 (cited on pages 119–121).

—— (1993). A small-scale turbulence model. *Physics of Fluids A: Fluid Dynamics* **5** (6), pp. 1472–1483 (cited on pages 119, 120).

Lynch, Peter (2022). Richardson's forecast: the dream and the fantasy. *arXiv preprint.* arXiv: `2210.01674 [hist-ph]` (cited on page 5).

Majda, Andrew J. and Andrea L. Bertozzi (2002). *Vorticity and Incompressible Flow.* Cambridge Texts in Applied Mathematics. Cambridge University Press (cited on page 61).

Marusic, Ivan and Susan Broomhall (2021). Leonardo da Vinci and fluid mechanics. *Annual Review of Fluid Mechanics* **53**, pp. 1–25 (cited on page 6).

Maslennikov, Oleg V. and Vladimir I. Nekorkin (2013). Dynamic boundary crisis in the Lorenz-type map. *Chaos: An Interdisciplinary Journal of Nonlinear Science* **23** (2), p. 023129 (cited on page 51).

McComb, W. David, Arjun Berera, Matthew Salewski, and Samuel Yoffe (2010). Taylor's (1935) dissipation surrogate reinterpreted. *Physics of Fluids* **22** (6), p. 061704 (cited on page 16).

McKeown, Ryan, Rodolfo Ostilla-Mónico, Alain Pumir, Michael P. Brenner, and Shmuel M. Rubinstein (2018). Cascade leading to the emergence of small structures in vortex ring collisions. *Physical Review Fluids* **3** (12), p. 124702 (cited on page 118).

—— (2020). Turbulence generation through an iterative cascade of the elliptical instability. *Science Advances* **6** (9), eaaz2717 (cited on pages 118, 120).

McKeown, Ryan, Alain Pumir, Shmuel M. Rubinstein, Michael P. Brenner, and Rodolfo Ostilla-Mónico (2022). Energy transfer and vortex structures: Visualizing the incompressible turbulent energy cascade. *arXiv preprint.* arXiv: `2204.09023 [flu-dyn]` (cited on pages 122, 126, 127).

Melander, Mogens V. and Fazle Hussain (1988). Cut-and-connect of two antiparallel vortex tubes. In: *Studying Turbulence Using Numerical Simulation Databases, 2.* Center for Turbulence Research, pp. 257–286 (cited on pages 119, 120).

—— (1993). Coupling between a coherent structure and fine-scale turbulence. *Physical Review E* **48** (4), p. 2669 (cited on pages 22, 119, 120).

Meneveau, Charles (1991). Analysis of turbulence in the orthonormal wavelet representation. *Journal of Fluid Mechanics* **232**, pp. 469–520 (cited on page 57).

—— (2011). Lagrangian dynamics and models of the velocity gradient tensor in turbulent flows. *Annual Review of Fluid Mechanics* **43** (1), pp. 219–245 (cited on page 34).

Meneveau, Charles and Thomas S. Lund (1994). On the Lagrangian nature of the turbulence energy cascade. *Physics of Fluids* **6** (8), pp. 2820–2825 (cited on pages 27, 57).

Moehlis, Jeff, Holger Faisst, and Bruno Eckhardt (2004). A low-dimensional model for turbulent shear flows. *New Journal of Physics* **6** (1), p. 56 (cited on page 35).

Moffatt, Henry Keith (1993). Spiral structures in turbulent flow. In: *New Approaches and Concepts in Turbulence.* Springer, pp. 121–129 (cited on pages 119, 120).

Moore, Derek William (1985). The interaction of a diffusing line vortex and an aligned shear flow. *Proceedings of the Royal Society of London. Series A: Mathematical and Physical Sciences* **399** (1817), pp. 367–375 (cited on page 121).

Mordant, Nicolas, Jean Delour, Emmanuel Lévêque, Alain Arnéodo, and Jean-François Pinton (2002). Long time correlations in Lagrangian dynamics: a key to intermittency in turbulence. *Physical Review Letters* **89** (25), p. 254502 (cited on page 30).

Mortensen, Mikael (2020). *MEK4300 Lecture notes.* URL: `https://mikaem.github.io/MEK4300/content/intro.html` (visited on 04/12/2023) (cited on page 115).

Moser, Robert D. (1994). Kolmogorov inertial range spectra for inhomogeneous turbulence. *Physics of Fluids* **6** (2), pp. 794–801 (cited on page 84).

Motoori, Yutaro and Susumu Goto (2019). Generation mechanism of a hierarchy of vortices in a turbulent boundary layer. *Journal of Fluid Mechanics* **865**, pp. 1085–1109 (cited on pages 5, 22).

Musacchio, Stefano and Guido Boffetta (2014). Turbulent channel without boundaries: The periodic Kolmogorov flow. *Physical Review E* **89** (2), p. 023004 (cited on page 92).

Nastrom, Gregory D., Kenneth S. Gage, and William H. Jasperson (1984). Kinetic energy spectrum of large-and mesoscale atmospheric processes. *Nature* **310** (5972), pp. 36–38 (cited on page 79).

Nelkin, Mark (1994). Universality and scaling in fully developed turbulence. *Advances in Physics* **43** (2), pp. 143–181 (cited on page 14).

Nomura, Keiko K. and Gary K. Post (1998). The structure and dynamics of vorticity and rate of strain in incompressible homogeneous turbulence. *Journal of Fluid Mechanics* **377**, pp. 65–97 (cited on pages 22, 58, 60).

Obukhov, Alexander M. (1941a). On the distribution of energy in the spectrum of turbulent flow. *Doklady Akademii Nauk SSSR* **32** (1), pp. 22–24 (cited on page 14).

—— (1941b). Spectral energy distribution in a turbulent flow. *Izvestiya Akademii Nauk, Seriya Geograficheskaya* **5**, pp. 453–466 (cited on page 14).

—— (1971). Some general properties of equations describing the dynamics of the atmosphere. *Academy of Sciences, USSR, Izvestiya, Atmospheric and Oceanic Physics* **7**, pp. 471–475 (cited on pages 35, 43, 47).

Ohkitani, Koji and Shigeo Kida (1992). Triad interactions in a forced turbulence. *Physics of Fluids A: Fluid Dynamics* **4** (4), pp. 794–802 (cited on page 11).

Ohkitani, Koji and Seigo Kishiba (1995). Nonlocal nature of vortex stretching in an inviscid fluid. *Physics of Fluids* **7** (2), pp. 411–421 (cited on pages 58, 60).

Ohkitani, Koji and Michio Yamada (1989). Temporal intermittency in the energy cascade process and local Lyapunov analysis in fully-developed model turbulence. *Progress of Theoretical Physics* **81** (2), pp. 329–341 (cited on pages 34, 35).

Onsager, Lars (1945). The distribution of energy in turbulence. In: *Minutes of the Meeting of the Metropolitan Section held at Columbia University, New York, November 9 and 10, 1945.* Vol. 68, p. 286 (cited on pages 9, 14, 21).

—— (1949). Statistical hydrodynamics. *Il Nuovo Cimento (1943-1954)* **6** (2), pp. 279–287 (cited on pages 14, 21, 119).

Panton, Ronald L. (2001). Overview of the self-sustaining mechanisms of wall turbulence. *Progress in Aerospace Sciences* **37** (4), pp. 341–383 (cited on page 28).

Parisi, Giorgio and Uriel Frisch (1985). On the singularity structure of fully developed turbulence. In: *Turbulence and Predictability in Geophysical Fluid Dynamics and Climate Dynamics*. Ed. by Michael Ghil, Roberto Benzi, and Giorgio Parisi. Elsevier, pp. 84–88 (cited on page 24).

Parpais, Sylvain and Jean-Pierre Bertoglio (1996). A spectral closure for inhomogeneous turbulence applied to turbulent confined flow. In: *Advances in Turbulence VI*. Springer, pp. 75–76 (cited on pages 84, 88).

Pawar, Suraj and Omer San (2019). CFD Julia: A learning module structuring an introductory course on computational fluid dynamics. *Fluids* **4** (3), p. 159 (cited on page 24).

Payne, Fred R. and John L. Lumley (1967). Large eddy structure of the turbulent wake behind a circular cylinder. *The Physics of Fluids* **10** (9), S194–S196 (cited on page 34).

Pearson, Bruce R., Tarek A. Yousef, Nils Erland L. Haugen, Axel Brandenburg, and Per-Åge Krogstad (2004). Delayed correlation between turbulent energy injection and dissipation. *Physical Review E* **70** (5), p. 056301 (cited on page 27).

Pearson, C. Frederick and Frederick H. Abernathy (1984). Evolution of the flow field associated with a streamwise diffusing vortex. *Journal of Fluid Mechanics* **146**, pp. 271–283 (cited on page 121).

Pinton, Jean-François, Peter C. W. Holdsworth, and Raúl Labbé (1999). Power fluctuations in a closed turbulent shear flow. *Physical Review E* **60** (3), R2452 (cited on page 30).

Podvin, Bérengère (2009). A proper-orthogonal-decomposition–based model for the wall layer of a turbulent channel flow. *Physics of Fluids* **21** (1), p. 015111 (cited on page 34).

Pope, Stephen B. (2000). *Turbulent Flows*. Cambridge University Press (cited on pages 9, 14, 89).

Pullin, Dale I. and Philip G. Saffman (1993). On the Lundgren–Townsend model of turbulent fine scales. *Physics of Fluids A: Fluid Dynamics* **5** (1), pp. 126–145 (cited on page 120).

—— (1998). Vortex dynamics in turbulence. *Annual Review of Fluid Mechanics* **30**, pp. 31–51 (cited on pages 22, 120).

Rackauckas, Christopher and Qing Nie (2017). DifferentialEquations.jl – A performant and feature-rich ecosystem for solving differential equations in Julia. *Journal of Open Research Software* **5** (1), p. 15 (cited on page 49).

Ravelet, Florent, Louis Marié, Arnaud Chiffaudel, and François Daviaud (2004). Multistability and memory effect in a highly turbulent flow: Experimental evidence for a global bifurcation. *Physical Review Letters* **93** (16), p. 164501 (cited on page 30).

Rempfer, Dietmar (2000). On low-dimensional Galerkin models for fluid flow. *Theoretical and Computational Fluid Dynamics* **14** (2), pp. 75–88 (cited on page 34).

Richardson, Lewis F. (1922). *Weather Prediction by Numerical Process*. (Available at `https://archive.org/details/weatherpredictio00richrich`). Cambridge University Press (cited on pages 5, 118).

Rogallo, Robert S. (1981). *Numerical Experiments in Homogeneous Turbulence*. Vol. 81315. National Aeronautics and Space Administration (cited on page 37).

Rössler, Otto E. (1976). An equation for continuous chaos. *Physics Letters A* **57** (5), pp. 397–398 (cited on pages 34, 47).

—— (1979). An equation for hyperchaos. *Physics Letters A* **71** (2-3), pp. 155–157 (cited on pages 34, 47).

Rubinstein, Robert and Timothy Clark (2022). *Reassessment of the Classical Turbulence Closures*. Cambridge Scholars Publishing (cited on pages 89, 90).

Rubinstein, Robert and Timothy T. Clark (2005). Self-similar turbulence evolution and the dissipation rate transport equation. *Physics of Fluids* **17** (9), p. 095104 (cited on pages 84, 90).

Rubinstein, Robert and Timothy T. Clark (2017). “Equilibrium” and “non-equilibrium” turbulence. *Theoretical and Applied Mechanics Letters* **7** (5), pp. 301–305 (cited on page 16).

Rubinstein, Robert, Timothy T. Clark, Daniel Livescu, and Li-Shi Luo (2004). Time-dependent isotropic turbulence. *Journal of Turbulence* **5** (1), p. 011 (cited on page 18).

Saddoughi, Seyed G. and Srinivas V. Veeravalli (1994). Local isotropy in turbulent boundary layers at high Reynolds number. *Journal of Fluid Mechanics* **268**, pp. 333–372 (cited on page 84).

Sadhukhan, Shubhadeep, Roshan Samuel, Franck Plunian, Rodion Stepanov, Ravi Samtaney, and Mahendra Kumar Verma (2019). Enstrophy transfers in helical turbulence. *Physical Review Fluids* **4** (8), p. 084607 (cited on pages 76, 77).

Sagaut, Pierre and Claude Cambon (2008). *Homogeneous Turbulence Dynamics.* Vol. 10. Springer (cited on page 119).

Sano, Masaki and Keiichi Tamai (2016). A universal transition to turbulence in channel flow. *Nature Physics* **12** (3), pp. 249–253 (cited on page 36).

Saw, Ewe-Wei, Denis Kuzzay, Davide Faranda, Alex Guittonneau, François Daviaud, Cecile Wiertel-Gasquet, Vincent Padilla, and Bérengère Dubrulle (2016). Experimental characterization of extreme events of inertial dissipation in a turbulent swirling flow. *Nature Communications* **7** (1), p. 12466 (cited on page 30).

Seshasayanan, Kannabiran, Vassilios Dallas, and Stephan Fauve (2021). Bifurcations of a plane parallel flow with Kolmogorov forcing. *Physical Review Fluids* **6** (10), p. 103902 (cited on page 36).

Seshasayanan, Kannabiran and Paul Manneville (2015). Laminar-turbulent patterning in wall-bounded shear flows: a Galerkin model. *Fluid Dynamics Research* **47** (3), p. 035512 (cited on page 35).

She, Zhen-Su, Eric Jackson, and Steven A. Orszag (1991). Structure and dynamics of homogeneous turbulence: models and simulations. *Proceedings of the Royal Society of London. Series A: Mathematical and Physical Sciences* **434** (1890), pp. 101–124 (cited on pages 58, 60).

She, Zhen-Su and Emmanuel Lévêque (1994). Universal scaling laws in fully developed turbulence. *Physical Review Letters* **72** (3), p. 336 (cited on page 24).

Shih, Hong-Yan, Tsung-Lin Hsieh, and Nigel Goldenfeld (2016). Ecological collapse and the emergence of travelling waves at the onset of shear turbulence. *Nature Physics* **12** (3), pp. 245–248 (cited on page 36).

Siggia, Eric D. (1977). Origin of intermittency in fully developed turbulence. *Physical Review A* **15** (4), p. 1730 (cited on pages 22, 35).

—— (1985). Collapse and amplification of a vortex filament. *The Physics of Fluids* **28** (3), pp. 794–805 (cited on page 22).

Šilnikov, Leonid Pavlovich (1965). A case of the existence of a denumerable set of periodic motions. In: *Doklady Akademii Nauk.* Vol. 160. 3. Russian Academy of Sciences, pp. 558–561 (cited on pages 34, 51).

Šilnikov, Leonid Pavlovich and Andrey Šilnikov (2007). *Shilnikov bifurcation.* URL: `http://www.scholarpedia.org/article/Shilnikov_bifurcation` (visited on 12/15/2022) (cited on page 33).

Silva, Carlos B da and José C. F. Pereira (2005). On the local equilibrium of the subgrid scales: The velocity and scalar fields. *Physics of Fluids* **17** (10), p. 108103 (cited on page 16).

Sreenivasan, Katepalli R. (1984). On the scaling of the turbulence energy dissipation rate. *The Physics of Fluids* **27** (5), pp. 1048–1051 (cited on pages 15, 16).

—— (1998). An update on the energy dissipation rate in isotropic turbulence. *Physics of Fluids* **10** (2), pp. 528–529 (cited on page 16).

Sreenivasan, Katepalli R. and Robert A. Antonia (1997). The phenomenology of small-scale turbulence. *Annual Review of Fluid Mechanics* **29** (1), pp. 435–472 (cited on page 14).

Steiros, Konstantinos (2022a). Balanced nonstationary turbulence. *Physical Review E* **105** (3), p. 035109 (cited on page 16).

—— (2022b). Turbulence near initial conditions. *Physical Review Fluids* **7** (10), p. 104607 (cited on page 16).

Strogatz, Steven H. (2014). *Nonlinear Dynamics and Chaos: With Applications to Physics, Biology, Chemistry, and Engineering*. Studies in Nonlinearity. Avalon Publishing (cited on page 34).

Svirsky, Anton, Corentin Herbert, and Anna Frishman (2023). Two-dimensional turbulence with local interactions: statistics of the condensate. *arXiv preprint*. arXiv: `2305.01574 [flu-dyn]` (cited on page 79).

Tabeling, Patrick (2002). Two-dimensional turbulence: a physicist approach. *Physics Reports* **362** (1), pp. 1–62 (cited on page 19).

Taira, Kunihiko, Steven L. Brunton, Scott T. M. Dawson, Clarence W. Rowley, Tim Colonius, Beverley J. McKeon, Oliver T. Schmidt, Stanislav Gordeyev, Vassilios Theofilis, and Lawrence S. Ukeiley (2017). Modal analysis of fluid flows: An overview. *AIAA Journal* **55** (12), pp. 4013–4041 (cited on page 34).

Taira, Kunihiko, Maziar S. Hemati, Steven L. Brunton, Yiyang Sun, Karthik Duraisamy, Shervin Bagheri, Scott T. M. Dawson, and Chi-An Yeh (2020). Modal analysis of fluid flows: Applications and outlook. *AIAA Journal* **58** (3), pp. 998–1022 (cited on page 34).

Tamai, Keiichi (2016). Big whorls, little whorls. *Nature Physics* (cited on page 6).

Tanogami, Tomohiro and Ryo Araki (2022). Information-thermodynamic bound on information flow in turbulent cascade. *arXiv preprint*. arXiv: `2206.11163 [stat-mech]` (cited on page v).

Tanogami, Tomohiro and Shin-ichi Sasa (2022). XY model for cascade transfer. *Physical Review Research* **4** (2), p. L022015 (cited on page 58).

Tao, Terence (2016). Finite time blowup for an averaged three-dimensional Navier-Stokes equation. *Journal of the American Mathematical Society* **29** (3), pp. 601–674 (cited on page 118).

Taylor, Geoffrey I. (1935). Statistical theory of turbulence. *Proceedings of the Royal Society of London. Series A: Mathematical and Physical Sciences* **151** (873), pp. 421–444 (cited on pages 16, 99).

—— (1938). Production and dissipation of vorticity in a turbulent fluid. *Proceedings of the Royal Society of London. Series A: Mathematical and Physical Sciences* **164** (916), pp. 15–23 (cited on pages 20, 21, 119).

Tennekes, Hendrik and John L. Lumley (1972). *A First Course in Turbulence*. MIT Press (cited on pages 14, 20–22, 88, 128).

Thomas, Vaughan L., Brian F. Farrell, Petros J. Ioannou, and Dennice F. Gayme (2015). A minimal model of self-sustaining turbulence. *Physics of Fluids* **27** (10), p. 105104 (cited on page 34).

Thomas, Vaughan L., Binh K. Lieu, Mihailo R. Jovanović, Brian F. Farrell, Petros J. Ioannou, and Dennice F. Gayme (2014). Self-sustaining turbulence in a restricted nonlinear model of plane Couette flow. *Physics of Fluids* **26** (10), p. 105112 (cited on page 34).

Tinney, Charles E., Mark N. Glauser, and Lawrence S. Ukeiley (2008). Low-dimensional characteristics of a transonic jet. Part 1. Proper orthogonal decomposition. *Journal of Fluid Mechanics* **612**, pp. 107–141 (cited on page 34).

Torre, Alberto de la and Javier Burguete (2007). Slow dynamics in a turbulent von Kármán swirling flow. *Physical Review Letters* **99** (5), p. 054101 (cited on page 30).

Touil, Hatem, Jean-Pierre Bertoglio, and Liang Shao (2002). The decay of turbulence in a bounded domain. *Journal of Turbulence* **3** (1), p. 049 (cited on page 89).

Tsinober, Arkady (1998). Is concentrated vorticity that important? *European Journal of Mechanics-B/Fluids* **17** (4), pp. 421–449 (cited on page 57).

—— (2000). Vortex stretching versus production of strain/dissipation. In: *Turbulence Structure and Vortex Dynamics*. Ed. by John C. Vassilicos and Julian C. R. Hunt. Cambridge University Press, pp. 164–191 (cited on pages 22, 119).

—— (2009). *An Informal Conceptual Introduction to Turbulence*. Vol. 92. Fluid Mechanics and Its Applications. (Second Edition of An Informal Introduction to Turbulence). Springer (cited on pages 14, 22, 23, 122).

Tsinober, Arkady, M. Ortenberg, and L. Shtilman (1999). On depression of nonlinearity in turbulence. *Physics of Fluids* **11** (8), pp. 2291–2297 (cited on pages 22, 119).

Tsuruhashi, Tomonori, Susumu Goto, Sunao Oka, and Tsuyoshi Yoneda (2022). Self-similar hierarchy of coherent tubular vortices in turbulence. *Philosophical Transactions of the Royal Society A* **380** (2226), p. 20210053 (cited on page 22).

Tuckerman, Laurette S., Matthew Chantry, and Dwight Barkley (2020). Patterns in wall-bounded shear flows. *Annual Review of Fluid Mechanics* **52** (1), pp. 343–367 (cited on page 35).

Valente, Pedro C. and Dallas (2017). Spectral imbalance in the inertial range dynamics of decaying rotating turbulence. *Physical Review E* **95** (2), p. 023114 (cited on page 16).

Valente, Pedro C., Ryo Onishi, and Brian M. de Silva (2014). Origin of the imbalance between energy cascade and dissipation in turbulence. *Physical Review E* **90** (2), p. 023003 (cited on page 16).

Valente, Pedro C. and John C. Vassilicos (2012). Universal dissipation scaling for nonequilibrium turbulence. *Physical Review Letters* **108** (21), p. 214503 (cited on page 100).

—— (2015). The energy cascade in grid-generated non-equilibrium decaying turbulence. *Physics of Fluids* **27** (4), p. 045103 (cited on pages 57, 60).

Van Doren, Jorn F. M., Renato Markovinović, and Jan-Dirk Jansen (2006). Reduced-order optimal control of water flooding using proper orthogonal decomposition. *Computational Geosciences* **10**, pp. 137–158 (cited on page 34).

van Veen, Lennaert and Susumu Goto (2016). Sub critical transition to turbulence in three-dimensional Kolmogorov flow. *Fluid Dynamics Research* **48** (6), p. 061425 (cited on pages 51, 53).

van Veen, Lennaert, Genta Kawahara, and Tatsuya Yasuda (2018). Transitions in large eddy simulation of box turbulence. *The European Physical Journal Special Topics* **227** (5), pp. 463–480 (cited on pages 37, 38, 51).

van Veen, Lennaert, Alberto Vela-Martín, and Genta Kawahara (2019). Time-periodic inertial range dynamics. *Physical Review Letters* **123** (13), p. 134502 (cited on pages 22, 30).

Vassilicos, John C. (2015). Dissipation in turbulent flows. *Annual Review of Fluid Mechanics* **47** (1), pp. 95–114 (cited on page 16).

Vela-Martín, Alberto (2019). Entropy, Chaos and Irreversibility in the Turbulence Energy Cascade. PhD thesis. Universidad Politécnica de Madrid (cited on pages 23, 122).

Vela-Martín, Alberto (2022). Subgrid-scale models of isotropic turbulence need not produce energy backscatter. *Journal of Fluid Mechanics* **937**, A14 (cited on page 18).

Vela-Martín, Alberto and Javier Jiménez (2021). Entropy, irreversibility and cascades in the inertial range of isotropic turbulence. *Journal of Fluid Mechanics* **915**, A36 (cited on pages 9, 16, 57).

Verma, Mahendra K. (2019). *Energy Transfers in Fluid Flows: Multiscale and Spectral Perspectives.* Cambridge University Press (cited on page 10).

Vincent, Angela and María B. Meneguzzi (1994). The dynamics of vorticity tubes in homogeneous turbulence. *Journal of Fluid Mechanics* **258**, pp. 245–254 (cited on page 118).

Waleffe, Fabian (1992). The nature of triad interactions in homogeneous turbulence. *Physics of Fluids A: Fluid Dynamics* **4** (2), pp. 350–363 (cited on page 11).

—— (1995). Hydrodynamic Stability and Turbulence: Beyond Transients to a Self-Sustaining Process. *Studies in Applied Mathematics* **95** (3), pp. 319–343 (cited on page 28).

—— (1997). On a self-sustaining process in shear flows. *Physics of Fluids* **9** (4), pp. 883–900 (cited on page 34).

Wan, Minping, Zuoli Xiao, Charles Meneveau, Gregory L. Eyink, and Shiyi Chen (2010). Dissipation-energy flux correlations as evidence for the Lagrangian energy cascade in turbulence. *Physics of Fluids* **22** (6), p. 061702 (cited on page 27).

Wang, Xueying, Hong-Yan Shih, and Nigel Goldenfeld (2022). Stochastic model for quasi-one-dimensional transitional turbulence with streamwise shear interactions. *Physical Review Letters* **129** (3), p. 034501 (cited on page 36).

Wang, Zhu, Imran Akhtar, Jeff Borggaard, and Traian Iliescu (2012). Proper orthogonal decomposition closure models for turbulent flows: a numerical comparison. *Computer Methods in Applied Mechanics and Engineering* **237**, pp. 10–26 (cited on page 34).

Weizsäcker, Carl Friedrich von (1948). Das spektrum der turbulenz bei grossen Reynoldsschen zahlen. *Zeitschrift für Physik* **124**, pp. 614–627 (cited on page 14).

Woodruff, Stephen L. and Robert Rubinstein (2006). Multiple-scale perturbation analysis of slowly evolving turbulence. *Journal of Fluid Mechanics* **565**, pp. 95–103 (cited on pages 18, 84).

Wu, Tong and Wouter J. T. Bos (2022). Cascades of enstrophy and helicity in turbulence without vortex stretching. *Physical Review Fluids* **7** (9), p. 094601 (cited on pages 78, 79, 114).

Wu, Wenwei, François G Schmitt, Enrico Calzavarini, and Lipo Wang (2021). A quadratic Reynolds stress development for the turbulent Kolmogorov flow. *Physics of Fluids* **33** (12), p. 125129 (cited on page 92).

Wu, Xiaohua (2023). New insights into turbulent spots. *Annual Review of Fluid Mechanics* **55**, pp. 45–75 (cited on page 35).

Wyngaard, John C. and O. R. Coté (1972). Cospectral similarity in the atmospheric surface layer. *Quarterly Journal of the Royal Meteorological Society* **98** (417), pp. 590–603 (cited on page 84).

Xiao, Dunhui, Fangxin Fang, Andrew G. Buchan, Christopher C. Pain, Ionel M. Navon, and Ann Muggeridge (2015). Non-intrusive reduced order modelling of the Navier–Stokes equations. *Computer Methods in Applied Mechanics and Engineering* **293**, pp. 522–541 (cited on page 34).

Yalnız, Gökhan, Björn Hof, and Nazmi Burak Budanur (2021). Coarse graining the state space of a turbulent flow using periodic orbits. *Physical Review Letters* **126** (24), p. 244502 (cited on page 34).

Yamada, Michio and Koji Ohkitani (1987). Lyapunov spectrum of a chaotic model of three-dimensional turbulence. *Journal of the Physical Society of Japan* **56** (12), pp. 4210–4213 (cited on page 34).

Yao, Jie and Fazle Hussain (2020). A physical model of turbulence cascade via vortex reconnection sequence and avalanche. *Journal of Fluid Mechanics* **883**, A51 (cited on pages 119, 120).

—— (2022). Vortex reconnection and turbulence cascade. *Annual Review of Fluid Mechanics* **54**, pp. 317–347 (cited on pages 118, 120).

Yasuda, Tatsuya, Susumu Goto, and Genta Kawahara (2014). Quasi-cyclic evolution of turbulence driven by a steady force in a periodic cube. *Fluid Dynamics Research* **46** (6), p. 061413 (cited on pages 32, 37).

Yasuda, Tatsuya and John C. Vassilicos (2018). Spatio-temporal intermittency of the turbulent energy cascade. *Journal of Fluid Mechanics* **853**, pp. 235–252 (cited on pages 57, 60).

Yeung, Pui-Keun, Diego A. Donzis, and Katepalli R. Sreenivasan (2012). Dissipation, enstrophy and pressure statistics in turbulence simulations at high Reynolds numbers. *Journal of Fluid Mechanics* **700**, pp. 5–15 (cited on page 7).

Yeung, Pui-Keun, Katepalli R. Sreenivasan, and Stephen B. Pope (2018). Effects of finite spatial and temporal resolution in direct numerical simulations of incompressible isotropic turbulence. *Physical Review Fluids* **3** (6), p. 064603 (cited on page 7).

Yeung, Pui-Keun, Xiaomeng M. Zhai, and Katepalli R. Sreenivasan (2015). Extreme events in computational turbulence. *Proceedings of the National Academy of Sciences* **112** (41), pp. 12633–12638 (cited on page 7).

Yoneda, Tsuyoshi (2020). *Invitation to mathematical fluid dynamics: From Millennium Problems to turbulence.* Japanese. SGC Library. (米田 剛，数理流体力学への招待: ミレニアム懸賞問題から乱流へ，SGCライブラリ，サイエンス社). SAIENSU-SHA (cited on page 22).

Yoneda, Tsuyoshi, Susumu Goto, and Tomonori Tsuruhashi (2022). Mathematical reformulation of the Kolmogorov–Richardson energy cascade in terms of vortex stretching. *Nonlinearity* **35** (3), p. 1380 (cited on pages 22, 119, 122, 123).

Yorke, James A. and Ellen D. Yorke (1979). Metastable chaos: The transition to sustained chaotic behavior in the Lorenz model. *Journal of Statistical Physics* **21** (3), pp. 263–277 (cited on page 51).

Yoshida, Kyo, Junzo Yamaguchi, and Yukio Kaneda (2005). Regeneration of small eddies by data assimilation in turbulence. *Physical Review Letters* **94** (1), p. 014501 (cited on page 114).

Yoshizawa, Akira (1984). Statistical analysis of the deviation of the Reynolds stress from its eddy-viscosity representation. *The Physics of Fluids* **27** (6), pp. 1377–1387 (cited on page 86).

—— (1994). Nonequilibrium effect of the turbulent-energy-production process on the inertial-range energy spectrum. *Physical Review E* **49** (5), p. 4065 (cited on pages 16, 83, 114).

Zheng, Yulin, Kohtaro Nakamura, Koji Nagata, and Tomoaki Watanabe (2023). Unsteady dissipation scaling in static-and active-grid turbulence. *Journal of Fluid Mechanics* **956**, A20 (cited on page 100).

Zhou, Ye (1993). Interacting scales and energy transfer in isotropic turbulence. *Physics of Fluids A: Fluid Dynamics* **5** (10), pp. 2511–2524 (cited on page 128).

Zhou, Yi, Koji Nagata, Yasuhiko Sakai, Tomoaki Watanabe, Yasumasa Ito, and Toshiyuki Hayase (2020). Energy transfer in turbulent flows behind two side-by-side square cylinders. *Journal of Fluid Mechanics* **903**, A4 (cited on page 16).